Ph.D. Thesis

Université of Limoges

ED 653 - Sciences et Ingénierie (SI)

Institut de Recherche sur les Céramiques (IRCER)

A thesis submitted to University of Limoges
in partial fulfillment of the requirements of the degree of

Doctor of Philosophy

Discipline / Spécialité : Matériaux céramiques et traitements de surface

Presented and defensed by
Munni Kumari

On April 24, 2024

Synthesis and characterization of polysilazane-derived low oxygen content β-SiAlON as host materials for blue- or green-emitting phosphors

Thèse dirigée par Samuel Bernard, Philippe Thomas

In front of a jury composed of:

Reviewers
M. Stéphane Jobic, Directuer de Recherche, CNRS, IMN, Nantes.
M. Michael Deschamps, Professeur, Université d'Orléans, CEMHTI, Orléans.

Examiners
Mme Christel Gervais, Professeure, Sorbonne Université, LCMCP, Paris.
M. Yuji Iwamoto, Professeur, NITech, Nagoya (Japan).
M. Samuel Bernard, Directuer de Recherche, CNRS, IRCER, Limoges.
M. Philippe Thomas, Directuer de Recherche, CNRS, IRCER, Limoges.

Guests
M. Olivier Masson, Professeur, University of Limoges, IRCER, Limoges.

Devoted to my mentors, parents, and friends

I am so clever that sometimes I don't understand a single word of what I am saying.
Oscar Wilde

Acknowledgements

This doctoral thesis was conducted at the Institute of Research for Ceramics (UMR CNRS 7315) in Limoges in collaboration with the Nagoya Institute of Technology, Japan, within the frame of an International Research Project (IRP) "Ceramics Materials for Societal Challenges".

I would like to express my sincere gratitude to Dr. Stéphane Jobic (Director of Research, CNRS, IMN, Nantes) and Prof. Michael Deschamps (University of Orléans, CEMHTI, Orléans) for graciously reviewing the thesis and providing invaluable contributions as reviewers. I also extend my heartfelt thanks to Prof. Christel Gervais (Sorbonne University, LCMCP, Paris) and Prof. Yuji Iwamoto (NITech, Nagoya, Japan) for their meticulous examination of this work.

I would also like to extend my gratitude to Dr. Samuel Bernard, Dr. Philippe Thomas, and Prof. Olivier Masson from the Institute of Research for Ceramics (IRCER) for their supervision and guidance. Over the course of three years, I had a rewarding working experience, learning significantly from their guidance and engaging in insightful discussions on the results.

I would like to express my gratitude to Prof. Yuji Iwamoto and Prof. Tomokatsu Hayakawa of the Department of Life Science and Applied Chemistry at Nagoya Institute of Technology, Japan, for hosting me at NITECH and facilitating the optical characterization. I extend my thanks to LABEX ∑-Lim from University of Limoges for funding my stay in Japan.

Special thanks go to Prof. Christel Gervais from LCMCP at Sorbonne Université in Paris for conducting NMR analyses and contributing to the scientific richness of our collaborations.

I want to express my deep gratitude to the individuals who played crucial roles in this work: the late Marion Vandenhende for heat-treatment and thermal treatments, Marina Soustre for thermogravimetric and powder analyses. I also thank Julie Cornette, Pierre Carles, Yan Launay, Etienne Laborde, and Richard Mayet for their consistent assistance with various installations at IRCER.

A heartfelt thank you to all my colleagues from both labs: doctors, doctoral students, engineers, technicians, and interns. I extend my gratitude to Dr. Gao for help in Japan, especially with documentation and characterization. I also appreciate the master students from Japan, including Shotaro, Miami, Sakurako, and many others, for making my trip memorable and presenting me with a farewell card.

During this thesis, I had the pleasure of working with an outstanding team of people, and I sincerely thank Mélanie for teaching me experiments, Maxime Balestrat, Maxime Cheype, Marwan, Bastian, Marina, Dorian, Fabian, and Florestan. It was also a pleasure to meet Roberta, Abhijeet, and Gabriel, if only for a short time.

I express my gratitude to former interns with whom I exchanged knowledge: FETTAHI Youssef, Sakurako Takazawa, Jin Mizutani, and Shotaro Inazuka.

I also want to thank all my office mates. Best wishes to Marine Cholin and Romain Trihan. Special thanks to those I shared coffee breaks with: Ravikant, Raghvender, Kinga, and everyone else.

I want to thank my family and close friends for always supporting and encouraging me during my thesis. They were there for me when things got tough, and I'm really grateful for their strong support.

Rights

Table of Contents

List of Figures

List of Tables

Introduction

In the modern age, the increasing need for energy driven by population growth has led to a widespread reliance on various fossil fuels to meet this demand. Unfortunately, this substantial dependence on fossil fuels results in the release of large amounts of greenhouse gases into the air when burning. Thus, greenhouse gases trap heat in our atmosphere giving rise to considerable environmental issues. In this context, if we focus our attention on lighting practices, it is worth noting that these practices have played a significant role in exacerbating these problems by driving up energy consumption. Acknowledging the pressing need for viable and effective lighting alternatives for reduced energy consumption and carbon footprint, **white light-emitting diodes (WLED)** have emerged as a revolutionary technology, fundamentally transforming the landscape of illumination.

The exceptional characteristics and advantages of WLED have propelled them to the forefront of modern lighting applications, effectively addressing crucial concerns regarding energy efficiency, lifespan, eco-friendliness, and light management. This is achieved by converting a significantly higher proportion of electrical energy into visible light when compared to traditional incandescent and fluorescent bulbs. This higher efficiency leads to substantial reductions in electricity consumption and, consequently, a noteworthy decrease in carbon emissions, contributing to a future that is more environmentally sustainable. Thus, as we advance toward a more sustainable and technologically advanced future, WLED serve as a symbol of progress, guiding us toward a brighter and more ecologically friendly world.

Phosphors, namely luminescence materials, consisting of a matrix (crystalline host) doped with a small amount of one or more activator ions (luminescent center), are key and technologically important components of WLED devices. Their luminescence properties determine the optical quality of WLED. Therefore, a lot of efforts are devoted in recent years and actually to the design and characterization of novel phosphors with the exploration and development of different emission colors for use in lighting and backlight display sources. Although it is possible to make phosphors with organic light converting materials, all commercial WLEDs use **inorganic phosphors** that are much more robust. In the category of inorganic phosphors, the **rare-earth series of elements**, which are also known as the lanthanides, are ideal for making luminescent centers, because they absorb light at shorter wavelengths (typically, blue and ultra-violet), before efficiently emitting at longer wavelengths. The excellent optical characteristics combined with the minimal thermal quenching of **oxynitride** compounds make

them appropriate host materials for phosphors to meet the technological challenges of the coming decades in the innovation cycle of energy technologies. They play a crucial role, affecting the energy levels of the dopant atoms and thus determining the absorption and emission wavelengths of the phosphor. The SiAlON stands out for phosphor-converted white light-emitting diode (pc-WLED) applications owing to its favorable combination of properties, including high thermal stability and efficient light emission. When SiAlON is doped with rare earth elements, it further enhances its performance, leading to improved color rendering and luminous efficacy, making it a compelling choice for achieving high-quality illumination in pc-WLED applications.

This thesis developed within the MITI (*Mission pour les Initiatives Transverses et Interdisciplinaires*) CNRS organization, lies within the frame of the International Research Project (IRP) 'ceramics materials for societal challenges' between the Institute of Research for Ceramics (IRCER, Limoges-France) and the Nagoya Institute of Technology (NITech, Nagoya-Japan) supported by CNRS.

This thesis entitled 'Synthesis and characterization of polysilazane-derived low oxygen content β-SiAlON ceramics as host materials for blue- or green-emitting phosphors' aims to explore the potential of **a precursor route** named **Polymer-Derived Ceramics (PDC)** to synthesize **β-SiAlON ceramics** as crystalline **host materials** doped with **rare earth cations** including Eu^{2+}, Eu^{3+}, and Ce^{3+}. This international collaboration has facilitated a thorough exploration of the design and characterization of rare-earth doped β-SiAlON phosphors from tailor-made preceramic polymers, paving the way for innovative and sustainable lighting solutions. Thus, the thesis is structured as follows:

- The **chapter 1** represents the **state-of-the-art**. It offers an extensive overview of the literature from the lighting technology to the PDC route. It also delves into the complexities of SiAlON ceramics, examining their crystal structures and properties.
- The **chapter 2** focuses on the **'materials and methods'** part and details the synthesis route from preceramic polymers to rare-earth doped β-SiAlON ceramics as well as the characterization tools which have been investigated in this work.
- The **chapter 3** targets the design of **polymer-derived β-SiAlON ceramics** by investigating the chemical modification of polysilazane with alane (Al source) leading to Al-modified polysilazanes. We conducted systematic studies to characterize these evolutive compounds at each step of the polymer-to-ceramic conversion. Extensive scrutiny of the microstructural properties of final materials is done.

- The **chapters 4 and 5** investigate **rare-earth cation-doped β-SiAlON ceramics** through the chemical modification of the Al-modified polysilazanes and doped with MCl_x (M = Eu, Ce; X = 2 and 3). We characterized the materials at each step of their elaboration process to understand the origin of the photoluminescence properties of β-SiAlON ceramics with Eu^{2+} and Eu^{3+} (Chapter IV) and Ce^{3+} (Chapter V). This comprehensive exploration sheds light on the potential of rare-earth doped β-SiAlON ceramics as advanced materials for next-generation lighting technologies.

The conclusion offers a summary of the major results which have been discussed in the manuscript and propose further perspectives to develop this topic in the frame of our International Research Project (IRP).

Chapter I.

State of the Art

I.1. Introduction

The rapid growth of the global population has led to a significant increase in energy consumption, inducing an immense pressure on fossil fuel reserves and worsening the urgent issue of global warming. According to a report from 2006, greenhouse gas emissions reached an alarming 1900 megatons (Mt) of carbon dioxide (CO_2) annually[1,2]. As a result, there is a pressing need to address this escalating energy demand, particularly in the **realm of lighting where energy consumption is substantial**[2–4]. One promising approach is to develop **highly efficient luminescent materials** to strongly reduce our energy consumption. Research and development play the key role in designing such materials and creating innovative technologies to confront this challenge directly.

By considering that the access to efficient lighting solutions remains unevenly distributed worldwide - a typical North American consumes approximately 100 Mlmh (million lumen-hours) of lighting annually, while a typical Indian consumes only 3 Mlmh[4,5] - projections indicate that by 2030, **the demand for lighting will increase by 80 %**[6–8]. This will inherently result in a doubling of greenhouse gas emissions[4,6,9]. The types of light bulbs used for household lighting contribute significantly to this energy consumption imbalance. For instance, incandescent light bulbs convert only 5 % of their electrical energy input into visible light, with the remaining energy lost as heat[5,10]. Compact fluorescent lamps offer an improvement, reaching around 20 % efficiency as a replacement for short-term incandescent bulbs[11–14]. **White light emitting diodes (WLED)** is the most recent technology for replacing traditional lighting devices like incandescent lamps and fluorescent lamps by virtue of great properties such as no toxic mercury, long lifetime, larger color gamut, higher brightness, high energetic efficiency, high luminescent efficiency, high safety and energy savings[6,8–10,15–17].

Chapter I presents an overview of the evolution of lighting technology over the course of centuries, along a literature review regarding phosphor converted (pc) WLED as a targeted technology of the work. Then, we will introduce SiAlON ceramics which are used as host materials for rare-earth elements and the Polymer-Derived Ceramics (PDC) route used as an innovative synthetic method to prepare β-SiAlON and its phosphors derivatives. Towards the conclusion of this first chapter, we will also provide an overview of the forthcoming chapters in the manuscript.

I.2. Evolution of Lighting Technology

I.2.1. History of lighting technology

Throughout human civilization, lighting has been an integral part of our daily lives, evolving from primitive methods of burning materials to the creation of sophisticated light sources (Figure I.1)[18].

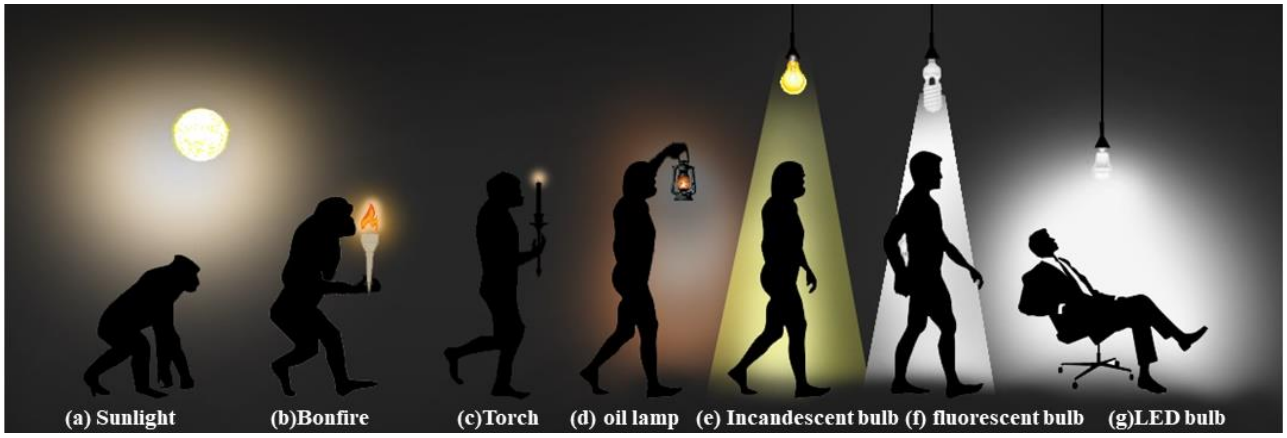

Figure I.1. Evolution of Lighting(a-g) from centuries[18].

The constant evolution of lighting technology has been primarily focused on two domains: luminescence and incandescence. Luminescence involves the process of exciting and de-exciting ionized gases under the influence of flowing electrons, resulting in light emission. Incandescence refers to the emission of visible electromagnetic radiation from a hot body, a phenomenon that occurs as a result of its temperature. These two fundamental principles have driven the relentless progress in the field of lighting, bringing us from humble beginnings to the remarkable illumination technologies we enjoy today[4,9,12].

The modern history of lighting can be traced back to the 19th century, marked by significant milestones in lighting technology. In 1809, Humphry Davy and Faraday made a groundbreaking invention with the creation of the first electric arc lamp, utilizing luminescence[12]. Later, in 1879, Thomas Edison patented the incandescent light bulb, revolutionizing the way we illuminate our surroundings[8]. Edison's efforts not only popularized electricity for mass-produced light sources but also played a crucial role in establishing the electric power grid[5,8,10,12]. Figure I.2. hereafter introduces the brief history of lighting and underlines some milestones in the LED development since 1970 where the first red LED was proposed[19]. Over time, traditional lighting sources like candles and kerosene lamps have gradually been replaced, but incandescent lights and gas discharge lamps still dominate the majority of our lighting environment today (Figure I.3(a))[20].

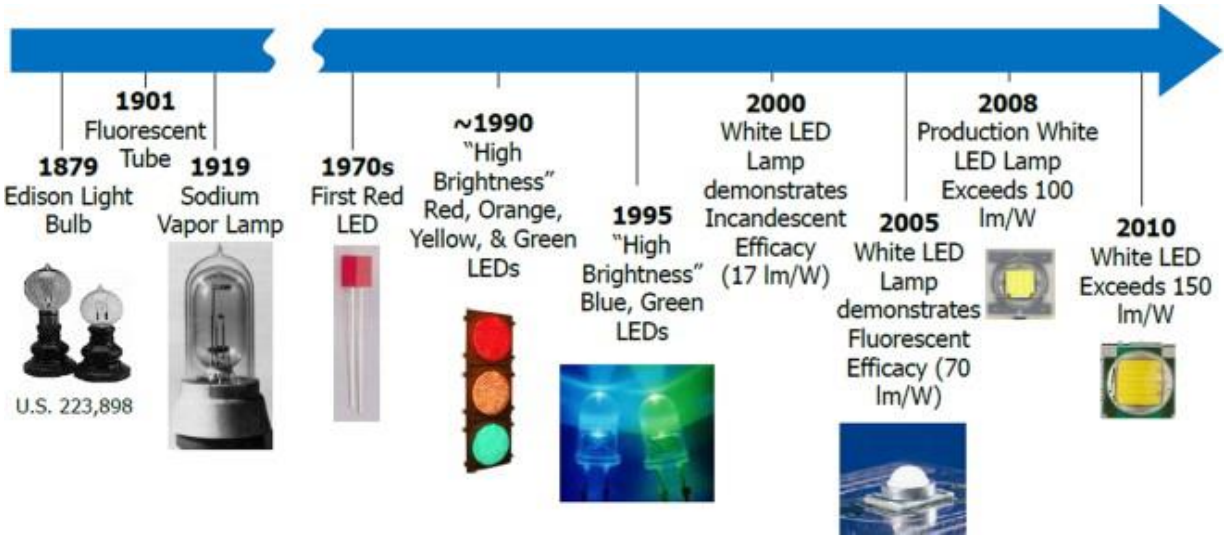

Figure I.2. Brief history of lighting, underlining some milestones in LED development[19].

Figure I.3. (a) Incandescent lamps[20] (b) High-pressure sodium lamp[21] (c) Fluorescent lamps[22] (d) Compact fluorescent lamp[23] (e) LED lights[24].

The journey of lighting advancement can be traced back to earlier demonstrations, such as James Bowman Lindsay's constant electric lighting system using a prototype of the light bulb in 1835 and Edward Shepard's electrical incandescent arc lamp in 1850[14]. Lighting technology has since evolved significantly, resulting in a variety of shapes and sizes based on different materials and prototypes with their advantages and disadvantages as presented successively in Figure I.3: from high-pressure mercury lamp (Figure I.3(b))[21] to Light Emitting Diode (LED)

(Figure I.3(e))[24,25] via low-pressure mercury lamps, specifically fluorescent lamps (Figure I.3 (c))[22] filled with mercury[3,6,8,9,12–14] and then Compact fluorescent lights (CFLs, Figure I.3 (d))[23] offering longer lifetimes and at least five times the efficiency of traditional incandescent bulbs, along with a good color rendering index. It is also important to add that high-pressure sodium lamps emerged in the 1960s as a significant innovation, swiftly supplanting mercury lamps in roadways, streets, and parks. High-pressure sodium lamps delivered superior light efficiency, boasted a longer lifespan of 20,000 hours (Table I.1), and featured a lower color temperature. Despite their popularity, they suffered from poor color rendering properties. Another noteworthy development was the introduction of metal halide lamps, structurally akin to mercury lamps but filled with metal halides in addition to mercury. These lamps provided substantial power output and a generous luminous flux, rendering them suitable for stadiums, shopping malls, industrial facilities, and transportation hubs. Nevertheless, they came with certain drawbacks, including a higher cost and relatively lengthier start-up and shutdown times[4,9,12,13] (Figure I.2). Table I.1 compares the light technologies from metal halides to LED[19,25].

Table I.1. Comparison of all the lights from metal halides to LED[19,25].

Lamp type	Luminous efficiency(lm/W)	Color rendering index	Color temperature/K	Life/h	Adjust the light
Fluorescent lamp	70~90	80	4000	20000	√
High-pressure mercury lamp	35~65	40~60	4500	15000	X
HPS	120~140	25	<2500	20000	√
Metal halide lamp	80~120	60~80	4000	20000	√
Electromagnetic induction lamp	85	>80	2700~6500	15000	X
LED lamp	110~130	>70	2700~6500	50000	√

Currently, many nations are phasing out incandescent light bulbs, with countries like Brazil and Venezuela doing so in 2005, France in 2010, and total elimination of their use in Europe by 2013 and in the United States by 2014[1,4]. This shift is driven by the low energy efficiency of incandescent bulbs. As lighting technology continues to advance, the focus remains on finding efficient, environmentally friendly, and safe lighting solutions to meet the diverse needs of the modern world[7,13,19]. Despite these advancements, it is important to highlight that around 1.5

billion people worldwide still lack access to electricity, making traditional lighting sources a necessity in their daily lives. As we strive for progress in lighting technology, it becomes crucial to address the global challenge of providing access to safe, efficient, and sustainable lighting solutions for all[1].

The Light Emitting Diode (LED), introduced in the sixteens, is now poised to replace traditional light bulbs with Solid-State Lighting (SSL). SSL offers energy and cost savings over incandescent and fluorescent bulbs, revolutionizes lighting design, and enables innovative applications[26]. By 2013, SSL bulbs had become affordable and readily available. Companies like Cree, Soraa, BridgeLux, Samsung, and Sharp entered the SSL market, competing with established bulb manufacturers. The development of SSL products followed a complex path of technological evolution, and this evolutionary process ultimately resulted in the creation of efficient white light[5,10,17,25]. The emergence of **white light-emitting diode (WLED) lamps** as the fourth-generation illumination source may eliminate usage of CFLs and Fluorescent lamps. WLED represent indeed a breakthrough in the quest for more energy-efficient and environmentally responsible lighting solutions[5,10,17,25]. Unlike conventional incandescent bulbs or fluorescent lamps, which rely on heating filaments or gas discharge to produce light, WLED leverage the fascinating properties of semiconductors. When an electric current pass through a semiconductor, it triggers the release of photons, generating bright and energy-efficient illumination[5,6]. As lighting technology continues to advance, the focus remains on finding more efficient, more environmentally friendly, and more safe lighting solutions to meet the diverse needs of our modern world.

I.2.2. From standard LED to pc-WLED

I.2.2.1. Standard LED

Initially, LED could only emit light in a single color, such as red, green, or yellow, which limited their practical applications as general light sources since they were incapable of producing white light. The breakthrough in creating WLED occurred in the 1990s when researchers and engineers successfully combined multiple colors of LED to generate a broad-spectrum white light[27]. One of the early methods used for achieving white light was known as "RGB blending." This technique involved combining red, green, and blue LED in varying intensities to create the appearance of white light to the human eye. While this method was a step towards white light generation, it had its limitations, including issues with color accuracy and efficiency[4,5,13,14].

Researchers therefore continued to explore alternative approaches to produce high-quality white light. Over time, advancements in LED technology and materials science led to the development of more sophisticated methods for creating white light in LED. One of the most successful methods involved using a blue LED coated with a phosphor material. When the blue light from the LED interacted with the phosphor, it generated a broader spectrum of light, including wavelengths that combine to form white light. This **phosphor-converted WLED (pc-WLED)** proved to be highly efficient and offered better color rendering compared to RGB blending[14]. As a result, it became the dominant method for producing WLED, revolutionizing lighting technology and paving the way for numerous applications in various industries. The continuous improvement and commercialization of WLED have since transformed the lighting industry, making them the go-to light source for energy-efficient and environmentally friendly lighting solutions in homes, businesses, outdoor lighting, and displays. Today, white light-emitting diodes are an integral part of our daily lives, contributing to a more sustainable and brighter future[5,10].

I.2.2.2. Phosphor-converted WLED

WLED have undergone remarkable technological advancements, primarily through two main approaches: multi-chip and single-chip systems. The pioneering indium gallium nitride (InGaN) blue LED chip was discovered in 1993 by three exceptional scientists: Isamu Akasaki, Hitoshi Amano, and Shuji Nakamura, earning them the prestigious Nobel Prize in Physics in 2014[28]. Since its introduction, blue LED-driven phosphor-converted (pc-)WLED have found widespread applications. To achieve high-quality pc-WLED, it is essential to utilize phosphors with excellent emission properties under blue light excitation[13].

Initially, the common approach involved combining a blue LED chip with a yellow-emitting phosphor, often utilizing the YAG:Ce^{3+} (YAG: yttrium aluminum garnet, $Y_3Al_5O_{12}$) compound as the preferred commercial yellow phosphor[29]. However, this method suffered from a drawback - a low color rendering index (CRI) due to the absence of red light. To overcome this limitation, a second type of pc-WLED, known as two pc-WLED, was developed by incorporating blue LED chips with two different phosphors emitting green and red lights alongside blue light[27,30,31]. The concept behind phosphor conversion involves the use of a blue LED as the primary light source, coated with a phosphor material. When the blue LED emits light, the phosphor absorbs some blue light and re-emits a broader spectrum of light, including yellow and red wavelengths. The combination of blue light from the LED and the re-emitted yellow and red light creates near-perfect white light visible to the human eye. This technique

revolutionized the efficient and consistent production of white light, enabling a wide range of practical applications for WLED[5,17].

As technology progressed, a new type of pc-WLED has emerged, capitalizing on efficient ultraviolet (UV) LED chips. This approach employs a UV LED chip to excite three types of red, green, and blue-emitting phosphors (Figure I.4). These UV-driven pc-WLED offer highly tunable emission colors and superior optical stability, making them a promising direction for the future development of solid-state lighting[6].

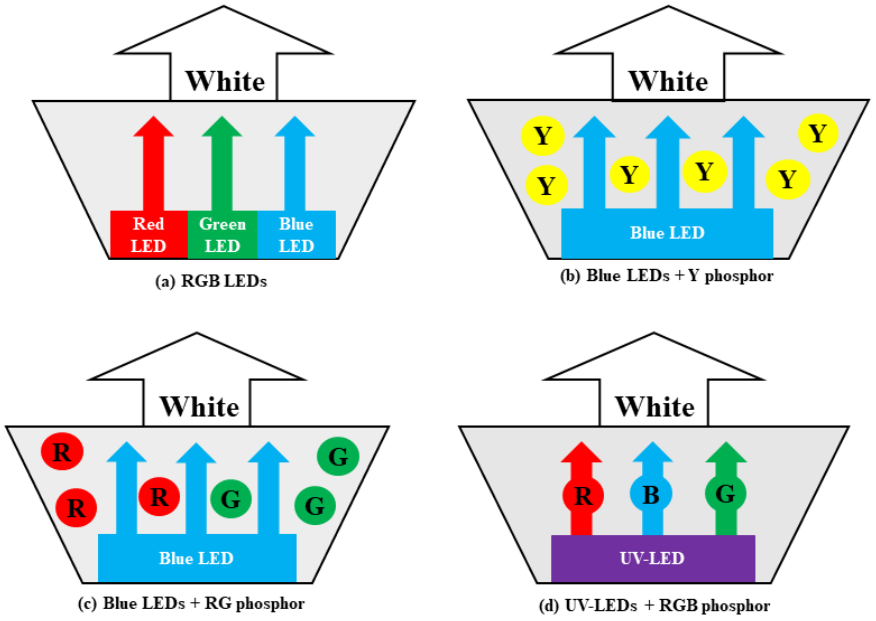

Figure I.4. Phosphor-converted LED types(a)-(d)[6].

To achieve optimal pc-WLED performance, significant efforts are devoted to discovering suitable phosphor materials. Phosphors consist of a host lattice and a small amount of "impurity" dopant acting as the activator. The host materials are typically inorganic, while the activator dopant can be transition metal ions with partially filled d subshells or rare-earth ions with partially filled 4f subshells. Currently, rare-earth-doped phosphors are the most popular choice due to their superior performance[27]. Xie et al. summarized the phosphor selection criteria, including appropriate emission and excitation spectra, high quantum efficiency, stability under varying working conditions, suitable particle size, and cost-effective fabrication[32].

pc-WLED offer numerous benefits over traditional lighting systems. They are highly efficient, with efficiency ten times higher than incandescent bulbs and even surpassing compact fluorescent lights. Furthermore, pc-WLED exhibit remarkable longevity, with a lifetime of up to 100,000 hours, due to the zero degradation of semiconductor materials during operation.

Additionally, pc-WLED are environmentally friendly, as they do not contain hazardous chemicals, making them a sustainable lighting option[6,8,10,16].

As technology continues to advance, researchers and manufacturers have then improved the efficiency, color rendering, and overall performance of pc-WLED, expanding their applications in various fields. Ongoing research and development focus on enhancing efficiency, color quality, and versatility, ensuring pc-WLED remain at the forefront of lighting technology. This is closely dependent on the selection of the **host material** used in phosphors.

I.2.2.3. Host Materials

Several requirements are highlighted to be host materials as luminescent centers in phosphors[27,29,33–35]:

- **Large crystal-field strength:** The host should have a strong crystal-field effect that can split the 5d energy levels of the rare-earth ions[34].
- **Strong covalent chemical bonding:** The host material should form strong covalent bonds with the rare-earth cations, which can lower the energy of the excited states of these ions[36,37].
- **Wide band gap:** The host should have a wide band gap to ensure optical transparency and the ability to accommodate the energy levels of the rare-earth cations[37].
- **Chemical and thermal stability:** The host material must possess excellent chemical and thermal stability to ensure its adaptability in various working environments[27,37].
- **Cost-effectiveness and ease of synthesis:** The ideal host material should be cost-effective and easy to synthesize.

One of the most well-known and widely used phosphor systems is the garnet system, which has the general formula $X_3Y_2Z_3O_{12}$ (X = Ca, Mg, Y, Lu; Y = Al; Z = Si, Ge). YAG: Ce^{3+} is a famous commercial yellow phosphor used in pc-WLED due to its excellent emission properties and thermal stability. Researchers have also explored alternative phosphors within the garnet system, such as $Y_3Al_5O_{12}:Eu^{2+}$ ($YAG:Eu^{2+}$)[38] and $Y_3(Al,Ga)_5O_{12}:Ce^{3+}$ ($YAGG:Ce^{3+}$)[39]. Other common phosphor systems include alkaline earth orthosilicates (e.g., [40]$Sr_2SiO_4:Eu^{2+}$, $Li_2SrSiO_4:Eu^{2+}$)[41], alkaline earth sulfides (e.g., MS: Eu^{2+}, M=Ca,Sr,Ba), and oxo-nitrido-alumosilicates (e.g., α-/β-SiAlON: Eu^{2+}). Recently, novel host crystals with an anti-perovskite type structure (AE_3MO_4F, AE = Sr, Ba, M = Si, Al)[42] have also been reported and gained attention. Oxynitride compounds offer several advantages in the context of phosphor materials when doped with rare-earth elements.

I.2.2.3.1. Oxynitrides as host materials

Phosphors used in WLED are supposed to display major characteristics[27,32,35,43] such as:

- high conversion efficiency and appropriate emission colors,
- good stability against oxidation and moisture,
- low thermal quenching.

Many host inorganic compounds including oxides and sulfides as the major ones have been explored and evaluated for suitability in WLED. Most oxide-based[30,27] phosphors have low absorption in visible light spectrum; thereby, they fail to be coupled with blue LEDs. Sulfates[44] are found to be thermally unstable and moisture sensitive. As a consequence, in the absence of protective coating layer, their luminescence degrades significantly.

In recent years, many researches have emerged in the field of mixed anion systems to develop novel properties. Using the vast, previous knowledge of oxides, the general approach for the design of mixed anion oxidic materials is to substitute in a given phase O^{2-} by its neighbour in the periodic table; F^-, S^{2-} or N^{3-} playing with the differences in electronegativity and polarizability of the anions to modify the electronic structure and therefore the properties[44,45]. To solve these issues related to the use of oxides and sulfides in phosphors, oxynitride-based phosphors have indeed been recently probed as new hosts for WLED.

From the viewpoint of luminescent materials, the **oxynitride system** offers several advantages besides their **good thermal stability**, **highly tunable emission colors**. They include enhanced **nephelauxetic effect,** a **crystal field splitting** (resulting in broader excitation and emission spectra) and a **small Stokes shift** (reducing energy loss). These benefits are attributed to the relatively small electronegativity and high polarizability of the nitrogen ligands[6].

The **nephelauxetic effect**, is influenced by the covalency of the host matrix. When rare-earth cations form a chemical bond with a ligand with high electronegativity, such as oxygen or fluorine, the chemical bond exhibits relatively high ionicity, resulting in a weaker nephelauxetic effect. Conversely, when they interact with ligand ions with lower electronegativity, such as nitrogen, the chemical bond becomes more covalent, and the electron cloud of the 4f orbitals of rare-earth cations expands, leading to a stronger nephelauxetic effect[34,37,46,47]. By considering the Europium (Eu^{2+}) cations as the most popular rare-earth dopants, the outermost electron configuration of Eu^{2+} is 4f, and its luminescence is attributed to the $4f^7 \rightarrow 4f^65d^1$ transition (Figure I.5)[48].

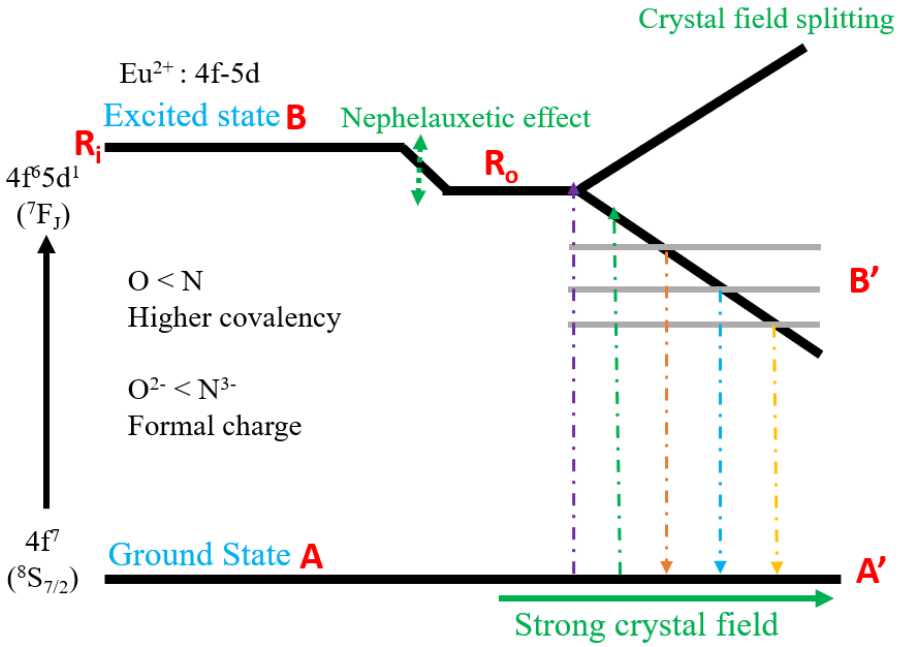

Figure I.5. Crystal field splitting and nephelauxetic effect of Eu^{2+}-doped SiAlON[48].

Thus, in Eu^{2+}-activated phosphors, a large nephelauxetic effect can reduce the electronic transition energy of the 4f-5d transition of Eu^{2+}, causing a redshift in both emission and excitation spectra, which is useful for tuning the emission color of the phosphors[32,34,49–51].

The **crystal field** splitting refers to the energy difference between the highest and lowest energy levels of the split 4f band, and it is influenced by the crystalline environment, including the coordination number of the rare-earth cations, the negative charge of the ligand ions, and the distance between the rare-earth cations and the ligand ions. The presence of the nephelauxetic effect and the crystal field splitting causes rare-earth cations with 4f-5d electronic transitions, such as Ce^{3+} (Figure I.6) and Eu^{2+}, to exhibit broad emission bands[52].

Therefore, host crystals with a large crystal field strength and strong covalency are typically preferred for these phosphors[34,53].During the relaxation process from the excited state to the ground state, the electron loses some energy due to a vibration relaxation leading to a shift in the emission peak of the phosphors.

As illustrated in Figure I.5, the configuration coordinate model of the Eu^{2+} transition in oxynitride host lattice. Electrons in the ground state 4f are excited by light (*e.g.*, blue light at 460 nm) and transfer to the excited $4f^65d^1$ state through process A-B[34,47]. Then, they move to the equilibrium position B' through lattice relaxation before returning to the ground state through B'-A', which emits green light. Due to the vibration relaxation of the lattice, the equilibrium position of the excited state is shifted, represented as R_i-R_o in the configuration

coordinate model shown in Figure I.5 and Figure I.6. This results in the emission process B'-A' having lower energy compared to the absorption process A-B. Consequently, the emission spectra's band maxima shift to the longer wavelength side (lower energy) of the excitation spectra, known as the **Stokes shift** in down-conversion phosphors. Usually, a small Stokes shift is preferred in the host matrix of the phosphors to reduce energy loss and improve quantum efficiencies[41,43,54,55].

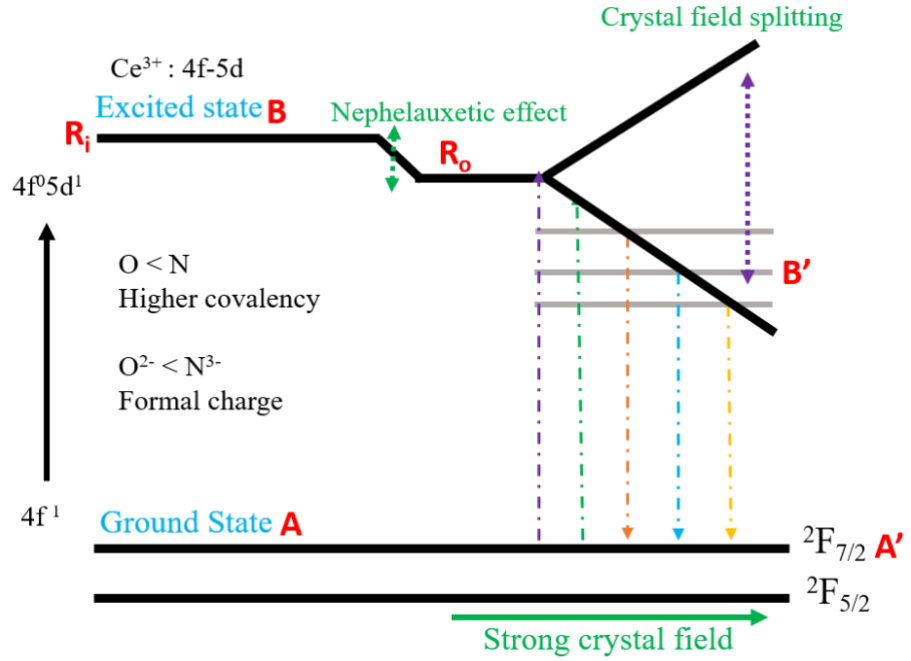

Figure I.6. Crystal field splitting and nephelauxetic effect of Ce^{3+}-doped SiAlON[52].

The class of oxynitrides usually consist in $Si/Al[O/N]_4$ tetrahedra where a partial Si-N in SiN_4 tetrahedra can be substituted by Al-O. These tetrahedron units are stacked together by sharing their corners to form a condensed framework resulting in a structural rigidity contribution to chemical and thermal luminescence stability. Additionally, tetrahedron units have different connecting ways providing different environments and can efficiently adjust the emission and absorption wavelengths[56–59]. As oxynitrides, **rare-earth-doped SiAlON** as host materials reports many advantages, primarily due to the unique properties of nitrogen as a ligand in the SiAlON network[27,36,37,45]. Such materials are described here after.

I.3. Silicon Aluminum OxyNitrides (SiAlON) as host materials for rare-earth luminescent centers

In the category of oxynitrides compounds, SiAlON represent ceramics known to have an incomparable balance of mechanical and thermal properties[60] that enable them to resist to extreme thermal shocks and to keep mechanical integrity at high temperatures. SiAlON

ceramics find high interests in the field of phosphors, because they preserve their chemical composition over a very wide range of doping of activator ions, which favors the adjustment and optimization of the luminescence properties. As a consequence, concentration quenching as observed with most inorganic phosphors is avoided[61]. The following section summarizes the major characteristics and benefits of SiAlON-based materials as well as the different synthesis approaches allowing them to be applied in WLED.

I.3.1. SiAlON compounds: Polymorphisms, crystal structure, doping and synthesis approaches

Besides silicon nitride (Si_3N_4), one of the most significant oxynitride compound is Silicon Aluminum OxyNitride labelled SiAlON with a wide range of composition and crystal structures. They can generally be described as solid solutions of Si_3N_4, SiO_2, Al_2O_3, and AlN. SiAlON compounds typically formed by partial substitution of Si-N bonds by Al-O bonds in a Si_3N_4 hexagonal crystal structure[62–64]. The two main forms of SiAlON are **α-SiAlON**[62,65–68] and **β-SiAlON**[46,62–64,67–71].

The β-SiAlON phase is isostructural with the β-Si_3N_4 phase, i.e. they crystallize with hexagonal symmetry and space group P63/m (earlier studies also proposed the non-centrosymmetric space group P63)[64,65,67,68]. α-SiAlONs crystallize with trigonal symmetry, space group P31c, and is isostructural with α-Si_3N_4. Note that in literature, β- and α-SiAlON are also referenced as β'- and α'-SiAlON. A third form, termed O'-SiAlON has orthorhombic symmetry (space $Cmc2_1$) and is isostructural with Si_2N_2O[72]. Another intergranular phase termed the JEM phase coexisted with α-sialon and studies revealed that the JEM phase forms when La and Ce are used as rare-earth metals[73].

In the following section, we will describe these two polymorphs of SiAlON focusing in particular on their crystal structure, their use as host materials for rare-earth elements and the synthesis methods to produce them and their phosphor derivatives as well. The O'-SiAlON and JEM-SiAlON are briefly described too.

I.3.1.1. β-SiAlON

β-SiAlON is derived from the atomic structure of β-Si_3N_4, where silicon (Si) is replaced by aluminum (Al). To maintain valency compensation, an equivalent concentration of nitrogen (N) atoms is replaced by oxygen (O) atoms[46,67,74,75]. This substitution leads to the formation of β-SiAlON with the general chemical formula $Si_{6-z}Al_zO_zN_{8-z}$, where $0 \leq z \leq 4.2$[62,63,76] and this corresponds to a one for one substitution of Si-N units by Al-O units, with a fixed 3:4 metal to

non-metal ratio. Both types of bonds have similar bond lengths, but the strength of the Al-O bonds is significantly higher than that of Si-N bonds. Because in SiAlON, Al is coordinated as AlO_4, which is different from the AlO_6 coordination found in alumina (Al_2O_3), the strength of the Al-O bonds is approximately 50% higher than in Al_2O_3. This difference in bond strength contributes to the superior properties (chemical stability, and high temperature stability) exhibited by SiAlON materials[64,71,77].

The crystal structure of β-SiAlON is depicted on the Figure I.7. The building units are $SiN_{4-x}O_x$ and $AlN_{4-y}O_y$ tetrahedra forming a corner-shared three-dimensional structure with continuous channels parallel to the c direction. The difference between Si-N and Al-O bond lengths is sufficiently small (1.74 Å for Si-N and 1.75 Å for Al-O) to allow for a large substitution while maintaining the parent β-Si_3N_4 structure, with the lattice parameters increasing with z[62,64,71].

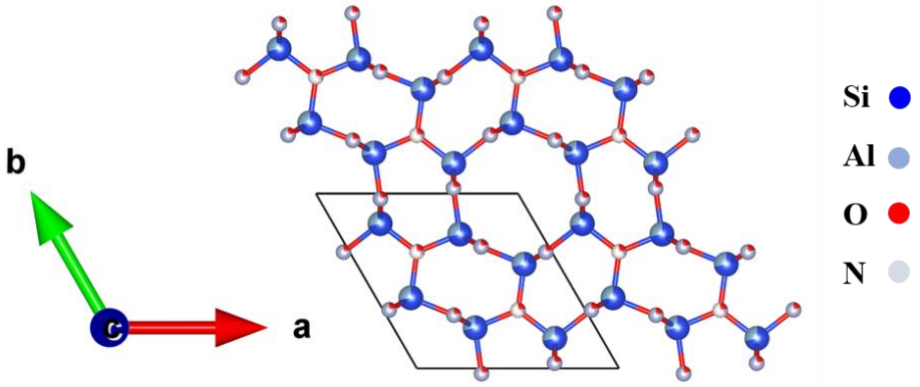

Figure I.7. Projection of the β-SiAlON crystal structure[65].

The β-SiAlON z-values can be determined from the measured lattice parameters using the mean of the following equations[78]:

$$a(Å) = 7.603 + 0.0296\ z \qquad \text{(I-1)}$$

$$c(Å) = 2.907 + 0.0255\ z \qquad \text{(I-2)}$$

Understanding the atomic ordering in SiAlON is of fundamental structural chemistry interest, particularly as SiAlON have found applications in more functional roles, such as being doped with relevant ions to produce efficient phosphor materials. In these cases, the crystal structure, particularly the local coordination around the luminescence centers, plays a crucial role[64,68].

The crystal symmetry of β-SiAlON obtained from X-ray diffraction (XRD) is the same as β-Si_3N_4 but it is highly complex to distinguish Si and Al or O and N atoms as their X-ray scattering factors are too close. The real structure of β-SiAlON is expected to be dominated by local clustering and intermediate-range ordering. The Okatoy model (Extended Huckel theory

(EHT)) suggested that the O atoms are connected to Al forming hexagonal rings and stacked along c directions to form Al-O tubes[53,79]. On the other hand, Dupree et al. investigations of the local structure using NMR analysis evidenced that the Al and O atoms are clustered in slabs within the a-b plane and inserted along the c direction[53,80].

Recently optical properties of SiAlON phases doped with 3d or 4f transition elements have been studied and allowed discussing on the crystal structure of β-SiAlON[40,49,51,81]. It was demonstrated that the luminescence wavelength of an ion in a matrix is strongly influenced by its neighboring anions. This brings us back to a problem that was addressed experimentally many years ago, namely the distribution of the O and N ions in the β-SiAlON structure[82,83]. Some authors concluded that Si is present only in the form of SiN_4 tetrahedra, while Al occurs as AlO_xN_{4-x} tetrahedra with variable x-values[84]. To explain these results, Dupree et al. assumed the presence of microdomains with partitioning of Al–O and Si–N bonds in layers[80]. Sjöberg et al. concluded from NMR and EXAFS measurements that 'the existence of mixed tetrahedra in the SiAlON is likely'[85]. However, all authors agreed that there is a strong tendency for the **formation of Al–O and Si–N bonds** rather than Al-N and Si–O[53,80,83,86].

I.3.1.2. α-SiAlON

The second phase of SiAlON that shares the same crystal structure as α-Si_3N_4 is known as α-SiAlON with the space group P31c[64]. The structure of α-Si_3N_4 has raised questions about its classification as a pure nitride or potentially as an oxynitride, incorporating structural oxygen and vacant lattice or interstitial sites[87,88]. α-Si_3N_4 as determined by different researchers vary widely and large differences in the unit-cell dimensions. The variation in cell parameters are[89,90]:

$$a(Å) = 7.778\text{-}7.818 + 0.001\text{-}0.003z \quad \text{(I-3)}$$

$$c(Å) = 5.617\text{-}5.591 + 0.001\text{-}0.004z \quad \text{(I-4)}$$

The c/a ratio shows variability between 0.715 and 0.725. This variance suggests that fluctuations in unit-cell dimensions are likely linked to compositional differences, specifically in oxygen content[91].

In α-SiAlON, aluminum (Al) replaces silicon (Si) in the tetrahedral structure, with some limited substitution of nitrogen (N) by oxygen (O). The valency requirements are met by adjusting the cations that occupy the interstitial sites. Various cations like yttrium (Y), calcium (Ca), lithium (Li), and neodymium (Nd) can be incorporated into the structure. α-SiAlON is based on α-$Si_{12}N_{16}$ and has an unit cell with the general composition $M_xSi_{12-(m+n)}Al_{(m+n)}O_nN_{(16-n)}$, where x

(<2) is determined by the valence of the M ion (M=Li, Ca, Mg, Y) $0.08<n<0.17$[65,68,75,92] , and m(Al-N) and n(Al-O) units replace (m + n)(Si-N) units. If the valency of M is ν, electroneutrality requires x = m/ν. Various equations in the literature establish connections between the n- and m-values of the α-SiAlON composition and the lattice parameter. Two crystal lattice parameters equations are below[93]:

Crystal lattice parameters(1)[94]:

$$a=7.752 + 0.036m + 0.02n \quad \text{(I-5)}$$

$$c=5.620 + 0.031m + 0.04n \quad \text{(I-6)}$$

Crystal lattice parameters(2)[94]:

$$a=7.752 + 0.045m + 0.009n \quad \text{(I-7)}$$

$$c=5.620 + 0.048m + 0.009n \quad \text{(I-8)}$$

Notably, both equations exhibit significant differences in their dependencies on the n value.

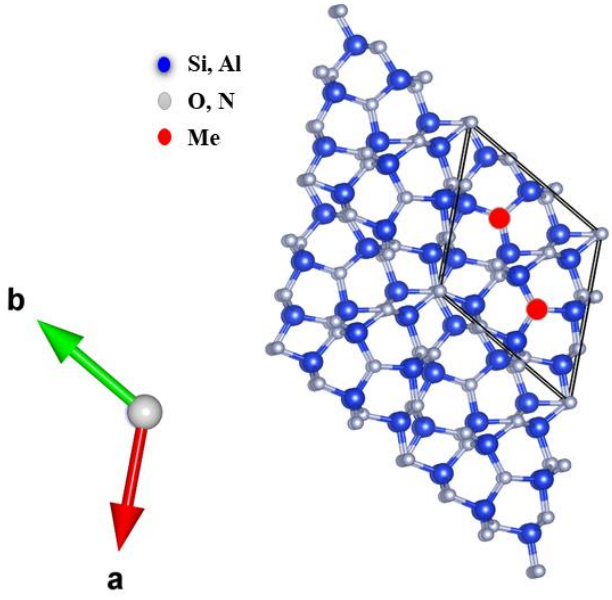

Figure I.8. Projection of α-SiAlON crystal structure[65].

The formation of α-SiAlON is analogous to β-SiAlON, where the α phase precipitates from an oxynitride liquid phase. During this process, the liquid content gradually decreases as the modifying cation becomes integrated into the α-SiAlON structure. In theory, it is possible to obtain a single-phase α-SiAlON, but in practice, some residual intergranular glass may remain after sintering[95,96]. With precise control over composition and sintering conditions, α-SiAlON ceramics with excellent high-temperature properties can be produced. The grains of α-SiAlON

typically exhibit a small, equiaxed morphology, resulting in materials with lower strength and toughness compared to β-SiAlON[62,64,97–99].

I.3.1.3. O'-SiAlON

O'-SiAlON displays the highest oxygen content and exhibits outstanding resistance to oxidation. It is characterized by the Si_2N_2O-type structure with slightly larger unit-cell dimensions[100–102]. O'-SiAlON is identified as a solid solution of Si_2N_2O and Al_2O_3 without changing the orthorhombic structure of Si_2N_2O and the atomic ratio of metal/non-metal = 2/3[64,101,103,104]. The general formula of O'-SiAlON is expressed as $Si_{2-x}Al_xO_{1+x}N_{2-x}$ with very limited solubility of aluminum and oxygen. Various values for x have been reported, ranging from 0.05-0.6[100,102].

I.3.1.4. JEM SiAlON

JEM SiAlON, is a specialized ceramic material and it has phase relationship within the Ln_2O_3–Si_3N_4–AlN–Al_2O_3 systems[105]. JEM SiAlON has consistently been regarded as an intergranular phase in La–Si–Al–O–N systems and denoted by the chemical formula $LaAl(Si_{6-z}Al_z)N_{10-z}O_z$[106]. The orthorhombic structure of JEM SiAlON is characterized by the space group Pbcn, featuring lattice parameters a = 9.4304(7) Å, b = 9.7689(8) Å, and c = 8.9386(6) Å[73]. Within this structure, the Al atoms and (Si, Al) atoms exhibit tetrahedral coordination with (N, O) atoms, forming an $Al(Si,Al)_6(N,O)^{3-}_{10}$ network[27,106]. The La atoms are situated within tunnels extending along the [0 0 1] direction and possess irregular coordination, interacting with seven (N, O) atoms at an average distance of 2.70 Å[27,106–108].

I.3.1.5. Rare-earth element-doped SiAlON and photoluminescence properties

SiAlON materials doped with rare-earth elements have attracted considerable interest for their photoluminescence properties. By incorporating rare-earth dopants into the SiAlON matrix, these materials possess unique optical characteristics, making them ideal candidate for pc-WLED. One remarkable attribute of rare-earth element-doped SiAlON is their adjustable photoluminescence by carefully selecting the rare-earth dopants and tailoring their content in the matrix.

In most studies, β-SiAlON has served as the preferred host material for rare-earth cations because the combination of chemical and thermal stability, tunable properties, wide bandgap, and compatibility with rare-earth ions[27,37]. Especially, it has been mainly used as a host for Eu^{2+}

cations[109,110]. Thus, the subsequent section provides a comprehensive exploration of the history and evolution of rare-earth element-doped β-SiAlON materials with rare-earth cations being Eu^{2+}, Eu^{3+} and Ce^{3+} as studied in the present thesis work. The aim is to provide a detailed look at how β-SiAlON investigations have evolved over time, highlighting advancements. This will help us to understand this material's history, properties, and potential uses as pc-WLED, offering insights into future possibilities.

I.3.1.5.1. β-SiAlON:Eu^{2+}

β-SiAlON:Eu^{2+} has shown outstanding thermal and chemical stabilities and excellent luminescence properties under ultraviolet or blue light irradiations, which make this phosphor a promising candidate for pc-WLED[111]. Thus, β-SiAlON:Eu^{2+} has been well reported as a very interesting narrow-band green phosphor[49,51] and its photoluminescence properties have been shown to be tuned by the modification of z in the β-$Si_{6-z}Al_zO_zN_{8-z}$ ($0 \leq z \leq 4.2$) formula as well as by the concentration of Eu^{2+} activator[34,46].

As an illustration, Xie et al.[112], who reported that both the z value and the Eu^{2+} concentration can be the factors that influence the emission intensity showed that the phase purity and Eu^{2+} solubility of the host β-SiAlON was improved by lowering the z value. Takahashi et al.[113] found indeed that the content of some elements, especially oxygen can affect the emission color and intensity[34,114–116]. Thus, the luminescence properties of this phosphors can be tailored by varying metal/cation and the oxygen/nitrogen ratio in the local environments of Eu^{2+} activator[47,112,117–119]. Finally, questions arise regarding the atomic site of Eu^{2+} and there have been several investigations conducted to evidence the atomic site of Eu^{2+} in β-SiAlON compounds.

The first theoretical prediction done by Li et al. showed that Eu^{2+} ions are situated in the channels parallel to the c-axis and directly connected to adjacent six N atoms[112]. Later, Kimoto et al.[118] directly observed the interstitial position of Eu^{2+} in the large hexagonal channels along the [0001] direction because of the lattice mismatch between Eu^{2+} and the Si^{4+} and Al^{3+} cations with the help of scanning transmission electron microscopy (STEM) techniques[118]. Then, Brgoch et al. proposed that Eu^{2+} ion occupied a distorted 12-coordinate interstitial site in the hexagonal channels by using extended X-ray absorption fine structure (EXAFS) measurements[120]. Recently, Wang et al. reported a highly symmetric EuN_9 coordination polyhedron using first-principal calculations and these coordination environments were directly responsible for electronic characteristic[50]. These researches on β-SiAlON:Eu^{2+} compounds

have suggested that by controlling z value and dopant concentration phase purity and emission intensity can be controlled[32,43].

I.3.1.5.2. β-SiAlON:Eu^{3+}

The choice to focus on Eu^{3+} in this field of research is often influenced by its smaller size compared to Eu^{2+}; thus, allowing it allows them to fit into specific crystal lattices more comfortably, influencing the material's electronic and optical characteristics[81,121,122]. This choice offers advantages such as enhanced luminescence efficiency and stability, making Eu^{3+} a preferred dopant in certain applications over Eu^{2+}. Researchers may prioritize Eu^{3+} for its distinct properties and the benefits it brings to the performance of materials in various contexts, particularly in areas like luminescent materials[108,119,123]. The unique emission properties of Eu^{3+} ions, especially in the visible range, render them valuable for applications like phosphors in LEDs[81,121,124]. Unfortunately, there is a scarcity of reports on β-SiAlON:Eu^{3+} due to spontaneous reduction of Eu^{3+} ions to Eu^{2+} ones in the presence of Al^{3+} cation during the densification process[99,109,125].

In a separate study, Li et al.[43] discovered that the presence of additional Eu^{3+} ions in a β-SiAlON matrix, referred to as "killer sites," negatively affects the emission intensity of β-SiAlON:Eu^{2+} phosphors. By reducing the amount of Eu^{3+}, they successfully improved the green-emitting properties at 540 nm. In fact, most luminescent materials contain a mixture of Eu^{2+} and Eu^{3+} valences, which can lead to reduced luminescence efficiency, particularly for diluted β-SiAlON:Eu^{2+} phosphors[43,126]. Distinguishing the valence of Eu ions based on their emission profiles is not effective, as the luminescence of Eu^{3+} is often quenched and challenging to observe[119,127]. Chen et al.[128] confirmed the coexistence of divalent and trivalent Eu ions in the Ca-doped α-SiAlON lattice through EELS (electron energy loss spectroscopy) investigations. It is reasonable to speculate the coexistence of Eu^{2+} and Eu^{3+} in the channel of β-SiAlON due to the size effect, where the smaller Eu^{3+} can more easily occupy the interstitial site. To enhance the luminescence efficiency of β-SiAlON:Eu^{2+}, reducing the number of luminescence killers (Eu^{3+}) and promoting the reduction of Eu^{3+} into Eu^{2+} is therefore crucial[51,54,119]. This reduction process requires two necessary conditions: first, the trivalent Eu^{3+} ion should replace a divalent cation in the host, and second, the substituted cation should have a similar radius to that of the divalent Eu^{2+} ion. Several approaches have been proposed to initiate the formation of Eu^{2+} from Eu^{3+} in inorganic luminescent materials, such as post-synthesis reduction in a strong reducing atmosphere or high-energy radiation[43,119]. For example, reactions between H_2 and mixed-valent Eu^{2+}/Eu^{3+} ions in glasses have shown to be effective in tailoring the cooperative performance

in single-compound phosphors with well-controlled Eu^{3+} and Eu^{2+} ions[119]. Li. et al.[43] reported that the luminescence efficiency of β-SiAlON: Eu^{2+} can be increased by 1.9% by subjecting it to post-annealing in a N_2-H_2 reducing atmosphere, promoting the reduction of Eu^{3+} to Eu^{2+}.

I.3.1.5.3. β-SiAlON:Ce^{3+}

Because α-SiAlON has large interstitial sites in the crystal structure to accommodate large rare-earth cations like Ce^{3+} for charge compensation, it has been mainly investigated in the past to host Ce^{3+}. However, in the past two decades, β-SiAlON:Ce^{3+} phosphors have attracted a lot of interest due to their distinct luminous characteristics and excellent potential for usage in phosphor-converted WLED (pc-WLED). β-SiAlON:Ce^{3+} have the same chemical properties as β-SiAlON:Eu^{2+}, which is formed by partial substitution of Si and N with Al and O[56,129]. The unique luminescent properties of β-SiAlON:Ce^{3+} phosphors are originated from transition of rare earth ions from ground state ($5d^1$) to exited state ($4f^1$). This transition of ions allows electric dipole transition which provide broad emission. Additionally, absorption and emission properties can be modulated by the host lattice due to strong interaction of the 5d-electron with the neighboring anion ligands. This interaction of ions can also affect symmetry and strength of the crystal field by degree of covalent bonding[56,58,129,130]. These factors lead to the exceptional long-wavelength emission of β-SiAlON:Ce^{3+}.

The first report on β-SiAlON:Ce^{3+} was done by Yurdakul et al.[131,132] and the observations were carried out unexceptionally along the [001] zone axis, which gave only the (x, y)-coordinates of rare-earth ions while the z zone still cannot be specified[131,133–136]. Xu et al.[114] reported that Ce dopants were readily distributed throughout the α-lattice but were scarcely visible within the channels along the [001] direction in the β-grain. Additionally, some reports suggested that emission intensity comes from entire region of β-SiAlON, including defects[137–139]. Recently, Gan et al.[139] reported that the Ce atoms occupy three distinct crystallographic sites. Two of these sites are interstitially located in the c-projected channels at z = 0.5 and z = 0.75, corresponding to 6- and 9-membered coordination centers with N(O) atoms, respectively. Surprisingly, the third site is a substitutional position for Si(Al). The broad emission band at 470 nm is attributed to the 9-coordinated Ce, while the narrow emission at 440 nm originates from the 6-coordinated Ce due to its weaker crystal field, resulting in a red-shift of the emission.

I.3.1.6. Synthesis of SiAlON and SiAlON-based phosphors

Silicon nitride (Si_3N_4) is used to manufacture high-temperature components in some of the most demanding industrial sectors worldwide. However, conventional sintering methods struggle to

produce fully dense and complex Si_3N_4 components, and alternative techniques represent significant additional costs. We may admit that SiAlON ceramics were engineered as a direct solution to these issues: they offer the advantage of easier densification by pressureless sintering compared with β-Si_3N_4 because of the lower eutectic temperature (~1300 °C) within the five-components M-Si-Al-O-N systems where M is Li, Mg, Ca, Y and L_n[62,62–64,71,140,141].

In the 70s, the solid solubility of Al_2O_3 in the β-Si_3N_4 lattice was independently discovered by sintering the powders at 1750 °C in the United Kingdom at the University of Newcastle-upon-Tyne (by Jack and Wilson)[142] and in Japan (by Oyama) around 1971-1972[64,71,143]. Further research conducted at Newcastle and Stuttgart and published four years later (1975–1976) established that β-SiAlON with the formula $Si_{6-z}Al_zO_zN_{8-z}$ where z values ranging from 0 to 4.2[71]. Oyama et al.[144] and Jack et al. made noteworthy findings suggesting that Al^{3+} cations could replace Si^{4+} in β-Si_3N_4 without altering the structure, provided that O^{2-} anions were simultaneously substituted for N^{3-}. These isomorphic solid solutions of β-Si_3N_4, with space group $P6_3$ or $P6_3/m$, were termed β-SiAlON[36,63,64,71].

Following the discovery of β-SiAlON, researchers soon realized that it was also possible to form solid solutions with a structure derived from α-Si_3N_4. This was achieved through the reaction of Si_3N_4 and lithium (Li) with aluminum or lithium aluminate ($LiAlO_2$) with Si_3N_4. It is important to note that the term "SiAlON" is used to describe materials containing Si, Al, O, and N, with a wide range of compositions and crystal structures[64].

I.3.1.6.1. Synthesis methods of SiAlON

In recent times, there has been significant interest in the synthesis of SiAlON ceramics and doped SiAlON powders, with a primary focus on controlling their physical properties and to achieve this, various chemical syntheses have been employed. There are several methods to prepare SiAlON ceramics. They include solid state reaction[145], microwave synthesis method[146], combustion method[146,147], gas reduction and nitridation[92] and carbothermal reduction and nitridation[147,148].

Solid state reaction: The solid-state reaction[100,149] method involves a careful combination of activators, host crystal, high-purity materials, and fluxes. This mixture is subjected to firing in an appropriate atmosphere. Subsequent to the firing process, the resulting blend undergoes crushing, milling, and sieving to remove any excess crushed and large particles. Occasionally, additional treatments are applied to the product's surface. In the synthesis of SiAlON through the solid-state process, reactants like carbonates (e.g., $CaCO_3$, Li_2CO_3), oxides (e.g., Al_2O_3,

Y_2O_3), nitrides (e.g., Si_3N_4, AlN), metals (e.g., Al, Si), and carbides (e.g., SiC) are utilized. The solid-state approach emerges as the most suitable and cost-effective for the large-scale production of SiAlON powders[26,69,100,150] although the main drawbacks of this process are the formation of multiple phases and glassy films at the grain boundaries. The formation of large coarse particles characterized by a diminished surface area and the occurrence of defects that negatively impact luminescence[75,149].

Microwave synthesis method: In microwave synthesis[151–153], rapid and uniform heating of the entire sample is crucial, with energy absorbed instantly. Two types of microwave apparatus are used: conventional ovens with multimode microwaves, and custom-tailored devices with single-mode microwaves focused on a small area. Reactants for SiAlON-based materials preparation via microwaves include various compositions. This method is efficient, saving energy and time, reducing manufacturing costs. Microwave synthesis offers advantages like short sintering time, enabling the development of new synthetic materials. While it promises benefits such as uniform heating, high yield, and energy efficiency, its full potential in large-scale ceramic production has not been fully realized[153]. The reason could be that unless we use a very expensive microwave reactor, they often achieve uneven heating of the solvent, so yields are not reproducible[152,153].

Combustion method: Combustion process[100,154,155], or self-propagating high-temperature synthesis (SHS), is an exothermic reaction method for synthesizing industrial ceramic materials. It eliminates the need for repeated heating and calcinations, relying on the heat evolved from the continuous reaction. This self-sustaining process, ignited by a fuel and oxidizer mixture, is advantageous due to its short sintering time, high purity of final products, simplicity, and low energy consumption. For sustained SHS, the combustion should involve a high-temperature exothermic reaction with an adiabatic temperature (T_{ad}) of ≥ 1800 °C, calculated based on thermodynamic parameters. SiAlON synthesis via SHS employs various reactants, contributing to its efficiency[38,75]. Nevertheless, the drawback arises from the elevated combustion temperatures, causing the melting of Si particles and leading to the complete nitridation process. To address this issue, a substantial quantity (50% by mass) of β-SiAlON product must be introduced. However, this adjustment leads to a reduction in the overall yield of the intended product[75,154,155].

Gas reduction and nitridation: In the gas reduction and nitridation (GRN) process[64,100,148], nitride and oxynitride phosphors are synthesized economically and effectively using commercially available oxides as starting powders. The reaction occurs in a tube furnace with

NH_3-CH_4 or NH_3 gas flows acting as nitriding and reducing agents. Purity of the nitride phosphors phase in the GRN reaction is influenced by parameters like firing temperature, gas flowing rate, heating rate, holding time, and post-annealing. By carefully controlling these processing parameters, highly efficient phosphors with a narrow particle size distribution and small particle size (1 ~ 2 μm) can be produced[92,116,156,157].

Carbothermal reduction and nitridation: The direct nitridation of silicon powder and the carbothermal reduction[147,148,158] of SiO_2 have proven to be effective in producing SiAlON ceramics[157]. Thus, the conventional production of SiAlON ceramics is performed via the powder metallurgy technique using starting powders of α-Si_3N_4, aluminum nitride (AIN), and Al_2O_3 (Eq. I-9).

$$(2\text{-}z/3)\ Si_3N_4 + (z/3)\ AlN + (z/3)\ Al_2O_3 \rightarrow \beta\text{-}Si_{6-z}Al_zO_zN_{8-z} \qquad \text{(I-9)}$$

The sintering mechanism of β-SiAlON ceramics involves dissolution, diffusion, and re-precipitation processes. Initially, Al_2O_3 and AlN react with silica (SiO_2) found on the particle surfaces of α-Si_3N_4 powder, resulting in the formation of a transient liquid phase[65,95,97,150]. The crystallization of α-SiAlON progresses through the dissolution of α-Si_3N_4 into the formed liquid phase, followed by re-precipitation as a solid solution of α-Si_3N_4 and Al_2O_3. Subsequently, the α-SiAlON dissolves into the liquid phase, and β-SiAlON re-precipitates from this transient liquid. The transient liquid is incorporated into the host SiAlON, leading to the final single-phase β-SiAlON ceramics. The α→β phase transformation process typically initiates at 1400 °C and is completed around 1800 °C[95–97,150,156,159].

The high covalency of the Si-N bond results in very low self-diffusivity of Si_3N_4, making it challenging to achieve densification through conventional solid-state sintering. Therefore, during the liquid-phase sintering of β-Si_3N_4, additives such as magnesium oxide (MgO), yttrium oxide (Y_2O_3), and Lanthanum oxide (La_2O_3) are employed to form a liquid phase that facilitates densification. However, the formation of intergranular glassy phases in the final products negatively impacts their high-temperature properties due to the softening of the glass phase above its transition point[65,95,96].

I.3.1.6.2. Synthesis approaches to dope SiAlON

Several studies have been conducted to dope SiAlON, in particular β-SiAlON such as the powder metallurgy route[145] and combustion synthesis[38] method. These studies have explored various chemical compositions and heat treatment conditions to optimize the photoluminescent properties of the phosphors. The concentration of Eu^{2+} and the z value (related to the

composition) have been identified as critical factors in determining the formation of β-SiAlON and the emission properties[55,74,120].

Hirosaki and his colleagues used the powder metallurgy route to fabricate green-emitting β-SiAlON:Eu^{2+} phosphors[86]. They mixed α-Si_3N_4, AlN, and europium (III) oxide (Eu_2O_3) powders and subjected the mixture to heat treatment at 1900 °C for 8 hours under N_2 gas pressure. The resulting phosphors displayed strong green emission centered at 535 nm and showed well-defined rod-like grain morphology. Notably, europium cations were incorporated into the host β-SiAlON lattice rather than existing within the amorphous phase, contributing to the excellent green emission properties[86].

Xie and Hirosaki[27] collaborated to explore the impact of different chemical compositions on β-SiAlON:Eu^{2+} phosphors using the powder metallurgy route[49,51].

In another study, Zhou and colleagues[38] used the combustion synthesis method to rapidly produce β-SiAlON:Eu^{2+} phosphors (Eq. I-10). They achieved single-phase β-SiAlON by adjusting the z value but observed a decrease in Eu^{2+} solubility and green emission intensity with higher z values.

$$Si + N_2 + Si_3N_4 + AlN + Al_2O_3 + SiO_2 + Eu_2O_3 \rightarrow Si_{6-z}Al_zO_zN_{8-z}:Eu^{2+} \qquad \text{(I-10)}$$

The synthesis conditions of β-SiAlON:Eu^{2+} phosphors are rather tough using the conventional solid-state reaction[51] or gas pressure sintering[160] approaches: these methods require very high synthesis temperatures - at least 1900 °C - and a nitrogen pressure (0.5–1.0 MPa). Moreover, the post-grinding treatment is needed to get relatively fine phosphor powders. Finally, only a tiny quantity of Eu^{2+} ions can be accommodated into the host lattice; thereby, there is still a bottleneck to considerably enhance the luminescence efficiency of rare-earth-doped SiAlON. As a consequence, it is a great challenge to develop alternative synthesis routes allowing increasing the luminescent activator content.

I.3.1.6.3. Preliminary works performed within the frame of the International Research Project “ceramics materials for societal challenges” (IRP-CERMAC).

In collaboration with the Nagoya Institute of Technology (NITECH), we recently achieved a breakthrough in synthesizing β-SiAlON:Eu^{2+} phosphors via the Polymer-Derived Ceramics (PDC) route. Our approach involved modifying perhydropolysilazane (PHPS) with $Al(OCH(CH_3)_2)_3$ and $EuCl_2$, forming N-Al bonds at room temperature and initiating N-Eu bond formation above 600 °C with HCl elimination up to 1000 °C in flowing N_2. The resulting phosphors, with a Al/Si ratio of 0.09, exhibited green emission under 460 nm excitation at a

1.48 at% Eu^{2+} concentration[110]. A similar outcome was reported using a two-step synthesis, where PHPS was chemically modified with $Al(OCH(CH_3)_2)_3$ and $AlCl_3$ in xylene at room temperature to 140°C, introducing Al into the PHPS network and controlling oxygen content. This method, combining the polymer-derived ceramics route with a non-hydrolytic sol-gel chemistry, produced β-SiAlON:Eu^{2+} phosphors (z = 0.55) with 0.35 at% Eu^{2+} and led to increased emission intensity[161]. In another report, we demonstrated via high-angle annular dark-field-scanning transmission electron (HAADF-STEM) microscopy the interstitial presence of Eu^{2+} within host β-SiAlON channels along the c-axis[162]. This collective research underscores the significance of the PDC route is tailoring the Eu^{2+} content in the β-SiAlON matrix and, as a consequence the-emission properties of β-SiAlON:Eu^{2+} phosphors[117]. However, PHPS – being highly reactive and expensive – can be unstable in some conditions of experiments which can limit its usage. Furthermore, using oxygen-containing Al source may drastically increase the oxygen content in the final material which is known to affect the stability of SiAlON materials. Thus, we propose the present work that consists to prepare low oxygen content β-SiAlON as host materials of Eu^{2+}, Eu^{3+} and Ce^{3+}.

In conclusion, the conventional powder metallurgy route is mostly investigated for fabricating β-SiAlON based phosphors. One issue of this method is the low rare-earth element content that can be introduced on the host materials. However, improving and designing or tailoring the luminescence properties of known materials for WLED, are challenging tasks. In general, their properties and performance strongly depend on the applied synthesis, phase composition and microstructure. Thus, a progress of the luminescence properties of known materials can be reached through the development of new synthetic routes. This is the core of this PhD thesis work. Developing precursor routes as those we recently investigated within our IRP CERMAC (*see above*) seems to represent a suitable alternative to control the element chemical contents in the final materials - therefore the luminescence efficiency of β-SiAlON:Eu^{2+} - while working under milder heat treatment conditions. This pathway is described here after.

I.4. The Polymer-Derived Ceramic (PDC) route

The era between 1950 and 1980 was at the origin of ceramic studies derived from preceramic polymers called polymer-derived ceramics (PDC). Indeed, the first conversion of molecular precursors into ceramics has been reported in the 1950s by Fritz and Raabe who investigated the thermal decomposition of alkyl silanes, although the initial purpose of this pioneering work was not the synthesis of SiC precursors[163]. Then, in the sixties, Si-based non-oxidic ceramics

derived from molecular precursors and preceramic polymers (although the terms 'preceramic polymers' was not employed at that time) was reported by Ainger and Herbert[164] as well as by Chantrell and Popper[165]. These works are usually considered as the pioneer studies performed in the field of PDC. All these fundamental works led a decade later to the production of silicon carbonitride (Si-C-N) fibers by Verbeek and colleagues[166] and silicon carbide (SiC) fibers by Yajima[167] from polysilazanes and polycarbosilanes, respectively. These works nicely marked the beginning of the new field of PDC and illustrated the contribution of the organosilicon precursor chemistry to the preparation of non-oxide ceramics. Still today, the production of polymer-derived SiC-based fibers is the typical example of the capacity of PDC to be produced industrially. In the intervening years, there has been much activity worldwide in the PDC field; especially by extending the potentialities of the PDC route toward the production of ceramics with compositions other than those containing silicon and with particular shapes, structures and textures by using an original way different from others techniques[168].

I.4.1. The multi-step PDC process

The PDC route implements inorganic/organometallic polymers, denoted as preceramic polymers, which are prepared from well-defined molecular precursors[169].

The main benefits of using molecular precursors and synthesizing preceramic polymers are:

- highest purity of final materials compared with those obtained by traditional powder technology. This is attributed to the use of precursors and polymers which allows easy purification of the reacting species by distillation or crystallization[168].
- high control of the homogeneity, atomic distribution and microstructure of ceramics[170].
- possibility to produce multi-component and hybrid (organic-inorganic) materials[165].
- high versatility in terms of processability because of the possibility to precisely control the physical state and rheological properties of preceramic polymers to be shaped using the same methods as for organic polymers or plastics. Alternatively, the ceramic powders (especially those with a complex composition difficult to prepare using the conventional preparative methods) derived from the preceramic polymers can be used in forming processes as performed through the conventional way of processing ceramics, *e.g.*, sintering[163,171–173].

A flow diagram of the single steps involved in the design of advanced ceramics from molecular precursors and preceramic polymers is shown in Figure I.9[168,169,174]. Processing ceramics via

preceramic polymers involves the synthesis (from molecular precursors as monomers), crosslinking (to form an infusible network) and transformation, *i.e.*, ceramization, *via* pyrolysis of these precursors at relatively moderate temperature, typically at 800-1200 °C, into amorphous covalently bound ceramics. Subsequently, an optional heat-treatment at higher temperature will achieve the crystallization of the amorphous ceramics[172].

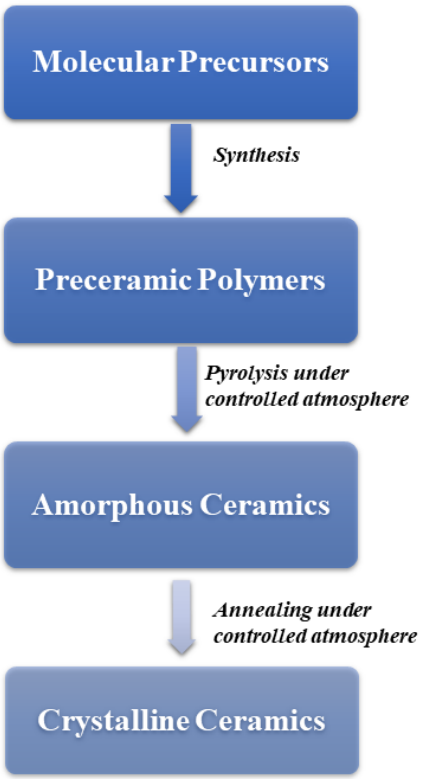

Figure I.9. Flow chart for the formation ceramics by using polymer derived ceramic route.

PDCs mainly belong to the Si-C-O-N system, *i.e.*, silicon carbide (SiC), oxycarbide (SiOC), nitride (Si_3N_4), carbonitride (SiCN) and oxycarbonitride (SiOCN) ceramics (*containing free carbon except nitrides*), using organosilicon polymers, *e.g.*, polycarbosilanes (Si-C backbone, PCS), polysiloxanes (Si-O backbone, PSO), polysilazanes (Si-N backbone, PSZ), as preceramic polymers[64,68,69,74].

The transformation of preceramic polymers into ceramics involves rearrangements, condensation reaction, and/or radical reactions, leading to the cleavage of chemical bonds, formation of new bonds, and elimination of organic groups. This process results in a mass loss that can be important (e.g., 70 %) whereas the polymer-to-ceramic transformation also leads to a significant increase in density[168,169,175]. Therefore, the main issue of preceramic polymers is their volume shrinkage occurring during their conversion into ceramics.

I.4.1.1. Preceramic polymers

Because of their commercial availability and low cost, chlorosilanes of the type $R_{4-x}SiCl_x$ ($1 \leq x \leq 4$) have been largely investigated as monomers for the synthesis of polysiloxanes by hydrolysis of Si-Cl bonds followed by subsequent condensation of the Si-OH intermediates to form Si-O-Si groups in polysiloxanes (Figure I.10)[176]. If ammonia is used instead of water, a similar reaction - known as ammonolysis - takes place and silylamines are formed, which can condense to give polysilazanes (Figure I.10)[70]. It should be mentioned that chlorosilanes can be mixed together to form blended precursors or co-polymers[177]. In addition, they can be modified before their reaction to add specific elements to the future polymer network such as boron using, for instance, borane dimethyl sulfide as a Lewis acid-base complex. Concerning the synthesis of SiC precursors, the common approach, extensively developed by Yajima et al.[167], consists of the synthesis of polysilanes (PS) via the Wurtz coupling method using chlorosilanes and alkali metals. The polysilanes are further converted into polycarbosilanes (PCS, $(-SiR_1R_2CH_2-)_n$) and more precisely '$[-SiH(CH_3)CH_2-]_n$' upon thermolysis through the Kumada rearrangement[167,178]. More complex structures containing Si, C, N and/or O in the three-dimensional polymeric network such as polysilylcarbodiimides can also be produced by non-oxidic sol–gel condensation reaction of chlorosilanes with bis(trimetylsilyl)carbodiimide $(Me_3Si)_2NCN$ as illustrated[179].

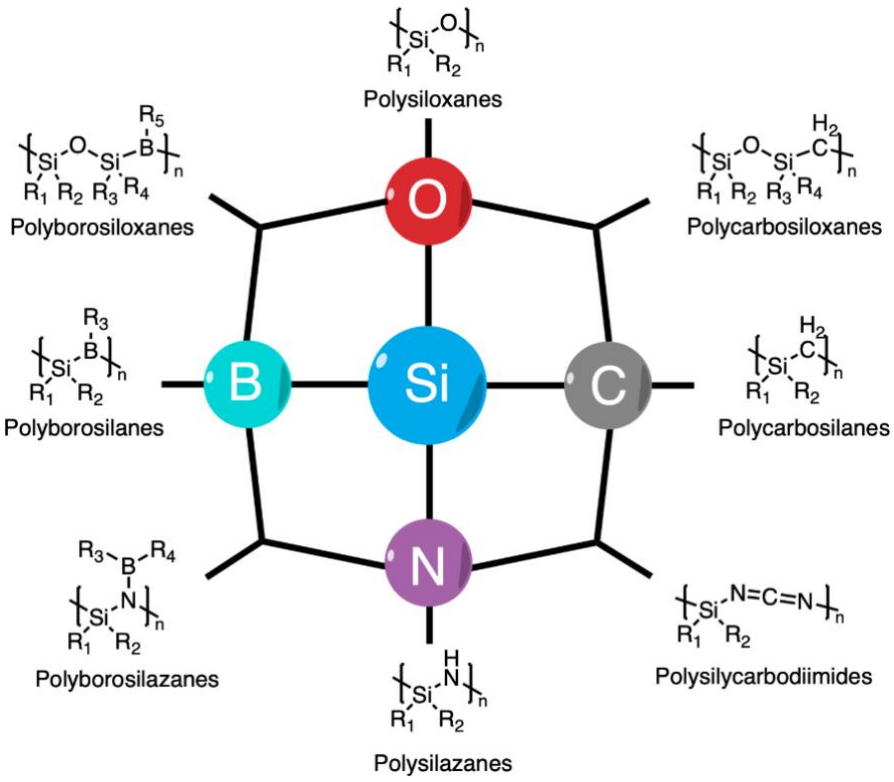

Figure I.10. Organosilicon precursors in the Si-C-N-O system ($R^1 = R^2 = H$, CH_3, $CH{=}CH_2$, *etc.*)[180].

Reports on the preparation, classification, and characterization of silazanes and polysilazanes date back to as early as 1885[168,174]. Subsequent studies continued until 1957, leading to the discovery of numerous cyclic oligosilazanes, which have been extensively reviewed in various articles[169,174,181]. During the 1950s and 1960s, researchers explored the synthesis of oligo- and polysilazanes as potential analogs to siloxanes and as precursors for silicon (carbo)nitrides and related materials. Today, silazanes are of particular interest because of their applications as silylating agents in synthetic chemistry and as single-source precursors for the design of ceramic materials prepared through vapor-, liquid-, and solid-phase pyrolysis[70,76,182]. Furthermore, their cost, although superior to that one of polysiloxanes – is significantly lower than that of polycarbosilanes. They are considered as precursors of SiAlON phases.

I.3.2.2. Thermo-chemical conversion of preceramic polymers into ceramics

Once the synthesis of preceramic polymers has been achieved, a thermo-chemical conversion is needed to deliver ceramics in amorphous state. The conversion of the preceramic polymers into amorphous ceramics usually consists of two steps: i) cross-linking processes at low temperatures (100-400 °C) leading to infusible hybrids, *i.e.*, organic-inorganic networks; and ii) ceramization at higher temperatures by pyrolysis up to 800-1200 °C and a optional subsequent annealing at high temperatures leads to equilibrium (crystalline) ceramics[172].

Cross-linking reduces the loss of low molecular weight components of the preceramic polymer, *i.e.,* oligomers, as well as their fragmentation processes during the further pyrolysis achieving the ceramization. Cross-linking is usually thermally activated *via* addition, substitution or condensation reactions using the reactive groups that did not react at the polymer level, *i.e.,* reactive groups with latent reactivity. In addition to this classical way, it can be assisted by the reactivity of the atmosphere, *e.g.,* ammonia, chlorine, *etc.,* with functional groups, or activated by an external process, *e.g.,* electron beam, UV, plasma, ….

The ceramization process of the cross-linked precursors involves a complex sequence of chemical and physical changes in which polymers evolve toward amorphous covalently-bonded ceramics. This occurs through various types of reactions mainly associated with the release of gaseous by-products from the reaction between the different functional groups present in the polymeric network[165,171–173]. The evolution of gaseous byproducts involves a weight loss upon the heat treatment. The ceramic yield, represented by ($m_{ceramic}/m_{polymer}$) x100 %, is a subject of major importance as it decides the general applicability of preceramic polymers as ceramic precursors[172]. The reactions which occur during ceramization can be investigated by means of

in-situ characterization, *e.g.,* gas chromatography-mass spectroscopy coupled with thermogravimetric analyses and *ex-situ* methods such as solid-state NMR and FTIR spectroscopies, and elemental analyses of pyrolysis intermediates isolated at different temperature during the conversion process. This combined characterization approach allows learning more about the mechanisms involved in the polymer-to-ceramic conversion.

The crystallization investigated by X-ray diffraction coupled with Raman spectroscopy and transmission electron microscopy can be not required for some organosilicon polymer-derived compositions. The reason is explained below.

I.4.1.2. Microstructural feature of PDC

Organosilicon polymers (*air- and moisture-sensitive compounds except those with oxygen in their backbone (e.g., polysiloxane)*) mostly drive towards non-equilibrium materials[183,184] through phenomena which cannot be found in other more conventional processes; thereby leading to new and frequently surprising material properties. Thus, the thermo-chemical conversion of preceramic polymers leads to amorphous structure which form a specific state which can be "isolated". Alternatively, it can represent an intermediate step toward the formation of the desired crystalline ceramics composed of thermodynamically stable phases corresponding to the overall composition of the amorphous network.

As an illustration, polymer-derived Si-O-C glasses, composed of a network of SiO_xC_{4-x} tetrahedra (*i.e.,* SiO_4, SiO_3C, SiO_2C_2, $SiOC_3$, and SiC_4) incorporating both Si–C and Si–O but no C–O bonds, are X-ray amorphous after pyrolysis and represent a typical example of a single-component PDC with an amorphous structure that persists up to very high temperatures[185,186]. The small amount of crystallization observed at T > 1500 °C produces SiC as a result of a carbothermal reaction between SiO_2 and C[141,187,188]. Similar observations can be made with Si-C-N materials as a second typical example of a single-component PDC with an amorphous structure that persists up to very high temperatures. The microstructure of polysilazane-derived Si-C-N ceramics (prepared at 800-1200 °C) consists of an amorphous Si-C-N matrix with tetrahedrally coordinated Si atoms bonded to either nitrogen or carbon or a mixture of carbon and nitrogen and can be therefore designated as SiC_xN_{4-x} and referred to a network of mixed bond tetrahedra as for Si-O-C systems (Figure I.11)[189]. Upon further heat-treatment, Si-C-N materials remain stable up to 1400-1500 °C; before starting to crystallize into Si_3N_4 that reacts with free carbon to form SiC. In contrast, Si-C-N ceramics derived from polysilylcarbodiimides do not contain any significant concentration of mixed bond tetrahedra[190] as previously described

for polysilazane-derived Si-C-N ceramics. Their microstructure is rather composed of nanodomains (1−3 nm in size) of amorphous Si_3N_4 and amorphous carbon (a-C) which is responsible for stability against crystallization at temperatures higher than those characteristics of the polysilazanes-derived ceramics (Figure I.11)[189].

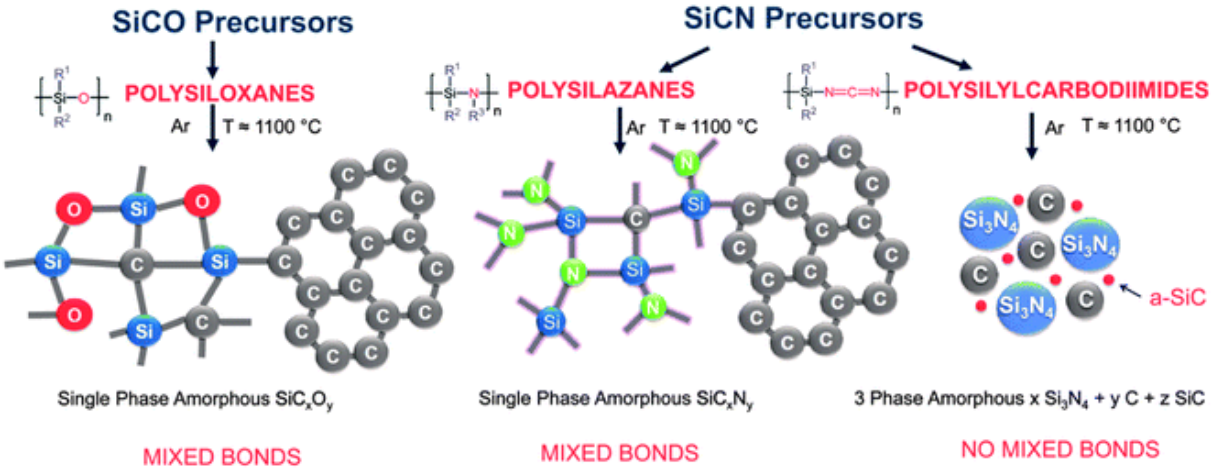

Figure I.11 Precursors used for the synthesis of polymer-derived Si-O-C and Si-C-N ceramics and sketches of the microstructure of their derived ceramics when pyrolyzed at 1100 °C under argon atmosphere[189].

The previous examples show that the microstructural feature of PDC is complex and they can consist of one single-phase component, *i.e.*, with a uniquely-defined chemical composition, or as a multi-component material composed of two or more phases, including solid solutions, composites and nanocomposites. The structures which are generated in PDCs are closely related to the temperature at which polymers have been heat-treated, to the nature of the atmosphere and to the polymer composition and structure[177,189,191,192].

Based on the possibility to tailor the microstructure of PDC, they can fulfill certain functions for applications requiring particular physical-chemical properties such as controlled thermal, electric, optical, magnetic, catalytic properties. As an illustration, PDC offer a panel of applications such as reinforcing agent[191], thermal barrier coating systems[172], membranes[193], catalysts[194], electrocatalysts[195], solar receivers[196] or thermoelectric materials[197], etc..

Such properties can be exacerbated through their interest to form complex shapes by playing with the rheology of polymers[198,199] in ways not realizable/compatible with other ceramic preparative methods. As an illustration, using additive manufacturing, on-demand 3D architectures can be designed[200–202]. However, we will not enter in details in this major characteristic which has been not investigated in the present thesis.

SiAlON ceramics can be prepared from preceramic polymer. However, the number of reports devoted to polymer-derived SiAlON ceramics is rather poor.

I.4.1.3. Polymer-derived SiAlON

Although the existence of polymer-derived SiAlON in an amorphous phase was assumed only on the basis of the chemical analysis in 1988[203], it is better to can consider that the first report appeared in 1992 *via* the modification of a polycarbosilane with aluminum alkoxide. The synthesis was followed by a pyrolysis in flowing ammonia at 1000 °C and then from 1000 to 1500 °C in flowing nitrogen[104]. β-SiAlON, as identified by X-ray diffraction after pyrolysis to 1500 °C, grew from amorphous silicon nitride network in which very fine amorphous alumina-based clusters were dispersed in the sample produced at 1000 °C. Later, a polyaluminosilazane was synthesized by the reaction of perhydropolysilazane (PHPS) with (ethyl acetoacetate) aluminumdiisopropoxide[204]. As in the previous report, amorphous SiAlON was obtained by pyrolysis of this polymer in a stream of ammonia to 1000 °C before the crystallization into O'-SiAlON (Si_2N_2O type-structure)[65,205] or JEM SiAlON (mullite type-structure)[65,106,205] upon heat treatment at 1500 °C in flowing nitrogen. In 2012, Parcianello et al.[206] reported the production of virtually pure β-SiAlON ceramics from a mixture of commercially available polysilazanes (to adjust the carbon content in the precursor) and γ-Al_2O_3 nanopowders pyrolyzed in nitrogen atmosphere in the 1300 °C–1600 °C range. In the two first reports, a large excess of oxygen was identified which is known to affect the SiAlON stability[151]. This is mainly related to the use of alkoxide compounds as aluminum complexes. In the last report; residual alumina is not excluded. This approach was also applied to polycarbosilane which was combined with aluminum hydroxide ($Al(OH)_3$) nanoparticles derived from Al(O-secBu)$_3$ to form SiAlON-based ceramics[209].

As shown previously, all the used aluminum complexes are based on oxygen which can introduce a relatively high oxygen content in the derived SiAlON sample. Therefore, in parallel to the work published with our colleagues from NITech, we have focused on the use of Durazane® 1800 and its reaction with an oxygen-free aluminum complex. To our knowledge, this has never been investigated for SiAlON. This is described in the Chapter III of this manuscript. Then, we explored the insertion of rare-earth elements in the Al-modified Durazane® 1800 in order to develop the photoluminescence properties of the derived phosphors as detailed in Chapter IV and V.

I.5. Conclusions

After a first section devoted to the evolution of lighting technologies, the major content of this first chapter dealt with two parts providing a literature survey of the major works done in the topic of SiAlON-based phosphors including their synthesis, microstructure and photoluminescence properties. Then, we focus our attention on the PDC route which has been investigated in this thesis to prepare SiAlON-based phosphors. Designing matter from atomistic to macroscopic scale is a unique attribute of the PDC route to solve the problems arising from ceramic manufacturing with traditional powder-based technologies. In particular, it allows a precise control over the chemical compositions and microstructure of advanced ceramics. Thus, the study described in this manuscript centers around the synthesis of β-SiAlON ceramic and rare-earth doped β-SiAlON ceramics with Eu^{2+}, Eu^{3+} and Ce^{3+} as doping elements through the exploitation of the chemistry of preceramic polymers.

Following the Chapter II which describes the experimental part, the 3rd chapter focuses on the synthesis of β-SiAlON ceramics by leveraging the reactivity between a commercially available polysilazane, Durazane1800, and an alane $AlH_3NC_2H_5(CH_3)_2$. Through a pyrolysis at 1000 °C in flowing ammonia, amorphous ceramics are formed. The subsequent annealing at 1600 °C for 2 hours under an N_2 atmosphere results in the formation of low oxygen content β-SiAlON. Characterization of the polymers involves techniques such as FTIR, NMR, elemental analysis, and TG, while the ceramics are characterized using NMR, elemental analysis, XRD, SEM, and TEM.

The 4th chapter outlines the formation of Eu-doped β-SiAlON ceramics via the use of rare-earth dopants derived from $EuCl_2$ and $EuCl_3$. Doping of low oxygen content β-SiAlON (prepared in Chapter III) occurs in the early stage of the process; thereby, at the molecular level. Characterization techniques, consistent with the previous chapter, are completed by optical property assessments, including lifetime measurements, quantum efficiency, photoluminescent emission, and excitation properties.

The 5th and final chapter is dedicated to the formation of Ce-doped low oxygen content β-SiAlON ceramics using $CeCl_3$ as rare-earth element precursor. The doping procedure and subsequent characterization procedures remain congruent with those discussed earlier.

Bibliography

(1) DTI, H. *The Energy Challenge Energy Review Report 2006*; Tech. rep., Department of Trade and Industry, UK, 2006.

(2) Energy, R. Energy Efficiency Trends in Residential and Commercial Buildings. **2010**.

(3) Klobut, K.; Ikäheimo, J.; Ihonen, J. Micro-CHP Technologies for Distributed Generation. *Int. Energy Agency Demand-Side Manag. Programme* **2012**, 1–57.

(4) Zissis, G.; Kitsinelis, S. State of Art on the Science and Technology of Electrical Light Sources: From the Past to the Future. *J. Phys. Appl. Phys.* **2009**, *42* (17), 173001.

(5) Sanderson, S. W.; Simons, K. L. Light Emitting Diodes and the Lighting Revolution: The Emergence of a Solid-State Lighting Industry. *Res. Policy* **2014**, *43* (10), 1730–1746.

(6) McKittrick, J.; Shea-Rohwer, L. E. Down Conversion Materials for Solid-State Lighting. *J. Am. Ceram. Soc.* **2014**, *97* (5), 1327–1352.

(7) Wang, L.; Xie, R.-J.; Suehiro, T.; Takeda, T.; Hirosaki, N. Down-Conversion Nitride Materials for Solid State Lighting: Recent Advances and Perspectives. *Chem. Rev.* **2018**, *118* (4), 1951–2009.

(8) Nakamura, S.; Krames, M. R. History of Gallium–Nitride-Based Light-Emitting Diodes for Illumination. *Proc. IEEE* **2013**, *101* (10), 2211–2220.

(9) Jia, Z. Comparison on Lamp Characteristics of Highway Tunnel Lighting System. In *IOP Conference Series: Earth and Environmental Science*; IOP Publishing, 2020; Vol. 510, p 052095.

(10) Chang, M.-H.; Das, D.; Varde, P. V.; Pecht, M. Light Emitting Diodes Reliability Review. *Microelectron. Reliab.* **2012**, *52* (5), 762–782.

(11) Kalyani, N. T.; Dhoble, S. J. Organic Light Emitting Diodes: Energy Saving Lighting Technology—A Review. *Renew. Sustain. Energy Rev.* **2012**, *16* (5), 2696–2723.

(12) Humphreys, C. J. Solid-State Lighting. *MRS Bull.* **2008**, *33* (4), 459–470.

(13) Patel, P. Solid-State Lighting: The Future Looks Bright. *MRS Bull.* **2011**, *36* (9), 678–680.

(14) Schubert, E. F.; Kim, J. K. Solid-State Light Sources Getting Smart. *Science* **2005**, *308* (5726), 1274–1278.

(15) Xu, J.; Funahashi, S.; Takahashi, K.; Nakanishi, T.; Hirosaki, N.; Takeda, T. Cyan-Emitting Sialon-Polytypoid Phosphor Discovered by a Single-Particle-Diagnosis Approach. *ECS J. Solid State Sci. Technol.* **2021**, *10* (11), 116002.

(16) Farsakoglu, O. F.; Hasirci, H. Y. Energy Optimization of Low Power LED Drivers in Indoor Lighting. *J Optoelectron Adv Mater* **2015**, *17*, 816–821.

(17) Schubert, E. F. *Light-Emitting Diodes*; E. Fred Schubert, 2018.

(18) *Molfino*.

(19) Tsao, J. Y.; Coltrin, M. E.; Crawford, M. H.; Simmons, J. A. Solid-State Lighting: An Integrated Human Factors, Technology, and Economic Perspective. *Proc. IEEE* **2010**, *98* (7), 1162–1179.

(20) *Glow realistic lamps incandescent light hang bulb vector image on VectorStock*. VectorStock.

(21) *high pressure sodium lamp HPS orange light, close-up view*.

(22) *Ballast And Fluorescent Lights*. indiamart.com.

(23) *Phasing Out Fluorescent Light Bulbs*.

(24) *J. Pinto & Associates, Inc. - Ophthalmic Consultant and Ophthalmology Practice Management Specialist, Ophthalmolgy Consulting, Ophthalmology Consultant, Strategic Planning for Ophthalmologists*.

(25) Yeh, N. G.; Wu, C.-H.; Cheng, T. C. Light-Emitting Diodes—Their Potential in Biomedical Applications. *Renew. Sustain. Energy Rev.* **2010**, *14* (8), 2161–2166.

(26) Azevedo, I. L.; Morgan, M. G.; Morgan, F. The Transition to Solid-State Lighting. *Proc. IEEE* **2009**, *97* (3), 481–510.

(27) Xie, R.-J.; Hirosaki, N. Silicon-Based Oxynitride and Nitride Phosphors for White LEDs—A Review. *Sci. Technol. Adv. Mater.* **2007**, *8* (7–8), 588.

(28) Kamarei, Z. B. Analysis for Science Librarians of the 2014 Nobel Prize in Physics: Invention of Efficient Blue-Light-Emitting Diodes. *Sci. Technol. Libr.* **2015**, *34* (1), 19–31.

(29) Ţucureanu, V.; Munteanu, D. Enhanced Optical Properties of YAG: Ce Yellow Phosphor by Modification with Gold Nanoparticles. *Ceram. Int.* **2019**, *45* (6), 7641–7648.

(30) Van De Haar, M. A.; Tachikirt, M.; Berends, A. C.; Krames, M. R.; Meijerink, A.; Rabouw, F. T. Saturation Mechanisms in Common LED Phosphors. *ACS Photonics* **2021**, *8* (6), 1784–1793.

(31) Yamada, S.; Emoto, H.; Ibukiyama, M.; Hirosaki, N. Properties of SiAlON Powder Phosphors for White LEDs. *J. Eur. Ceram. Soc.* **2012**, *32* (7), 1355–1358.

(32) Xie, R.-J.; Hirosaki, N.; Li, Y.; Takeda, T. Rare-Earth Activated Nitride Phosphors: Synthesis, Luminescence and Applications. *Materials* **2010**, *3* (6), 3777–3793.

(33) Zhuo, Y.; Hariyani, S.; You, S.; Dorenbos, P.; Brgoch, J. Machine Learning 5d-Level Centroid Shift of Ce3+ Inorganic Phosphors. *J. Appl. Phys.* **2020**, *128* (1).

(34) Wang, S.; Song, Z.; Kong, Y.; Xia, Z.; Liu, Q. Crystal Field Splitting of 4fn−1 5d-Levels of Ce^{3+} and Eu^{2+} in Nitride Compounds. *J. Lumin.* **2018**, *194*, 461–466.

(35) Tao, Y.; Yang, C.; Qin, J. Organic Host Materials for Phosphorescent Organic Light-Emitting Diodes. *Chem. Soc. Rev.* **2011**, *40* (5), 2943–2970.

(36) Masubuchi, Y. Synthesis, Structure and Properties of New Functional Oxynitride Ceramics. *J. Ceram. Soc. Jpn.* **2013**, *121* (1410), 142–149.

(37) Takeda, T.; Xie, R.-J.; Suehiro, T.; Hirosaki, N. Nitride and Oxynitride Phosphors for White LEDs: Synthesis, New Phosphor Discovery, Crystal Structure. *Prog. Solid State Chem.* **2018**, *51*, 41–51.

(38) Zhou, Y.; Yoshizawa, Y.; Hirao, K.; Lenčéš, Z.; Šajgalík, P. Preparation of Eu-Doped β-SiAlON Phosphors by Combustion Synthesis. *J. Am. Ceram. Soc.* **2008**, *91* (9), 3082–3085.

(39) Wang, L.; Zhang, J.; Wang, L.; Liang, Y.; Xu, F.; Xu, L.; Liang, X.; Chen, Q.; Xiang, W. A Promising All-Inorganic Green-Emitting YAGG: Ce Phosphor-in-Glass for Laser Lighting. *J. Mater. Chem. C* **2022**, *10* (18), 7167–7175.

(40) Saradhi, M. P.; Varadaraju, U. V. Photoluminescence Studies on Eu2+-Activated Li2SrSiO4 a Potential Orange-Yellow Phosphor for Solid-State Lighting. *Chem. Mater.* **2006**, *18* (22), 5267–5272.

(41) Hu, Y.; Zhuang, W.; Ye, H.; Zhang, S.; Fang, Y.; Huang, X. Preparation and Luminescent Properties of (Ca1-x, Srx) S: Eu^{2+} Red-Emitting Phosphor for White LED. *J. Lumin.* **2005**, *111* (3), 139–145.

(42) Lee, J. S.; Unithrattil, S.; Im, W. B. Color-Tunable Binary Solid-Solution Phosphor,$(Sr_3SiO_5)_{1-x}(Sr_3AlO_4F)$ x, for White LEDs: Energy Transfer Mechanism between Ce^{3+} and Tb^{3+}. *J. Alloys Compd.* **2013**, *555*, 297–303.

(43) Li, S.; Wang, L.; Tang, D.; Cho, Y.; Liu, X.; Zhou, X.; Lu, L.; Zhang, L.; Takeda, T.; Hirosaki, N. Achieving High Quantum Efficiency Narrow-Band β-Sialon: Eu^{2+} Phosphors for High-Brightness LCD Backlights by Reducing the Eu3+ Luminescence Killer. *Chem. Mater.* **2018**, *30* (2), 494–505.

(44) Smet, P. F.; Moreels, I.; Hens, Z.; Poelman, D. Luminescence in Sulfides: A Rich History and a Bright Future. *Materials* **2010**, *3* (4), 2834–2883.

(45) Fuertes, A. Synthetic Approaches in Oxynitride Chemistry. *Prog. Solid State Chem.* **2018**, *51*, 63–70.

(46) Ching, W.-Y.; Huang, M.-Z.; Mo, S.-D. Electronic Structure and Bonding of β-SiAlON. *J. Am. Ceram. Soc.* **2000**, *83* (4), 780–786.

(47) Dorenbos, P. Energy of the First 4f7 -4f6 5d Transition of Eu2þ in Inorganic Compounds. *J. Lumin.* **2003**, *104* (4), 239–260.

(48) Xing, Y.; Zhu, Y.; Chang, C.; Wang, Y.; Wang, Y. New Synthetic Method and the Luminescent Properties of Green-Emitting β-Sialon: Eu^{2+} Phosphors. *J. Mater. Sci. Mater. Electron.* **2017**, *28*, 9464–9470.

(49) GREEN, A.; XIE, R.-J.; HIROSAKI, N.; LI, H.-L.; LI, Y.; MITOMO, M. Synthesis and Photoluminescence Properties of β-Sialon: Eu^{2+} ($Si_{6-z}Al_zO_zN_{8-z}$:Eu^{2+}). *J. Electrochem. Soc.* **2007**, *154* (10).

(50) Wang, F.; Guo, J.; Wang, S.; Qu, B.; Song, Z.; Zhang, S.; Geng, W.-T.; Liu, Q. Yellow Persistent Luminescence and Electronic Structure of Ca-α-Sialon: Eu2+. *J. Alloys Compd.* **2020**, *821*, 153482.

(51) Xie, R.-J.; Hirosaki, N.; Li, H.-L.; Li, Y. Q.; Mitomo, M. Synthesis and Photoluminescence Properties of β-Sialon: Eu^{2+}(Si6-zAlzOzN8-z:Eu2+): A Promising Green Oxynitride Phosphor for White Light-Emitting Diodes. *J. Electrochem. Soc.* **2007**, *154* (10), J314.

(52) Dierre, B.; Xie, R.-J.; Hirosaki, N.; Sekiguchi, T. Blue Emission of Ce^{3+} in Lanthanide Silicon Oxynitride Phosphors. *J. Mater. Res.* **2007**, *22* (7), 1933–1941.

(53) Boyko, T. D.; Gross, T.; Schwarz, M.; Fuess, H.; Moewes, A. The Local Crystal Structure and Electronic Band Gap of β-Sialons. *J. Mater. Sci.* **2014**, *49* (8), 3242–3252.

(54) Wu, H.; Fei, G. T.; Ma, X. L.; Hu, Z. M.; Gao, X. D.; Wei, Y. S.; Zhang, J.; De Zhang, L. Eu^{2+}-Activated Green-Emitting Phosphor Obtained from Eu 3+ Ions Doping Zeolite-3A in Air Surroundings and Its Efficient Green Light-Emitting Diodes. *Nanoscale Res. Lett.* **2019**, *14* (1), 1–7.

(55) Chiu, Y.-C.; Huang, C.-H.; Lee, T.-J.; Liu, W.-R.; Yeh, Y.-T.; Jang, S.-M.; Liu, R.-S. Eu 2+-Activated Silicon-Oxynitride Ca3Si2O4N2: A Green-Emitting Phosphor for White LEDs. *Opt. Express* **2011**, *19* (103), A331–A339.

(56) Ryu, J. H.; Won, H. S.; Park, Y.-G.; Kim, S. H.; Song, W. Y.; Suzuki, H.; Yoon, C.-B.; Kim, D. H.; Park, W. J.; Yoon, C. Photoluminescence of Ce3+-Activated β-SiAlON Blue Phosphor for UV-LED. *Electrochem. Solid-State Lett.* **2009**, *13* (2), H30.

(57) Yurdakul, H.; Turan, S. The Valance Determination of Cerium Ions in α-SiAlON by Electron Energy Loss Spectroscopy Analysis. *Microsc. Microanal.* **2008**, *14* (S3), 19–22.

(58) Wang, T.; Xia, Z.; Xiang, Q.; Qin, S.; Liu, Q. Relationship of 5d-Level Energies of Ce3+ with the Structure and Composition of Nitride Hosts. *J. Lumin.* **2015**, *166*, 106–110.

(59) Gan, L.; Mao, Z.-Y.; Zhang, Y.-Q.; Xu, F.-F.; Zhu, Y.-C.; Liu, X.-J. Effect of Composition Variation on Phases and Photoluminescence Properties of β-SiAlON: Ce3+ Phosphor. *Ceram. Int.* **2013**, *39* (4), 4633–4637.

(60) Guo, F.; Yin, Z.; Li, X.; Yuan, J. Spark Plasma Sintering of α/β-SiAlON Ceramic End Mill Rods: Electro–Thermal Simulation, Microstructure, Mechanical Properties, and Machining Performance. *J. Adv. Ceram.* **2023**, *12* (9), 1777–1792.

(61) Kshetri, Y. K.; Chaudhary, B.; Dhakal, D. R.; Lee, S. W.; Kim, T.-H. Ho-SiAlON Ceramics as Green Phosphors under Ultra-Violet Excitations. *Materials* **2022**, *15* (19), 6715.

(62) Hampshire, S. Silicon Nitride Ceramics–Review of Structure, Processing and Properties. *J. Achiev. Mater. Manuf. Eng.* **2007**, *24* (1), 43–50.

(63) Krstic, Z.; Krstic, V. D. Silicon Nitride: The Engineering Material of the Future. *J. Mater. Sci.* **2012**, *47* (2), 535–552.

(64) Raju, C. B.; Verma, S.; Sahua, M. N.; Jain, P. K.; Choudary, S. Silicon Nitride/SiAlON Ceramics—a Review. **2001**.

(65) Cao, G. Z.; Metselaar, R. . . Alpha.'-Sialon Ceramics: A Review. *Chem. Mater.* **1991**, *3* (2), 242–252.

(66) Rosenflanz, A.; Chen, I.-W. Phase Relationships and Stability of A′-SiAlON. *J. Am. Ceram. Soc.* **1999**, *82* (4), 1025–1036.

(67) Izhevskiy, V. A.; Genova, L. A.; Bressiani, J. C.; Aldinger, F. Progress in SiAlON Ceramics. *J. Eur. Ceram. Soc.* **2000**, *20* (13), 2275–2295.

(68) Jack, K. H. Sialons and Related Nitrogen Ceramics. *J. Mater. Sci.* **1976**, *11* (6), 1135–1158.

(69) Ekström, T.; Nygren, M. SiAION Ceramics. *J. Am. Ceram. Soc.* **1992**, *75* (2), 259–276.

(70) Kroke, E.; Li, Y.-L.; Konetschny, C.; Lecomte, E.; Fasel, C.; Riedel, R. Silazane Derived Ceramics and Related Materials. *Mater. Sci. Eng. R Rep.* **2000**, *26* (4–6), 97–199.

(71) Riley, F. L. Silicon Nitride and Related Materials. *J. Am. Ceram. Soc.* **2000**, *83* (2), 245–265.

(72) Asada, S.; Ueki, M.; Sugiyama, M. O′-B′ Sialon Ceramics. *J. Mater. Sci.* **1993**, *28* (14), 3789–3792.

(73) Grins, J.; Shen, Z. J.; Nygren, M.; Ekström, T. Preparation and Crystal Structure of JEM-Phase Ln $(Si_{6-z}Al_{L+z})(N_{10-z}O_z)$(z-1.0, Ln= La, Ce, Nd, S). *J Mater Chem* **1995**, *5*, 2001–2006.

(74) Cozzan, C.; Griffith, K. J.; Laurita, G.; Hu, J. G.; Grey, C. P.; Seshadri, R. Structural Evolution and Atom Clustering in β-SiAlON: β-Si6–z Al z O z N8–z. *Inorg. Chem.* **2017**, *56* (4), 2153–2158.

(75) El-Amir, A. A. M.; El-Maddah, A. A.; Ewais, E. M. M.; El-Sheikh, S. M.; Bayoumi, I. M. I.; Ahmed, Y. M. Z. Sialon from Synthesis to Applications: An Overview. *J. Asian Ceram. Soc.* **2021**, *9* (4), 1390–1418.

(76) Interrante, L. V.; Moraes, K.; Liu, Q.; Lu, N.; Puerta, A.; Sneddon, L. G. Silicon-Based Ceramics from Polymer Precursors. *Pure Appl. Chem.* **2002**, *74* (11), 2111–2117.

(77) *What are Sialon Ceramics?*. International Syalons.

(78) Ekström, T.; Käll, P. O.; Nygren, M.; Olsson, P. O. Dense Single-Phase β-Sialon Ceramics by Glass-Encapsulated Hot Isostatic Pressing. *J. Mater. Sci.* **1989**, *24* (5), 1853–1861.

(79) Okatov, S. V.; Ivanovskii, A. L. Chemical Bonding and Atomic Ordering Effects in β-SiAlON. *Int. J. Inorg. Mater.* **2001**, *3* (7), 923–930.

(80) Dupree, R.; Lewis, M. H.; Smith, M. E. Okatov. *J. Appl. Crystallogr.* **1988**, *21* (2), 109–116.

(81) Joshi, B.; Gyawali, G. Understanding the Luminescence in Yb3+ Co-Doped Sialon: Eu2+/Eu3+ Transparent Phosphor Ceramic Plate. *J. Korean Ceram. Soc.* **2022**, *59* (3), 329–337.

(82) Qin, X.; Liu, X.; Huang, W.; Bettinelli, M.; Liu, X. Lanthanide-Activated Phosphors Based on 4f-5d Optical Transitions: Theoretical and Experimental Aspects. *Chem. Rev.* **2017**, *117* (5), 4488–4527.

(83) Fang, C. M.; Metselaar, R. Site Preferences in β-Sialon from First-Principles Calculations. *J. Mater. Chem.* **2003**, *13* (2), 335–337.

(84) Wild, S.; Elliott, H.; Thompson, D. P. Combined Infra-Red and X-Ray Studies of β-Silicon Nitride and B′-Sialons. *J. Mater. Sci.* **1978**, *13* (8), 1769–1775.

(85) Sjöberg, J.; Ericsson, T.; Lindqvist, O. Local Structure of B′-Sialons: An EXAFS Study Study. *J. Mater. Sci.* **1992**, *27*, 5911–5915.

(86) Hirosaki, N.; Kocer, C.; Ogata, S.; Tatsumi, K. Ab Initio Characterization of the Mechanical and Electronic Properties of β-SiAlON (Si6-zAlzOzN8-z; Z= 0–5). *Phys. Rev. B* **2005**, *71* (10), 104105.

(87) Wang, C.-M.; Pan, X.; Ruhle, M.; Riley, F. L.; Mitomo, M. Silicon Nitride Crystal Structure and Observations of Lattice Defects. *J. Mater. Sci.* **1996**, *31* (20), 5281–5298.

(88) Messier, D. R.; Riley, F. L.; Brook, R. J. The ?/? Silicon Nitride Phase Transformation. *J. Mater. Sci.* **1978**, *13* (6), 1199–1205.

(89) Hardie, D.; Jack, K. H. Crystal Structures of Silicon Nitride. *Nature* **1957**, *180* (4581), 332–333.

(90) Kato, K.; Inoue, Z.; Kijima, K.; Kawada, I.; Tanaka, H.; Yamane, T. Structural Approach to the Problem of Oxygen Content in Alpha Silicon Nitride. *J. Am. Ceram. Soc.* **1975**, *58* (3–4), 90–91.

(91) Riley, F. L. *Progress in Nitrogen Ceramics*; Springer Science & Business Media, 2012; Vol. 65.

(92) Ekström, T.; Mackenzie, K. J.; Brown, I. W.; White, G. V. α-Sialon Ceramics Synthesised from a Clay Precursor by Carbothermal Reduction and Nitridation. *J. Mater. Chem.* **1998**, *8* (4), 977–983.

(93) Herrmann, M.; Kurama, S.; Mandal, H. Investigation of the Phase Composition and Stability of the α-SiAlONs by the Rietveld Method. *J. Eur. Ceram. Soc.* **2002**, *22* (16), 2997–3005.

(94) Sun, W.; Tien, T.; Yen, T. Solubility Limits of α'-SiAION Solid Solutions in the System Si,Al,Y/N,O. *J. Am. Ceram. Soc.* **1991**, *74* (10), 2547–2550.

(95) Rosenflanz, A.; Chen, I.-W. Kinetics of Phase Transformations in SiAlON Ceramics: I. Effects of Cation Size, Composition and Temperature. *J. Eur. Ceram. Soc.* **1999**, *19* (13–14), 2325–2335.

(96) Rosenflanz, A.; Chen, I.-W. Kinetics of Phase Transformations in SiAlON Ceramics: II. Reaction Paths. *J. Eur. Ceram. Soc.* **1999**, *19* (13–14), 2337–2348.

(97) Camuşcu, N.; Thompson, D. P.; Mandal, H. Effect of Starting Composition, Type of Rare Earth Sintering Additive and Amount of Liquid Phase on Aa⇆ β Sialon Transformation. *J. Eur. Ceram. Soc.* **1997**, *17* (4), 599–613.

(98) LEE, D.-D.; KANG, S.-J. L.; YOON, D. N. Mechanism of Grain Growth and α-β'Transformation During Liquid-Phase Sintering of B′-Sialon. *J. Am. Ceram. Soc.* **1988**, *71* (9), 803–806.

(99) Mandal, H. New Developments in α-SiAlON Ceramics. *J. Eur. Ceram. Soc.* **1999**, *19* (13–14), 2349–2357.

(100) El-Amir, A. A. M.; El-Maddah, A. A.; Ewais, E. M. M.; El-Sheikh, S. M.; Bayoumi, I. M. I.; Ahmed, Y. M. Z. Sialon from Synthesis to Applications: An Overview. *J. Asian Ceram. Soc.* **2021**, *9* (4), 1390–1418.

(101) Trigg, M. B.; Jack, K. H. The Fabrication of O?-Sialon Ceramics by Pressureless Sintering. *J. Mater. Sci.* **1988**, *23* (2), 481–487.

(102) Wada, H.; Wang, M. J. Phase Relationship between ??- And O?-Sialon at 1623 K. *J. Mater. Sci.* **1993**, *28* (3), 669–676.

(103) Liu, X.; Qu, D.; Luo, X.; Guo, Y.; Cui, Y. The Effects of β-Si3N4 on the Formation and Oxidation of β-SiAlON. *High Temp. Mater. Process.* **2020**, *39* (1), 247–255.

(104) Soraru, G. D.; Ravagni, A.; Campostrini, R.; Babonneau, F. Synthesis and Characterization of β'-SiAlON Ceramics from Organosilicon Polymers. *J. Am. Ceram. Soc.* **1991**, *74* (9), 2220–2223.

(105) Izhevskiy, V. A.; Genova, L. A.; Bressiani, J. C.; Aldinger, F. Progress in SiAlON Ceramics. *J. Eur. Ceram. Soc.* **2000**, *20* (13), 2275–2295.

(106) Huang, S.; Huang, Z.; Ouyang, X.; Yin, L.; Huang, J.; Liu, Y.; Fang, M. Investigation on Lanthanide-Dependent z Value of JEM-Phase Sialon. *RSC Adv.* **2014**, *4* (13), 6556–6559.

(107) Wang, C.-Y.; ten Kate, O. M.; Takeda, T.; Hirosaki, N. Efficient and Thermally Stable Blue-Emitting Ce3+ Doped LaAl (Si6- ZAlz)(N10- ZOz)(JEM: Ce) Phosphors for White LEDs. *J. Mater. Chem. C* **2017**, *5* (32), 8295–8300.

(108) Takahashi, H.; Matsushima, Y. Luminescent Properties of RE-Doped Mullite (Al6Si2O13) Phosphors (RE= Ce3+, Eu2+, Ce3+-Tb3+, and Eu3+). *ECS Trans.* **2018**, *88* (1), 237.

(109) Jiang, J.-X.; Wang, P.-L.; He, W.-B.; Chen, W.-W.; Zhuang, H.-R.; Cheng, Y.-B.; Yan, D.-S. Eu Stabilized α-Sialon Ceramics Derived from SHS-Synthesized Powders. *Mater. Lett.* **2005**, *59* (2–3), 205–209.

(110) Gao, Y.; Iwasaki, R.; Hamana, D.; Iihama, J.; Honda, S.; Kumari, M.; Hayakawa, T.; Bernard, S.; Thomas, P.; Iwamoto, Y. Green Emitting B$\ubeta$-SiAlON:Eu $^{2+}$ Phosphors Derived from Chemically Modified Perhydropolysilazanes. *Int. J. Appl. Ceram. Technol.* **2023**, *20* (1), 153–165.

(111) Xie, R.-J.; Hintzen, H. T. Optical Properties of (Oxy) Nitride Materials: A Review. *J. Am. Ceram. Soc.* **2013**, *96* (3), 665–687.

(112) Xie, R.-J.; Hirosaki, N.; Mitomo, M.; Yamamoto, Y.; Suehiro, T.; Sakuma, K. Optical Properties of Eu2+ in α-SiAlON. *J. Phys. Chem. B* **2004**, *108* (32), 12027–12031.

(113) Takahashi, K.; Yoshimura, K.; Harada, M.; Tomomura, Y.; Takeda, T.; Xie, R.-J.; Hirosaki, N. On the Origin of Fine Structure in the Photoluminescence Spectra of the β-Sialon: Eu2+ Green Phosphor. *Sci. Technol. Adv. Mater.* **2012**.

(114) Xu, F.; Sourty, E.; Zeng, X.; Zhang, L.; Gan, L.; Mou, X.; Shi, W.; Zhu, Y.; Huang, F.; Zhao, J. Atomic-Scaled Investigation of Structure-Dependent Luminescence in Sialon: Ce Phosphors. *Appl. Phys. Lett.* **2012**, *101* (16), 161904.

(115) Zhang, X.; Fang, M.-H.; Tsai, Y.-T.; Lazarowska, A.; Mahlik, S.; Lesniewski, T.; Grinberg, M.; Pang, W. K.; Pan, F.; Liang, C. Controlling of Structural Ordering and Rigidity of β-SiAlON: Eu through Chemical Cosubstitution to Approach Narrow-Band-Emission for Light-Emitting Diodes Application. *Chem. Mater.* **2017**, *29* (16), 6781–6792.

(116) Yurdakul, H.; Ceylantekin, R.; Turan, S. A Novel Approach on the Synthesis of β-SiAlON: Eu2+ Phosphors from Kaolin through Carbothermal Reduction and Nitridation (CRN) Route. *Adv. Appl. Ceram.* **2014**, *113* (4), 214–222.

(117) Gao, Y.; Iihama, J.; Hamana, D.; Iwasaki, R.; Honda, S.; Asaka, T.; Kumari, M.; Hayakawa, T.; Bernard, S.; Thomas, P. Polymer-Derived β-SiAlON: Eu2+ Phosphors. *Int. J. Appl. Ceram. Technol.* **2022**.

(118) Kimoto, K.; Xie, R.-J.; Matsui, Y.; Ishizuka, K.; Hirosaki, N. Direct Observation of Single Dopant Atom in Light-Emitting Phosphor of β-SiAlON: Eu2+. *Appl. Phys. Lett.* **2009**, *94* (4).

(119) Gao, Y.; Murai, S.; Shinozaki, K.; Qiu, J.; Tanaka, K. Phase-Selective Distribution of Eu2+ and Eu3+ in Oxide and Fluoride Crystals in Glass-Ceramics for Warm White-Light-Emitting Diodes. *ACS Appl. Electron. Mater.* **2019**, *1* (6), 961–971.

(120) Brgoch, J.; Gaultois, M. W.; Balasubramanian, M.; Page, K.; Hong, B.-C.; Seshadri, R. Local Structure and Structural Rigidity of the Green Phosphor β-SiAlON: Eu2+. *Appl. Phys. Lett.* **2014**, *105* (18).

(121) Yang, F.; Qiao, L.; Ren, H.; Yan, F.; Xie, Z. Synthesis and Luminescence Properties of Color-Tunable Dy3+/Eu3+: CeAlON Phosphors. *Ceram. Int.* **2017**, *43* (11), 8406–8410.

(122) Li, S.; Wang, L.; Tang, D.; Cho, Y.; Liu, X.; Zhou, X.; Lu, L.; Zhang, L.; Takeda, T.; Hirosaki, N. Achieving High Quantum Efficiency Narrow-Band β-Sialon: Eu2+ Phosphors for High-Brightness LCD Backlights by Reducing the Eu3+ Luminescence Killer. *Chem. Mater.* **2018**, *30* (2), 494–505.

(123) Biswas, A.; Friend, C. S.; Prasad, P. N. Spontaneous Reduction of Eu3+ Ion in Al Co-Doped Sol–Gel Silica Matrix during Densification. *Mater. Lett.* **1999**, *39* (4), 227–231.

(124) Prasad, V. R.; Damodaraiah, S.; Babu, S.; Ratnakaram, Y. C. Structural, Optical and Luminescence Properties of Sm3+ and Eu3+ Doped Calcium Borophosphate Phosphors for Reddish-Orange and Red Emitting Light Applications. *J. Lumin.* **2017**, *187*, 360–367.

(125) Shen, Z.; Nygren, M.; Wang, P.; Feng, J. Eu-Doped Alpha-Sialon and Related Phases. *J. Mater. Sci. Lett.* **1998**, *17* (20), 1703–1706.

(126) Shioi, K.; Hirosaki, N.; Xie, R.-J.; Takeda, T.; Li, Y. Q. Synthesis, Crystal Structure and Photoluminescence of Eu-α-SiAlON. *J. Alloys Compd.* **2010**, *504* (2), 579–584.

(127) Zavala-Sanchez, L. A.; Hirata, G. A.; Novitskaya, E.; Karandikar, K.; Herrera, M.; Graeve, O. A. Distribution of Eu^{2+} and Eu^{3+} Ions in Hydroxyapatite: A Cathodoluminescence and Raman Study. *ACS Biomater. Sci. Eng.* **2015**, *1* (12), 1306–1313.

(128) Chen, X.; Gan, L.; Zhang, Z.; Lu, P.; Zeng, X.; Zhang, L.; Yao, H.; Xu, F.; Zhao, J. Ca-α-SiAlON: Eu Phosphors: Oxidation States, Energy Transfer, and Emission Enhancement by Incorporation-Aimed Surface Engineering. *ACS Appl. Mater. Interfaces* **2017**, *9* (36), 30982–30991.

(129) Yang, Z.; Zhao, Z.; Shi, Y.; Wang, C.; Wu, Q.; Wang, Y. Luminescence Properties and Energy Transfer of Ce 3+, Tb3+-Coactivatedβ-SiAlON Phosphors. *J. Am. Ceram. Soc.* **2013**, *96* (6), 1815–1820.

(130) Xu, F.; Sourty, E.; Shi, W.; Mou, X.; Zhang, L. Direct Observation of Rare-Earth Ions in α-Sialon: Ce Phosphors. *Inorg. Chem.* **2011**, *50* (7), 2905–2910.

(131) Yurdakul, H.; Idrobo, J. C.; Okunishi, E.; Pennycook, S. J.; Turan, S. Atomic-Scale Imaging and Identification of Rare-Earth Dopants in SiAlON Interfaces.

(132) Yurdakul, H.; Idrobo, J. C.; Pennycook, S. J.; Turan, S. Towards Atomic Scale Engineering of Rare-Earth-Doped SiAlON Ceramics through Aberration-Corrected Scanning Transmission Electron Microscopy. *Scr. Mater.* **2011**, *65* (8), 656–659.

(133) Hirosaki, N.; Suehiro, T.; Yamamoto, Y.; Mitomo, M. Ce-Doped α-Sialon Phosphor. In *Preprints of Annual Meeting of The Ceramic Society of Japan Preprints of Fall Meeting of The Ceramic Society of Japan Preprints of Annual Meeting of The Ceramic Society of Japan*, *2003*; The Ceramic Society of Japan, 2003; pp 112–112.

(134) Mishin, A. N.; Potapov, S. 5d-4f Radiative Transitions in Ce-Doped Si3.. A1OyN4.. y Solid Solutions. In *Proceedings of SPIE*; 2002; Vol. 4766, p 143.

(135) Chernovetz, B. V.; Feopentov, A. V.; Grekov, F. F.; Mikhrim, S. B.; Mishin, A. N.; Potapov, A. S. 5d-4f Radiative Transitions in Ce-Doped Si3xAlxOyN4-y Solid Solutions. In *XI Feofilov Symposium on Spectroscopy of Crystals Activated by Rare-Earth and Transition Metal Ions*; SPIE, 2002; Vol. 4766, pp 142–147.

(136) Dorenbos, P. 5d-Level Energies of Ce3+ and the Crystalline Environment. IV. Aluminates and “Simple” Oxides. *J. Lumin.* **2002**, *99* (3), 283–299.

(137) Olsson, P.-O. Crystal Defects and Coherent Intergrowth of α-and β-Crystals in Y-Ce Doped Sialon Materials. *J. Mater. Sci.* **1989**, *24*, 3878–3887.

(138) Xu, F. F.; Bando, Y.; Mitomo, M. Domain Boundaries in Ce-α-SiAlON as Revealed by HRTEM. In *Key Engineering Materials*; Trans Tech Publ, 2003; Vol. 253, pp 89–102.

(139) Gan, L.; Xu, F.-F.; Zeng, X.-H.; Li, Z.-S.; Mao, Z.-Y.; Lu, P.; Zhu, Y.-C.; Liu, X.-J.; Zhang, L.-L. Multiple Doping Structures of the Rare-Earth Atoms in β-SiAlON: Ce Phosphors and Their Effects on Luminescence Properties. *Nanoscale* **2015**, *7* (26), 11393–11400.

(140) Xie, R.-J.; Hirosaki, N. Silicon-Based Oxynitride and Nitride Phosphors for White LEDs—A Review. *Sci. Technol. Adv. Mater.* **2007**, *8* (7–8), 588.

(141) Renlund, G. M.; Prochazka, S.; Doremus, R. H. Silicon Oxycarbide Glasses: Part II. Structure and Properties. *J. Mater. Res.* **1991**, *6* (12), 2723–2734.

(142) Jack, K. H.; Wilson, W. I. Ceramics Based on the Si-Al-ON and Related Systems. *Nat. Phys. Sci.* **1972**, *238* (80), 28–29.

(143) Vakifahmetoglu, C.; Zeydanli, D.; Colombo, P. Porous Polymer Derived Ceramics. *Mater. Sci. Eng. R Rep.* **2016**, *106*, 1–30.

(144) Oyama, Y.; Kamigaito, O. Solid Solubility of Some Oxides in Si3N4. *Jpn. J. Appl. Phys.* **1971**, *10* (11), 1637.

(145) Eser, O.; Kurama, S. A Comparison of Sintering Techniques Using Different Particle Sized β-SiAlON Powders. *J. Eur. Ceram. Soc.* **2012**, *32* (7), 1343–1347.

(146) Ramesh, R.; Pomeroy, M. J.; Chu, H.; Datta, P. K. Effect of Gaseous Environment on the Corrosion of β-Sialon Materials. *J. Eur. Ceram. Soc.* **1995**, *15* (10), 1007–1014.

(147) Neal, G. S.; Smith, M. E.; Trigg, M. B.; Drennan, J. Solid-State NMR Examination of the Formation of β-Sialon by Carbothermal Reduction and Nitridation of Halloysite Clay. *J. Mater. Chem.* **1994**, *4* (2), 245–251.

(148) Ekström, T.; Mackenzie, K. J.; Brown, I. W.; White, G. V. α-Sialon Ceramics Synthesised from a Clay Precursor by Carbothermal Reduction and Nitridation. *J. Mater. Chem.* **1998**, *8* (4), 977–983.

(149) Navrotsky, A.; Risbud, S. H.; Liang, J.; Leppert, V. J. Thermochemical Insights into Rapid Solid-State Reaction Synthesis of β-Sialon. *J. Phys. Chem. B* **1997**, *101* (46), 9433–9435.

(150) Acikbas, N. C.; Yurdakul, H.; Mandal, H.; Kara, F.; Turan, S.; Kara, A.; Bitterlich, B. Effect of Sintering Conditions and Heat Treatment on the Properties, Microstructure and Machining Performance of α-β-SiAlON Ceramics. *J. Eur. Ceram. Soc.* **2012**, *32* (7), 1321–1327.

(151) Hong, D.; Yin, Z.; Guo, F.; Yuan, J. Microwave Synthesis of Duplex α/β-SiAlON Ceramic Cutting Inserts: Modifying m, n, z Values, Synthesis Temperature, and Excess Y2O3 Synthesis Additive. *J. Adv. Ceram.* **2022**, *11* (4), 589–602.

(152) Priecel, P.; Lopez-Sanchez, J. A. Advantages and Limitations of Microwave Reactors: From Chemical Synthesis to the Catalytic Valorization of Biobased Chemicals. *ACS Sustain. Chem. Eng.* **2019**, *7* (1), 3–21.

(153) Panneerselvam, M.; Rao, K. J. A Microwave Method for the Preparation and Sintering of B′-SiAlON. *Mater. Res. Bull.* **2003**, *38* (4), 663–674.

(154) Niu, J.; Nakamura, T.; Nakatsugawa, I.; Akiyama, T. Reaction Characteristics of Combustion Synthesis of β-SiAlON Using Different Additives. *Chem. Eng. J.* **2014**, *241*, 235–242.

(155) Liu, G.; Chen, K.; Li, J. Combustion Synthesis of SiAlON Ceramic Powders: A Review. *Mater. Manuf. Process.* **2013**, *28* (2), 113–125.

(156) Weimer, A. W.; Eisman, G. A.; Susnitzky, D. W.; Beaman, D. R.; McCoy, J. W. Mechanism and Kinetics of the Carbothermal Nitridation Synthesis of α-Silicon Nitride. *J. Am. Ceram. Soc.* **1997**, *80* (11), 2853–2863.

(157) Neal, G. S.; Smith, M. E.; Trigg, M. B.; Drennan, J. Solid-State NMR Examination of the Formation of β-Sialon by Carbothermal Reduction and Nitridation of Halloysite Clay. *J. Mater. Chem.* **1994**, *4* (2), 245–251.

(158) Li, F. J.; Wakihara, T.; Tatami, J.; Komeya, K.; Meguro, T. Synthesis of β-SiAlON Powder by Carbothermal Reduction–Nitridation of Zeolites with Different Compositions. *J. Eur. Ceram. Soc.* **2007**, *27* (6), 2535–2540.

(159) Mandal, H.; Thompson, D. P.; Ekström, T. Reversible A⇌ Sialon Transformation in Heat-Treated Sialon Ceramics. *J. Eur. Ceram. Soc.* **1993**, *12* (6), 421–429.

(160) Chung, J. H.; Ryu, J. H. Photoluminescence and LED Application of β-SiAlON: Eu2+ Green Phosphor. *Ceram. Int.* **2012**, *38* (6), 4601–4606.

(161) Gao, Y.; Hamana, D.; Iwasaki, R.; Iihama, J.; Honda, S.; Kumari, M.; Hayakawa, T.; Bernard, S.; Thomas, P.; Iwamoto, Y. Chemical Route for Synthesis of β-SiAlON:Eu2+ Phosphors Combining Polymer-Derived Ceramics Route with Non-Hydrolytic Sol-Gel Chemistry. *J. Sol-Gel Sci. Technol.* **2022**, *104* (3), 711–723.

(162) Gao, Y.; Iihama, J.; Hamana, D.; Iwasaki, R.; Honda, S.; Asaka, T.; Kumari, M.; Hayakawa, T.; Bernard, S.; Thomas, P.; Iwamoto, Y. Polymer-derived B-SiAlON:Eu $^{2+}$ Phosphors. *Int. J. Appl. Ceram. Technol.* **2023**, *20* (2), 768–779.

(163) Fritz, G.; Raabe, B. Bildung Siliciumorganischer Verbindungen. V. Die Thermische Zersetzung von Si(CH $_3$) $_4$ Und Si(C_2H_5)$_4$. *Z. Für Anorg. Allg. Chem.* **1956**, *286* (3–4), 149–167.

(164) Ainger, F. W.; Herbert, J. M. The Preparation of Phosphorus-Nitrogen Compounds as Non-Porous Solids. In *ANGEWANDTE CHEMIE-INTERNATIONAL EDITION*; WILEY-V CH VERLAG GMBH MUHLENSTRASSE 33-34, D-13187 BERLIN, GERMANY, 1959; Vol. 71, pp 653–653.

(165) Chantrell, P. G.; Popper, P. Inorganic Polymers and Ceramics. *Spec. Ceram.* **1965**, *67*.

(166) Verbeek, W. Production of Shaped Articles of Homogeneous Mixtures of Silicon Carbide and Nitride, December 10, 1974.

(167) Yajima, S.; Hayashi, J.; Omori, M.; Okamura, K. Development of a Silicon Carbide Fibre with High Tensile Strength. *Nature* **1976**, *261* (5562), 683–685.

(168) Colombo, P.; Mera, G.; Riedel, R.; Soraru, G. D. Polymer-Derived Ceramics: 40 Years of Research and Innovation in Advanced Ceramics. *Ceram. Sci. Technol.* **2013**, 245–320.

(169) He, J.; Song, M.; Chen, K.; Kan, D.; Zhu, M. Polymer-Derived Ceramics Technology: Characteristics, Procedure, Product Structures, and Properties, and Development of the Technology in High-Entropy Ceramics. *Crystals* **2022**, *12* (9), 1292.

(170) Bernard, S.; Miele, P. Polymer-Derived Boron Nitride: A Review on the Chemistry, Shaping and Ceramic Conversion of Borazine Derivatives. *Materials* **2014**, *7* (11), 7436–7459.

(171) Barroso, G.; Li, Q.; Bordia, R. K.; Motz, G. Polymeric and Ceramic Silicon-Based Coatings–a Review. *J. Mater. Chem. A* **2019**, *7* (5), 1936–1963.

(172) Barroso, G. S.; Krenkel, W.; Motz, G. Low Thermal Conductivity Coating System for Application up to 1000 C by Simple PDC Processing with Active and Passive Fillers. *J. Eur. Ceram. Soc.* **2015**, *35* (12), 3339–3348.

(173) Lale, A.; Schmidt, M.; Mallmann, M. D.; Bezerra, A. V. A.; Acosta, E. D.; Machado, R. A. F.; Demirci, U. B.; Bernard, S. Polymer-Derived Ceramics with Engineered Mesoporosity: From Design to Application in Catalysis. *Surf. Coat. Technol.* **2018**, *350*, 569–586.

(174) Riedel, R.; Seher, M.; Mayer, J.; Szabó, D. V. Polymer-Derived Si-Based Bulk Ceramics, Part I: Preparation, Processing and Properties. *J. Eur. Ceram. Soc.* **1995**, *15* (8), 703–715.

(175) Mitomo, M.; Hirosaki, N.; Nishimura, T.; Xie, R.-J. Microstructure Control in Silicon Nitride Ceramics-A Review. *J. Ceram. Soc. Jpn.* **2006**, *114* (1335), 867–872.

(176) *Moretto, H.-H., Schulze, M., Wagner, G. (2000). Silicones.*

(177) Weinmann, M.; Zern, A.; Aldinger, F. Stoichiometric Silicon Nitride/Silicon Carbide Composites from Polymeric Precursors. *Adv. Mater.* **2001**, *13* (22), 1704–1708.

(178) Birot, M.; Pillot, J.-P.; Dunogues, J. Comprehensive Chemistry of Polycarbosilanes, Polysilazanes, and Polycarbosilazanes as Precursors of Ceramics. *Chem. Rev.* **1995**, *95* (5), 1443–1477.

(179) Mera, G.; Navrotsky, A.; Sen, S.; Kleebe, H.-J.; Riedel, R. Polymer-Derived SiCN and SiOC Ceramics–Structure and Energetics at the Nanoscale. *J. Mater. Chem. A* **2013**, *1* (12), 3826–3836.

(180) Barrios, E.; Zhai, L. A Review of the Evolution of the Nanostructure of SiCN and SiOC Polymer Derived Ceramics and the Impact on Mechanical Properties. *Mol. Syst. Des. Eng.* **2020**, *5* (10), 1606–1641.

(181) Salameh, C.; Bernard, S.; Gervais, C.; Babonneau, F.; Bruma, A.; Malo, S.; Miele, P. Chemistry of a Series of Aluminum-Modified Polysilazanes: Synthesis, Pyrolysis Behaviour and Microstructural Evolution. *J. Eur. Ceram. Soc.* **2019**, *39* (2–3), 183–194.

(182) Funayama, O.; Tashiro, Y.; Aoki, T.; Isoda, T. Synthesis and Pyrolysis of Polyaluminosilazane. *J. Ceram. Soc. Jpn.* **1994**, *102* (1190), 908–912.

(183) Mera, G.; Gallei, M.; Bernard, S.; Ionescu, E. Ceramic Nanocomposites from Tailor-Made Preceramic Polymers. *Nanomaterials* **2015**, *5* (2), 468–540.

(184) Durif, C.; Wynn, M.; Balestrat, M.; Franchin, G.; Kim, Y.-W.; Leriche, A.; Miele, P.; Colombo, P.; Ionescu, E.; Bernard, S. Polymer-Derived Ultra-High Temperature Ceramics (UHTCs) and Related Materials. **2019**.

(185) Widgeon, S. J.; Sen, S.; Mera, G.; Ionescu, E.; Riedel, R.; Navrotsky, A. 29Si and 13C Solid-State NMR Spectroscopic Study of Nanometer-Scale Structure and Mass Fractal Characteristics of Amorphous Polymer Derived Silicon Oxycarbide Ceramics. *Chem. Mater.* **2010**, *22* (23), 6221–6228.

(186) Stabler, C.; Ionescu, E.; Graczyk-Zajac, M.; Gonzalo-Juan, I.; Riedel, R. Silicon Oxycarbide Glasses and Glass-ceramics: "All-Rounder" Materials for Advanced Structural and Functional Applications. *J. Am. Ceram. Soc.* **2018**, *101* (11), 4817–4856.

(187) Bois, L.; Maquet, J.; Babonneau, F.; Bahloul, D. Structural Characterization of Sol-Gel Derived Oxycarbide Glasses. 2. Study of the Thermal Stability of the Silicon Oxycarbide Phase. *Chem. Mater.* **1995**, *7* (5), 975–981.

(188) Saha, A.; Raj, R. Crystallization Maps for SiCO Amorphous Ceramics. *J. Am. Ceram. Soc.* **2007**, *90* (2), 578–583.

(189) Widgeon, S.; Mera, G.; Gao, Y.; Stoyanov, E.; Sen, S.; Navrotsky, A.; Riedel, R. Nanostructure and Energetics of Carbon-Rich SiCN Ceramics Derived from Polysilylcarbodiimides: Role of the Nanodomain Interfaces. *Chem. Mater.* **2012**, *24* (6), 1181–1191.

(190) Iwamoto, Y.; Völger, W.; Kroke, E.; Riedel, R.; Saitou, T.; Matsunaga, K. Crystallization Behavior of Amorphous Silicon Carbonitride Ceramics Derived from Organometallic Precursors. *J. Am. Ceram. Soc.* **2004**, *84* (10), 2170–2178.

(191) Viard, A.; Miele, P.; Bernard, S. Polymer-Derived Ceramics Route toward SiCN and SiBCN Fibers: From Chemistry of Polycarbosilazanes to the Design and Characterization of Ceramic Fibers. *J. Ceram. Soc. Jpn.* **2016**, *124* (10), 967–980.

(192) Seitz, J.; Bill, J.; Egger, N.; Aldinger, F. Structural Investigations of Si/C/N-Ceramics from Polysilazane Precursors by Nuclear Magnetic Resonance. *J. Eur. Ceram. Soc.* **1996**, *16* (8), 885–891.

(193) Sandra, F.; Ballestero, A.; Tsampas, M. N.; Vernoux, P.; Balan, C.; Iwamoto, Y.; Demirci, U. B.; Miele, P.; Bernard, S. Silicon Carbide-Based Membranes with High Soot Particle Filtration Efficiency, Durability and Catalytic Activity for CO/HC Oxidation and Soot Combustion. *J. Membr. Sci.* **2016**, *501*, 79–92.

(194) Glatz, G.; Schmalz, T.; Kraus, T.; Haarmann, F.; Motz, G.; Kempe, R. Copper-Containing SiCN Precursor Ceramics (Cu@SiCN) as Selective Hydrocarbon Oxidation Catalysts Using Air as an Oxidant. *Chem. – Eur. J.* **2010**, *16* (14), 4231–4238.

(195) Ferreira, R. K. M.; Miled, M. B.; Nishihora, R. K.; Christophe, N.; Carles, P.; Motz, G.; Bouzid, A.; Machado, R.; Masson, O.; Iwamoto, Y. Low Temperature in Situ Immobilization of Nanoscale Fcc and Hcp Polymorphic Nickel Particles in Polymer-Derived Si–C–O–N (H) to Promote Electrocatalytic Water Oxidation in Alkaline Media. *Nanoscale Adv.* **2023**, *5* (3), 701–710.

(196) Balestrat, M.; Cheype, M.; Gervais, C.; Deschanels, X.; Bernard, S. Advanced Nanocomposite Materials Made of TiC Nanocrystals in Situ Immobilized in SiC Foams with Boosted Spectral Selectivity. *Mater. Adv.* **2023**, *4* (4), 1161–1170.

(197) Kousaalya, A. B.; Zeng, X.; Karakaya, M.; Tritt, T.; Pilla, S.; Rao, A. M. Polymer-Derived Silicon Oxycarbide Ceramics as Promising Next-Generation Sustainable Thermoelectrics. *ACS Appl. Mater. Interfaces* **2018**, *10* (3), 2236–2241.

(198) Duperrier, S.; Bernard, S.; Calin, A.; Sigala, C.; Chiriac, R.; Miele, P.; Balan, C. Design of a Series of Preceramic *B* -Tri(Methylamino)Borazine-Based Polymers as Fiber Precursors: Shear Rheology Investigations. *Macromolecules* **2007**, *40* (4), 1028–1034.

(199) Ouyang, T.; Gottardo, L.; Bernard, S.; Balan, C.; Miele, P. Tuning of the Viscoelastic Properties of Melt-Spinnable Boron-and Silicon-Based Preceramic Polymers. *J Appl Polym Sci* **2013**, *128*, 248–257.

(200) Zanchetta, E.; Cattaldo, M.; Franchin, G.; Schwentenwein, M.; Homa, J.; Brusatin, G.; Colombo, P. Stereolithography of SiOC Ceramic Microcomponents. *Adv. Mater. Deerfield Beach Fla* **2015**, *28* (2), 370–376.

(201) Eckel, Z. C.; Zhou, C.; Martin, J. H.; Jacobsen, A. J.; Carter, W. B.; Schaedler, T. A. Additive Manufacturing of Polymer-Derived Ceramics. *Science* **2016**, *351* (6268), 58–62.

(202) de Hazan, Y.; Penner, D. SiC and SiOC Ceramic Articles Produced by Stereolithography of Acrylate Modified Polycarbosilane Systems. *J. Eur. Ceram. Soc.* **2017**, *37* (16), 5205–5212.

(203) Yu, Y. F.; Mah, T. I. Silicon Oxynitride and Si-AI-ON Ceramics from Organosilicon Polymers. *Ultrastruct. Process. Adv. Ceram. Ed JD Mackenzie DR Ulrich J Wiley Sons N. Y.* **1988**, *773*.

(204) Funayama, O.; Tashiro, Y.; Aoki, T.; Isoda, T. Synthesis and Pyrolysis of Polyaluminosilazane. *J. Ceram. Soc. Jpn.* **1994**, *102* (1190), 908–912.

(205) Zabolotskii, A. V.; Dolgushev, N. V.; Suvorov, S. A. [No Title Found]. *Inorg. Mater.* **2002**, *38* (3), 224–226.

(206) Parcianello, G.; Bernardo, E.; Colombo, P. Optimization of Phase Purity of B′-Sialon Ceramics Produced from Silazanes and Nano-Sized Alumina. *J. Am. Ceram. Soc.* **2012**, *95* (7), 2148–2154.

(207) Bernardo, E.; Colombo, P.; Hampshire, S. SiAlON-Based Ceramics from Filled Preceramic Polymers. *J. Am. Ceram. Soc.* **2006**, *89* (12), 3839–3842.

(208) Mackenzie, K. J. D.; Meinhold, R. H.; White, G. V.; Sheppard, C. M.; Sherriff, B. L. Carbothermal Formation of B′-Sialon from Kaolinite and Halloysite Studied by 29 Si and 27 Al Solid State MAS NMR. *J. Mater. Sci.* **1994**, *29*, 2611–2619.

(209) Soraru, G. D.; Ravagni, A.; Campostrini, R.; Babonneau, F. Synthesis and Characterization of β'-SiAlON Ceramics from Organosilicon Polymers. *J. Am. Ceram. Soc.* **1991**, *74* (9), 2220–2223.

Chapter II.

Synthesis and Characterization Methods

II.1. Introduction

This second chapter focuses on detailing the compounds used for synthesis including precursors and solvents and the materials which have been produced as well as the processes which implemented them going from the polymer synthesis to the heat-treatments. Additionally, it provides a detailed description of all the characterization tools employed in subsequent chapters.

The chapter's structure can be summarized as follows:

1) **Chemical Modifications of a commercially-available preformed polymers**

In this section, the chapter describes the commercial polymer and the necessary reagents for its chemical modification in solution. These modifications involve the incorporation of aluminum (Al) and rare-earth metals including Europium and Cerium (Eu and Ce) at the molecular level. The synthesis techniques used for these chemical modifications is also addressed.

2) **Heat-treatments**

This section delves into the heat-treatment procedures, ranging from the pyrolysis of polymers to various annealing treatments to convert the chemically modified polymers into SiAlON-based ceramics and their doped derivatives. Gas Pressure Sintering (GPS) as a sintering method is also detailed.

3) **Characterization Techniques**

The final part of the chapter revolves around the characterization techniques employed at different stages of material development. These techniques help in understanding the properties and characteristics of the materials effectively.

II.2. Materials

The manipulation of the different compounds, *i.e.*, the polymer, the solvent and the metal and rare-earth element-containing compounds, is carried out in a purified argon atmosphere passing through a column of phosphorus pentoxide and then through a vacuum/argon line by means of standard Schlenk techniques (Figure II.1 (a)). The cleaned glassware is stored in an oven at 95 °C overnight before being connected to the vacuum/argon line, assembled and pumped under vacuum for 30 min. and then filled with argon. All chemical products are handled in an argon-filled glove box (Jacomex, Campus-type; O_2 and H_2O concentrations kept at ≤0.1 ppm and ≤0.8 ppm, respectively) (Figure II.1(b)).

Figure II.1. (a) Schlenk line for synthesis experiments and (b) argon-filled glovebox for precursor manipulation.

Toluene (99.85%, Extra Dry over Molecular Sieve, AcroSeal™) is purchased from Acros Organics. Other compounds are described in the following sections. Hereafter, we first describe the starting compounds and then the synthesis of SiAlON and rare earth-doped SiAlON precursors before their heat-treatment and the characterization methods through the tools described in the last part of this chapter.

II.2.1. Durazane® 1800

Polysilazanes (PSZ) are composed of silicon and nitrogen atoms (linked together) in their main chains and hydrogen atoms or organic substituents attached to silicon and nitrogen atoms. Based on the presence of different organic or inorganic functional groups in their chemical structures,

PSZ form a wide family of products with interesting properties, which may lead to many practical applications (as for example Architecture & construction (exterior and interior surfaces), Industry (machinery, components, plant) and Mobility (automotive, aerospace, marine). In this thesis, we have focused our work on the use of a poly (vinyl methyl)-co-(methyl) silazane which is a commercially available polymer known under the trademark Durazane® 1800 (Figure II.2).

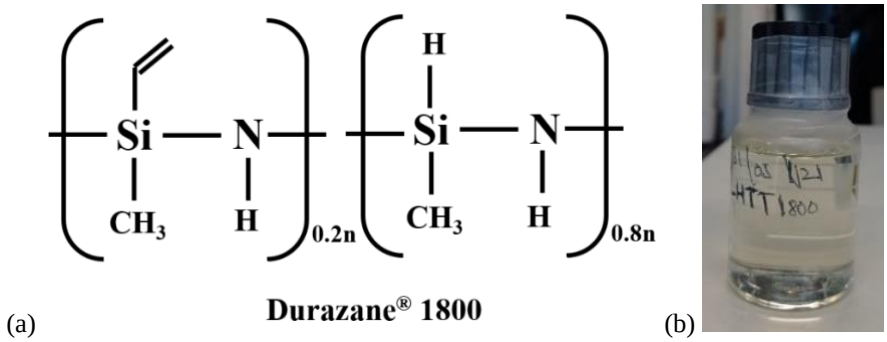

Figure II.2. (a) Structure and (b) Physical state of Durazane® 1800.

Durazane®1800 is a copolymer with 20% molar vinyl functions and contains silicon (Si), carbon (C), hydrogen (H) and nitrogen (N) elements. It comes in the form of a very slightly yellowish transparent viscous liquid with main properties detailed in Table II.1.

Table II.1. Main properties of Durazane® 1800.

Properties	Durazane®
Density	1.00g.cm^{-3}
Appearance	Transparent, slightly yellowish
Viscosity	20-50 Pas at 20°C
Solubility	THF, Toluene, Hexane, Acetone
Flash point	16.5°C
Curing temperature	175-200°C

Durazane® 1800 is provided in a 1 L container by durXtreme GmbH, Ulm (Germany) and then stored in a fridge and used as-received. The elemental analysis gave the following element contents[1]: Si, 41.3; C, 27.3; N, 22.7; H, 8.3; O, 0.4. $[Si_{1.0}C_{1.5}N_{1.1}H_{5.5}]_n$ (Normalized to total 100 wt.% (totals of wt.% was 98.9 wt.%) and reference to $Si_{1.0}$. Oxygen content (below 2 wt.%) is omitted in the empirical formulae. Attenuated total reflectance (ATR)-Fourier Transform Infrared (FTIR) spectroscopy and ^{1}H Nuclear Magnetic Resonance (NMR) spectroscopies

allowed to characterized the bond and the chemical environments in the polymer[1]: FTIR (ATR/cm^{-1}): ν(N−H) = 3381 (s), ν (C−H in vinyl) = 3058 (m), ν (C−H in methyl) = 2954 (s), 2902 (m) and 2848 (w), ν (Si−H) = 2123 (s), δ (C=C) = 1594 (w), δ (=C-H) = 1405 (w), δ (Si−CH_3) = 1251 (m), δ(N-H): 1169 (s), δ (C=C/=CH_2) = 947 (w), ν (N−Si−N) = 897 (vs), δ (Si-CH_3) = 787 (m); ^{1}H NMR (300 MHz, $CDCl_3$, δ/ppm): 0.4–0.1 (br, SiC**H**$_3$), 1.1–0.5 (br, N**H**), 4.9–4.4 (br, Si**H**), 6.3–5.7 (br, vinyl). Durazane® 1800 has been used as a preformed polymer labelled PSZ to be modified by an alane (Al complex) and then by rare earth chlorides which are described in following sections.

II.2.2. Alane N, N-dimethylethylamine

Alane *N, N*-dimethyl ethylamine (Figure II.3) is a metal complex to be used as a selective reducing agent. Alane *N, N*-dimethyl ethylamine $AlH_3{\cdot}NC_2H_5(CH_3)_2$ labelled DMEA, (0.5 M solution in toluene) was obtained from Sigma-Aldrich company and used for synthesis without further purification. Its main properties are detailed in Table II.2.

Figure II.3. Alane *N, N*-dimethyl ethylamine[2].

Table II.2. Properties of Alane *N, N*-dimethyl ethylamine[2].

Properties	**$AlH_3{\cdot}NC_2H_5(CH_3)_2$**
Concentration	0.5M in Toluene
Density	0.837g/ml at 25°C
Apparence	Colorless
Formula Weight	103.15 g/mol

II.2.3. Rare-earth Elements

Three rare-earth cations have been considered in the present work: Eu^{2+}, Eu^{3+} and Ce^{3+}. Their precursors are detailed below (Figure II.4 and Table II.3). All the rare-earth has been come from sigma-Aldrich company.

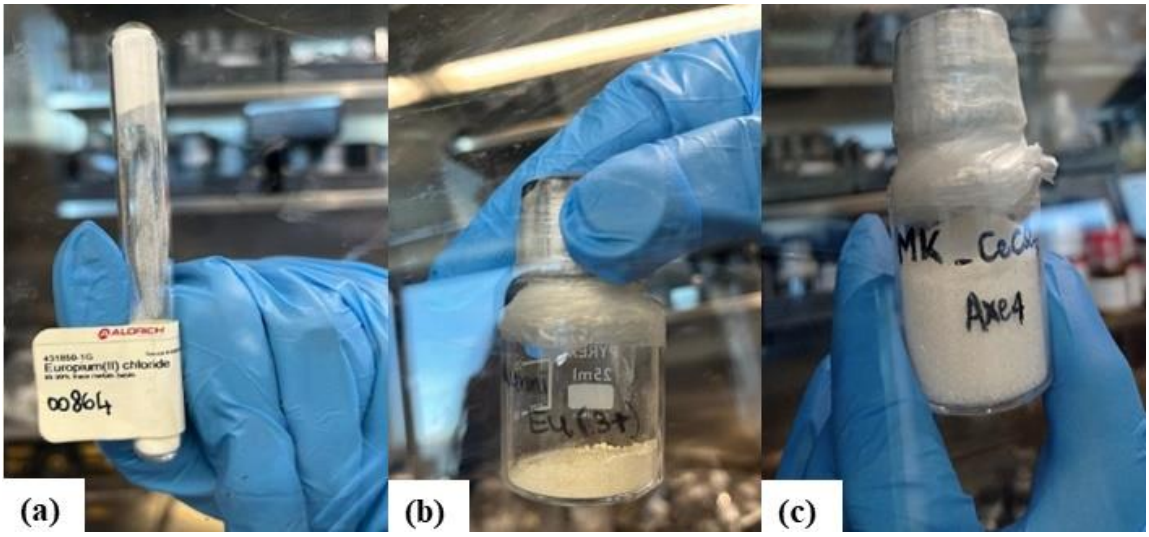

Figure II.4. Physical appearance of (a) $EuCl_2$[3] (b) $EuCl_3$[4] (c) $CeCl_3$[5].

Table II.3. Physical and Chemical State[3–5].

Property	$EuCl_2$	$EuCl_3$	$CeCl_3$
Appearance (Color)	White	Grey	White
Appearance (Form)	Powder or Chunks	Crystal and lumps	Anhydrous Beads
Purity (%)	99.99	99.99	99.9
Density (g/cm^3 at 25°C)	4.9	4.89	3.97
Formula weight (g/mol)	222.87	258.32	246.48

II.2.3.1. Europium dichloride ($EuCl_2$)

Europium dichloride is an inorganic compound and displays the chemical formula $EuCl_2$ (Figure II.4 (a)). It has bright blue fluorescence if it gets irradiated under UV light. The physical and chemical properties of $EuCl_2$ is mentioned in Table II.3.

II.2.3.2. Europium trichloride ($EuCl_3$)

Trivalent europium chloride displays the chemical formula $EuCl_3$ (Figure II.4(b)). The physical and chemical properties of $EuCl_3$ is mentioned in Table II.3.

II.2.3.3. Cerium trichloride ($CeCl_3$)

Cerium chloride ($CeCl_3$) is also known as cerium trichloride (Figure II.**4** (c)). The physical and chemical properties of $CeCl_3$ is mentioned in Table II.**3**.

II.3. Synthesis approach

II.3.1. SiAlON precursor synthesis

The reaction between PSZ and DMEA occurs in toluene in a two-neck round-bottom flask (Figure II.5(a)) to form after three days of reaction, an air- and moisture-sensitive aluminum-modified PSZ we labeled PAlSZX (X being the Si:Al ratio).

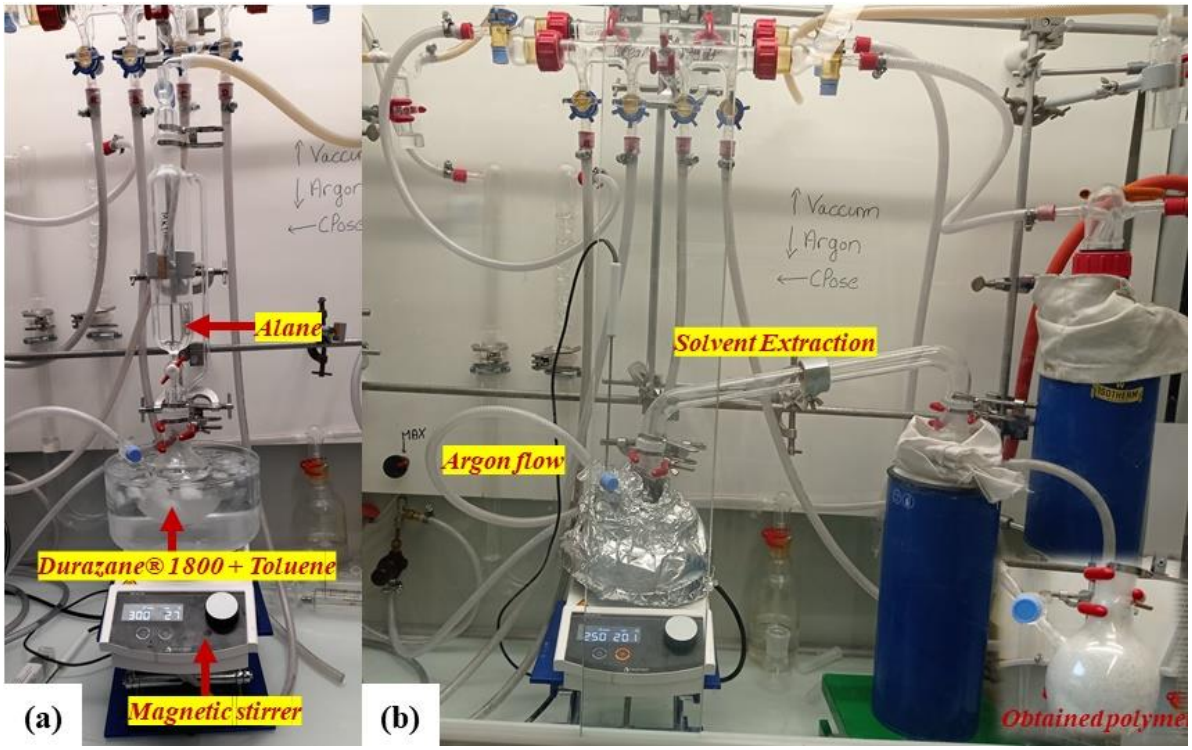

Figure II.5. Polymer synthesis procedure: (a) Reaction between PSZ and DMEA (b) Solvent Extraction of polymer and obtained polymer.

A series of precursor has been prepared: they exhibit different and controlled Si: Al molar ratios varying from 30 (**PAlSZ30**) to 3 (**PAlSZ3**). In a typical experiment targeting the Si:Al ratio 3, a solution of 5.0 g (77.7 mmol) of PSZ in 50ml toluene is introduced in a two-neck round bottom flask fitted with an addition funnel and a gas input tube After cooling the flask to 0 °C, 51.6 mL (25.8 mmol) of DMEA (25.8 mmol) is introduced into the funnel and added drop-by-

drop to the PSZ solution while stirring continuously. When the addition is complete, the temperature is naturally raised to RT and the solution is stirred for additional three days. The solvent is then extracted via an ether bridge (60 °C/0.1 mbar Figure II.5(b)) to release an air- and moisture-sensitive aluminum-modified PSZ labeled **PAlSZ3** (3 being the Si:Al ratio) that appears as a white powder in 96–98% reaction yield, which is then kept in a glovebox[1].

II.3.2. Doping strategy

The doping of our materials with rare-earth cations (Eu^{2+}, Eu^{3+}, Ce^{3+}) was done to extend the application of SiAlON-based materials towards WLEDs. The strategy consisted in modifying the SiAlON precursors with rare-earth chlorides. In a typical experiment targeting the fixed Si:Al ratio 3 and the Ce:Si ratio 0.005; a solution of 5.0 g (77.7 mmol) of PSZ and 95.37 mg (0.387 mmol) $CeCl_3$ were mixed in the glovebox. After that 50 ml toluene is introduced in a two-neck round bottom flask fitted with an addition funnel and a gas input tube. After cooling the flask to 0 °C, 51.6 mL of DMEA (25.8 mmol) is introduced into the funnel and added drop-by-drop to the PSZ solution while stirring continuously. When the addition is complete, the temperature is naturally raised to RT and the solution is stirred for additional three days. The solvent is then extracted via an ether bridge (60 °C/0.1 mbar) to release an air- and moisture-sensitive Ce-doped aluminum-modified PSZ labeled **PAlCe0.005SZ3** that appears as a white powder in 96–98% reaction yield, which is then kept in the glovebox. The rare-earth addition was done at different Eu^{2+} or Eu^{3+}, or Ce^{3+}:Si ratios (from 0.005 to 0.05) according to the same procedure as depicted above, in order to find out the highest luminescence efficiency in the final material[1,6,7].

II.4. Thermal Treatment

II.4.1. Pyrolysis

As-synthesized precursors are first pyrolyzed at 1000 °C in flowing ammonia. The procedure consists to handle the sample in the glove-box, to introduce a controlled quantity in an alumina boat to be introduced in airtight tube under argon atmosphere to prevent any oxygen contamination of the samples during the transfer from the glove-box to the furnace. The airtight tube is introduced and then open into a silica tube from a horizontal furnace (Thermoconcept® ROK70/500/11) in flowing argon and the alumina boat containing the precursor powders is pushed to the heat zone of the furnace (see Figure II.6).

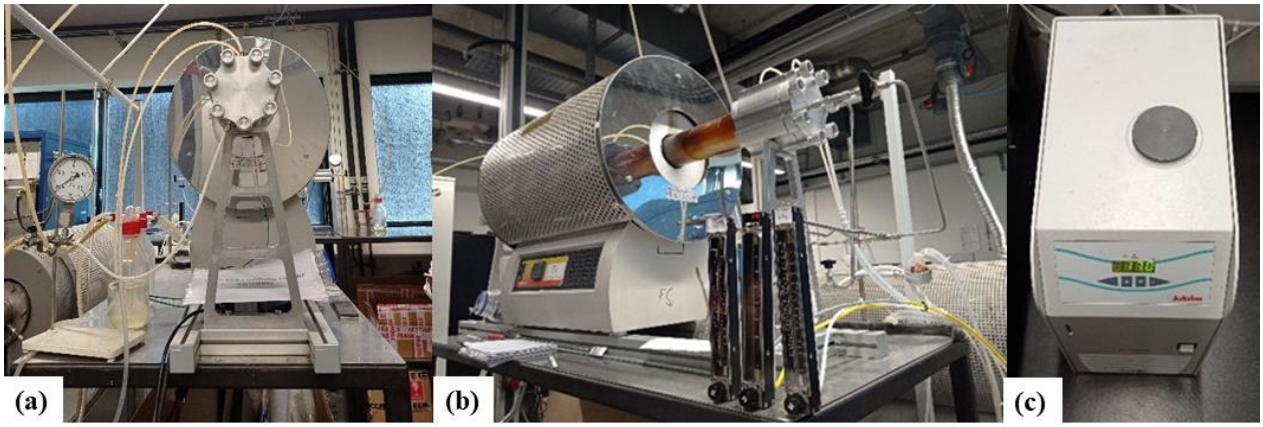

Figure II.6. Furnace setup for pyrolysis[8].

The furnace tube is then evacuated (0.1 mbar) for 30 min. and refilled with purified ammonia (99.99%) to atmospheric pressure. Subsequently, the samples are subjected to a cycle of ramping of 5 °C/min to 1000 °C in flowing ammonia (dwelling time of 2 h at 1000 °C). A constant flow (120 mL/min) of ammonia is passed through the tube during the pyrolysis cycle. After cooling under argon atmosphere, the inorganic compounds labelled PAlSZX-10 (X being the Si:Al ratio and 10 being the two first digits of the temperature at which the polymer has been exposed) and PAlRECl_xYSZ3-10 (RE being the rare-earth element, x = 2 or 3 and Y the RE:Si ratio) is transferred inside the airtight tube towards the glove-box to be stored for further heat-treatment.

II.4.2. Further heat-treatments

For higher temperature investigations (T > 1000 °C), two strategies have been followed. In a first strategy, as-pyrolyzed samples are subsequently introduced in a graphite furnace (Nabertherm VHT-GR, Figure II.7 (a)) to be pumped under vacuum (0.1 mbar), refilled with nitrogen and maintained under a constant flow of argon (200 mL/min) during the whole heat treatment. The program consisted of a 5 °C/min heating ramps up to the maximum temperature fixed in the range 1400–1800 °C, dwelling at the selected temperature for 2 h and cooling down to RT at 5 °C.min^{-1}. Samples were labeled PAlSZX-T (with X being the Si:Al ratio and T being the two first digits of the temperature at which the polymer had been exposed (14 for 1400°C, 16 for 1600°C and 18 for 1800 °C)). and PAlRECl_xSZ3-T (RE being the rare-earth element, x = 2 or 3 and Y the RE:Si ratio).

In a second strategy, Gas pressure sintering (GPS) of ammonia-treated samples has been investigated. This process involves applying high temperature and isostatic pressure (uniform pressure from all directions) to the material to achieve consolidation and densify the material.

IRC CHINO CORPORATION (Nagoya, Japan) furnace (Figure II.7 (b)) was used to sinter the PAlSZX-10 and PAlREYSZ3-10 samples at 1800°C (10°C/min) dwelling there for 2 h.

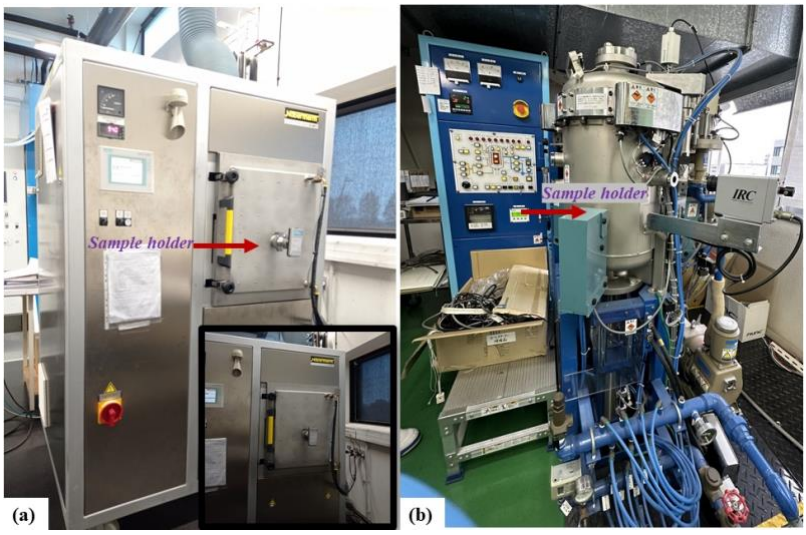

Figure II.7. (a) Graphite furnace for heat-treatment[9] (b) GPS Sintering furnace[10].

II.5. Characterization of samples

II.5.1. Fourier Transform Infrared (FTIR) spectroscopy

Fourier transform infrared spectroscopy (FTIR) in absorbance over a range spectrum from 4000 to 400cm^{-1} has made it possible to identify the chemical bonds present within the polymers. The chemical structures of the polymers were determined using FTIR (Nicolet Magna 550 Fourier transform-infrared spectrometer) spectroscopy. Air-sensitive solid polymers (5%) are mixed at with potassium bromide (KBr) inside glove box to be then pressed under 5T in the form of pellets and analyzed in transmission mode. Liquid polymers are analyzed using two commercial windows of KBr in transmission mode. OMNIC software is used for the acquisition and spectra processing.

II.5.2. Solid-state Nuclear Magnetic Resonance (NMR) spectroscopy

Nuclear Magnetic Resonance (NMR) analysis have made it possible to identify the environments around specific elements constituting polymers, intermediates reactions and ceramics. Because of the solid state of the majority of samples going from polymers to ceramics, solid-state NMR has been investigated in collaboration with LCMCP from Sorbonne university (Prof. Christel Gervais). ^{13}C, ^{15}N and ^{29}Si NMR spectra were recorded on a Bruker AVANCE 300 spectrometer (7.0 T, $\nu_0(^1H)$ = 300.29 MHz, $\nu_0(^{13}C)$ = 75.51 MHz, $\nu_0(^{15}N)$ = 30.44 MHz, $\nu_0(^{29}Si)$ = 59.66 MHz) using a 4mm Bruker probe and a spinning frequency of 10 kHz. ^{13}C and ^{15}N CP MAS (Cross Polarization Magic Angle Spinning) experiments were

recorded with ramped-amplitude cross-polarization in the ^{1}H channel to transfer magnetization from ^{1}H to ^{13}C or ^{15}N. (Recycle delay = 3 s, CP contact time = 1 ms, optimized ^{1}H spinal-64 decoupling). Single pulse ^{29}Si MAS NMR and ^{15}N spectra were recorded with a recycle delay of 60 s. ^{27}Al MAS NMR spectra were recorded at different fields (7.0 T, 11.6 T or 16.4 T on Bruker AVANCE 300, 500 and 700 spectrometers) using a 4mm Bruker probes and a spinning frequency of 14 kHz. Chemical shift values were referenced to tetramethylsilane for ^{13}C and ^{29}Si, CH_3NO_2 for ^{15}N and $Al(NO_3)_3$ for ^{27}Al.

II.5.3. Thermogravimetric Analysis (TGA)

Thermogravimetric analysis (TGA) of the polymers were carried out using a 449 F3 thermobalance (Netzsch) fitted with a SiC oven (Figure II.8). The crucibles used are made of alumina and the scavenging atmosphere is argon. The thermal cycle is fixed with a rate of heating equal to 5 °C/min up to 1000 °C. The ceramic yield was measured by calculating the difference between final and starting mass with respect to temperature from 30 to 1000 °C. respectively.

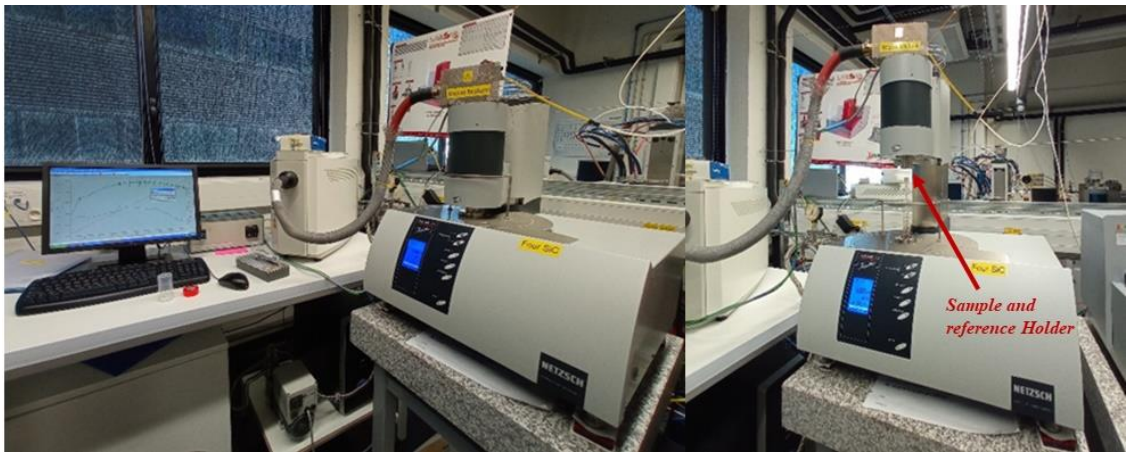

Figure II.8. TG/ATG spectrometer[11].

The pyrolyzed powder (1000 °C), subjected to a high-temperature thermogravimetric analysis (TGA) using a TGA SETSYS 2400 apparatus in Limoges, France, under a nitrogen atmosphere with a heating rate of 5 °C/min until reaching 1800 °C. The high temperature TGA was conducted to investigate mass loss phenomena at elevated temperatures.

II.5.4. X-ray Diffraction (XRD)

The phase composition of ceramic samples as powders was determined by X-ray diffraction (XRD) analyses (Bruker AXS D8 Discover, CuKα radiation, Billerica, Massachusetts, USA). The powders used are ground beforehand in an agate mortar and the massifs are analyzed

directly after polishing. The assembly used is a D8 Advance assembly (BRUKER) in θ-2θ type configuration Bragg-Brentano with copper anticathode and germanium front monochromator. The scans were performed in the range of $2\theta \in \langle 5°; 140° \rangle$ with a step of 0.015° and an exposure time of 0.7 s. The diffraction patterns were analyzed using the Diffrac + EVA software with the JCPDS-ICDD database and the program Fullprof[12] for the Rietveld refinements. Scale factor, cell parameters, Ni isotropic displacement parameter and line width parameters were refined for each phase. The profile shapes were modelled with the pseudo-Voigt function within the Thompson-Cox-Hastings formulation.

II.5.5. Elemental Analysis

Chemical analyses of the polymers were performed by hot gas extraction techniques using a Horiba Emia-321V model making possible to highlight the presence of carbon (C) and using a Horiba EMGA-830 allowing the detection of nitrogen (N), oxygen (O) and hydrogen (H) by using nickel crucibles.

The Si, Al and rare-earth element contents of both the polymer and ceramics have been measured at Mikroanalytisches Labor Pascher (Remagen, Germany).

II.5.6. Transmission Electron Microscopy (TEM)

Transmission electron microscopy (TEM) observations were carried out with a JEOL JEM 2100F equipment. Powders are dispersed in a drop of water which is then deposited on the sample holder, consisting of a grid of copper covered with a carbon film. The observation is carried out after evaporation of the solvent. The crystallographic data could be obtained by the method of diffraction of electrons in area selection.

II.5.7. Photoluminescence Emission and Excitation Analysis/ Quantum Efficiency

Photoluminescence spectroscopy, often referred to as PL, is when light energy, or photons, stimulate the emission of a photon from any matter. It is a non-contact, nondestructive method of probing materials. In essence, light is directed onto a sample, where it is absorbed and where a process called photo-excitation can occur. The photo-excitation causes the material to jump to a higher electronic state, and will then release energy, (photons) as it relaxes and returns back to a lower energy level. The emission of light or luminescence through this process is photoluminescence, PL. The PL emission and excitation spectra were recorded at RT using a fluorescence spectrometer (model F-7000, Hitachi, Nagoya, Japan, Figure II.9) with a xenon

(Xe) lamp. In addition, quantum efficiency of photoluminescent materials was also calculated by the same machine just by using different sample holder and using different software.

Figure II.9. Fluorescence Spectrometer[13].

The term "quantum efficiency" refers to the effectiveness with which a material or device converts incident photons, which are particles of light, into usable electrical energy. In the context of application, the terms internal quantum efficiency (IQE) and external quantum efficiency (EQE) are calculated by using the given equation.

Internal Quantum Efficiency (IQE) pertains to the rate at which a device converts absorbed photons into charge carriers (either electrons or holes) within its active region. It quantifies how efficiently the device generates electron-hole pairs in response to a specific number of absorbed photons. IQE considers various factors, including material properties, carrier recombination mechanisms, and internal losses within the device[14].

$$IQE = \frac{Electrons/Sec.}{AbsorbedPhotons/Sec.} = \frac{EQE}{1 - Reflection - Transmission} \quad \text{(II-1)}$$

External Quantum Efficiency (EQE) assesses a device's ability to convert incident photons into electrical current that can be recovered as usable energy. It considers photons that are absorbed, generate electron-hole pairs, and contribute to the device's external electrical output. EQE accounts for both the internal processes within the device and external factors such as light trapping, reflection, transmission, and the collection of charge carriers[15].

$$EQE = \frac{Electrons/sec.}{Photons/sec.} \quad \text{(II-2)}$$

II.5.8. Luminescent Lifetime decay

Time-resolved fluorescence spectroscopy examines the variation in fluorescence emitted by a sample as it is exposed to UV, visible, or near-IR light. The fluorescence lifetime of a substance typically indicates the average duration that the molecule remains in its excited state before returning to the ground state. This decline in fluorescence can be observed across a broad time span, ranging from picoseconds to milliseconds and even longer. The photoluminescent material's lifetime was determined using the Oriel Instruments InstaSpec V system located in Nitech at Nagoya, Japan. To measure the photoluminescent lifetime we used Sodium Salytilate as reference at 350 nm which have internal efficiency 30.9 % and external quantum efficiency 21.6 %.

Photoluminescent decay refers to the process in which a material emits light subsequent to the absorption of photons. Photoluminescent decay ensues through the excitation of electrons and can be attributed to electronic transition relaxation processes, which may be radiative or non-radiative in nature[16–18].

The luminescence decay of the samples is by using the decay curves show a non-linear decay, which can be reasonably fitted using a bi-exponential function[19].

$$I = A_1 \exp(-\frac{t}{\tau_1}) + A_2 \exp(-\frac{t}{\tau_2}) \quad \text{(II-3)}$$

where *I* is the luminescence intensity; A1 and A2 are constants; t is the time; and T1 and T2 are the lifetimes for the exponential components. The effective decay time T can be calculated according to the formula:

$$\tau = \frac{A_1\tau_1^2 + A_2\tau_2^2}{A_1\tau_1 + A_2\tau_2} \quad \text{(II-4)}$$

II.5.9. Diffuse Reflectance Spectroscopy

Optical absorption is the process by which a substance absorbs electromagnetic radiation, usually light. When photons from light interact with matter, they can be absorbed, causing electrons in atoms or molecules of matter to move to higher energies. The energy of an absorbed photon is the energy difference between the electron's initial electronic state and its final between the matches. This absorption process is represented by an absorption spectrum, which shows the absorption intensity at different wavelengths[20].

The optical absorption was measured by using a JASCO V-670 spectrometer (Figure II.10) in the ultraviolet and visible regions of the electromagnetic spectrum. When light passes through

or is reflected from a sample, the amount of light absorbed is the difference between the incident radiation (I_o) and the transmitted radiation (I). The amount of light absorbed is expressed as absorbance. Transmittance, or light that passes through a sample, is usually given in terms of a fraction of 1 or as a percentage and is defined as follows:

$$T = I / I_o \text{ or } \%T = I/I_o \times 100 \qquad \text{(II-5)}$$

Absorbance is defined as follows: $A = -\log T$

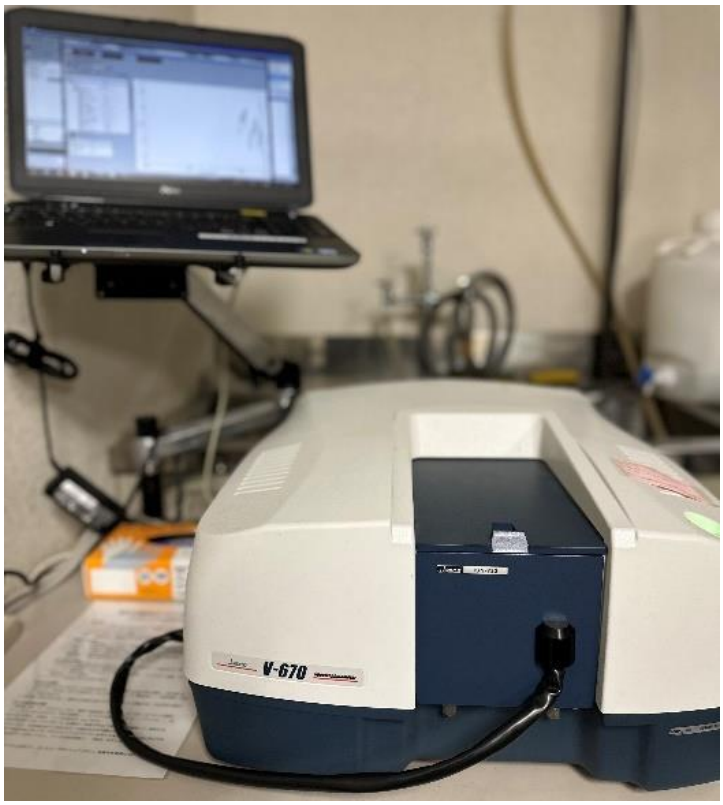

Figure II.10. UV-Vis Spectrometer[21].

II.5.10. Scanning Electron Microscopy-Cathodoluminescence (SEM-CL)

Scanning Electron Microscopy-Cathodoluminescence (SEM-CL) was performed using a JEOL electron microscope (Figure II.11), which operates at a resolution between 5000x to 20000x. The CL properties were analyzed using a CL spectrometer on a field-emission SEM, with simultaneous recording of secondary electron (SE) and CL images. To generate panchromatic images, the emitted light was directly focused on the broadband photomultiplier tube (PMT) detection system. By analyzing both SEM and CL images of the specimen, valuable optical information about the structural defects can be extracted. This approach allows for the assessment of inorganic materials containing structural defects with exceptional spatial

resolution (better than 1 µm) when combined with the structural data obtained from SEM images.

Figure II.11. SEM/CL microscopy[22].

II.5.11. Extended X-ray Absorption Fine Structure (EXAFS)

The Extended X-ray Absorption Fine Structure (EXAFS) measurements were performed at synchrotron radiation research center Nagoya, Japan. EXAFS and XANES (X-Ray Absorption Near Edge structure) are regions of the spectrum obtained from X-ray Absorption Spectroscopy. EXAFS corresponds to the oscillating part of the spectrum to the right of the absorption edge (appearing as a sudden, sharp peak), starting at roughly 50 eV and extending to about 1000 eV above the edge.

Bibliography

(1) Salameh, C.; Bernard, S.; Gervais, C.; Babonneau, F.; Bruma, A.; Malo, S.; Miele, P. Chemistry of a Series of Aluminum-Modified Polysilazanes: Synthesis, Pyrolysis Behaviour and Microstructural Evolution. *J. Eur. Ceram. Soc.* **2019**, *39* (2–3), 183–194.

(2) *Alane N,N-dimethylethylamine complex solution 0.5 M in toluene | 124330-23-0*.

(3) *Europium(II) chloride 99.99% trace metals basis | 13769-20-5*.

(4) *Europium(III) chloride anhydrous, powder, 99.99% trace metals basis | 10025-76-0*.

(5) *CeCl3 | Sigma-Aldrich*.

(6) Gao, Y.; Iihama, J.; Hamana, D.; Iwasaki, R.; Honda, S.; Asaka, T.; Kumari, M.; Hayakawa, T.; Bernard, S.; Thomas, P. Polymer-Derived β-SiAlON: Eu2+ Phosphors. *Int. J. Appl. Ceram. Technol.* **2022**.

(7) Fonblanc, D.; Lopez-Ferber, D.; Wynn, M.; Lale, A.; Soleilhavoup, A.; Leriche, A.; Iwamoto, Y.; Rossignol, F.; Gervais, C.; Bernard, S. Crosslinking Chemistry of Poly (Vinylmethyl-Co-Methyl) Silazanes toward Low-Temperature Formable Preceramic Polymers as Precursors of Functional Aluminium-Modified Si–C–N Ceramics. *Dalton Trans.* **2018**, *47* (41), 14580–14593.

(8) *Split-type tube furnaces 1100°C | Thermconcept Ofenlösungen*.

(9) *Nabertherm High-Temperature Vacuum Furnaces*. ProfiLab24 Nabertherm High-Temperature Vacuum Furnaces.

(10) *High-Temperature Fixed Point Blackbody Furnace IR-R80 series – CHINO Corporation*.

(11) *STA 449 F3 Jupiter*. NETZSCH - Analyzing and Testing. Leading in Thermal Analysis, Rheology and Fire Testing.

(12) Rodríguez-Carvajal, J.; Rosenkranz, S.; Medarde, M.; Lacorre, P.; Fernandez-Díaz, M. T.; Fauth, F.; Trounov, V. Neutron-Diffraction Study of the Magnetic and Orbital Ordering in 154 SmNiO 3 and 153 $EuNiO_3$. *Phys. Rev. B* **1998**, *57* (1), 456–464.

(13) Corporation, H. H.-T. *Fluorescence Spectrophotometer F-7000*. Hitachi High-Tech Corporation.

(14) Shim, J.-I. Internal Quantum Efficiency. In *III-Nitride Based Light Emitting Diodes and Applications*; Seong, T.-Y., Han, J., Amano, H., Morkoç, H., Eds.; Topics in Applied Physics; Springer Singapore: Singapore, 2017; Vol. 133, pp 163–207.

(15) Armin, A.; Zarrabi, N.; Sandberg, O. J.; Kaiser, C.; Zeiske, S.; Li, W.; Meredith, P. Limitations of Charge Transfer State Parameterization Using Photovoltaic External Quantum Efficiency. *Adv. Energy Mater.* **2020**, *10* (41), 2001828.

(16) Weber, M. J. Luminescence Decay by Energy Migration and Transfer: Observation of Diffusion-Limited Relaxation. *Phys. Rev. B* **1971**, *4* (9), 2932–2939.

(17) Wang, C.-Y.; Takeda, T.; ten Kate, O. M.; Xie, R.-J.; Takahashi, K.; Hirosaki, N. Synthesis and Photoluminescence Properties of a Phase Pure Green-Emitting Eu Doped JEM Sialon ($LaSi_{6-z}Al_{1+z}N_{10-z}O_z$, z 1) Phosphor with a Large Red-Shift of Emission and Unusual Thermal Quenching Behavior. *J. Mater. Chem. C* **2016**, *4* (43), 10358–10366.

(18) Suda, Y.; Kamigaki, Y.; Miyagawa, H.; Takeda, T.; Takahashi, K.; Hirosaki, N. Luminescence and Afterglow Due to Defects in β-SiAlON Crystal Powder. *J. Phys. Appl. Phys.* **2020**, *53* (16), 165108.

(19) Long, Q.; Wang, C.; Ding, J.; Li, Y.; Wu, Q.; Wang, Y. Synthesis and Luminescence Properties of a Novel Red-Emitting $LiSr_4(BN_2)_3$: Eu^{2+} Phosphor. *Dalton Trans.* **2015**, *44* (32), 14507–14513.

(20) Cui, X.; Ruan, Q.; Zhuo, X.; Xia, X.; Hu, J.; Fu, R.; Li, Y.; Wang, J.; Xu, H. Photothermal Nanomaterials: A Powerful Light-to-Heat Converter. *Chem. Rev.* **2023**, *123* (11), 6891–6952.

(21) *UV-670 UV-VIS Spectrophotometer from Jasco*. News-Medical.net.

(22) *Scanning Electron Microscope (SEM) | Products | JEOL Ltd.* Scanning Electron Microscope (SEM) | Products | JEOL Ltd.

Chapter III.

Synthesis and characterization of low oxygen content β-SiAlON Ceramics

Chapter III. Synthesis and characterization of low oxygen content β-SiAlON Ceramics 95

III.1. Introduction

In this chapter, we exploit the polymer-derived ceramics (PDC) route to form β-SiAlON ceramics. This route has been scarcely discussed in the literature (*see Chapter I*) most probably because of the complex chemistry to design SiAlON precursors (*i.e.*, metalorganic polymers) and to limit the oxygen content in final ceramics.

We propose an effective approach (Figure III.1) that consists of modifying a commercially-available liquid polysilazane – namely Durazane®1800-via its reaction with an oxygen-free aluminum complex, the alane *N*, *N*-dimethyl ethylamine as we published in 2018[1].

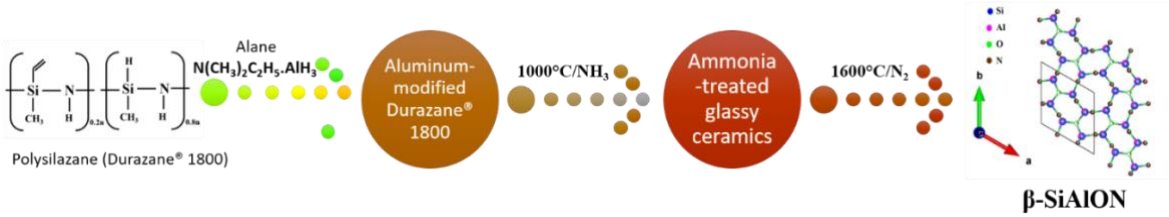

Figure III.1. Flow diagram of the preparation of β-SiAlON from Durazane®1800.

Thus, we first confirmed the reactivity of the Durazane®1800 with alane *N*, *N*-dimethylethylamine through the synthesis of a series of precursors with various Si:Al ratio. Then, we investigated the reactivity of the Al-modified Durazane®1800 with ammonia up to 1000 °C that is expected to lead to materials composed of Si, Al and N. Because of the supposed lack of oxygen in the latter, we applied a time-controlled air exposure of ammonia-treated samples at room temperature to introduce the O element in the amorphous ceramics and ultimately form the β-SiAlON phase upon heat-treatment at 1600 °C in flowing nitrogen (Figure III.1). Indeed, the control of the oxygen content is better achieved on ammonia-treated samples rather than on polymers. The latter is so sensitive to air and moisture that the oxygen content will be uncontrollable and most probably too high in the compound whereas we would like to avoid the formation of oxygen-rich SiAlON ceramics.

The precursors were subjected to characterization investigations such as FTIR-ATR and solid-state NMR spectroscopies, and elemental analysis. The conversion of the precursors into ceramic was followed by solid-state NMR spectroscopy through the characterization of pyrolysis intermediates. Final materials were extensively characterized using X-ray diffraction (assisted by Rietveld refinement), NMR spectroscopy, and elemental analysis. Microstructural analysis was performed via high-resolution TEM. Thus, we conducted systematic studies to characterize the evolutive material at each step of the process in order to understand the limitations and opportunities of this approach which has never been reported to form β-SiAlON.

III.2. Result and Discussion

III.2.1. Synthesis of SiAlON precursors

As mentioned in the introduction, aluminium-modified polysilazanes are synthesized by the reaction of alane N,N-dimethylethylamine $AlH_3{\cdot}NC_2H_5(CH_3)_2$ (DMEA as an aluminum source) with a commercially available Durazane® 1800 labelled PSZ according to our published procedure[1] detailed in the experimental part(Chapter II).

In general, the modification of polysilazanes with alane hydrides relies on hydroalumination (involving AlH from alane and vinyl groups from polysilazane: -Si-CH=CH_2 + Al-H → -Si-CH_2-CH_2-Al- and/or -Si-CH(Al-)-CH_3) and/or dehydrocoupling (involving AlH from Alane and NH groups from polysilazane: -Al-H + H-N- → -Al-N-) reactions[1]. Such reactions inherently increase the polymer branching.

Herein, we have synthesized a set of four representative polymers we labelled PAlSZX (X being the Si:Al ratio; $2.5 \leq X \leq 30$) according to different molar ratios (equivalent to the Si:Al ratio) between PSZ (by considering the monomeric unit) and DMEA. This range of ratios has been selected to form β-SiAlON with a relatively low z in their typical formula β-$Si_{6-z}Al_zO_zN_{8-z}$ in which $0 < z < 4.2$; thereby limiting the oxygen content in the final material.

In agreement with our previous report[1], polymer branching was confirmed because of the gradual introduction of Al in PSZ samples involving a transition from a low viscous liquid (PSZ) to a high viscous-liquid state (**PAlSZ30** and **PAlSZ15**) as illustrated in Figure III.2(a) and (b). The further increase of the Al content in such samples (i.e., decrease of X from **PAlSZ5** to **PAlSZ3**) delivered solid samples (Figure III.2(c) and (d)).

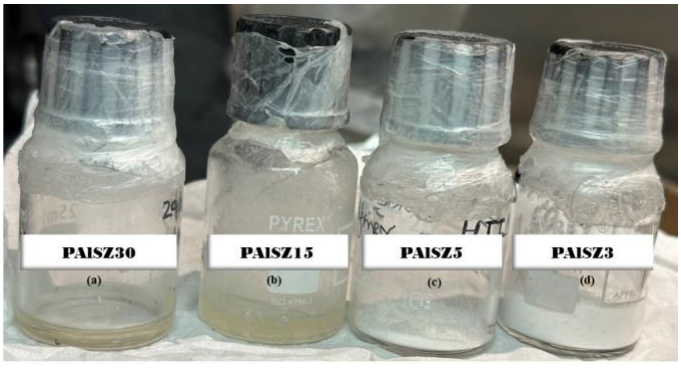

Figure III.2. Polymer samples : (a) **PAlSZ30** (b) **PAlSZ15** (c) **PAlSZ5** (d) **PAlSZ3**.

The elemental analysis data (Table III.1) of the most representative sample, i.e., **PAlSZ3**, gives a chemical formula of $\mathbf{Si_{1.0}Al_{0.3}N_{0.9}C_{2.0}H_{4.0}}$ which suggests that the precursor synthesis occurs as targeted: the Si:Al ratio measured from the elemental analyses fits with the targeted value

fixed before the synthesis (3) and the oxygen content is very low and comparable to the pristine polymer (PSZ, $Si_{1.0}C_{1.5}N_{1.1}H_{5.5}$).

Table III.1. Elemental analysis results of **PAlSZ3**.

Samples	Si	Al	O	N	C	H	Empirical formula*
	in (wt.%)						
PSZ	41.3	-	0.4	22.7	27.3	8.3	$\mathbf{Si_{1.0}C_{1.5}N_{1.1}H_{5.5}}$
PAlSZ3	35.5	11.4	1.6	16.6	30.4	5.1	$\mathbf{Si_{1.0}Al_{0.3}N_{0.9}C_{2.0}H_{4.0}}$

** reference to $Si_{1.0}$ and oxygen content omitted because of a content < 2wt. %.*

The higher carbon content in the **PAlSZ3** sample compared to that one in PSZ indicates the presence of $NC_2H_5(CH_3)_2$ groups coming from the Al-based complex as side groups[1]. Whereas the presence of such groups should increase the proportion of hydrogen, the lower hydrogen content rather reflects the occurrence of dehydrocoupling reactions (-Al-H + H-N- → -Al-N-) involving H_2 which induce polymer branching. The nitrogen content slightly decreases compared to PSZ whereas it could increase because of the presence of $NC_2H_5(CH_3)_2$ groups from the Al-based complex as side groups. Thus, this confirms that N elements are involved in other reactions such as dehydrocoupling reactions. This discussion is highlighted by FTIR (Figure III.3) and by solid-state NMR (Figure III.4(a), (b), (c) and (d)) spectroscopies.

The FTIR spectra (Figure III.3) have been normalized to the band of the methyl groups (1251 cm^{-1}), which are not expected to participate in the reaction between alane and PSZ. The readers should consider that the solid polymers are analyzed as pellets by mixing with potassium bromide (KBr) whereas experiments of liquid polymers are done by putting the polymer between two commercial windows of KBr; thereby the band resolution differs. Therefore, we present two graphs in Figure III.3: (a) for liquid PAlSZX ($30 \leq X \leq 15$) and (b) for solid compounds: PAlSZX ($5 \leq X \leq 3$) with PSZ as a reference. Absorption bands encompass the characteristic vibrations of PSZ:

- νN-H stretching at 3380 cm^{-1}, and the vibration of the -NH unit bridging two silicon atoms at 1169 cm^{-1},
- vinyl silyl groups (CH_2=CH–Si–) via the bands attributed to C–H vibrations at 3050 cm^{-1}, C=C stretching at 1592 cm^{-1}, and scissoring of terminal methylene at 1401 cm^{-1},
- Si-methyl groups with two bands located at 2957 and 2901 cm^{-1} and assigned to the C–H stretching and one more intense band at 1252 cm^{-1} ($\delta(Si{-}CH_3)$),

- Si-H groups through the strong absorption band at 2123 cm^{-1},
- the large band within the 1000-500 cm^{-1} range includes overlapping contributions related to Si-N stretching in Si-N-Si units, Si-C bond stretching as well as deformation of vinyl and Si-H units[1]. More precisely, it is attributed to Si-N stretching in Si-N-Si units at around 895 cm^{-1} and Si-C bond stretching at around 790 cm^{-1}. (CH_3)-Si wagging modes[2], C=C/=CH_2 vibration modes, Si-H scissor and Si-H wagging mode[2] expected around 970 cm^{-1}, 930 cm^{-1}, 910/860 cm^{-1} and 650 cm^{-1}, respectively.

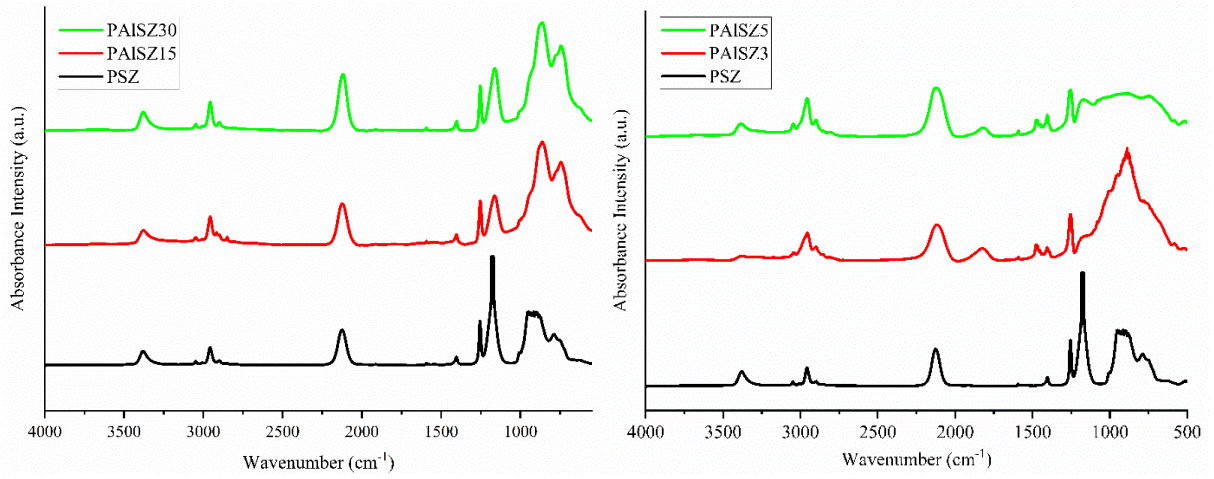

(a) (b)

Figure III.3. FTIR-ATR spectra of (a) liquid PAlSZX ($30 \leq X \leq 15$) and (b) of solid PAlSZX ($5 \leq X \leq 3$).

The most obvious changes occurring in the spectra of PAlSZX ($30 \leq X \leq 3$) samples compared to the spectrum of PSZ are:

(i) The decrease of the intensity of the bands assigned to N-H bonds at 3382 cm^{-1} - indicating the occurrence of dehydrocoupling reactions (-Al-H + H-N- → -Al-N-) and the continuous branching of PSZ via the formation of Al-N bonds in its network upon Al content increase[1].

(ii) As a consequence of i): the significant enlargement of the intense band below 1000 cm^{-1}, especially for solid compounds with a high Al content - reflecting the increase of the portion of Al-N bonds which is characterized by a band emerging at 670-710 cm^{-1}[3,4].

(iii) The gradual appearance of a band assigned to C-H bond deformation at 1478 cm^{-1} confirming the introduction of tertiary amines (-NR_3 (R = CH_3 and C_2H_5)) coming from DMEA[5], in the polysilazane network as suggested from elemental analyses.

(iv) The gradual appearance of a new band at 1819 cm^{-1} for samples with the highest Al content (**PAlSZ5** and **PAlSZ3**). This band is related to Al-H bonds whose vibrations

give rise to absorptions in this range of wavenumbers[3,4]. This probably indicates that at a certain level of alane addition, Al-H bonds, do not react anymore most probably because of the steric hindrance around NH groups. Thus, polymer branching is inhibited.

Beside this, vinyl groups are still present in PAlSZX ($30 \leq X \leq 3$) samples according to the continuous identification of the related bands even in the **PAlSZ3** sample with the highest Al content. Therefore, FTIR experiments confirm that introduction of Al via hydroalumination reactions (-Si-CH=CH_2 + Al-H → -Si-CH_2-CH_2-Al- and/or -Si-CH(Al-)-CH_3) is significantly limited and mainly dehydrocoupling reactions occur.

Solid-state NMR spectroscopy has been investigated on the **PAlSZ3** sample in which structural changes are the most obvious (Figure III.4).

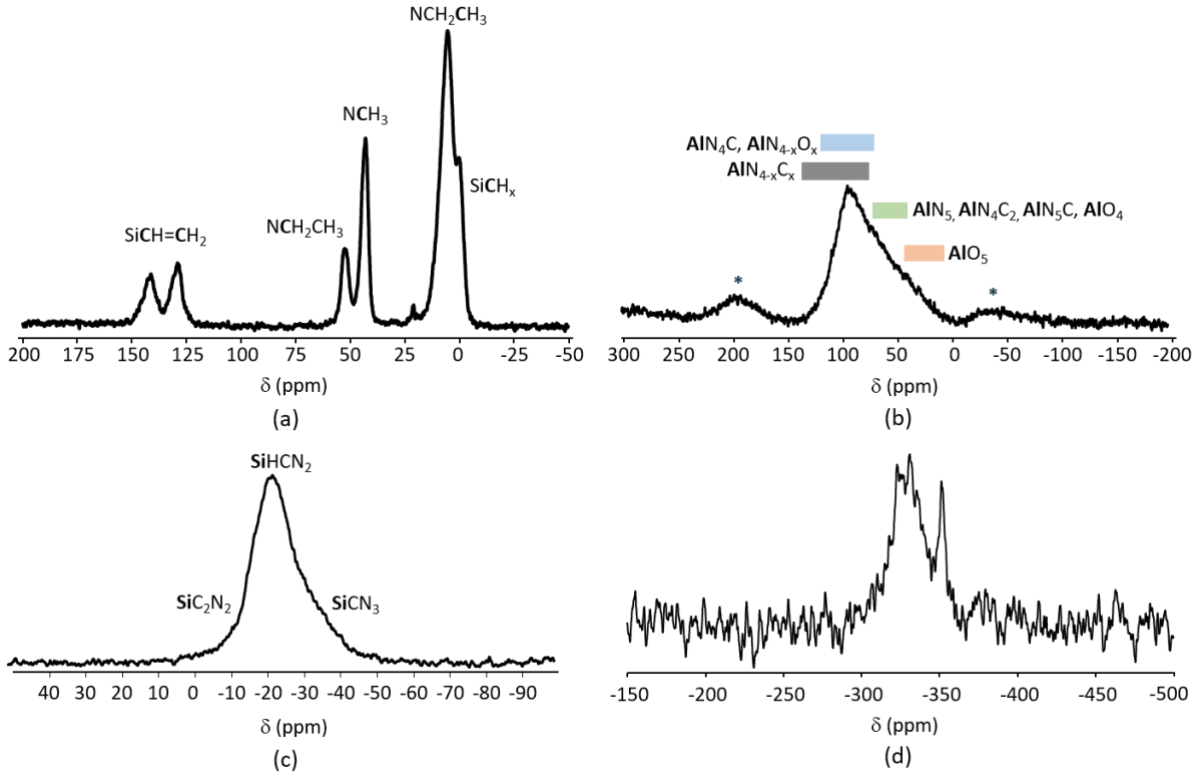

Figure III.4. Solid-state NMR spectra of **PAlSZ3**: (a) ^{13}C CP MAS, (b) ^{27}Al MAS (* indicate spinning sidebands), (c) ^{29}Si MAS, (d) ^{15}N CP MAS.

Magic Angle Spinning (MAS) has been applied to produce spectra with a better resolution[6]. The cross-polarization (CP) technique has been used for ^{13}C and ^{15}N NMR experiments to obtain spectra with reasonable acquisition times and signal-to-noise ratios[7]. Thus, when combined with MAS, polarization from abundant nuclei like H can be transferred to dilute or rare nuclei like C, N in order to enhance signal to noise and reduce waiting time between

successive experiments. Such powerful techniques will be applied in Chapter III, IV and V on precursors, pyrolysis intermediates and final materials. In the explanation of solid-state NMR spectroscopy, the emphasis on bold letters means the element which is considered (C, Al, Si, and N) in the chemical environment.

The solid-state ^{13}C cross-polarization magic angle spinning (CP MAS) NMR spectrum (Figure III.4(a)) of the **PAlSZ3** sample reveals six distinct signals at chemical shifts of 2, 21, 47, 52, 130, and 145 ppm, respectively. The broad signal at 2 ppm exhibited a shoulder at -3 ppm, indicating carbon atoms linked to silicon through aliphatic groups such as Si**C**H_3 units present in PSZ, with negative chemical shift values[8]. The signal around 2 ppm likely originated from carbon atoms in N-**C**H_2-**C**H_3 units, found in DMEA, or Si-**C**H_2-Al environments resulting from hydroalumination of C=C units in PSZ. However, the presence of signals at 130 and 115 ppm characteristic of vinyl groups (already present in PSZ), highlights the poor contribution of these groups to link Al in the PSZ network. This confirms that hydroalumination is limited; thus, we attributed this signal at 2 ppm to N**C**H_2**C**H_3 groups. Resonances at 47 and 52 ppm corresponded to carbon atoms connected to nitrogen[9], more particularly to -NR_3 (R = **C**H_3 and **C**$_2H_5$) groups present in DMEA as identified by FTIR spectroscopy.

To complete our investigation, the experimental solid-state ^{27}Al MAS NMR spectrum of the **PAlSZ3** sample has been recorded at 11.6 T (Figure III.4 (b)). However, the ^{27}Al line shapes are distorted and broadened by quadrupolar interactions[10] because ^{27}Al has a spin of 5/2. Moreover, these quadrupolar interactions depend on the symmetry of the Al sites: the higher the symmetry, the smaller the quadrupolar interaction and therefore, AlN_4 and AlO_4 signals are expected to be much narrower than signals of mixed AlCN or AlON environments. Even at high field, the MAS spectrum remains broad and lacks resolution. Thus, the spectrum displays a main and very broad signal extending from 0 to 140 ppm and centered at around 95 ppm causing significant overlap of the different peaks. This means that clear cut resolution and accurate quantification is highly challenging. One of the main pieces of structural information that can be deduced directly from the chemical shift is the coordination number of the aluminum cation as shown in Figure III.5 for different classes of compound either in solution or in the solid state[11]. The general trend shows that aluminum atoms occurring in a hexa-coordinated environment are usually characterized by higher field resonances than those of the tetra-coordinated aluminum, while five-coordinate complexes exhibit intermediate shifts. It clearly appears that the ^{27}Al chemical shift is principally influenced by the electronegativity effect of the ligand and reflects the change of the electronic density in the *p* bonding orbitals.

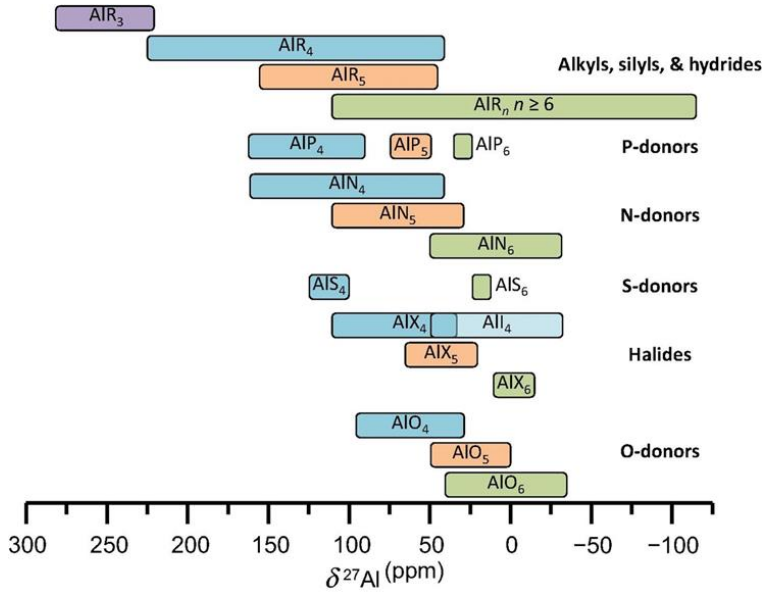

Figure III.5 ^{27}Al NMR chemical shift range as a function of coordination number of aluminum (six or higher in green; five in orange; four in blue; three in purple) and as a function of ligand type[11].

Based on both Figure III.5, the position of the signal present in the ^{27}Al MAS NMR spectrum of **PAlSZ3** (Figure III.4(b)) and elemental analyses (low oxygen content), the spectrum is mainly composed of carbon- and nitrogen-containing environments. As a consequence, we tentatively attributed the signal present in the ^{27}Al MAS NMR spectrum of **PAlSZ3** to **Al**$N_{4-x}C_x$ ($0 \leq C \leq 4$)[1] environments which includes several contributions such as **Al**N_3C units at around 130 ppm and **Al**N_4 environments at 110 ppm[12]. However, its broadness towards lower shifts can indicate the presence of **Al**N_4C or **Al**N_xO_{4-x} (x = 1, 2) units at 70-120 ppm[13], **Al**N_5, **Al**N_4C_2, **Al**N_5C or **Al**O_4 environments at 45-70 ppm[10,12,13] and possibly **Al**O_5 at 5-45ppm[11]. Indeed, although the elemental analysis of the **PAlSZ3** sample confirmed the very limited contribution of oxygen in the polymer (characterization done on-site), it is important to mention that an oxygen contamination (therefore introduction of oxygen in the polymer) of the precursors may occur because of their high sensitivity towards air and moisture. Thus, the storage and time which is inherently imposed between synthesis and the NMR spectroscopy characterization done in Paris can be a cause of the post-synthesis oxygen contamination of the polymer and the identification of oxygen-containing environments by solid-state ^{27}Al NMR spectroscopy. Excluding the fact that the precursor synthesis does not involve oxygen introduction in the **PAlSZ3** sample and considering that the ^{27}Al signal of alane appears around 145 ppm[12], solid-state ^{27}Al MAS NMR spectroscopy confirms here the establishment of **Al**-N bonds in PSZ which inherently occurs through dehydrocoupling reactions.

The solid-state ^{29}Si NMR MAS spectrum (Figure III.4(c)) of **PAlSZ3** is composed of a dominant signal centered at -21 ppm; a chemical shift value consistent with a **Si**HCN_2 environment which can be identified in the given structure of PSZ[14]. However, the broadness of this signal also suggest the presence of **Si**C_2N_2 and **Si**CN_3 groups[15]; the former is also identified in PSZ. Thus, the introduction of Al in PSZ does not affect the main chain of the polymer and highlights that Al is present in side groups.

The experimental ^{15}N CP MAS NMR spectrum (Figure III.4(d)) of the **PAlSZ3** sample shows two main signals centered around -325 ppm and -353 ppm. **N**HSi_2 environments in the silazane backbone are known to emerge as a signal between – 335 ppm[15] and – 325 ppm[9]; thereby confirming their identification in **PAlSZ3** . The signal of Al-N$(CH_3)_3$ groups has been reported to emerge at – 355 ppm[16]. Therefore, the presence of Al-N$C_2H_5(CH_3)_2$ groups can be confirmed through the signal at -353 ppm. Besides, two diffuse signals can be identified around -370 ppm and -290 ppm. ^{15}N chemical shift values of **N**$Al_{4-x}H_x$ (x = 1-3) environments are calculated between -330 and -370 ppm[17]. This can confirm the presence of Al-H bonds in the polymer as revealed by FTIR spectroscopy. ^{15}N signal of Al**N**$_4$ environments in AlN are observed at -295 ppm.; thereby possibly indicating the establishment of Al-N bonds in the polymer as confirmed by ^{27}Al MAS NMR spectroscopy.

The combination of multinuclear (^{27}Al, ^{13}C, ^{15}N and ^{29}Si,) solid-state NMR data with results derived from elemental analyses and FTIR confirms our published observations on similar polymers: **the modification of PSZ with DMEA allows the controlled and tailored introduction of Al in the PSZ network via main dehydrocoupling reactions (**Figure III.6**)**.

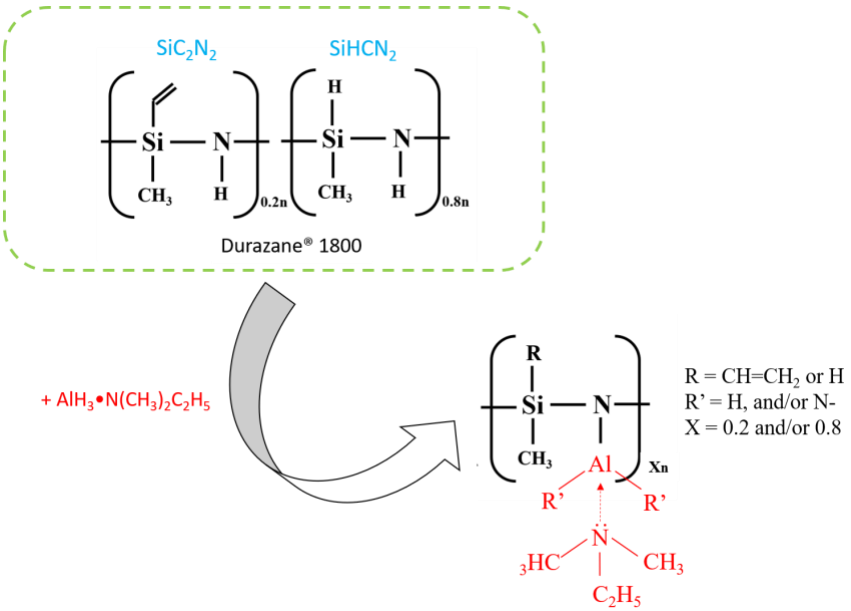

Figure III.6. Representation of chemical environments identified in **PAlSZ3**.

Such reactions allow polymer branching of the low viscous liquid PSZ to form solid compounds with the increase of the Al content via the **main formation of -Al-N- units**. At a certain level of reaction, polymer branching is restricted because of the steric hindrance imposed by the presence of Al. As a consequence, solid compounds contain $-(-N)_{3-x}(H)_xAl:NR_3$ (R = CH_3 and C_2H_5) as side groups. Thus, Figure III.6 propose a simplified structure of **PAlSZ3**.

III.2.2. Precursor-to-β-SiAlON conversion

This section is shared into two parts. The first part reports the thermo-chemical transformation of precursors which have been previously investigated as they are subjected to gradual heating, starting from RT to 1000 °C in flowing ammonia and then exposure to air for 1 minutes before their storage in the glovebox. This stage is associated with weight losses because of the transformation of preceramic polymers into inorganic compounds - mostly amorphous ceramics through the release of gaseous by-products[18]. However, it has to be mentioned that we could not investigate TG experiments of the samples – while it represents a major characterization tool for preceramic polymers – because of the lack of TG experiments working in flowing ammonia. Therefore, to gain a thorough understanding of the main reactions governing the transformation of precursors into amorphous ceramics (obtained at 1000 °C), we have selected the representative **PAlSZ3** compound and we have investigated the evolution of its chemical environment upon pyrolysis at 300, 700 and 1000 °C by solid-state NMR spectroscopy. We then present elemental analysis results to understand our procedure that consists to expose in air the samples pyrolyzed at 1000 °C for 1 minute. In the second part, we focus on the high temperature conversion of ammonia-treated samples which is associated with structural changes[18]. In the present case, it consists to crystallize the amorphous ceramics formed at 1000 °C into β-SiAlON ones. Again, solid-state NMR spectroscopy has been investigated to follow the evolution of the chemical environment of **PAlSZ3-**derived ceramics upon heat-treatment to 1600 °C. Solid-state NMR experiments have been supported by elemental analysis, X-ray diffraction (XRD) (which has been extended to samples heat-treated to 1800 °C) assisted by Rietveld refinement and HR-TEM observations.

As indicated in the experimental part, it is important to explain the procedures for pyrolyzing precursors in ammonia flow and charactering them by elemental analyses and solid-state NMR to understand the results in the following sections. A certain quantity of precursors is put in an alumina crucible and the latter is then introduced in an airtight tube. This step is achieved in a glovebox under argon. Thus, the precursor is under protective atmosphere. Then, the precursor

in the airtight tube is transferred to the furnace tube which is open from one side to work under strong argon flow. The airtight tube is quickly open (side of the furnace) to be put inside the furnace tube (edge of the tube). The other side of the airtight tube is then open once placed in the furnace tube and the crucible containing the precursor is push to the heating zone in flowing argon; the furnace tube is then close and put under vacuum. In our opinion, contamination by air is relatively limited. In contrast, to pick up the precursor after pyrolysis in flowing ammonia, the furnace tube works at room temperature under strong argon flow. The airtight tube is open at both side and put at the edge of the furnace tube to flow argon inside. We draw the as-pyrolyzed precursors from the heating zone to be put in the airtight tube. The latter is drawn from the edge of the furnace and close as fast as possible outside the furnace tube (thus in air) and transferred to the glovebox to be stored. It takes in general 1 min of transfer. Oxygen contamination could be envisioned; at least with air- and moisture-sensitive products. Elemental analyses (H, C, N and O) are done on-site which is expected to reflect the right element content of materials. Solid-state NMR spectroscopy is done in Paris which still increases the chances to oxidize the pyrolyzed precursors although all the precaution are taken; thereby NMR spectra can be affected by the post-pyrolysis oxidation of analyzed samples.

III.2.2.1. Pyrolysis of precursors in flowing ammonia: Chemical environment evolution

We firstly investigated solid-state ^{13}C CP MAS NMR spectroscopy (Figure III.7 (a)). However, it has been only possible on the sample pyrolyzed at 300°C (**PAlSZ3_3**) despite the fact that proton–carbon CP was applied to enhance the ^{13}C signal. Indeed, the experimental ^{13}C CP MAS NMR spectrum of the **PAlSZ3_7** sample and other samples could not be recorded with CP due to the low number of remaining protons linked to carbon in this system. This demonstrates the strong reactivity of ammonia towards specific carbon-based groups bearing by the polymer: signals related to NCH_2CH_3 and NCH_3 groups (resonances at 47 and 52 ppm) as side groups vanished indicating that they react with ammonia in the early stage of the polymer-to-ceramic conversion process most probably via transamination reactions ($-NR + NH_3 \rightarrow -NH + NRH_2$ ($R = CH_3, C2H_5$)). Besides, ^{15}N CP MAS NMR spectra could neither recorded.

^{27}Al MAS NMR spectroscopy has been then investigated and the corresponding spectra are reported in Figure III.7(b). Heat-treatment at 300 °C in flowing ammonia shows that the polymer network is retained in the **PAlSZ3_3** compound. However, it confirms the consumption of carbon based on the fact that the signal sharpens (it extends from 0 to 120 ppm)

and the maximum shifts towards 90 ppm. This indicates firstly the disappearance of AlN_3C environments (130 ppm). It could confirm the role of ammonia to release carbon-based groups but we cannot omit the fact that oxidation also occurs. Secondly, it highlights the presence of several contributions at 70-120 ppm, at 45-70 ppm, at 5-45 ppm and in the range -5-15 ppm which are difficult to attribute.

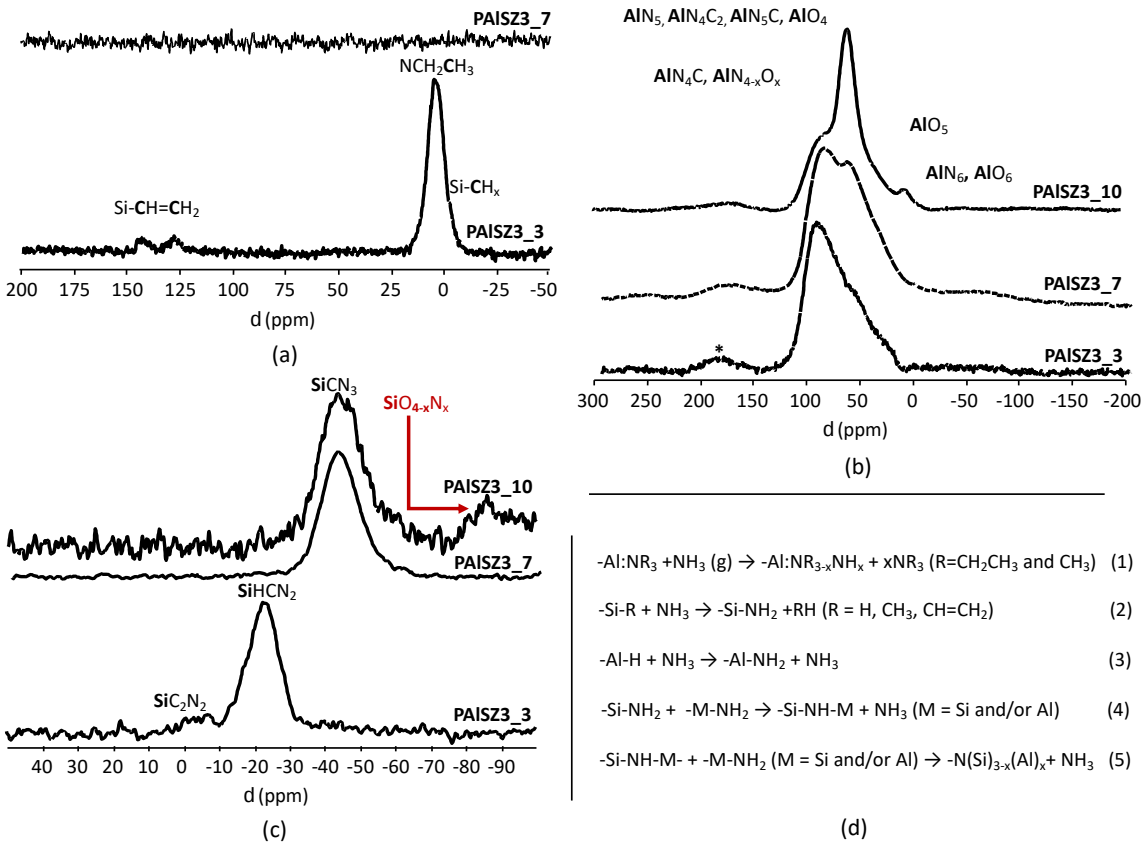

Figure III.7. Solid-state NMR spectra of **PAlSZ3**-derived pyrolysis intermediates: (a) ^{13}C MAS NMR, (b) ^{27}Al MAS (* indicate spinning sidebands, recorded at 11.6 T) and (c) ^{29}Si MAS NMR. (d) Proposed pyrolysis mechanisms.

Based on Figure III.5, it is clear that the **PAlSZ3_3** sample exhibit oxygen- and/or nitrogen-containing environments. Thus, these contributions could represent **Al**N_4C or **Al**N_xO_{4-x} (x = 1, 2) environments[13], **Al**N_5 **Al**N_4C_2, **Al**N_5C or **Al**O_4 environments[11–13], **Al**O_5 environments[11] and **Al**N_6 or **Al**O_6 environments[11], respectively. As mentioned in the introduction of this section and for the polymer as well, the oxygen-based units – if present - are probably not the result of a reaction occurring during the heat-treatment at 300 °C. As the temperature reached 700 °C (**PAlSZ3_7**), the same environments are confirmed. However, because of the role of ammonia to reduce carbon, we suggest that AlN_xO_{4-x} ($0 \leq x \leq 4$) and **Al**Y_6 and **Al**Y_5 (Y = N and/or O) environments are rather anticipated.

The spectrum of the **PAlSZ3_10** sample confirms the evolution towards a carbon-free sample: it indicates the presence of a main signal at a position that could be attributed to **Al**N_5, **Al**O_4 environments[11–13] in the spectrum. In addition, we can identify a small contribution of **Al**N_6 or **Al**O_6 environments[11] in the spectrum. It is important to mention that in SiAlON, Al is expected to be coordinated as AlO_4 and not as AlO_6 found in (Al_2O_3)[19,20]. However, such environments have already been identified in β-SiAlON by solid-state NMR: Butler et al.[21] measured at 9.4 T the ^{27}Al chemical shifts of AlN_4 tetrahedra (110 ppm) and AlO_6 octahedra (3 ppm) in Si-Al-O-N phases. Dupree et al.[22] reported MAS ^{27}Al NMR studies at 8.5 T of various β-SiAlON and found AlO_6 (4 ppm), AlO_4 (66 ppm) and AlN_4 (104-109 ppm) signals. Thus, residual AlO_6 environments are envisioned.

As mentioned in the introduction of this section, post-oxidation of pyrolyzed precursors can be envisioned during the transfer from the furnace to the glovebox and also from the glovebox to the NMR investigations and this is probably the two reasons to identify oxygen-based environment in the ammonia-treated samples. To highlight the oxygen contamination of **PAlSZ3_10** when exposed to air at room temperature (RT), we followed the evolution of the oxygen content in the **PAlSZ3_10** sample after different times of exposure to air at RT from 1 min (**PAlSZ3_10_1min.** which corresponds to the conventional time to transfer the pyrolyzed precursor to the glove-box for storage under argon) to 1 week (**PAlSZ3_10_1 week**). After exposure, the **PAlSZ3_10** is stored in the argon-filled glovebox to be prepared for O, N and H analyses. The results are depicted in Table III.2.

Table III.2. Evolution of the O, N, H contents in the **PAlSZ3_10** sample pyrolyzed in flowing ammonia and then exposed in air at RT for controlled time. Comparison is done with the same sample pyrolyzed in flowing nitrogen (**PAlSZ3_10N_2_1min.)**.

Samples	O%	N%	H%
	in wt. %		
PAlSZ3_10_1min.	4.5	29.8	0.1
PAlSZ3_10_30min.	5.2	31.4	1.0
PAlSZ3_10_1/2 day	5.1	26.7	1.0
PAlSZ3_10_1 day	9.0	26.2	1.6
PAlSZ3_10_1 week	13.7	22.0	2.0
PAlSZ3_10N_2_1min.	0.8	18	1.2

We can observe that there is an obvious effect of the time of exposure in air on the oxygen content of the **PAlSZ3_10** sample: It increased from 4.5 wt.% (conventional exposure) to 13.7 wt.% after 1 week of exposure and this increase is done to the detriment of the nitrogen content.

In addition, the hydrogen content increases most probably because of surface hydrolysis. In comparison, we analyzed the O, N and H contents of the precursor pyrolyzed at 1000 °C in flowing nitrogen. It is labelled **PAlSZ3_10N$_2$_1min.**; 1 min being the conventional time for the transfer from the furnace to the glovebox. This sample can be considered as free of oxygen (< 2 wt. %). Besides, we can clearly see in Table III.2 the interest of ammonia to enrich samples with nitrogen.

We investigated ^{27}Al solid-state NMR spectroscopy of the **PAlSZ3_10N$_2$_1min.** sample (Figure III.8). Whereas, we can clearly see a relatively narrow signal around 60 ppm in the spectrum of the **PAlSZ3_10** sample, it is almost absent in **PAlSZ3_10N$_2$_1min.**. Thus, this confirms that the signal is assigned to AlO_4 environments. In **PAlSZ3_10N$_2$_1min.**, the obtained signal – despite its broadness – reflects the presence of **Al**$N_{4-x}C_x$ ($0 \leq C \leq 4$) environments. Thus, oxygen contamination occurs with ammonia-treated samples confirming their extreme sensitivity to oxidation/hydrolysis. Considering that oxygen content affects the stability of SiAlON ceramics, we have selected the conventional time to transfer the ammonia-treated precursors to the glove-box for storage under argon; thereby a time exposure of 1 min for our further experiments in order limit as much as possible oxygen contamination.

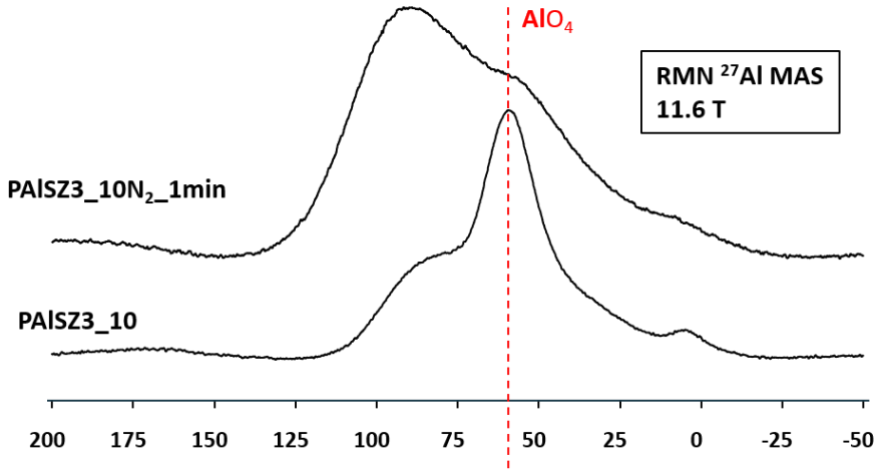

Figure III.8. Solid-state ^{27}Al MAS NMR investigations of **PAlSZ3_10N$_2$_1min** recorded at 11.6 T.

We investigated the same compounds by ^{29}Si MAS NMR spectroscopy. The corresponding spectra generated from the representative **PAlSZ3** sample are depicted in Figure III.7(c). They show that a heat-treatment at 300°C (**PAlSZ3_3**) in flowing ammonia does not change fundamentally the chemical environment of the polymer: the spectrum exhibits a major signal at 22 ppm (**Si**HN_2) although it tends to sharpen because of the decrease of the contributions of **Si**C_2N_2 and **Si**CN_3 groups (i.e., carbon-based groups are reduced by ammonia treatment). Thus, we can confirm that the compound is still in its polymeric stage and that ammonia is highly

reactive towards carbon-based units in the early stage of the process. A transition occurs from 300 to 700 °C (**PAlSZ3_7**): a solitary broad signal emerges at -44 ppm; a position fitting with the presence of **Si**CN_3 units[20] in the materials. However, its broadness (the signal extends from -60 to 30 ppm) indicates the presence of **Si**N_4 environments too. We therefore confirm that the major conversion of the precursor into an inorganic material occurs in the temperature range 300 - 700 °C in flowing ammonia. However, side 'organic' groups (containing carbon and hydrogen atoms) are probably still present in the materials. This is confirmed when investigating the ^{29}Si MAS NMR spectrum of the **PAlSZ3_10** sample (Figure III.7(c)). The same broad signal is present along with the identification of a diffuse signal at -85 ppm which can be attributed to $SiO_{4-x}N_x$ units[23,24] because of the short exposure to air to introduce oxygen in the network of the compound.

On the basis of the structural assignment, pyrolytic decomposition pathways from **PAlSZ3** can be outlined. They are described in Figure III.7(d). It has to be mentioned that we did not consider oxygen post-contamination below 1000 °C. Therefore, the mechanisms which are suggested in Figure III.7(d) do not consider the involvement of the oxygen element. **The low temperature regime of the conversion is mainly associated with transamination reactions** as depicted in eq. (1) of Figure III.7(d) leaving a multi-coordinate -N- species bound to Al in extended networks. Then, **in the temperature range 300 - 700 °C, NH_3 can react with Si-R (R = $CH=CH_2$, CH_3, H) bonds (especially Si-H which are sensitive to nucleophilic substitution to form Si-NH_2 units** as shown in eq. (2) of Figure III.7(d) **and Al-NH_2 groups** identified in **PAlSZ3** (Figure III.7(d), eq. 3), **which can further condense into Si-NH-M-units (M= Si and /or Al)** (Figure III.7(d), eq. 4) **and then into $N(Si)_{3-x}(Al)_x$ units** (Figure III.7(d), eq.5); thereby, ultimately forming Si-N and Al-N bonds after heat-treatment at 1000 °C in ammonia atmosphere. Thus, the majority of the carbon-based groups bearing by the polymer are released in this temperature range while the material is enriched with nitrogen. As an illustration the C and N contents of the **PAlSZ3_10** sample are 1.4 and 29.8 wt.%, respectively (Table III.3).

Table III.3. Elemental analysis of **PAlSZ3_10** sample.

Samples	Si	Al	O	N	C	H
	in wt. %					
PAlSZ3_10	*	*	4.5	29.8	1.4	0.1

**not measured*

The time-controlled RT oxidation after the pyrolysis at 1000 °C in flowing ammonia proceeds by selective oxidation of Al; thus, it affects mainly the Al environment by forming $AlN_{4-x}O_x$, AlO_4 and a limited portion of AlO_6 units besides SiN_4 environments. The limited carbon

content in the compounds produced at 1000 °C (Table III.3) confirms the role of ammonia to form carbon-free PDC.

III.2.2.2. High temperature heat-treatment of ammonia-treated samples: Chemical environment and microstructural evolutions

Ammonia-treated samples are amorphous as revealed by X-ray diffraction (XRD, Figure III.9).

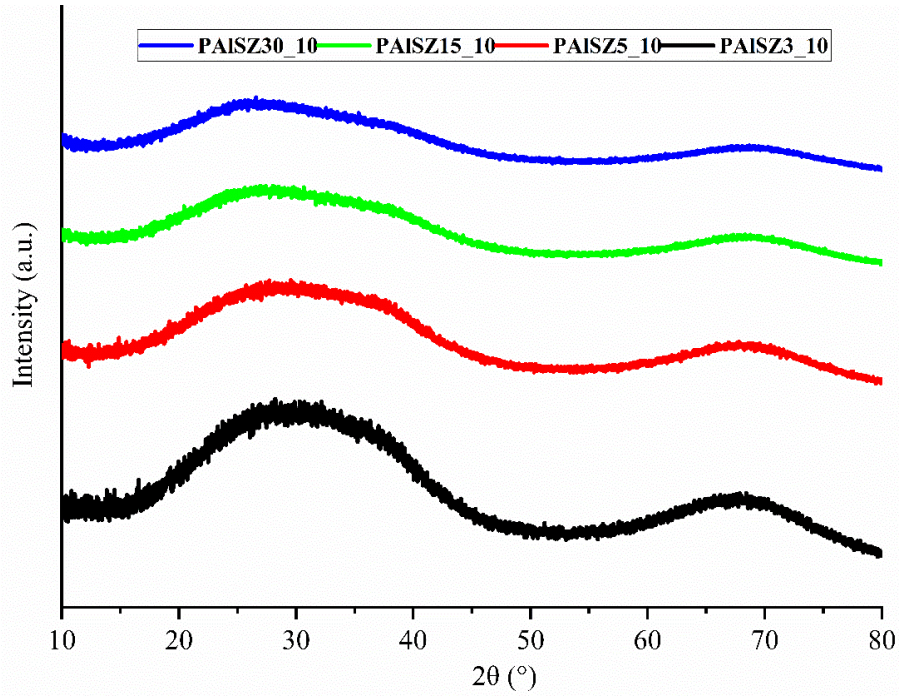

Figure III.9. X-ray diffraction (XRD) patterns of PAlSZX_10 samples ($3 \leq X \leq 30$).

Thus, in this section, we focus on the second part of the conversion consisting to crystallize the amorphous ceramics (formed at 1000 °C) into the β-SiAlON compounds. Again, solid-state NMR is used to follow the evolution of the chemical environments in the evolutive compounds at high temperature under flowing nitrogen. This is complemented by X-ray diffraction (XRD) assisted by Rietveld refinement, chemical composition measurements and high resolution-transmission electronic microscopy (HR-TEM) of samples isolated at different temperatures. XRD investigations achieved at room temperature consist in following the structural evolution of the ammonia-treated materials labelled PAlSZX_10 samples ($3 \leq X \leq 30$); (Figure III.9) upon their subsequent heat-treatment at 1400°C (PAlSZX_14 samples ($3 \leq X \leq 30$); Figure III.10), 1600 °C (PAlSZX_16 samples ($3 \leq X \leq 30$); Figure III.11) and 1800 °C (PAlSZX_18 samples ($3 \leq X \leq 30$); Figure III.12) dwelling at each temperature for 2 h (*See experimental part for more details*).

Upon heat-treatment of PAlSZX_10 samples ($3 \leq X \leq 30$) to 1400 °C (PAlSZX_14 ($3 \leq X \leq 30$), the XRD patterns reported in Figure III.10 distinguish two series of compounds.

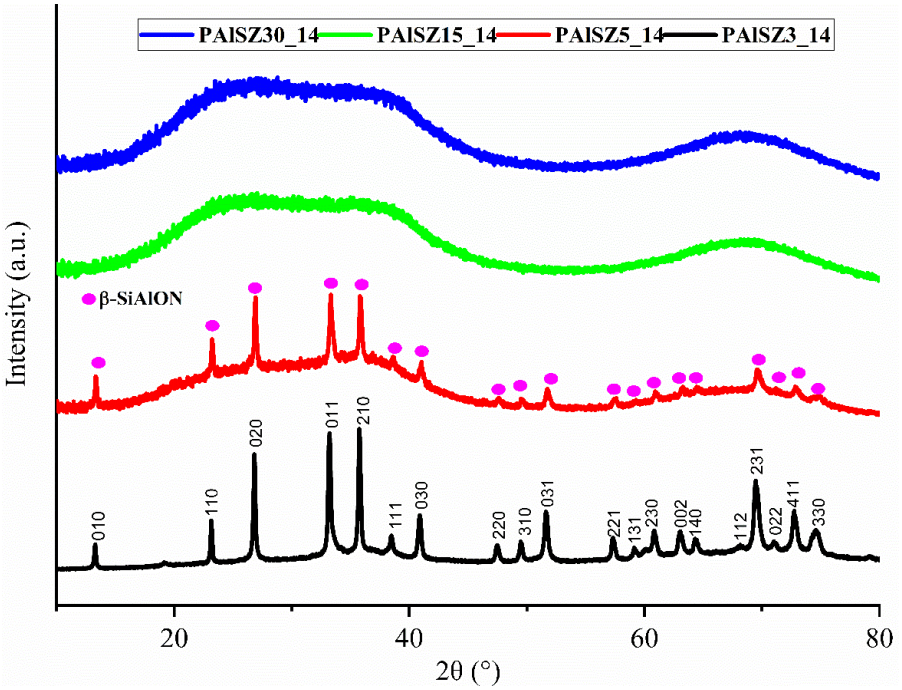

Figure III.10. X-ray diffraction (XRD) patterns of PAlSZX_14 samples ($3 \leq X \leq 30$).
Indices of the XRD peaks of the β-SiAlON are given for PAlSZ3_14 sample.

We can distinguish samples with the highest Si:Al ratio namely **PAlSZ15_14** and **PAlSZ30_14** displaying highly broad peaks characteristic of amorphous solids and samples with the lowest ratio namely **PAlSZ5_14** and **PAlSZ3_14** exhibiting sharp peaks corresponding the β-SiAlON[25–27] (PDF 01-077-0755) phase. These two samples (**PAlSZ5_14** and **PAlSZ3_14)** are only partially crystallized has suggested by simultaneous presence of diffraction peaks and a diffuse signal in the base line. The crystallization is higher in **PAlSZ3_14** sample and in addition, we can also see few additional peaks corresponding to very small amounts of secondary phases.

Crystal growth occurs for the first series of amorphous samples only after heat-treatment to 1600 °C (**PAlSZ30_16**; **PAlSZ15_16**) as shown in Figure III.11. It gives rise to three phases, identified as α-Si_3N_4[28] (PDF 04-005-5074), β-SiAlON[26,27] (PDF 01-077-0755) wurtzite w-AlN[4,17] (PDF 00-008-0262)[29] where intensity of α-Si_3N_4 are higher. Similarly, **PAlSZ3_16** and **PAlSZ5_16** samples show the highest intensity for β-SiAlON phase with few signals related to w-AlN phase. In addition, contrarily to samples heated at lower temperature, there is no visible characteristics of amorphous phase suggesting that the all samples are (almost) fully crystallized.

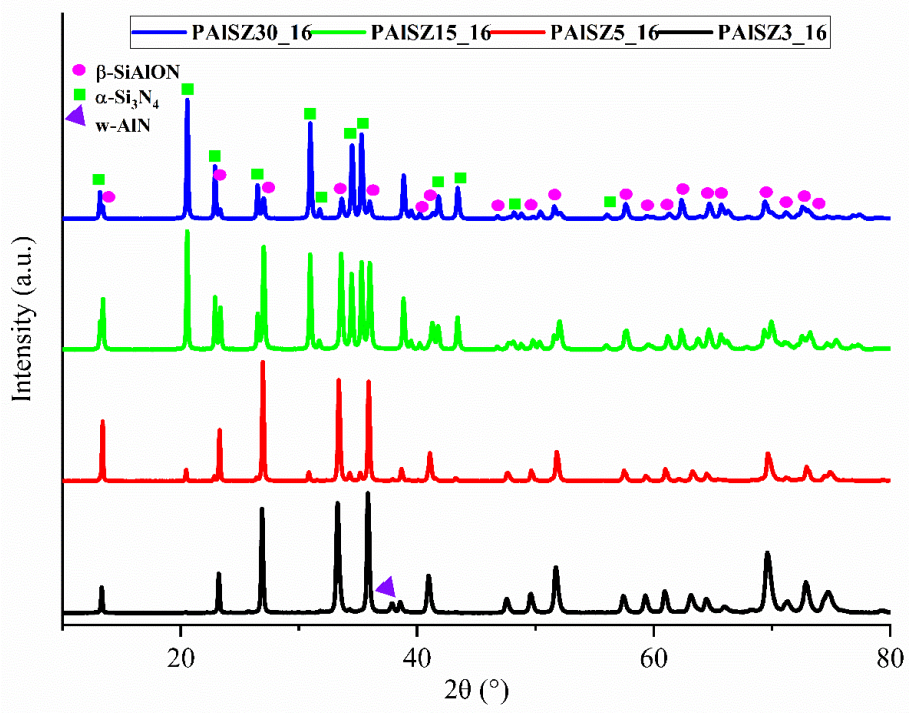

Figure III.11 X-ray diffraction (XRD) patterns of PAlSZX_16 samples ($3 \leq X \leq 30$).

The presence of these phases will be confirmed below by using Rietveld refinement where hkl indices can be found in given PDF file. These phases are identified as well after heat-treatment to 1800 °C (PAlSZX_18 ($3 \leq X \leq 30$); Figure III.12).

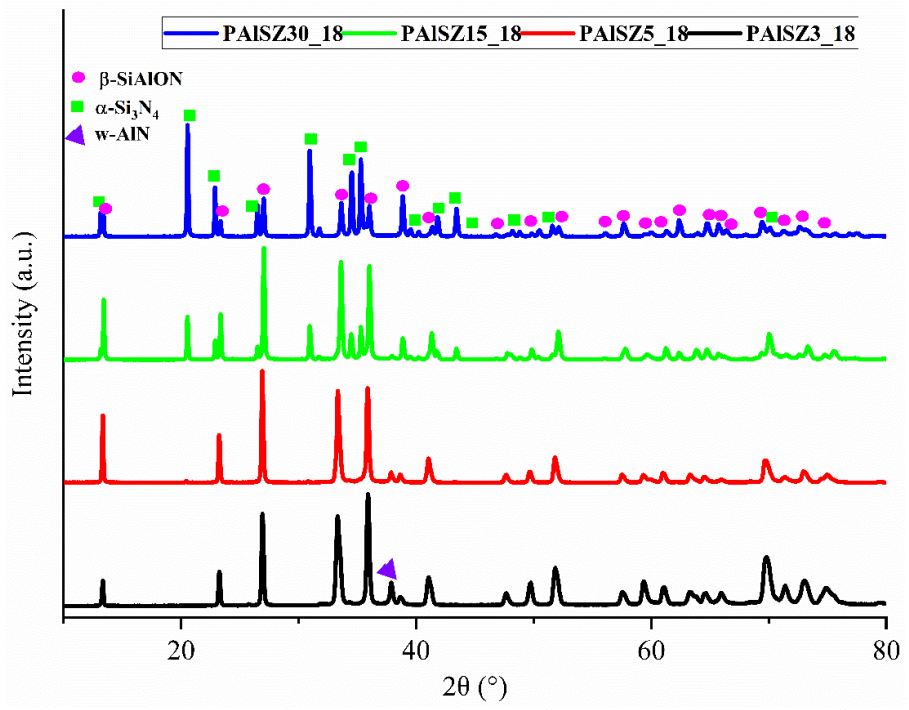

Figure III.12 X-ray diffraction (XRD) patterns of **PAlSZX_18** samples ($3 \leq X \leq 30$).

We can observe that α-Si_3N_4 peak intensities are significantly reduced in **PAlSZ5_18** and **PAlSZ3_18** samples. This demonstrates that, the structural evolution (and the phase content) is closely affected by the Si:Al ratio as expected.

As mentioned above, the Rietveld refinement has been used to confirm the presence of the phases proposed and identified for the samples **PAlSZ3_16** and **PAlSZ3_18** and to quantify them (Figure III.13).

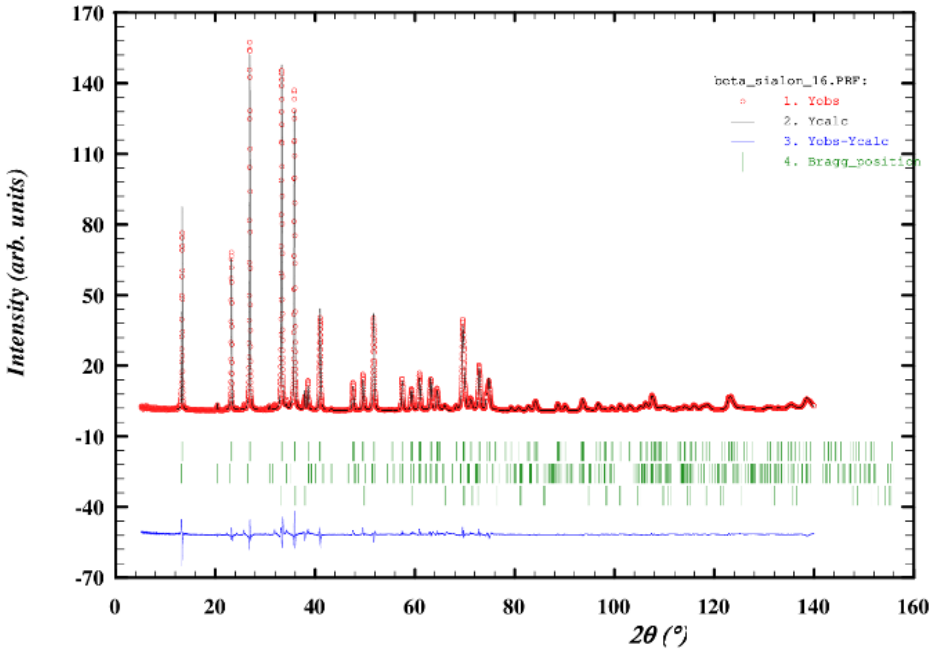

(a)

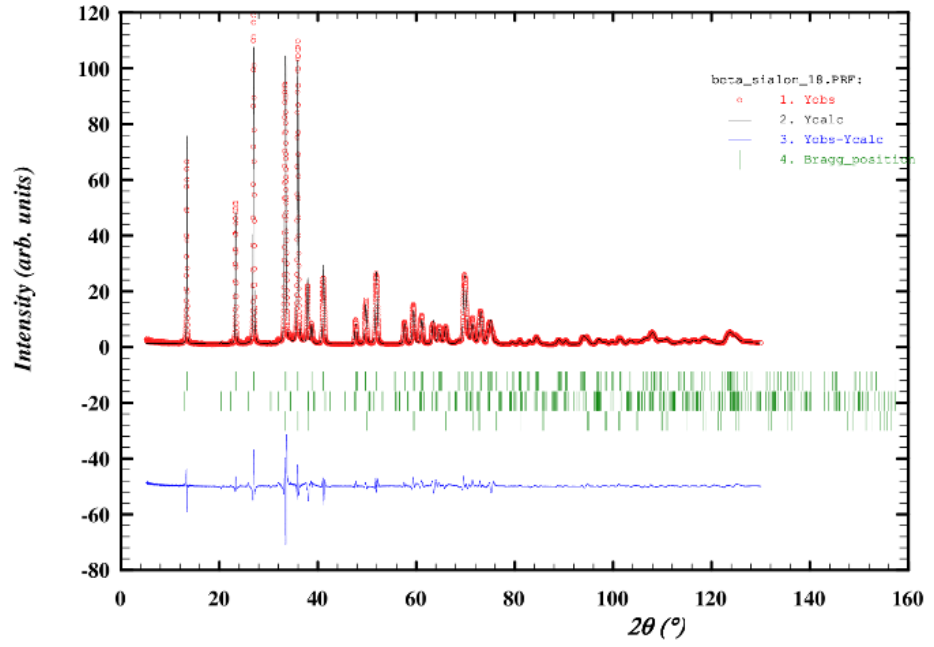

(b)

Figure III.13. Rietveld refinement of XRD patterns of (a) **PAlSZ3_16**, (b) **PAlSZ3_18**. *Observed (crosses) and calculated (red line) XRD patterns. Green vertical lines indicate positions of Bragg reflections. Blue line represents difference plot (observed/calculated) on the same scale.*

Both samples exhibited crystalline behaviour, featuring the highest content of the β-SiAlON phase. The Rietveld refinement were performed using three phases (β-SiAlON, α-Si_3N_4, w-AlN). The primary refined parameters included scale factors, background, sample positioning error, cell parameters (excluding α-Si_3N_4 in the **PAlSZ3_18** sample, where cell parameters were fixed due to too low phase content). The line profile shape and breadth and atomic positions we refined only for the highest content phase 'β-SiAlON.'

The Rietveld fit of the two XRD patterns are depicted in Figure III.13, where the black crosses and red line represent the observed and calculated patterns, respectively. The overall quality of the fit is good but it falls short of perfection, particularly for **PAlSZ3_18**, where some discrepancies in intensity and profile width are visible. This results in relatively poor figures of merit (R_p=9.96%, R_{wp}=12.2%, R_{exp}=1.64% and GofF= 7.4) for **PAlSZ3_16** and (R_p=15.2%, R_{wp}=18.5%, R_{exp}=1.77% and GofF=10.4) for **PAlSZ3_18**. It is expected that these discrepancies have little effect on the key refined parameters, which are documented in Table III.4. The values in parentheses represent the estimated errors on the last digit (corresponding to twice the estimated standard deviation calculated by Rietveld refinement). Parameters marked with an asterisk (*) were fixed during refinement due to the too low phase percentage. Additionally, the symbol "-" denotes parameters could not be refined.

Table III.4. Phase compositions and cell parameters of the **PAlSZ3_16** and **PAlSZ3_18** sample.

Samples	**PAlSZ3_16**			**PAlSZ3__18**		
Phase parameters	**β-SiAlON**	**α-Si_3N_4**	**w-AlN**	**β-SiAlON**	**α-Si_3N_4**	**w-AlN**
Cristallite size (nm)	119.50 (8)	-	-	-	-	-
Micro-strain (%)	0.211 (4)	-	-	0.093 (4)	-	-
a, b (Å)	7.646 (1)	7.788 (1)	3.111 (2)	7.628 (4)	7.788*	3.109 (2)
c (Å)	2.941 (4)	5.676 (6)	4.989 (4)	2.930 (2)	5.676*	4.992 (2)
Cell Volume(Å^3)	148.913 (4)	298.18 (1)	41.830 (6)	147.677 (8)	298.18 (1)	41.797 (4)
Phase frac. (%)	92.4 (8)	1.8 (1)	5.8 (2)	77.6 (1)	0.70 (6)	21.7 (8)

*() are the estimated errors on the last digit, * fixed parameters and - Not refined.*

The Rietveld refinement presented in Table III.4 shows that the refined cell parameters are a = b = 7.646 Å, and c = 2.941 Å for β-SiAlON. According to the relation between the cell parameters and the compositions given in chapter in Chapter I (a(Å) = 7.603 + 0.0296 z, c(Å) = 2.907 + 0.0255 z) it is possible to obtain the z value. The obtained z value is 1.4, which lies

with the range of z accepted for β-SiAlON ($0 \leq z \leq 4.2$) confirms Si:Al ratio fixed in the early stage of the process (3) and highlight the low oxygen content in our materials which will be confirmed later by elemental analyses. For α-Si_3N_4 in **PAlSZ3_16**, the refined cell parameters are a = b = 7.788 Å, c = 5.676 Å which aligns with the range of cell parameters mentioned in Chapter I for α-Si_3N_4.

It should also be noticed that α-SiAlON requires a metal cation and high enough oxygen content to form which is not the case here. All this suggest that we indeed have α-Si_3N_4. Finally, the Rietveld refinement of **PAlSZ3_16** samples also confirms the presence of w-AlN with the refined cell parameters very close to the reference values (a, b = 3.111 Å, c = 4.989 Å). With an increase in temperature, there is a decrease in cell parameters (refined cell parameters are a = b = 7.628 Å, and c = 2.930 Å) and volume for the **PAlSZ3_18** sample, as indicated in Table III.4.

The obtained z value is 0.9 which still lies with the range of z accepted for β-SiAlON ($0 \leq z \leq 4.2$) and this confirms the presence of β-SiAlON. Simultaneously, the w-AlN phase content increases from 5.8 % (**PAlSZ3_16**) to 21.7 % (**PAlSZ3_18**), likely due to thermal decomposition at high temperature and low N_2 pressure. The β-SiAlON phase content decreases from 92.4 % (**PAlSZ3_16**) to 77.6 % (**PAlSZ3_18**), while the α-Si_3N_4 phase decreases from 1.8 % (**PAlSZ3_16**) to 0.7 % (**PAlSZ3_18**). Thus, decompositions reactions seem to occur upon heat-treatment of **PAlSZ3_16** sample above 1600 °C. This is highlighted in the high-temperature (HT) TG curve of the **PAlSZ3_10** sample (Figure III.14) which 'simulates' the heat-treatment of ammonia-treated samples (obtained at 1000 °C) up to 1800 °C (however, the dwelling time is limited to 10 min. instead of 2 hours in the furnaces) in flowing nitrogen.

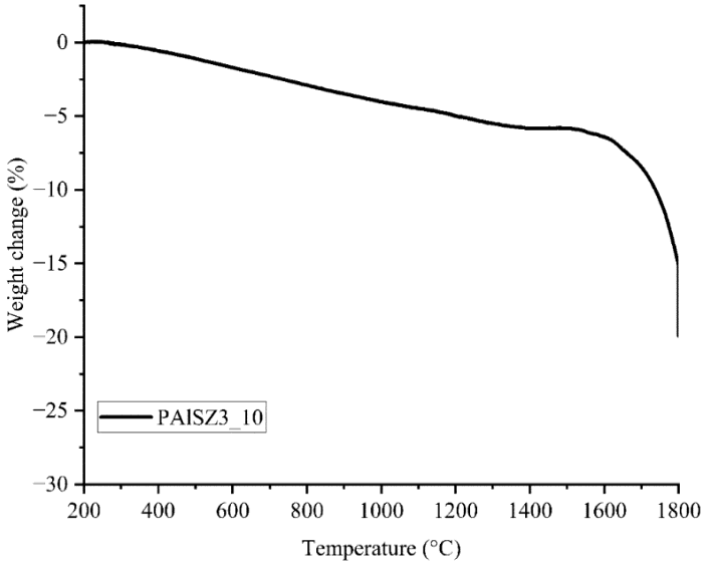

Figure III.14. High-temperature TG analysis of the **PAlSZ3_10** sample.

As depicted in Figure III.14, the low weight loss (3 %) below 1000 °C caused by desorption of molecules is followed by a two-step weight loss between 1000 and 1800 °C: a first weight loss (around 6 %) from 1000 to around 1400 °C in which residual carbon and hydrogen-containing units are released (see Table III.3 for the elemental compositions of the **PAlSZ3_10** sample) and a second one more significant from 1550 °C to 1800 °C (about 11 %). By combining results gained from Rietveld refinement an HT-TG analyses, we suggest that 'SiAlON' is decomposed in our system by releasing SiO resulting in AlN formation. Besides, Si_3N_4 is decomposed into silicon (liquid) releasing nitrogen (N_2). Therefore, we have considered the **PAlSZ3_16** samples for further experiments. Besides, we were also able to refine few microstructural parameters like crystal size and micro-strains. The **PAlSZ3_16** sample exhibits a quite large apparent crystallite size of about 120 nm with a relatively low amount of micro-strains of about (0.211 %). For **PAlSZ3_18**, the crystallite size could not be determined because of too small line broadening, suggesting that crystallite size exceeds the limit measurable with diffractometer setup (a few hundred nanometers). The increase of size is consistent with the decrease of micro-strains to 0.09%. To conclude, **PAlSZ3_16** displays the highest β-SiAlON phase content with the lowest phase percentage of secondary phases.

The assessment of the phase micro-/nanostructure of the **PAlSZ3_16** sample by transmission electron microscopy (TEM, Figure III.15) showcases a fully crystallized compound. It is composed of β-SiAlON crystals (Figure III.15(a-c)) as confirmed in the corresponding Selected Area Electron Diffraction (SAED, Figure III.15 (d)) patterns: it is composed of well-defined and distinct spots (3.8 Å) that can be ascribed to the (110), (011), (220) planes of the hexagonal structure of β-SiAlON[30]. The marked interplanar d spacing 1.92 Å corresponds to that of the 220-lattice plane of β-SiAlON.

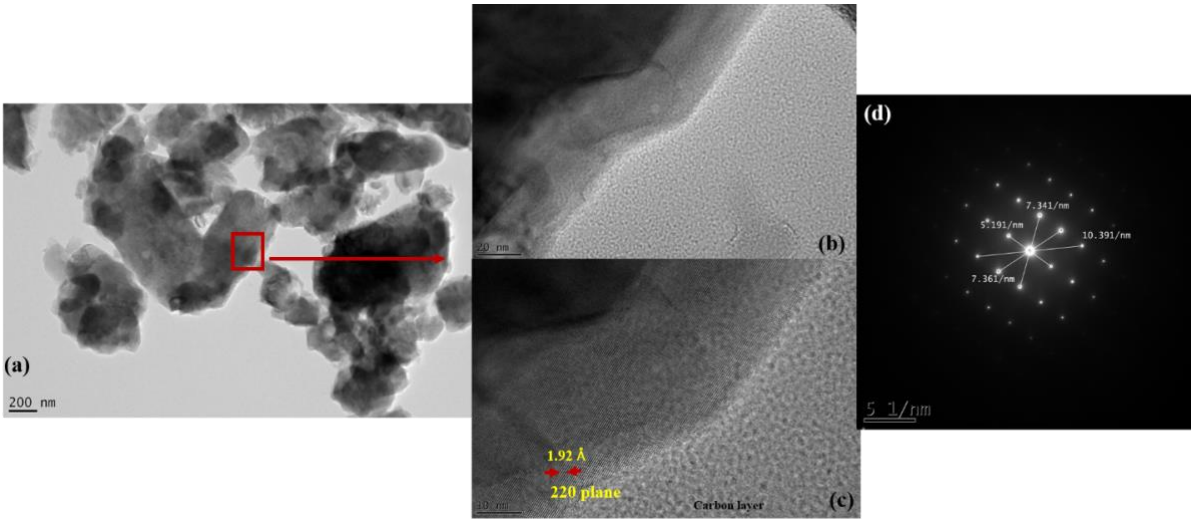

Figure III.15 HRTEM investigation of **PAlSZ3_16**.

As reported in Figure III.16(a), the **PAlSZ3_16** sample displays in its ^{29}Si MAS NMR spectrum a sharp signal at −48 ppm matching well with the value in the literature for 4-fold coordinated Si atoms[31].

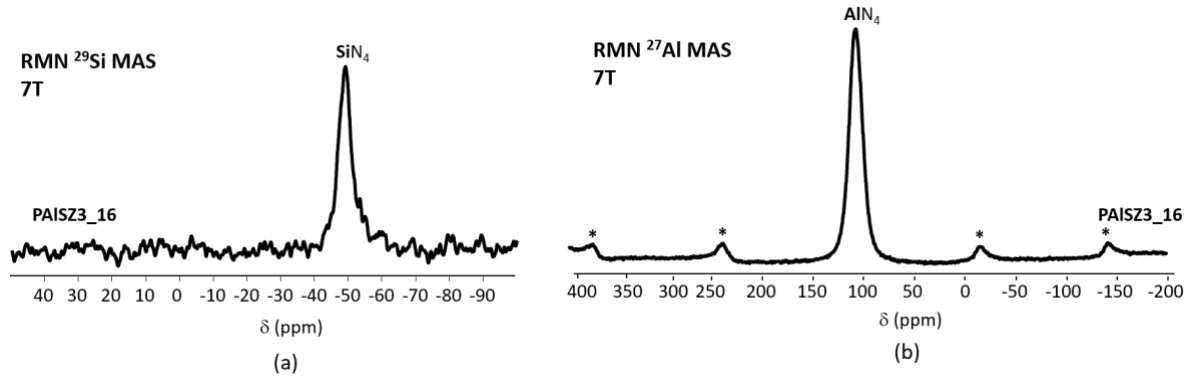

Figure III.16. Solid-state NMR spectra of the **PAlSZ3_16** sample: (a) ^{29}Si MAS NMR and (b) ^{27}Al MAS NMR recorded at 7 T. (* indicate spinning sidebands).

In the β-SiAlON host, Al atoms are surrounded by N with a portion of O because charge compensation requires that at least one of the nearest neighbors to Al is O. ^{27}Al MAS NMR of Figure III.16 (b) demonstrates a spectrum with one sharp peak at 115 ppm, a position close to the values found for **Al**N_4 and for **Al**ON_3 environments[25]. However, $AlON_3$ signals, less symmetrical than AlN_4 one, are expected to be broader. The presence of oxygen is confirmed by element analysis (see Table III.5). An oxygen content of 3.8 wt. % has been measured in the **PAlSZ3_16** sample.

Table III.5. Elemental analysis of the **PAlSZ3_16** sample.

Sample	Si	Al	O	N	C	H	Empirical Formula**
	in wt. %						
PAlSZ3_16	47.9	16.7	3.8	31.4	0.2	0.0	$Si_{1.0}Al_{0.4}O_{0.1}N_{1.3}$

**Silicon has been referred as $Si_{1.0}$.*

Elemental analysis investigations allow calculating a chemical formula of **$Si_{1.0}Al_{0.4}O_{0.1}N_{1.3}$** (referenced to $Si_{1.0}$). We omitted the presence of carbon in the formula because of its low content (0.2 wt. %). We can observe that the Si:Al ratio fixed in the precursor is more or less retained; thus, we can emphasize the interest of the PDC approach to finely control the chemical composition of ceramics. If we consider Si and Al contents, this empirical formula allows calculating a z value of 1.7 by considering the typical composition expected for β-SiAlON: β-$Si_{6-z}Al_zO_zN_{8-z}$ ($0 < z < 4.2$); a value close to that one calculated by Rietveld refinement for the same sample (1.4). By considering z = 1.7, a chemical formula of **$Si_{1.0}Al_{0.4}O_{0.4}N_{1.3}$** is expected if referenced to $Si_{1.0}$: whereas N content fits well with the theory, we confirm that the O content in our system is below the value expected for β-SiAlON. Therefore, we can conclude that we

form low oxygen β-SiAlON materials upon pyrolysis of the **PAlSZ3** sample at 1000 °C in flowing ammonia followed by the heat-treatment of ammonia-treated samples at 1600 °C in flowing nitrogen. This will be the sample which will be used as host materials for europium and cerium in chapters IV and V, respectively.

III.3. Conclusion

This chapter described the design of low oxygen β-SiAlON ceramics using aluminum-modified polysilazanes as precursors and ammonia and nitrogen as atmospheres during pyrolysis and annealing treatments. Initially, the chapter outlines the polymer synthesis that consisted to prepare a series of precursors with different Si:Al (X; $2.5 \leq X \leq 30$) ratios from the commercially available Durazane® 1800. This range of ratios has been selected to form β-SiAlON with a relatively low z in their typical formula $\beta\text{-}Si_{6-z}Al_zO_zN_{8-z}$ in which $0 < z < 4.2$; thereby limiting the oxygen content in the final material. Durazane® 1800 is a liquid precursor and its modification by alane induced a gradual polymer branching with the decrease of the Si:Al ratio leading ultimately to solid state compounds. Complementary characterization revealed that the synthesis occurs through major dehydrocoupling reactions forming Al-N bonds up to a certain Si:Al ratio at which polymer branching is hindered (between 3 and 5) and even stopped (3) involving the presence of Al-H bonds in the system. Polymers also bear tertiary amine as side groups.

The subsequent pyrolysis under ammonia at 1000 °C followed by a time-controlled exposure in air involves the formation of amorphous ceramics. During this stage, it has been shown that the low temperature regime of the conversion is mainly associated with transamination reactions and the temperature range 300 – 700 °C involves nucleophilic and coupling reactions leading to the formation of $N(Si)_{3-x}(Al)_x$ units in the system at 1000 °C. The time-controlled RT oxidation after the pyrolysis at 1000 °C in flowing ammonia proceeded by selective oxidation of Al; thus, forming in part oxygen-containing Al environments besides SiN_4 environments. Further heat-treatments of ammonia-treated samples at high temperature resulted in the complete crystallization (at 1600 °C) of the compounds into a major phase namely β-SiAlON along with secondary phases including $\alpha\text{-}Si_3N_4$ and/or w-AlN phases. Then decomposition reactions occurs. The β-SiAlON phase content increases with the decrease of the Si:Al ratio: the **PAlSZ3_16** sample showed the highest β-SiAlON phase content (more than 92 %) among all the samples. It represents a low oxygen β-SiAlON material which has been

selected for the further doping with Eu^{2+} and Eu^{3+} in Chapter IV and with Ce^{3+} cations in Chapter V.

Bibliography

(1) Fonblanc, D.; Lopez-Ferber, D.; Wynn, M.; Lale, A.; Soleilhavoup, A.; Leriche, A.; Iwamoto, Y.; Rossignol, F.; Gervais, C.; Bernard, S. Crosslinking Chemistry of Poly (Vinylmethyl-Co-Methyl) Silazanes toward Low-Temperature Formable Preceramic Polymers as Precursors of Functional Aluminium-Modified Si–C–N Ceramics. *Dalton Trans.* **2018**, *47* (41), 14580–14593.

(2) Shariatmadar Tehrani, F.; Goh, B. T.; Muhamad, M. R.; Rahman, S. A. Pressure Dependent Structural and Optical Properties of Silicon Carbide Thin Films Deposited by Hot Wire Chemical Vapor Deposition from Pure Silane and Methane Gases. *J. Mater. Sci. Mater. Electron.* **2013**, *24* (4), 1361–1368.

(3) Termoss, H.; Bechelany, M.; Toury, B.; Brioude, A.; Bernard, S.; Cornu, D.; Miele, P. Shaping Potentialities of Aluminum Nitride Polymeric Precursors: Preparation of Thin Coatings and 1D Nanostructures in Liquid Phase. *J. Eur. Ceram. Soc.* **2009**, *29* (5), 857–861.

(4) Gerges, T.; Salles, V.; Bernard, S.; Journet, C.; Jaurand, X.; Chiriac, R.; Ferro, G.; Brioude, A. AlN Hollow-Nanofilaments by Electrospinning. *Nanotechnology* **2015**, *26* (8), 085603.

(5) Frigo, D. M.; Van Eijden, G. J. M.; Reuvers, P. J.; Smit, C. J. Preparation and Properties of Alane Dimethylethylamine, a Liquid Precursor for MOCVD. *Chem. Mater.* **1994**, *6* (2), 190–195.

(6) Polenova, T.; Gupta, R.; Goldbourt, A. Magic Angle Spinning NMR Spectroscopy: A Versatile Technique for Structural and Dynamic Analysis of Solid-Phase Systems. *Anal. Chem.* **2015**, *87* (11), 5458–5469.

(7) Rovnyak, D. Tutorial on Analytic Theory for Cross-polarization in Solid State NMR. *Concepts Magn. Reson. Part A* **2008**, *32A* (4), 254–276.

(8) Schmidt, M.; Durif, C.; Acosta, E. D.; Salameh, C.; Plaisantin, H.; Miele, P.; Backov, R.; Machado, R.; Gervais, C.; Alauzun, J. G.; Chollon, G.; Bernard, S. Molecular-Level Processing of Si-(B)-C Materials with Tailored Nano/Microstructures. *Chem. – Eur. J.* **2017**, *23* (67), 17103–17117.

(9) Bechelany, M. C.; Proust, V.; Lale, A.; Miele, P.; Malo, S.; Gervais, C.; Bernard, S. Nanocomposites through the Chemistry of Single-Source Precursors: Understanding the Role of Chemistry behind the Design of Monolith-Type Nanostructured Titanium Nitride/Silicon Nitride. *Chem. – Eur. J.* **2017**, *23* (4), 832–845.

(10) Smith, M. E.; van Eck, E. R. Recent Advances in Experimental Solid State NMR Methodology for Half-Integer Spin Quadrupolar Nuclei. *Prog. Nucl. Magn. Reson. Spectrosc.* **1999**, *34* (2), 159–201.

(11) Haouas, M.; Taulelle, F.; Martineau, C. Recent Advances in Application of ^{27}Al NMR Spectroscopy to Materials Science. *Prog. Nucl. Magn. Reson. Spectrosc.* **2016**, *94*, 11–36.

(12) Toyoda, R.; Kitaoka, S.; Sugahara, Y. Modification of Perhydropolysilazane with Aluminum Hydride: Preparation of Poly (Aluminasilazane) s and Their Conversion into Si–Al–N–C Ceramics. *J. Eur. Ceram. Soc.* **2008**, *28* (1), 271–277.

(13) Jung, W.-S.; Chae, S.-A. ^{27}Al MAS NMR Spectroscopic Identification of Reaction Intermediates in the Carbothermal Reduction and Nitridation of Alumina. *Mater. Chem. Phys.* **2010**, *123* (2–3), 610–613.

(14) Balestrat, M.; Lale, A.; Bezerra, A. V. A.; Proust, V.; Awin, E. W.; Machado, R. A. F.; Carles, P.; Kumar, R.; Gervais, C.; Bernard, S. In-Situ Synthesis and Characterization of Nanocomposites in the Si-Ti-N and Si-Ti-C Systems. *Molecules* **2020**, *25* (22), 5236.

(15) Gervais, C.; Babonneau, F.; Ruwisch, L.; Hauser, R.; Riedel, R. Solid-State NMR Investigations of the Polymer Route to SiBCN Ceramics. *Can. J. Chem.* **2003**, *81* (11), 1359–1369.

(16) Berger, F.; Weinmann, M.; Aldinger, F.; Müller, K. Solid-State NMR Studies of the Preparation of Si−Al−C−N Ceramics from Aluminum-Modified Polysilazanes and Polysilylcarbodiimides. *Chem. Mater.* **2004**, *16* (5), 919–929.

(17) Schulz, S.; Bauer, T.; Hoffbauer, W.; auf der Günne, J. S.; Doerr, M.; Marian, C. M.; Assenmacher, W. Stepwise Conversion of a Single Source Precursor into Crystalline AlN by Transamination Reaction. *J. Solid State Chem.* **2008**, *181* (3), 530–538.

(18) Gupta, R. K.; Mishra, R.; Kumar, S.; Ranjan, A.; Manocha, L. M.; Prasad, N. E. Development of Polycarbosilane (PCS) Polymer and PCS-Derived SiC Fibers and Their Composites. In *Handbook of Advanced Ceramics and Composites*; Mahajan, Y. R., Johnson, R., Eds.; Springer International Publishing: Cham, 2020; pp 913–928.

(19) Bräuniger, T.; Kempgens, P.; Harris, R. K.; Howes, A. P.; Liddell, K.; Thompson, D. P. A Combined 14N/27Al Nuclear Magnetic Resonance and Powder X-Ray Diffraction Study of Impurity Phases in β-Sialon Ceramics. *Solid State Nucl. Magn. Reson.* **2003**, *23* (1–2), 62–76.

(20) Kempgens, P.; Harris, R. K.; Yu, Z.; Thompson, D. P. Structural Characterization of Li α-Sialon Ceramics by High-Resolution ^{27}Al and ^{29}Si NMR Spectroscopy. *J. Mater. Chem.* **2001**, *11* (10), 2507–2512.

(21) Butler, N. D.; Dupree, R.; Lewis, M. H. The Use of Magic-Angle-Spinning NMR in Structural Studies of Si-Al-O-N Phases. *J. Mater. Sci. Lett.* **1984**, *3* (5), 469–470.

(22) Marchetti, P. S.; Kwon, D.; Schmidt, W. R.; Interrante, L. V.; Maciel, G. E. High-Field Boron-11 Magic-Angle Spinning NMR Characterization of Boron Nitrides. *Chem. Mater.* **1991**, *3* (3), 482–486.

(23) Widgeon, S. J.; Sen, S.; Mera, G.; Ionescu, E.; Riedel, R.; Navrotsky, A. ^{29}Si and ^{13}C Solid-State NMR Spectroscopic Study of Nanometer-Scale Structure and Mass Fractal Characteristics of Amorphous Polymer Derived Silicon Oxycarbide Ceramics. *Chem. Mater.* **2010**, *22* (23), 6221–6228.

(24) Mackenzie, K. J. D.; Meinhold, R. H.; White, G. V.; Sheppard, C. M.; Sherriff, B. L. Carbothermal Formation of B′-Sialon from Kaolinite and Halloysite Studied by ^{29}Si and ^{27}Al Solid State MAS NMR. *J. Mater. Sci.* **1994**, *29*, 2611–2619.

(25) Cozzan, C.; Griffith, K. J.; Laurita, G.; Hu, J. G.; Grey, C. P.; Seshadri, R. Structural Evolution and Atom Clustering in β-SiAlON: β-$Si_{6-z}Al_zO_zN_{8-z}$. *Inorg. Chem.* **2017**, *56* (4), 2153–2158.

(26) Ekström, T.; Käll, P. O.; Nygren, M.; Olsson, P. O. Dense Single-Phase β-Sialon Ceramics by Glass-Encapsulated Hot Isostatic Pressing. *J. Mater. Sci.* **1989**, *24* (5), 1853–1861.

(27) Seymour, V. R.; Smith, M. E. Distinguishing between Structural Models of B′-Sialons Using a Combined Solid-State NMR, Powder XRD, and Computational Approach. *J. Phys. Chem. A* **2019**, *123* (45), 9729–9736.

(28) Marchand, R.; Laurent, Y.; Lang, J.; Le Bihan, M. T. Structure Du Nitrure de Silicium α. *Acta Crystallogr. B* **1969**, *25* (10), 2157–2160.

(29) Morris, M. C. *Standard X-Ray Diffraction Powder Patterns: Data for 58 Substances*; US Department of Commerce, National Bureau of Standards, 1981; Vol. 25.

(30) Gan, L.; Xu, F.-F.; Zeng, X.-H.; Li, Z.-S.; Mao, Z.-Y.; Lu, P.; Zhu, Y.-C.; Liu, X.-J.; Zhang, L.-L. Multiple Doping Structures of the Rare-Earth Atoms in β-SiAlON: Ce Phosphors and Their Effects on Luminescence Properties. *Nanoscale* **2015**, *7* (26), 11393–11400.

(31) Gervais, C. Solid-State NMR Applied to Si-Based Polymer Derived Ceramics: A Review. *Open Ceram.* **2023**, 100376.

Chapter IV.

Low oxygen content β-SiAlON as host materials for green-emitting Eu^{2+}-based phosphors

IV.1. Introduction

Among all the rare earth ions, Eu ion is one of the most widely selected and used activators, its adjustable valence of Eu^{2+} and Eu^{3+} ions can function as an emission center in the host material. In general, the emission of Eu ion is sensitive to the crystal field, and the drastic spectral changes are closely related to the oxidation state of Eu.

The divalent europium ion (Eu^{2+}) exhibits broad emission bands with tunable color ranging from the ultraviolet to red spectral region originated from the parity-allowed inter-configurational $4f^6 5d^1$-$4f^7$ transition[1]. Besides, the influence of the 5d orbit of Eu^{2+} is strongly dependent on the environment of the crystal; thereby, the emission of Eu^{2+} is strongly affected by the crystal field and covalence of the matrix lattice. In the particular case of β-SiAlON selected as host ceramics[2–4], β-SiAlON:Eu^{2+} is accepted as the most promising green phosphor for wide color gamut WLED backlights. It exhibits exceptional luminescence efficiency when exposed to ultraviolet, violet, and blue light, making it an ideal choice for pc-WLED[5,6]. However, mixed Eu valences (Eu^{2+} and Eu^{3+}) are inevitably present in the lattice of most luminescent material, so that the concentration of Eu^{2+} contributing to the luminescence is further reduced, which is especially serious for the application. This is particularly understandable by considering the size effect[7,8]: it is reasonable to speculate the coexistence of Eu^{2+} and Eu^{3+} in the channel of β-SiAlON because the smaller Eu^{3+} can be more easily incorporated into the interstitial site.

The coexistence of Eu^{3+} with the Eu^{2+} luminescence center limits the photoluminescence intensity of β-SiAlON:Eu^{2+} to a great extent[9–13] and it is considered that Eu^{3+} plays the role of "killer sites" in β-SiAlON:Eu^{2+} as already discussed in Chapter I[14–16]. The term "killer sites" often refers to specific defect sites or lattice positions within the crystal structure where certain dopant ions or atoms can be present which can lower the emission intensity[17]. Therefore, in order to improve the quantum efficiency of β-SiAlON:Eu^{2+}, it is importance to reduce the number of luminescence killers (Eu^{3+}) and enhance the reduction of Eu^{3+} into Eu^{2+}[11]. However, to understand this effect of Eu^{3+}, it is important to follow its behaviour in the host material. In addition in this task, there is still a bottleneck to significantly improve the luminescence efficiency of β-SiAlON:Eu^{2+} because only quite a small amount of Eu^{2+} ions can be accommodated into the host lattice. The low dopant concentration thus leads to a smaller number of photons involved in the luminescence process. As an illustration, Hirosaki et al. first reported β-SiAlON:Eu^{2+} phosphor with the Eu^{2+} doping concentration of only 0.296 mol%, and

the internal and external quantum efficiencies under the 450 nm excitation were limited to be 50 % and 33 %, respectively[18]. Precursor routes could allow increasing this concentration.

This contribution involves the use of low oxygen content β-SiAlON compounds prepared in Chapter III as host materials for Eu^{2+} and Eu^{3+} cations through the controlled introduction of $EuCl_2$, and $EuCl_3$ in **PAlSZ3**. We have varied the content of divalent and trivalent europium in **PAlSZ3** (*i.e.*, the $Eu^{2+ \text{ or } 3+}$:Si (Y) ratio with $0.005 \leq Y \leq 0.05$) to form β-SiAlON with controlled concentrations (which can be high) of Eu after pyrolysis in flowing ammonia at 1000 °C followed by high temperature heat-treatment based on the conventional procedure detailed in Chapter III. As a proof of concept, we explored Gas Pressure Sintering (GPS) of ammonia-treated samples at high temperature to follow the effect of a nitrogen pressure on the phase composition, the microstructure and, consequently, the optical properties of samples.

As detailed in earlier chapters, the precursors underwent comprehensive characterization, including FTIR and solid-state NMR spectroscopies, as well as elemental analysis. The transformation of precursors into ceramics was monitored using solid-state NMR spectroscopy of pyrolysis intermediates. Final materials underwent thorough analysis using X-ray diffraction assisted by Rietveld refinement, NMR spectroscopy, elemental analyses, and high-resolution transmission electron microscopy (TEM) for microstructural insights.

It is important to note that all the results regarding Eu^{3+}-doped samples are not presented and discussed as those of Eu^{2+}-doped samples because of a lot of similitude between samples in terms of chemistry and microstructure. Thus, when a significant difference in these results occurred; the results of β-SiAlON:Eu^{3+} have been reported and discussed.

An extensive evaluation of the optical properties of the ceramics was conducted. This involved photoluminescence (PL)/photoluminescence excitation (PLE), cathodoluminescence (CL), optical absorption, and the determination of photoluminescent material lifetimes. These analyses provided valuable insights into the luminescent behaviors exhibited by the investigated compounds.

IV.2. Result and Discussion

IV.2.1. Synthesis and characterization of β-SiAlON:$Eu^{2+/3+}$ precursors

The introduction of europium chloride in **PAlSZ3** (Chapter III) was carried out by varying the europium content via the Eu:Si ratio (Y) from 0.005 to 0.05 leading to a series of four samples for each cation labeled PAlEuCl$_x$YSZ3 (x = 2, 3; 0.005 ≤ Y ≤ 0.05). Thus, EuCl$_X$ (x = 2, 3) and PSZ are mixed together according to the targeted Eu:Si ratio and then, the mixture is put in toluene. Subsequently, the alane is added to the mixture while maintaining a fixed (3) during precursor synthesis as done in Chapter III. After chemical reaction and solvent extraction, the resulting samples are delivered as solid compounds (mostly white) at room temperature.

Elemental analysis, particularly with the representative **PAlEuCl$_2$0.005SZ3** sample, confirms that the measured Si:Al ratio aligns with that one fixed before doing the reaction between PSZ and alane (3), as specified in Table IV.1. Additionally, the results in Table IV.1 indicate that the oxygen content in all samples is minimal and comparable to the pristine polymer (**PAlSZ3**, $Si_{1.0}Al_{0.3}N_{0.9}C_{2.0}H_{4.0}$) while N and C contents are quite close (*H content of **PAlEuCl$_2$0.05SZ3** sample is very high for an unknown reason*). Thus, the addition of alane occurs as in PSZ to form **PAlSZ3** indicating that the prior addition of EuCl$_2$ does not affect the further reaction between PSZ and alane. Regarding the measured Eu:Si ratio, it fits with the one fixed upon precursor preparation but chlorine is present. Because the measured Eu:Cl ratio is found to be 0.5 as in EuCl$_2$, we tentatively conclude that chloride ions – known as weak nucleophiles - do not react with reactive groups bearing by PSZ.

Table IV.1. Elemental composition of **PAlEuCl$_2$0.005SZ3**.

Samples	Si	Al	O	N	C	H	Eu	Cl	Empirical formula*
	in wt.%								
PAlSZ3	35.5	11.4	1.0	16.6	30.4	5.1	-	-	$Si_{1.0}Al_{0.3}N_{0.9}C_{2.0}H_{4.0}$
PAlEuCl$_2$0.005SZ3	32.8	10.6	1.3	16.6	32.7	4.7	0.9	0.4	$Si_{1.0}Al_{0.4}N_{1.1}C_{2.7}H_{4.0}Eu_{0.005}Cl_{0.01}$
PAlEuCl$_2$0.05SZ3	28.1	9.0	1.0	15.9	27.3	8.1	7.5	3.1	$Si_{1.0}Al_{0.3}N_{1.1}C_{2.3}H_{8.0}Eu_{0.05}Cl_{0.09}$

** reference to $Si_{1.0}$ and oxygen content omitted because of a content < 2wt. %.*

The poor changes in the elemental analysis results are reflected in the FTIR (Figure IV.1) and solid-state NMR (Figure IV.2) spectroscopy results. Investigations have been only focused on Eu^{2+}-doped samples because of similar results for Eu^{3+}-doped samples. FTIR investigation has

been done for all polymers whereas we particularly selected the **PAlEuCl$_2$0.005SZ3** and **PAlEuCl$_2$0.05SZ3** samples for solid-state NMR investigations.

As shown in Figure IV.1, there is no effect of the Eu:Si ratio on the band positions and intensity in the FTIR spectra of PAlEuCl$_2$YSZ3 ($0.005 \leq Y \leq 0.05$). In addition, no bands appear nor disappear in their corresponding spectra compared to the spectrum of **PAlSZ3**. Therefore, FTIR experiments indicate that dehydrocoupling reactions between Al-H and N-H bonds are not hindered by the presence of $EuCl_2$ (nor $EuCl_3$) and confirm that they represent the main reactions governing the synthesis of these precursors as it occurred during the synthesis of **PAlSZ3**.

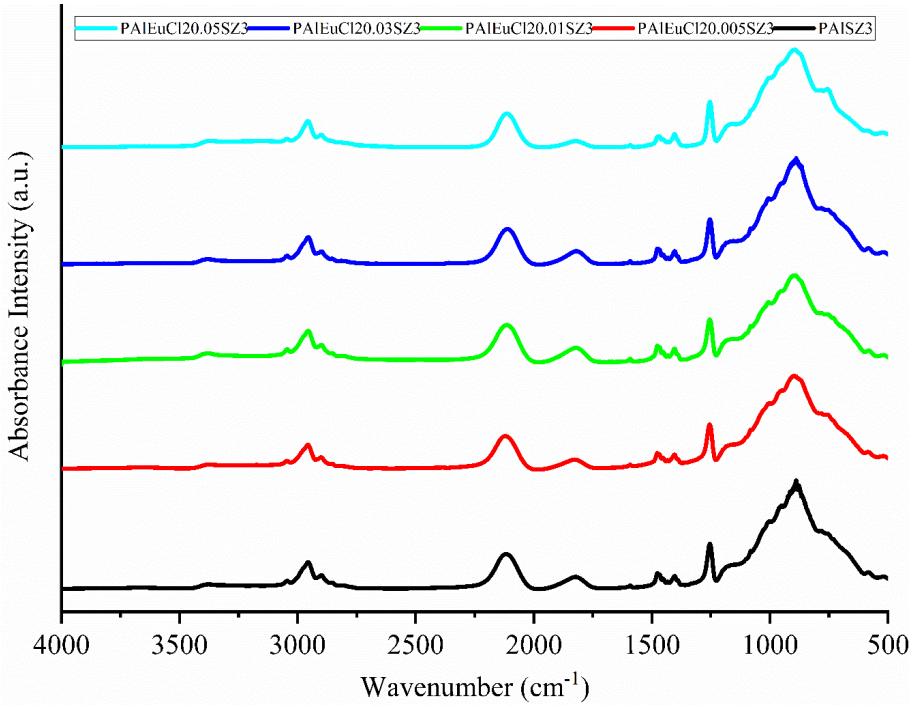

Figure IV.1. FTIR spectra of the **PAlEuCl$_2$YSZ3** samples ($0.005 \leq Y \leq 0.05$).

The solid-state NMR spectra of the **PAlEuCl$_2$0.005SZ3** and **PAlEuCl$_2$0.05SZ3** samples are depicted in Figure IV.2. As for FTIR spectroscopy, solid-state NMR does not reveal any difference in the chemical environments of carbon (a), aluminum (b), silicon (c) and nitrogen (d) elements when comparing them with the spectra of the **PAlSZ3** sample. Therefore, despite the fact that we changed the Eu:Si ratio at molecular scale, elemental analysis and FTIR and solid-state NMR spectroscopies of precursors have evidenced that the addition of different amounts of $EuCl_2$ in PSZ does not affect the further incorporation of Al.

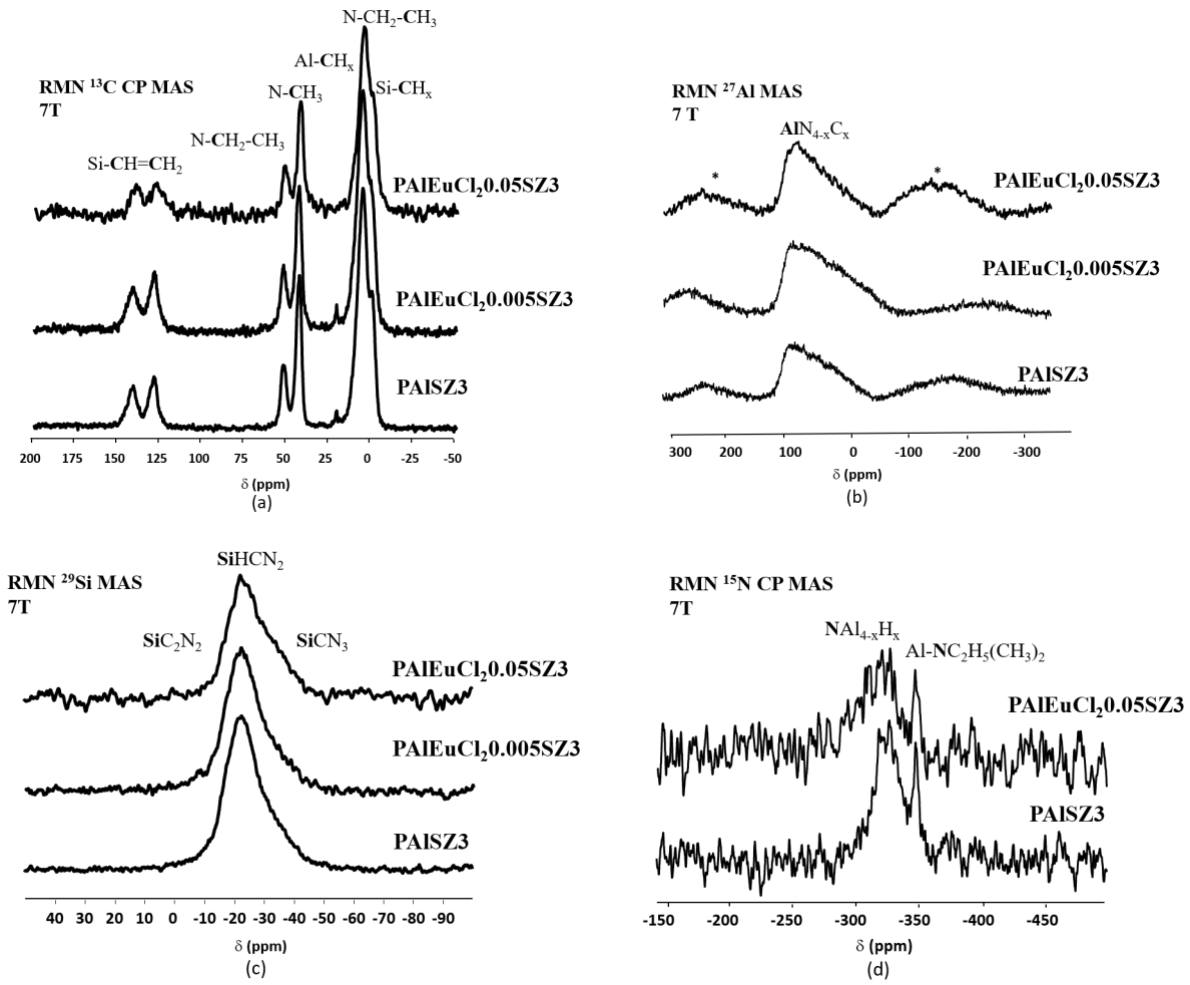

Figure IV.2. Solid-state NMR spectra of **PAlSZ3**, **PAlEuCl$_2$0.005SZ3** and **PAlEuCl$_2$0.05SZ3**: (a) ^{13}C CP MAS, (b) ^{27}Al MAS (* indicate spinning sidebands), (c) ^{29}Si MAS, (d) ^{15}N CP MAS.

Based on elemental analysis and solid-state NMR spectroscopy, we would have suggested that the introduction of $EuCl_2$ (and $EuCl_3$) in the PSZ network occurs via coordination reactions; that is N atoms from the silylamino ligands used their electron pair to form covalent bonds with Eu^{2+} (and Eu^{3+}). Coordination reactions are well known in polysilazanes when using transition metals such as cobalt[19] and nickel[20]. However, coordination via silylamino groups is known to red-shift the N-H bond band in the FTIR spectroscopy. This is not observed here using $EuCl_2$ nor $EuCl_3$ although it is known that Eu^{3+}-containing complexes form air-stable complexes with most electronegative atoms such as oxygen and nitrogen, partially because Eu^{3+} is a hard Lewis acid[21]. In contrast, the number of Eu^{2+}-containing complexes is small according to the fact that Eu^{2+} is a softer Lewis acid than Eu^{3+} because of its lower charge density. **Consequently, it is most probable that we have $EuCl_2$ (and $EuCl_3$) distributed in the PAlSZ3 network without any interaction**.

IV.2.2. Preceramic precursor to Ceramics (β-SiAlON:Eu^{2+}) conversion by thermal treatment

This section is shared into three parts: the first one describes the thermo-chemical transformation of precursors upon heat-treatment to 1000°C in flowing ammonia following by an exposition in air for 1 minute before being stored in a glovebox. Then, ammonia-treated samples underwent two types of high temperature treatments: a conventional one up to 1800 °C in flowing nitrogen as applied in Chapter III and a treatment through Gas Pressure Sintering (GPS) up to 1800 °C in flowing nitrogen.

IV.2.2.1. Heat-treatment of precursors up to 1000 °C in flowing ammonia

Ammonia-treated samples including **PAlEuCl$_2$0.005SZ3_10** and **PAlEuCl$_2$0.05SZ3_10** have been investigated by elemental analyses, solid-state NMR spectroscopy and/or X-ray diffraction (XRD) and compared to their analogs without europium and already characterized in Chapter III: **PAlSZ3_10**. It has to be mentioned that solid-state NMR spectroscopy has been only investigated around silicon and aluminum and that we do not report the results regarding Eu^{3+}-doped samples which match those of Eu^{2+}-doped samples.

The ^{29}Si MAS NMR spectrum of the **PAlEuCl$_2$0.005SZ3_10** sample (Figure IV.3 (a)) does not allow identifying any effect of the addition of a very low content of $EuCl_2$ in the early stage of the process on the chemical environment of silicon in the derived ammonia-treated samples. Compared to the ^{29}Si MAS NMR spectrum of **PAlSZ3_10**, **Si**CN_3 and **Si**N_4 environments are still identified through the broad signal at -45 ppm although the presence of Eu^{2+} in the **PAlEuCl$_2$0.005SZ3_10** seems to prevent the appearance of the diffuse signal at -85 ppm attributed to $SiO_{4-x}N_x$ units. This is consistent with the small AlO_4 signal in the corresponding ^{27}Al NMR spectrum (*see discussion later*). The ^{29}Si MAS NMR spectra of the **PAlEuCl$_2$0.05SZ3_10** is extremely noisy with very diffuse signals even after long acquisitions. This can be possibly due to the formation of radicals around silicon that kills magnetization. The magnetic effect leads to signal dispersion, posing difficulties in observing clear peaks and obtaining detailed insights into the chemical environment[22,23]. That is why higer field spectra are better.

A broader signal characterizes the ^{27}Al MAS NMR spectra of **PAlEuCl$_2$0.005SZ3_10** and **PAlEuCl$_2$0.05SZ3_10** (Figure IV.3 (b)) compared to the signal identified in the spectrum of the **PAlSZ3_10** sample. This signal indicates the presence of **Al**$N_{4-x}O_x$ ($0 \leq x \leq 4$) including **Al**O_4 environments as in **PAlSZ3_10**. However, its broadness could also highlight a higher content of **Al**O_6 environment (signal around 10 ppm) in Eu-doped samples; a coordination of

Al which is found in alumina (Al_2O_3) and has been also identified in SiAlON phases as mentioned in Chapter III. Such environments are also found in *o*-$EuAlO_3$[24].

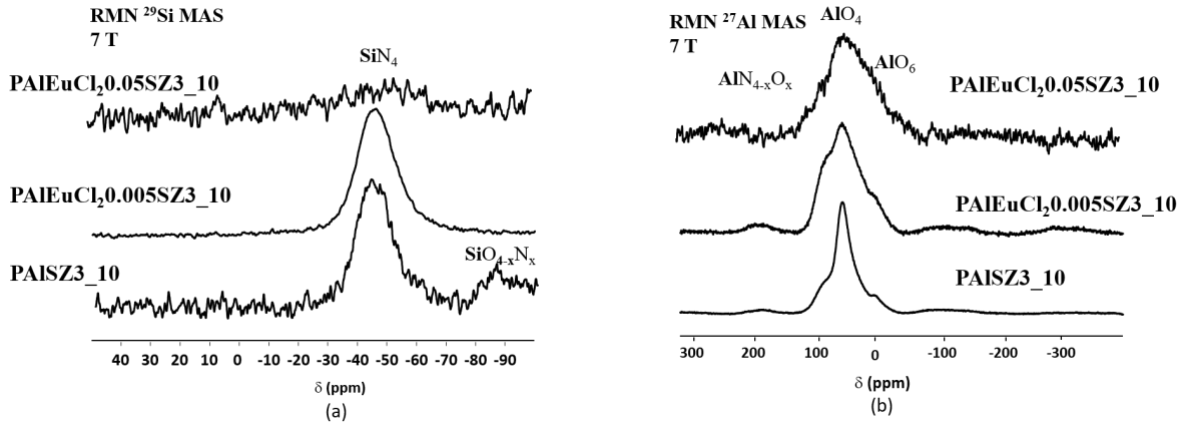

Figure IV.3. Solid-state NMR spectra of **PAlSZ3_10**, **PAlEuCl$_2$0.005SZ3_10** and **PAlEuCl$_2$0.05SZ3_10** samples: (a) ^{29}Si MAS NMR and (b) ^{27}Al MAS NMR.

Oxygen, nitrogen, hydrogen and carbon content analyses confirm that there is a slight increase of the oxygen content in **PAlEuCl$_2$0.005SZ3_10** and **PAlEuCl$_2$0.05SZ3_10** with respect to the **PAlSZ3_10** (Table IV.2).

Table IV.2. Elemental analysis of **PAlSZ3_10**, **PAlEuCl$_2$0.005SZ3_10** and **PAlEuCl$_2$0.05SZ3_10** samples.

Samples	O	N	H	C
	in (wt. %)			
PAlSZ3_10	4.5	29.8	0.1	1.4
PAlEuCl$_2$0.005SZ3_10	6.8	31.9	0.6	0.3
PAlEuCl$_2$0.05SZ3_10	6.2	26.6	0.2	0.8

This increase is consistent with the fact that Eu acts as an efficient oxygen gatherer, i.e. it is easily oxidized in the presence of oxygen or when embedded in an oxide[25]. Therefore, the increase of the oxygen content in **PAlEuCl$_2$0.005SZ3_10** and **PAlEuCl$_2$0.05SZ3_10** might be related to the formation of Eu-O bonds in the material. Table IV.2 shows that the content of other elements as H, C and N is quite similar between samples while all Eu-doped samples are amorphous as for the **PAlSZ3_10** sample studied in Chapter III. This is demonstrated by XRD in Figure IV.4 for Eu^{2+}-doped samples. Hence, the high-temperature treatment of these materials should lead to their crystallization as discussed in the following section.

As a conclusion of this part, we can suggest that the mechanisms involving Si and Al environments and governing the pyrolysis of Eu-doped **PAlSZ3** samples in ammonia atmosphere at 1000 °C do not differ compared to those controlling the conversion of **PAlSZ3**

into amorphous ceramics: **pyrolysis of the PAlEuCl$_x$YSZ3 (x = 2, 3; 0.005 ≤ Y ≤ 0.05) samples at 1000 °C in flowing ammonia leads to the formation of Si-N, Al-O and Al-N bonds in the amorphous ceramics**. However, **the presence of Eu in the amorphous network increases the oxygen content in the ammonia-treated samples most probably through the formation of Eu-O bonds**. The presence of environments such as those found in *o*-$EuAlO_3$ is suggested.

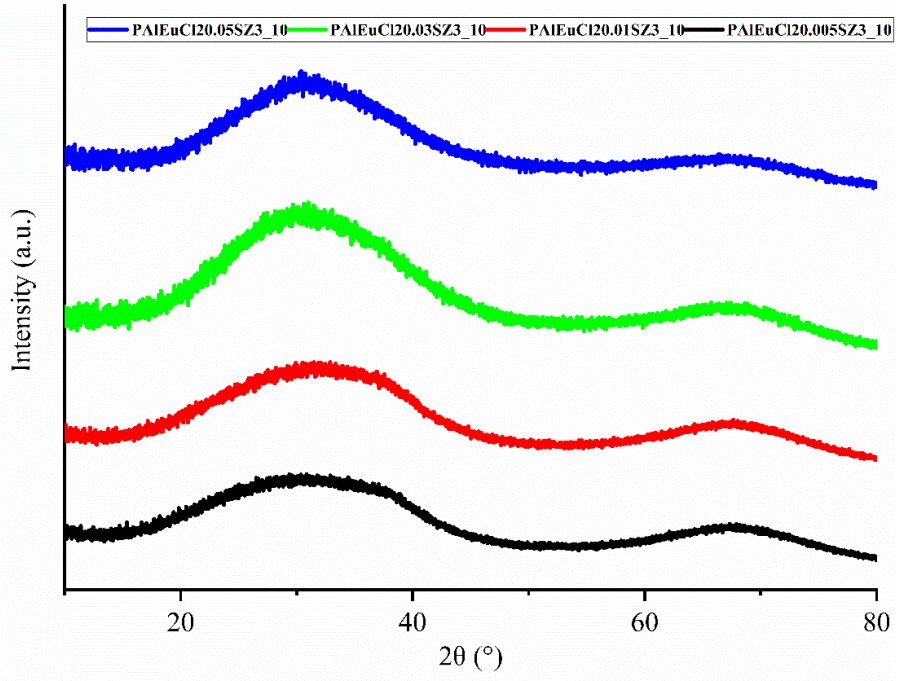

Figure IV.4. X-ray diffraction (XRD) patterns of PAlEuCl$_2$YSZ3_10 (0.005 ≤ Y ≤ 0.05).

IV.2.2.2. High-temperature treatment of amorphous ceramics up to 1800 °C in flowing nitrogen

In this section, we applied the high-temperature procedure we already investigated in Chapter III; we defined it as a conventional high-temperature heat-treatment and it will be discussed in a first sub-section. In a second sub-section, we will investigate the GPS process as a proof of concept.

IV.2.2.2.1. Conventional high-temperature heat-treatment of ammonia-treated samples

The high-temperature heat-treatment of **PAlEuCl$_2$0.005SZ3_10**, and **PAlEuCl$_2$0.05SZ3_10** samples at 1600 °C (we considered this temperature based on the results obtained in Chapter III) in flowing nitrogen favors the formation of **Si**N_4 and **Al**N_4 environments as for **PAlSZ3_10** (Chapter III) which can be identified in NMR result plot in Figure IV.5. ^{29}Si MAS and ^{27}Al MAS spectra of **PAlEuCl$_2$0.005SZ3_16** and **PAlEuCl$_2$0.05SZ3_16** samples indeed indicate the emergence of sharp signals at −48 (**Si**N_4) ppm and at 115 (**Al**N_4) ppm. The chemical shift

anisotropy (spinning sidebands) is much more pronounced in **PAlEuCl$_2$0.05SZ3_16** sample. Moreover, sharp shape peak is significantly broader for these sample which can be due to paramagnetic interactions according to the highest Eu content.

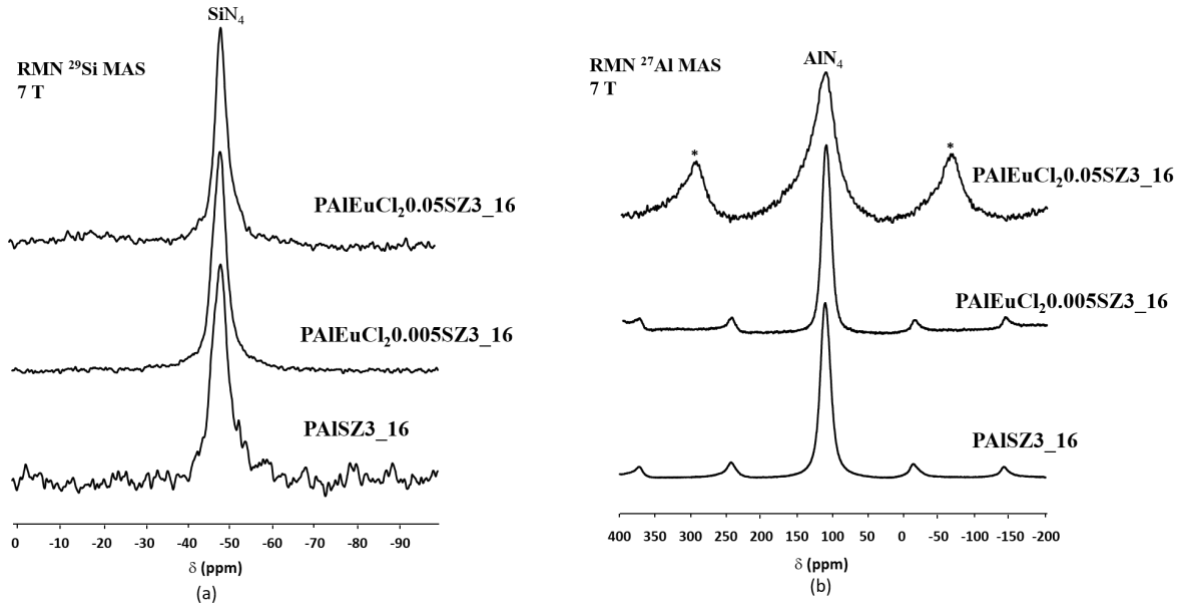

Figure IV.5. Solid-state NMR spectra of **PAlSZ3_16**, **PAlEuCl$_2$0.005SZ3_16** and **PAlEuCl$_2$0.05SZ3_16** samples: (a) ^{29}Si MAS NMR and (b) ^{27}Al (b) MAS NMR (* indicate spinning sidebands).

Whereas element analysis confirms the presence of oxygen in these samples with a minimum content of 2.7 wt.% (Table IV.3) for the **PAlEuCl$_2$0.005SZ3_16** sample, it is worth noting that we could not identify oxygen-based environments in NMR which could be due to low oxygen concentration.

Table IV.3. Elemental analysis of **PAlSZ3_16**, **PAlEuCl$_2$0.005SZ3_16** and **PAlEuCl$_2$0.05SZ3_16** samples.

Samples	Si	Al	O	N	H	C	Eu	Empirical formula*
	in wt. %							
PAlSZ3_16	47.9	16.7	3.8	31.4	0.0	0.2	-	**$Si_{1.0}Al_{0.4}O_{0.1}N_{1.3}$**
PAlEuCl$_2$0.005SZ3_16	46.4	16.3	2.7	33.4	0.03	0.01	1.0	**$Si_{1.0}Al_{0.4}O_{0.1}N_{1.3}Eu_{0.006}$**
PAlEuCl$_2$0.05SZ3_16	34.2	3.4	3.9	30.4	0.0	0.0	1.6	**

** reference to $Si_{1.0}$; ** not calculated.*

The oxygen content measured in Eu-doped samples is indeed in the range of that one measured for the **PAlSZ3_16** sample and the chemical formula of the **PAlEuCl$_2$0.005SZ3_16** sample matches the chemical formula of the **PAlSZ3_16** sample (excluding Eu content). Therefore, we confirm that the introduction of Eu^{2+} at the molecular scale does not affect the composition of

polysilazane-derived β-SiAlON and that the O content in our system is below the value expected in β-SiAlON. In contrast, the **PAlEuCl$_2$0.05SZ3_16** sample was very hard to mineralize; therefore, we suggest that the elemental analysis does not represent the real composition of the material.

X-ray diffraction (XRD) analysis was employed to monitor the structural changes occurring in PAlEuCl$_x$YSZ3_10 (x = 2, 3; 0.005 ≤ Y ≤ 0.05) samples upon heat-treatment up to 1600 °C. The XRD patterns of PAlEuCl$_2$YSZ3_14 (0.005 ≤ Y ≤ 0.05) and PAlEuCl$_2$YSZ3_16 (0.005 ≤ Y ≤ 0.05) samples are depicted in Figure IV.6 and Figure IV.7 respectively. Again, no differences have been observed with Eu^{3+}-doped samples.

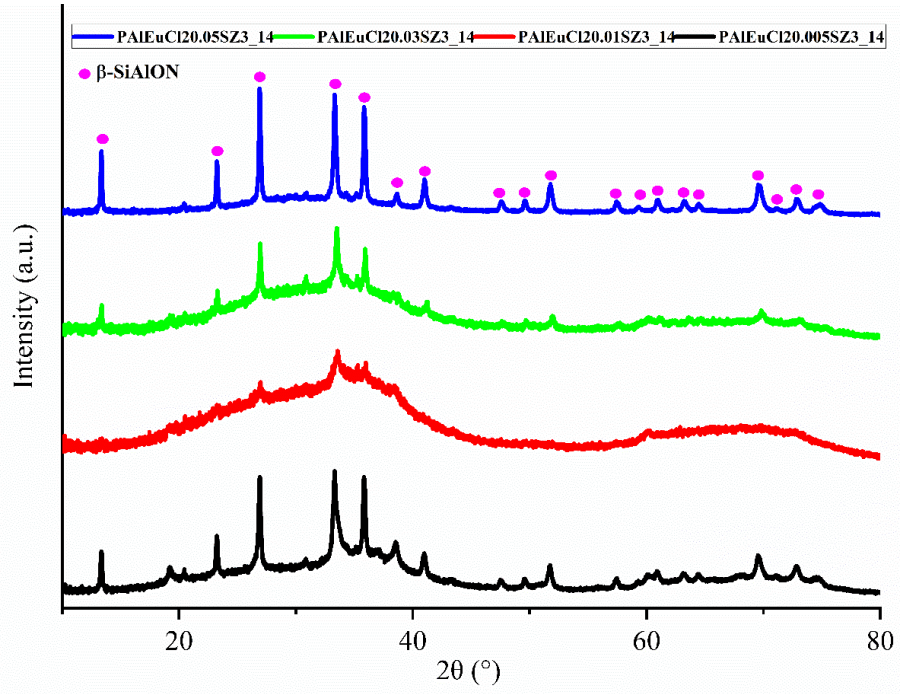

Figure IV.6. X-ray diffraction (XRD) patterns of PAlEuCl$_2$YSZ3_14 (0.005 ≤ Y ≤ 0.05).

The XRD patterns are shown in Figure IV.6 for PAlEuCl$_2$YSZ3_14 samples (0.005 ≤ Y ≤ 0.05). The majority of peaks are characteristic of the β-SiAlON phase (PDF 01-077-0755). They reveal that the degree of crystallization of the material significantly changes from a sample to another one with a link with the Eu:Si ratio. We observed that the amount of crystalline phase increases with the increase of Eu:Si ratio, except for the lowest Eu content sample (**PAlEuCl$_2$0.005SZ3_14**). These outcomes show the influence of the dopant on the structural alterations within the ceramic material. Upon reaching a temperature of 1600°C (Figure IV.7), whatever the Eu content in the samples, the XRD patterns indicate the growth of crystalline phases: β-SiAlON (PDF 01-077-0755), α-Si_3N_4 (PDF 04-005-5074) and w-AlN (PDF 00-008-0262). In addition, for the highest Eu:Si ratio (**PAlEuCl$_2$0.05SZ3_16**) we noticed the presence

of small amount of a forth crystalline phase. The diffraction peaks of this phase can be indexed with an aluminum-silicon-oxynitride phase (PDF 01-090-2337)[26] reported recently in literature and containing europium as well as lithium. *Although in our sample we do not have Li, we decided to use this phase as a structure model for the subsequent Rietveld Refinement quantitative analysis. In the following we called this phase model 'Oxynitride-type' phase.*

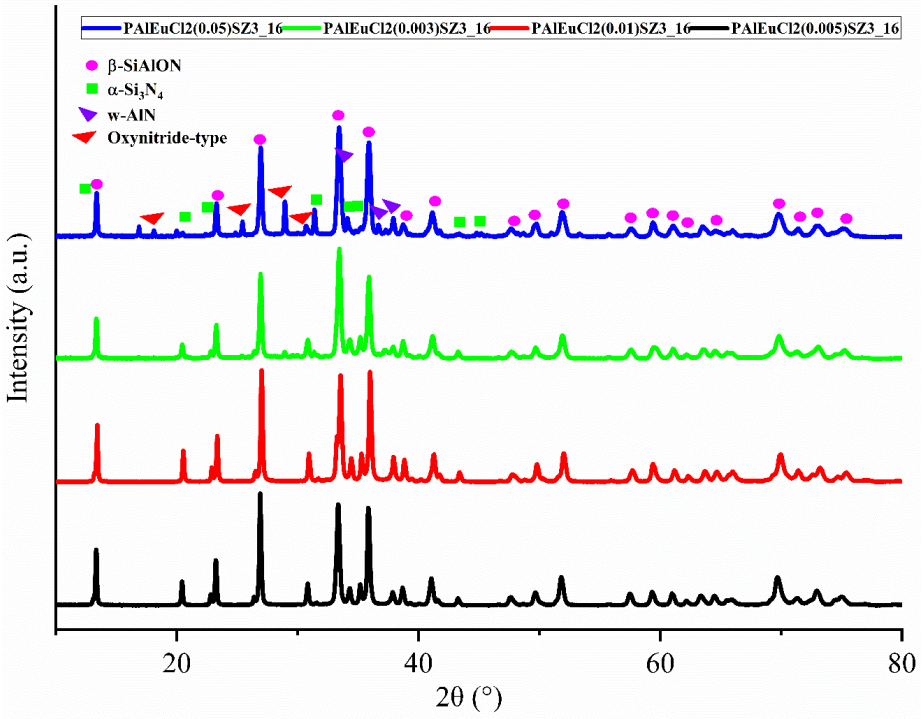

Figure IV.7. X-ray diffraction of PAlEuCl$_2$YSZ3_16 ($0.005 \leq Y \leq 0.05$).

Similarly to Chapter III, Rietveld refinement was employed for quantitative analysis and to validate the existence of the proposed phases in the **PAlEuCl$_2$0.005SZ3_16** (Figure IV.8(a)) and **PAlEuCl$_2$0.05SZ3_16** (Figure IV.8(b)) samples, i.e. lowest and highest Eu:Si ratio samples. The Rietveld refinements were performed using 3 phases (β-SiAlON, α-Si$_3$N$_4$ and w-AlN) for **PAlEuCl$_2$0.005SZ3_16** sample and 4 phases (β-SiAlON, α-Si$_3$N$_4$, w-AlN and the Oxynitride-type phase discussed above) for **PAlEuCl$_2$0.05SZ3_16** sample. The main refined parameters were scale factors, background, sample positioning error, and cell parameters as explained in Chapter III. For the β-SiAlON phase we also refined the line profile shape, breadth, and atomic positions. The values in parentheses indicate the estimated errors on the last digit, corresponding to twice the estimated standard deviation calculated by Rietveld refinement. Parameters denoted with the symbol "-" indicate they were not refined (because of too small quantity of phase). The Rietveld fit of the two XRD patterns illustrated in Figure IV.8 demonstrates overall good quality, but again far from perfection, especially for the **PAlEuCl$_2$0.05SZ3_16** sample where discrepancies in intensities are clearly observed.

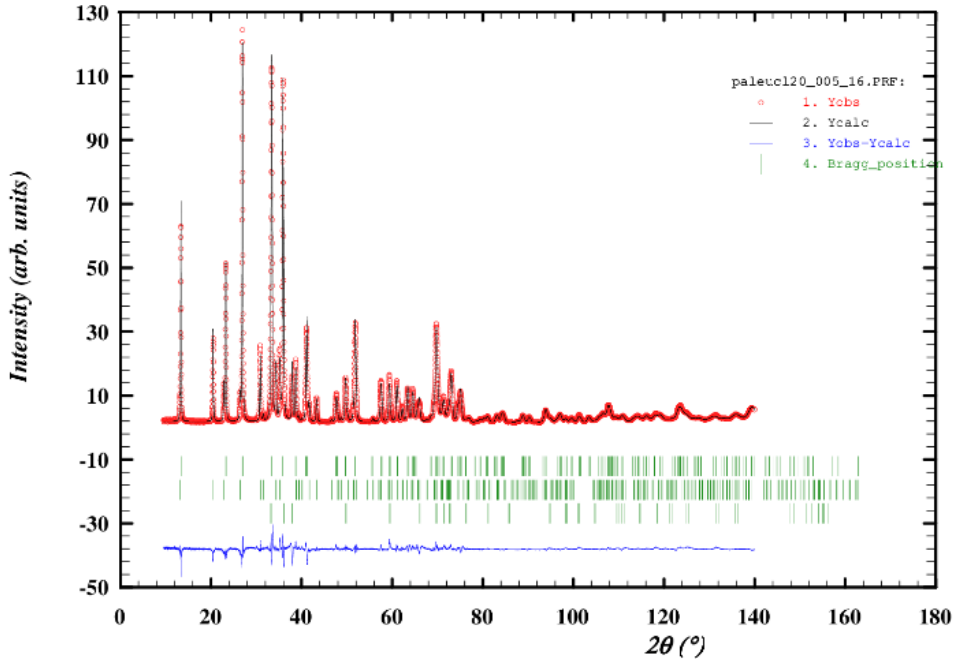

(a)

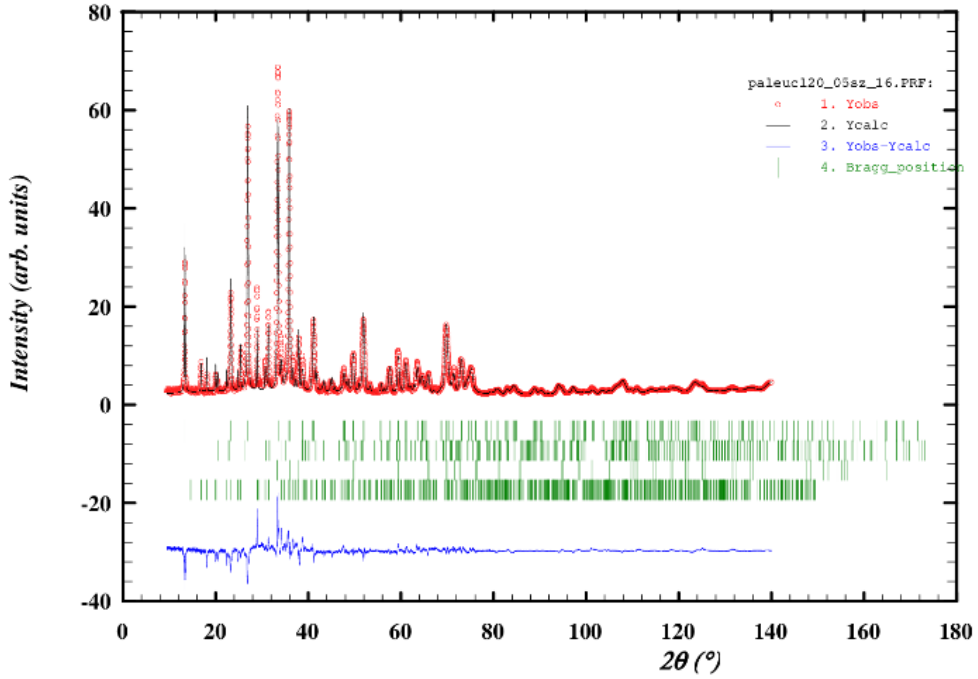

(b)

Figure IV.8. Rietveld refinement of XRD patterns of the **PAlEuCl$_2$0.005SZ3_16** (a) and **PAlEuCl$_2$0.05SZ3_16** (b) samples. *Observed (crosses) and calculated (red line) XRD patterns. Green vertical lines indicate positions of Bragg reflections. Blue line represents difference plot (observed/calculated) on the same scale.*

This results in relatively poor figures of merit (R_p=9.21%, R_{wp}=10.9%, R_{exp}=1.55% and GofF= 7.0) for **PAlEuCl$_2$0.005SZ3_16** and (R_p=17.1%, R_{wp}=18.4%, R_{exp}=2.20% and GofF=8.4) for **PAlEuCl$_2$0.005SZ3_16**. These discrepancies are not expected to have a significant impact on the relevant refined parameters. The main results are outlined in Table IV.4.

Table IV.4. Main parameters obtained from Rietveld Refinement of the XRD patterns of **PAlEuCl$_2$0.005SZ3_16** and **PAlEuCl$_2$0.05SZ3_16**. (*The symbol '–' denotes that the corresponding parameter is not refined).*

Samples	**PAlEuCl$_2$0_005SZ3_16**			**PAlEuCl$_2$0_05SZ3_16**			
Phase parameters	**β-SiAlON**	**α-Si_3N_4**	**w-AlN**	**β-SiAlON**	**α-Si_3N_4**	**w-AlN**	**Oxynitride-Type**
Cristallite size (nm)	148.4 (5)	-	-	110.7 (3)	-	-	-
Micro-strain (%)	0.272 (8)	-	-	0.408 (6)	-	-	-
a, b (Å)	7.637 (6)	7.780 (8)	3.112 (8)	7.638 (2)	7.792 (2)	3.108 (4)	12.123 (4)
c (Å)	2.932 (4)	5.661 (2)	4.990 (8)	2.926 (8)	5.667 (2)	4.995 (4)	4.894 (2)
Cell Volume(Å^3)	148.11 (2)	296.64 (8)	41.856 (4)	147.86 (8)	297.99 (2)	41.796 (6)	622.99 (6)
Phase fraction (%)	68.7 (2)	18.7 (2)	12.8 (2)	75.6 (8)	5.5 (3)	13.4 (3)	5.7 (1)

For **PAlEuCl$_2$0.005SZ3_16** sample**,** the refined cell parameters for β-SiAlON are a = b = 7.637 Å, and c = 2.932 Å which are clearly larger than those of β-Si_3N_4, confirming the presence of β-SiAlON. For α-Si_3N_4 the refined cell parameters are a = b = 7.780 Å, c = 5.661 Å, aligning with the range specified in Chapter I for α-Si_3N_4. Additionally, the refined cell parameters of of w-AlN is closely aligned with the reference values (a, b = 3.112 Å, c = 4.990 Å). The amount of β-SiAlON phase is only 69%, which is much less than the one obtained for **PAlSZ3_16** sample without Eu (92 %). Both the crystallite size (148 nm) and micro-strains (0.27 %) values for β-SiAlON are in the same range as those obtained for the sample without Eu doping under the same heating conditions (**PAlSZ3_16**) which displays a crystallite size of 120 nm and micro-strains of 0.21 %, as discussed in Chapter III.

With an increased concentration of $EuCl_2$ in **PAlEuCl$_2$0.05SZ3_16**, there is not much variation in cell parameters for β-SiAlON (a = b = 7.638 Å, c = 2.926 Å) and volume, as indicated in Table IV.4. The lattice parameter obtained for α-Si_3N_4 are still in the range of values expected for α-Si_3N_4 according to reference given in Chapter I. The oxynitride-type phase for **PAlEuCl$_2$0.05SZ3_16** has the lattice parameters a = b = 12.123 Å and c = 4.894 Å, which is similar to the reference data (a = 12.121 Å, c = 4.893 Å)[26].

The Rietveld refinement shows that the increase in the Eu content leads to changes in the phase content. The β-SiAlON phase content increases from 68.7 % (**PAlEuCl$_2$0.005SZ3_16**) to 75.6

% (**PAlEuCl$_2$0.05SZ3_16**), while the α-Si_3N_4 phase content decreases from 18.7 % to 13.4 % the w-AlN content remaining constant and the oxynitride-type phase appearing. This increase in Eu content also seems to lead to a slight decrease of the size of the β-SiAlON crystallites, from approximately 150 nm to 110 nm (associated with slight increase in micro-strain).

From the present Rietveld refinement results, it is not easy to conclude about the effective insertion of Eu within the β-SiAlON host structure. Indeed, although the cell parameters of the β-SiAlON do not change, within experimental errors, with Eu concentration (See Chapter III for sample without Eu), we observed at the same time a large change of β-SiAlON and secondary phases content (i.e. inducing a change of composition of β-SiAlON) from one sample to another. Consequently, we cannot exclude that change of cell parameters induced by change of composition can be compensated by insertion of Eu. This question will be addressed by luminescence and elemental analysis mapping studies of sample in the following sections.

IV.2.2.2.2. Gas Pressure Sintering of ammonia-treated samples

Gas pressure sintering (GPS) is applied to nitride ceramics which are thermodynamically unstable at higher temperatures with the objective to suppress their dissociation[27]. Furthermore, Qi Wang et al. demonstrated that optimizing nitrogen pressure can significantly improve both the structural and photoluminescence properties of the resultant material[28]. Regarding β-SiAlON, GPS achieves the production of pure compounds by catalyzing an intense nitridation reaction between silicon and nitrogen under elevated nitrogen pressure[29]. This pressure increase promotes the volatilization of secondary phases, facilitating the formation of β-SiAlON during sintering[29,30]. This process results in a substantial amount of Si_3N_4, exhibiting enhanced reactivity with O_2 (if present) and dispersion during the nucleation stage.[29,31,32] The theoretical framework suggests that finer pores undergo shrinkage to a stable size before larger ones. Following this, larger pores become active, with those surpassing a critical size expanding instead of shrinking, forming homogeneously larger crystallites[29,33,34].

In chapter III, we showed that the **PAlSZ3_16** sample (with 92 % of β-SiAlON) decomposed above 1600 °C based on high-temperature thermogravimetric analyses. As a consequence, we limited the heat-treatment process at 1600 °C to develop SiAlON ceramics and the Eu-doped SiAlON samples as discussed previously. GPS is expected to shift this composition at higher temperature allowing us to increase this final temperature. Hence, we have considered ammonia-treated samples and in particular the **PAlEuCl$_2$0.05SZ3_10** sample to be heat-treated

at 1800 °C with GPS and deliver the **PAlEuCl$_2$0.05SZ3_GPS18** sample. The examination of **PAlEuCl$_2$0.05SZ3_GPS18** sample involved XRD analysis aided by Rietveld refinements.

The XRD pattern of the **PAlEuCl$_2$0.05SZ3_GPS18** sample is presented in Figure IV.9.

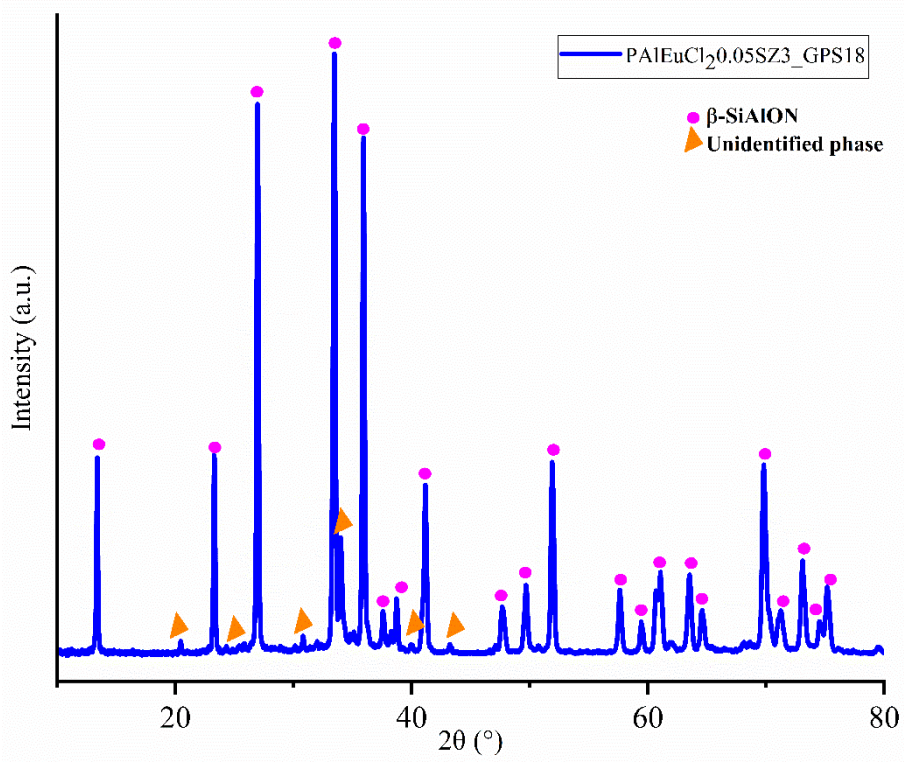

Figure IV.9. X-ray diffraction (XRD) pattern of **PAlEuCl$_2$0.05SZ3_GPS18** sample.

Interestingly, it shows peaks mainly attributed to the β-SiAlON phase. As expected, GPS acts effectively and serves the purpose to suppress the formation of Si_3N_4 and avoid the decomposition of the β-SiAlON phase which results in the formation of w-AlN (by releasing SiO). In addition to peaks attributed to the β-SiAlON phase, we can observe a few small intensity peaks corresponding to an unidentified phase (Figure IV.9 (orange color)).

The Rietveld refinement was done by using one phase β-SiAlON and the Rietveld fit is depicted in Figure IV.10. Although the fit is satisfactory, there are significant discrepancies in intensity. This results in poor figures of merit (R_p =25.6 %, R_{wp} = 31.3 %, R_{exp} = 2.05 %, and GofF = 15).

After the gas pressure sintering of the **PAlEuCl$_2$0.05SZ3_10** sample does not change the cell parameter (a = b=7.633 Å and c = 2.928 Å), within the experimental error. Finally, in addition to form almost pure β-SiAlON, GPS also tends to slightly increase the crystallite size of β-SiAlON phase (from 148 nm to 174 nm) and slightly decrease the strain (from 0.4 % to 0.2 %) which can be useful to influence photoluminescent properties.

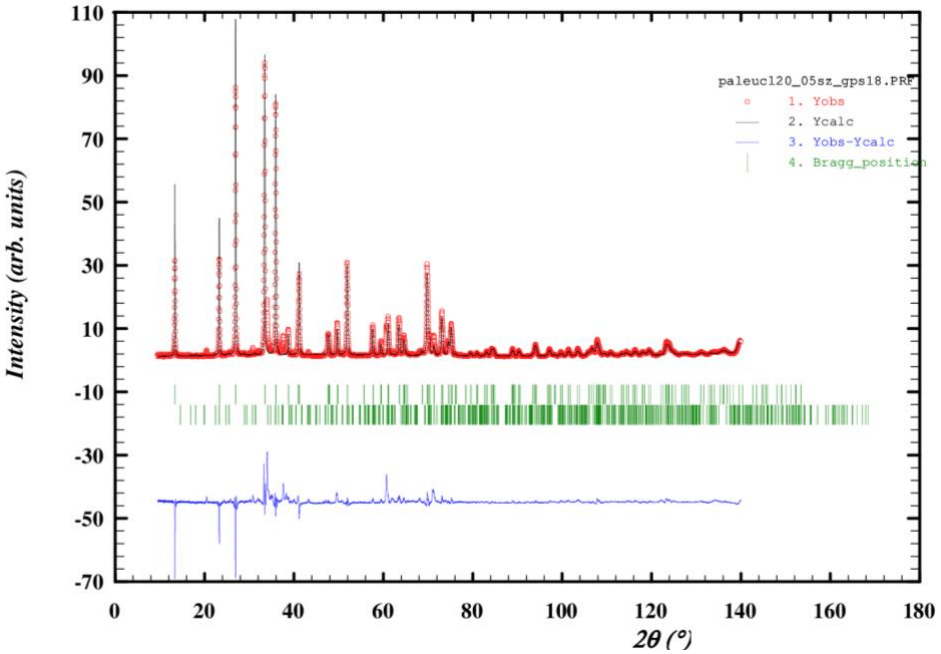

Figure IV.10. Rietveld refinement of the XRD pattern of the **PAlEuCl$_2$0_05SZ3_GPS18** sample.

Observed (crosses) and calculated (red line) XRD patterns. Green vertical lines indicate positions of Bragg reflections. Blue line represents difference plot (observed/calculated) on the same scale.

Table IV.5. Cells parameter obtained from Rietveld refinement of **PAlEuCl$_2$0_005SZ3_18** sample.

Samples	**PAlEuCl$_2$0_05SZ3_GPS18**
Phase parameters	**β-SiAlON**
Cristallite size (nm)	174.3 (8)
Micro-strain (%)	0.18 (4)
a, b (Å)	7.633 (2)
c (Å)	2.928 (8)
Cell Volume(Å^3)	147.75 (8)

In the next section, we further go in more details regarding the microstructural investigation of these samples using electron microscopy.

IV.2.2.2.3. Microstructural investigation of final materials

The analysis of microstructures involves the examination of materials at both microscopic and nanoscale levels, employing various techniques such as scanning electron microscopy (SEM) in conjunction with cathode-luminescence (CL) and transmission electron microscopy (TEM). In this procedure, CL is employed to generate panchromatic images by transmitting UV light (at 350nm) to discern whether the emission emanates from the crystallite or the grain boundary. SEM contributes high-resolution images by scanning, enabling the exploration of surface

morphology, while TEM offers insights into crystal details at the nanoscale, including diffraction patterns.

SEM/CL analysis was carried out to examine the microscale morphology of the **PAlEuCl$_2$0.05SZ3_16** and is depicted in Figure IV.11.

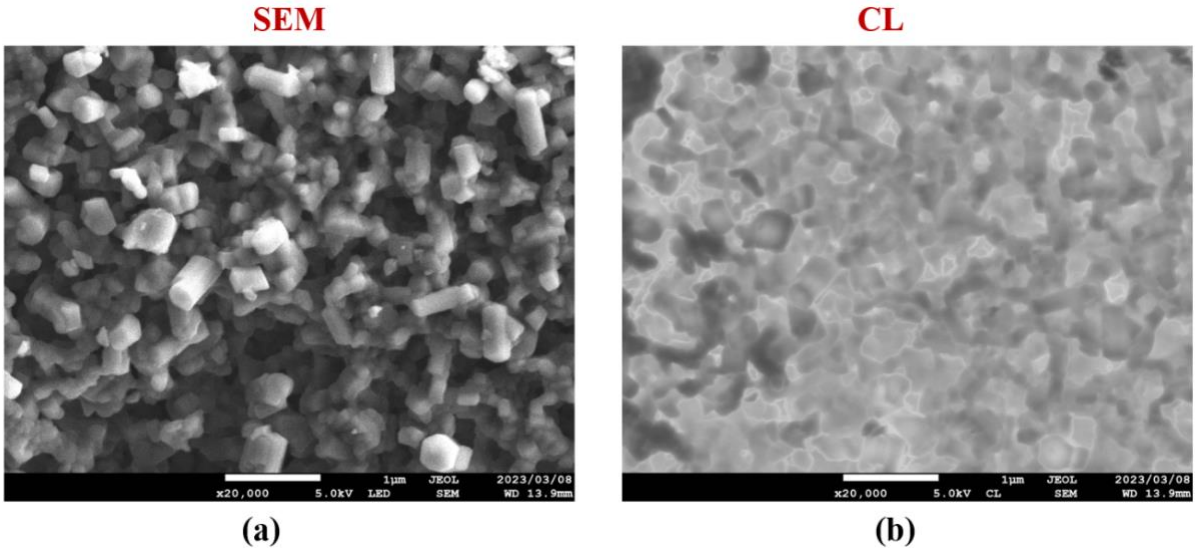

Figure IV.11. Scanning electron microscopy (SEM); (a) and Cathodoluminescence (CL); (b) image of **PAlEuCl$_2$0.05SZ3_16** ceramics.

The morphology shows cylindrical shapes made of β-SiAlON displaying luminescence uniformly across the material (Figure IV.11(b)), including the domains containing impurities, and exhibiting small crystallite sizes (Figure IV.11(a)). By reaching a lower scale, TEM measurements (Figure IV.12) conducted on the **PAlEuCl$_2$0.005SZ3_16** (a) and **PAlEuCl$_2$0.05SZ3_16** (b) samples confirm the high crystallinity of the samples. The SAED pattern recorded for **PAlEuCl$_2$0.005SZ3_16** (Figure IV.12(a)) allowed observing the diffraction of the (010), (020) and (011) planes at 13°, 27° and 33°, respectively. TEM observations of the **PAlEuCl$_2$0.05SZ3_16** (Figure IV.12(b)) sample reveal the presence of larger cylindrical crystallites. The SAED patterns exhibited peaks at 13° (010), 65° (041), and 68° (112). The Eu doping is reflected in the mapping and the chemical composition of **PAlEuCl$_2$0.05SZ3_16** sample where Eu can be seen homogenously distributed within all over structure which confirms doping (Figure IV.13).

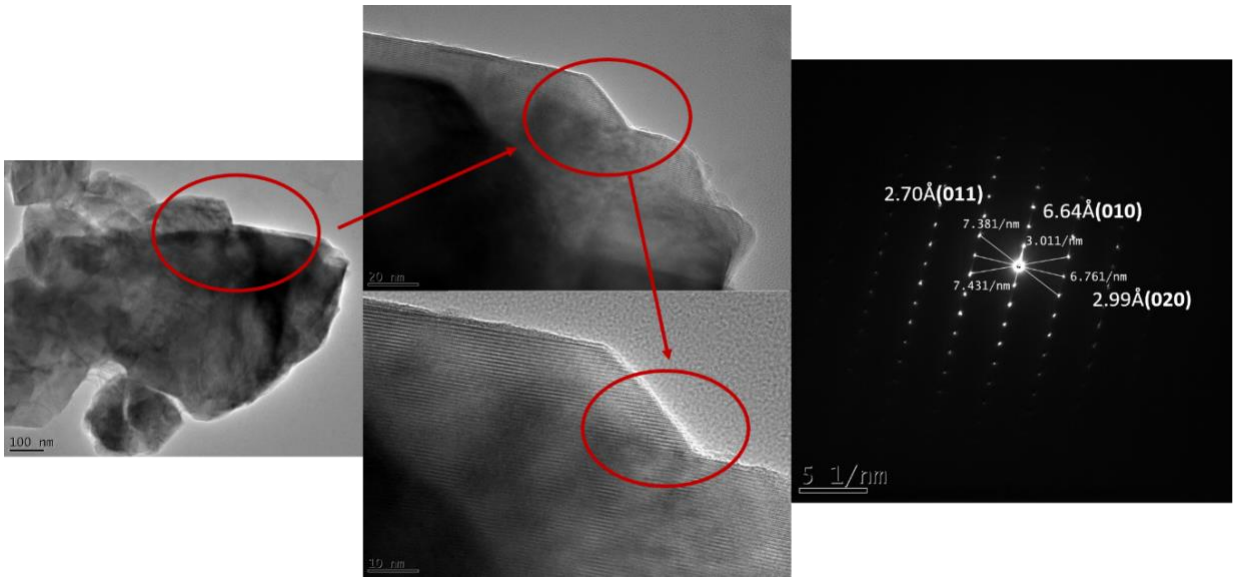

(a)

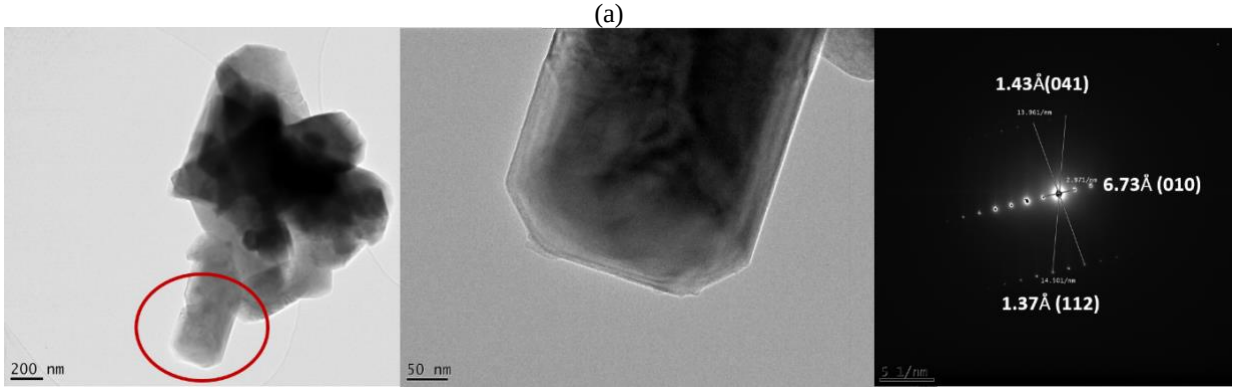

(b)

Figure IV.12. TEM images and corresponding SAED patterns for the **PAlEuCl$_2$0.005SZ3_16** (a) and **PAlEuCl$_2$0.05SZ3_16** (b) samples.

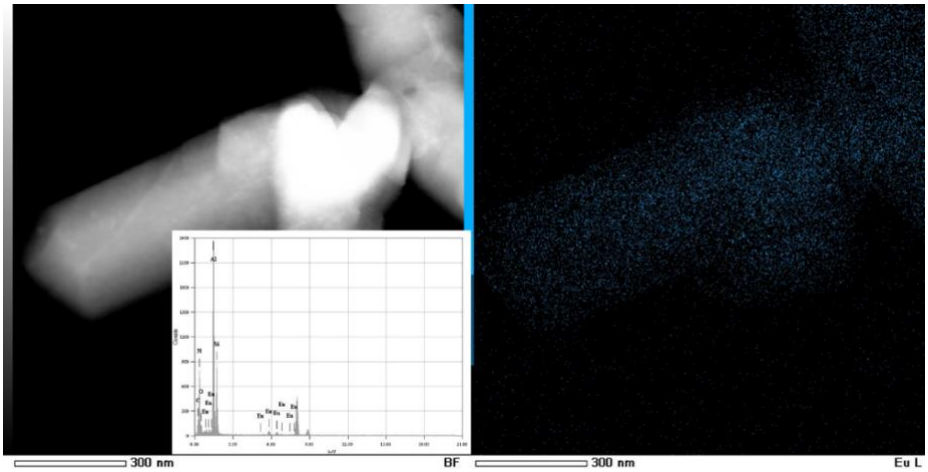

Figure IV.13. Mapping and chemical composition of **PAlEuCl$_2$0.05SZ3_16**.

Figure IV.14 showcases the microstructural features of the **PAlEuCl$_2$0.05SZ3_GPS18** sample (Figure IV.14(a) and (b)), illustrating some cylindrical shape crystallites known to be β-SiAlON.

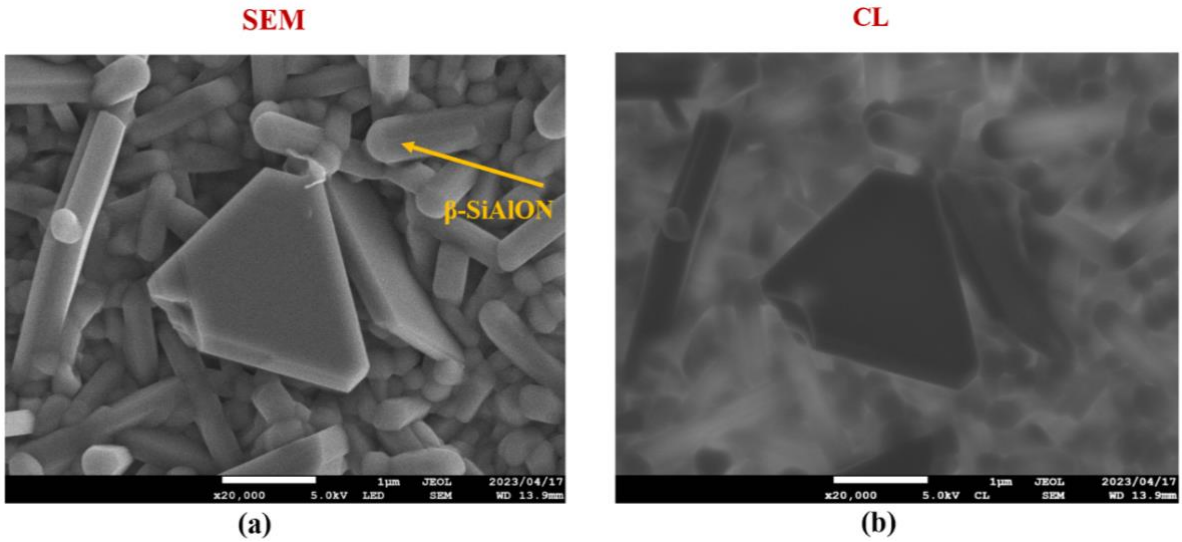

Figure IV.14. (a) Scanning electron microscopy (SEM) and (b) Cathodoluminescence (CL images of **PAlEuCl$_2$0.05SZ3_GPS18** ceramics.

Despite the fact that the **PAlEuCl$_2$0.05SZ3_GPS18** sample is locally composed of unknown particles (polyploid) (Figure IV.14(a)) which do not show any emission via CL images (Figure IV.14(b)), we can clearly confirm that **luminescence comes out throughout all cylindrical particles**. This part confirms that GPS unveiled an improved morphology characterized by larger crystallite sizes and the **emergence of luminescence originating from the host lattice (β-SiAlON)**. Nevertheless, certain impurities, notably polyploids, did not exhibit any luminescent properties. In Figure IV.15, the TEM image of **PAlEuCl$_2$0.05SZ3_GPS18** is presented, and the diffraction pattern has been identified at two locations.

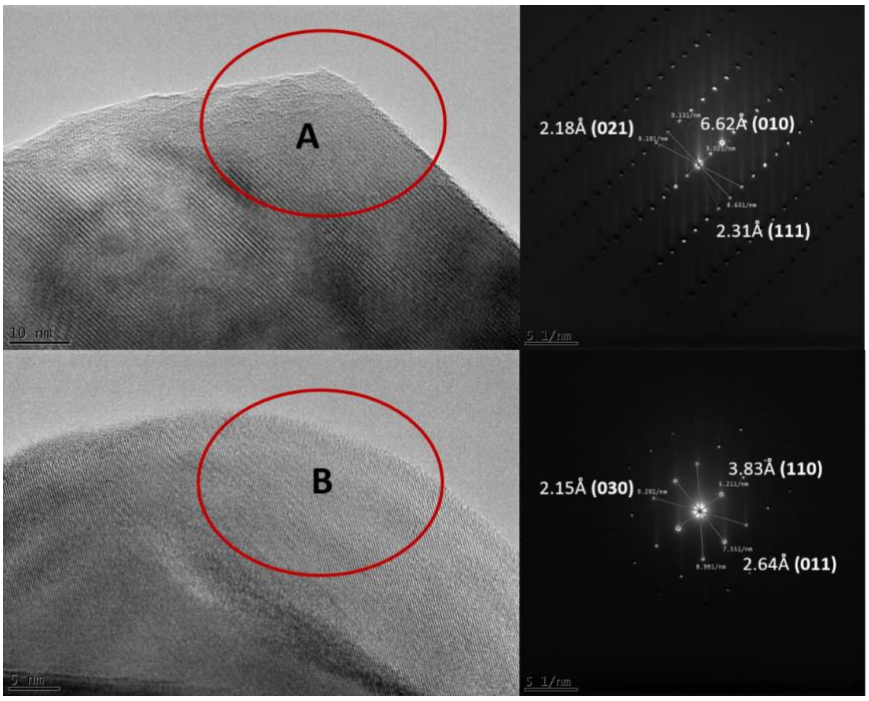

Figure IV.15. Transmission electron microscopy of **PAlEuCl$_2$0.05SZ3_GPS18** sample.

Notably, even after Gas Pressure Sintering, no intergranular or amorphous phase was detected. In spot **A**, a diffraction pattern was observed at 13° (010), 41° (021), and 38° (111). At spot **B**, the diffraction pattern was noted at 23° (110), 33° (011), and 41° (030).

In summary, the analysis of all samples confirms the existence of the crystalline β-SiAlON phase, with mapping indicating a uniform distribution of Eu within the β-SiAlON crystallite. The use of GPS successfully suppressed secondary phases, resulting in longer crystallites and a homogeneous distribution with only a few polytypoid crystals. The SEM/CL image exhibited uniform luminescence across the β-SiAlON and secondary phase. However, after GPS treatment, luminescence is now solely coming from the cylindrical crystallite (referred to as β-SiAlON), and not from polytypoid crystals.

IV.3. Optical properties analysis

IV.3.1. Photoluminescent analysis

Photoluminescence (PL) is the process in which a material absorbs photons and then emits them as light. This involves excitation and emission steps. The excitation spectrum reveals the relationship between the intensity of excitation light at various wavelengths and resulting emission intensity, aiding in determining the optimal excitation wavelength[2,35,36]. The emission spectrum illustrates the intensity of emitted light at different wavelengths, offering insights into material energy levels and transitions. In essence, photoluminescence spectra provide valuable information on electronic and optical properties, facilitating the design and optimization of materials for specific applications[2,37,38].

Figure IV.16 represent the photoluminescence (PL) excitation and emission spectra of the **PAlEuCl$_2$YSZ3_16** ($0.005 \leq Y \leq 0.05$) and **PAlEuCl$_2$0.05SZ3_GPS18** samples. The excitation spectra ($\lambda_{ex.}$= 538 nm) and emission spectra ($\lambda_{em.}$ = 410 nm, 460 nm) were recorded at room temperature where these wavelengths are important for application as pc-WLED.

In the excitation spectra (recorded at 538 nm) presented in Figure IV.16(a), **PAlEuCl$_2$YSZ3_16**) samples ($0.005 \leq Y \leq 0.05$) exhibit a similar shape of excitation spectrum characterized by a dominant broad peak around 284-287 nm, 367 nm and 460nm. These peaks are attributed to the absorptions of the host lattice and the $4f^7$-$4f^6 5d^1$ transitions of the dopant Eu^{2+} cations[39–42]. The rise in Eu:Si (Y) concentration ($0.005 \leq Y \leq 0.05$) results in an increase in the excitation intensity, although the **PAlEuCl$_2$0.01SZ3_16** sample does not follow this trend. The **PAlEuCl$_2$0.05SZ3_16** sample exhibited the highest excitation, likely attributed to

its higher Eu content, resulting in increased Eu transition from f-d orbital. Consequently, we performed GPS on the **PAlEuCl$_2$0.05SZ3_16** sample, now referred to as **PAlEuCl$_2$0.05SZ3_GPS18**, revealing three prominent bands at 287 nm, 405 nm, and 464 nm and two small band at 340 nm and 367 nm, these peaks correspond to the f-d transition of Eu^{2+} cations, effectively doubling the overall intensity.

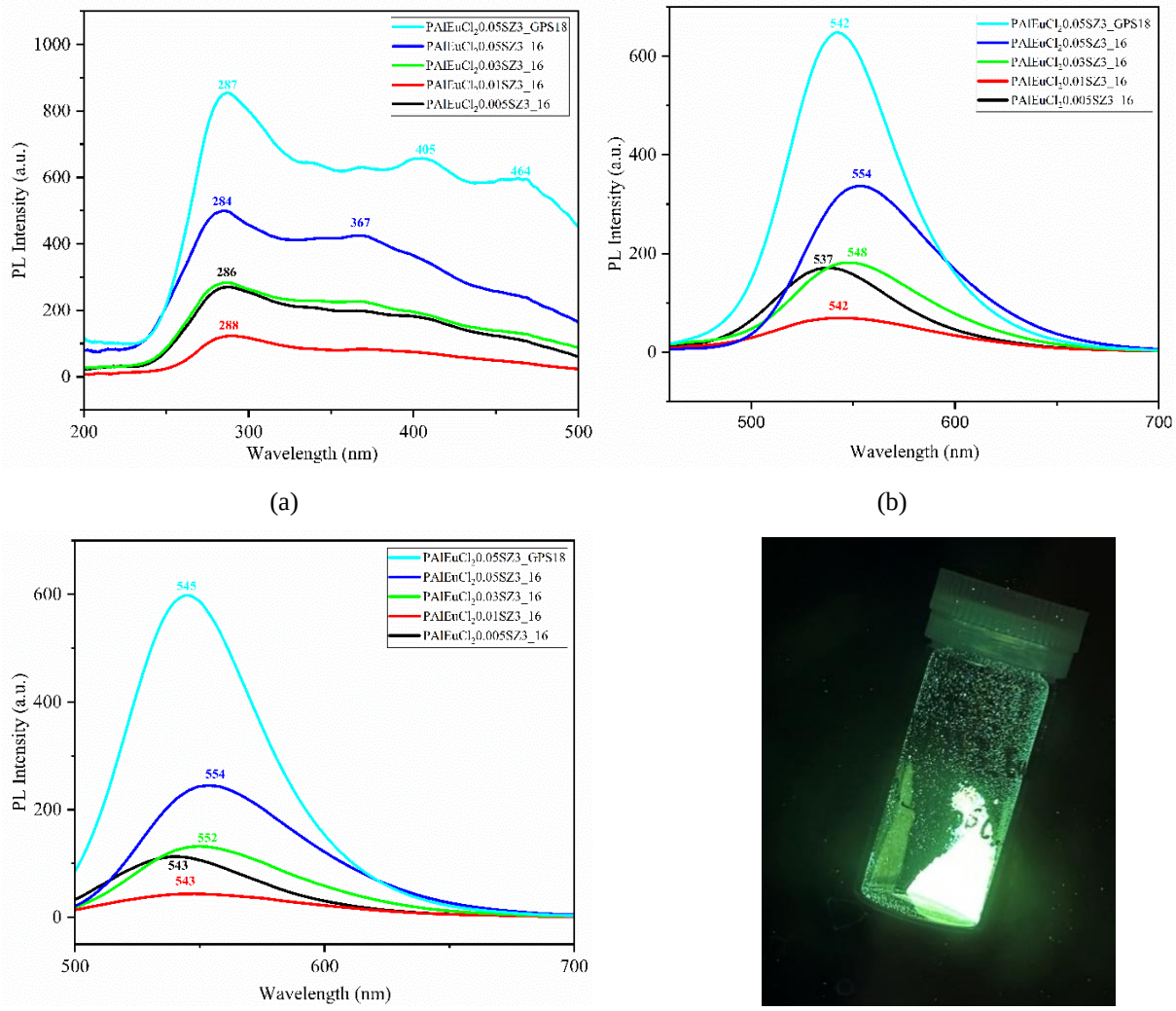

(a) (b)

(c) (d)

Figure IV.16. Photoluminescence (PL) (a) Excitation spectra monitored at ($\lambda_{em.}$= 538 nm); emission spectra monitored under violet and blue wavelength (b) $\lambda_{ex.}$= 410 nm and (c) $\lambda_{ex.}$= 460 nm (d) **PAlEuCl$_2$0.05SZ3_GPS18** sample excited at $\lambda_{ex.}$= 365 nm and shows green emission which matches PL spectra result.

The emission spectra of **PAlEuCl$_2$YSZ3_16** and **PAlEuCl$_2$0.05SZ3_GPS18** at 410 nm and 460 nm are depicted in Figure IV.16 (b) and (c). All these samples exhibit green emission in the range of 542-554 nm under excitation at 410 and 460nm; for example, **PAlEuCl$_2$0.05SZ3_GPS18** sample shows green emission even after excitation at 365nm (Figure IV.16(d)). The increase in Eu:Si (Y) ratio ($0.005 \leq Y \leq 0.05$) leads to a general increase

in the emission intensity (with the still exception of the **PAlEuCl$_2$0.01SZ3_16** sample for unknown reasons). In general, a shift to longer wavelength (542-554 nm) and to increase in emission intensity is identified by increasing the Eu:Si (Y) ratio ($0.005 \leq Y \leq 0.05$). The shift to longer wavelength indicates higher Eu ion concentrations, increased interactions between adjacent ions can lead to non-radiative processes, dissipating energy as heat instead of light. This transfer affects the overall emission spectrum. The exchange interaction between adjacent Eu ions, a common mechanism, can distort the local crystal field, influencing energy levels and causing a shift in emitted light towards longer wavelengths—a phenomenon known as "concentration quenching"[17,43]. The implementation of GPS (**PAlEuCl$_2$0.05SZ3_GPS18**) has a substantial impact on enhancing the green emission intensity (by two times), as depicted in the Figure IV.16(b), and (c) which might come from phase purity and crystallite growth as shown in Figure IV.9 and Table IV.5. Compared to $EuCl_2$-doped ceramics, $EuCl_3$-doped ceramics exhibit similar luminescent behavior under identical excitation conditions thus results are not commented.

IV.3.2. Luminescent decay

Photoluminescent decay refers to the process in which a material emits light subsequent to the absorption of photons. In the case of β-SiAlON: Eu^{2+} ceramics, the photoluminescent decay can be elucidated by considering the interaction between Eu ions and the crystal lattice, followed by the relaxation of excited states. Photoluminescent decay ensues through the excitation of electrons and can be attributed to electronic transition relaxation processes, which may be radiative or non-radiative in nature[44–46]. The duration required for excited Eu ions to revert to their ground state is denoted as the lifetime of the excited states. It is a measure of how long the material can emit light after excitation. The lifetime can vary depending on factors such as the concentration of Eu dopants, crystal defects, temperature, and composition of the host β-SiAlON ceramics[35,47–49].

Figure IV.17, illustrates the decay curve of **PAlEuCl$_2$YSZ3_16** ($0.005 \leq (Y) \leq 0.05$) samples and of the **PAlEuCl$_2$0.05SZ3_GPS18** sample and the condition to observe luminescent decay is at wavelength of 350 nm and at room temperature. The decay curves were derived from the equations (Eq II.3 and II.4) described in Chapter II.

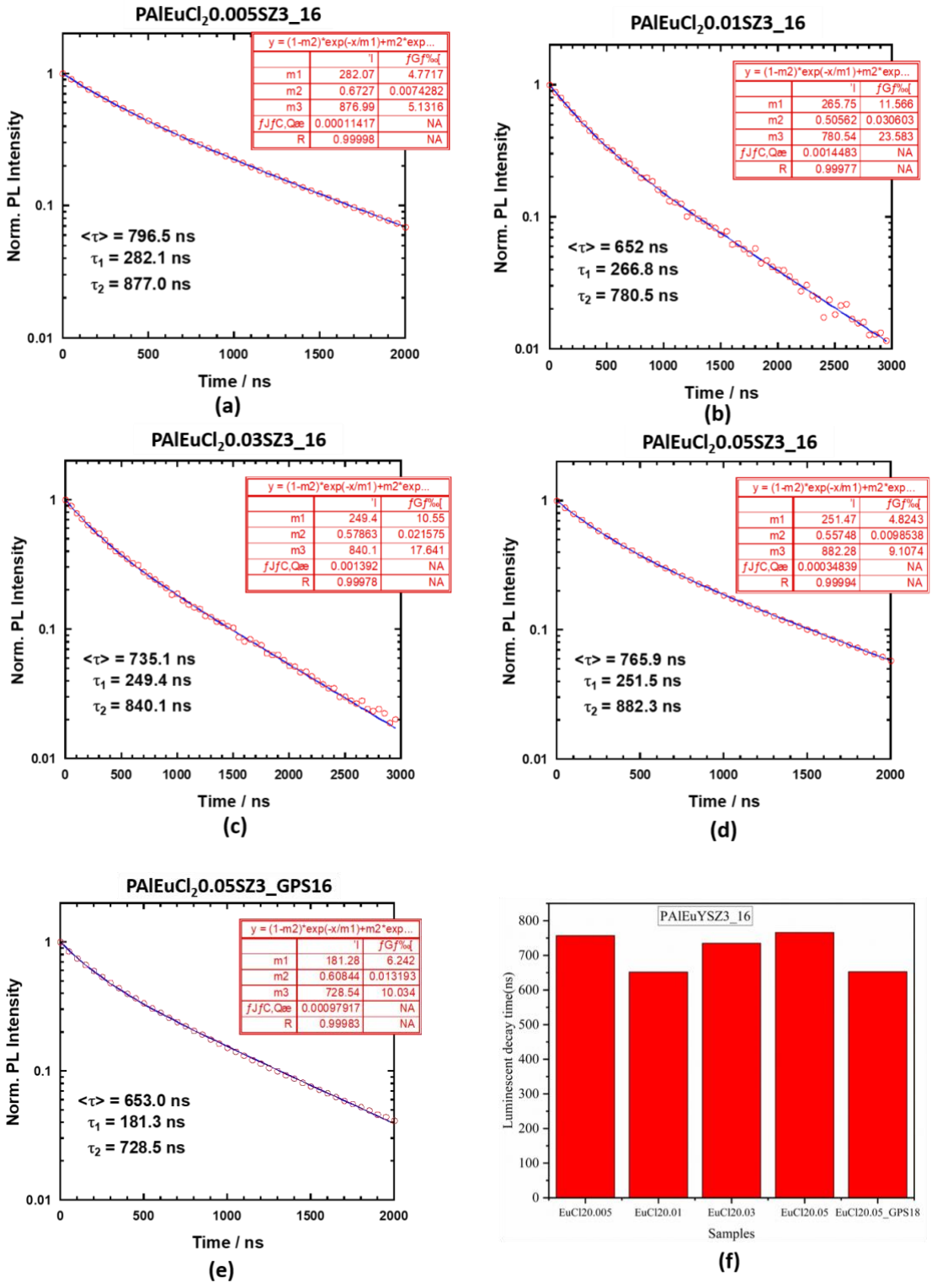

Figure IV.17. Photoluminescent Lifetime decay of (a) **PAlEuCl$_2$0.005SZ3_16**, (b) **PAlEuCl$_2$0.01SZ3_16**, (c) **PAlEuCl$_2$0.03SZ3_16**, (d) **PAlEuCl$_2$0.05SZ3_16**, (e) **PAlEuCl$_2$0.05SZ3_GPS18**; (f) comparison of luminescent decay time.

The lifetimes of all the samples were observed within the range of 650-800 nanoseconds, which is higher than a typical range for Eu^{2+} ions[5,35,39,50] which can be associated with excitation

wavelength (as it can vary based on excitation wavelength). The decay time of PAlEuCl$_2$YSZ3_16 samples ($0.01 \leq Y \leq 0.05$) initially exhibits an increase in luminescent decay time with rising Eu concentration. This phenomenon is attributed to the energy transfer from high-energy Eu^{2+} sites to low-energy Eu^{2+} sites. The high-energy Eu^{2+} sites, characterized by faster decay, contribute more significantly to the emission in samples with lower Eu concentrations[45]. Notably, the duration of the photoluminescent decay process is longer for the **PAlEuCl$_2$0.005SZ3_16** sample with the lowest concentration of Eu^{2+} (Figure IV.17(a)) which can happen due to electronic structures that allow for less efficient transitions between excited and ground states may exhibit longer decay time. The **PAlEuCl$_2$0.05SZ3_GPS18** (Figure IV.17(e)) has led to a reduction in the lifetime, possibly due to crystal structures may facilitate faster energy transfer and emission processes, resulting in a shorter decay time due to lower secondary phases[51], as indicated in Figure IV.17(e).

To conclude, the decay time of a luminescent material is influenced by various factors related to its electronic structure, crystal structure, impurities and dopant. Luminescence with shorter wavelength decays faster than luminescence with longer wavelength, that is in accordance with quantum mechanics which predicts that the radiative transition probability is proportional to third power of photon energy[52] that's why higher dopant concentration samples have longer decay time. That's why, as we examine the trend, it becomes evident that at higher dopant concentrations, the decay time increases, which can be attributed to the higher density of dopants and the promotion of non-radiative processes[44,46,51].

IV.3.3. Optical absorption

UV-visible diffuse reflectance spectra of PAlEuCl$_2$YSZ3_16 ($0.005 \leq Y \leq 0.05$) ceramics are depicted in Figure IV.18 and measured across the 200-1000 nm range. These measured samples exhibited a color spectrum ranging from white to dark yellow, depending on the concentration of Eu, and displayed robust absorption within the ultraviolet-visible portion of the electromagnetic spectrum. For PAlEuCl$_2$YSZ3_16 samples ($0.005 \leq Y \leq 0.05$, Figure IV.18, the absorption range falls between 270-600 nm, attributable to the absorption of Eu^{2+} ions undergoing electronic transitions from the ground state (4f) to the excited state (5d). Interestingly, as the concentration of Eu^{2+} ions increased, the absorption edge slightly shifted toward longer wavelengths, indicating a red-shift phenomenon. This red-shift ultimately contributes to the green emission observed in all the samples. Notably, all the samples depicted in Figure IV.18 exhibit roughly equivalent absorption in the UV and visible spectra, except

PAlEuCl$_2$0.05SZ3_16 and **PAlEuCl$_2$0.05SZ3_GPS18** which possibly associated with the presence of lattice defects. The estimated optical band gap for β-SiAlON:Eu^{2+} was approximately 4.4 eV (278 nm), and this value remained relatively consistent across all the samples. Furthermore, the optical absorption remained notably strong in the UV-Vis region at 365 nm.

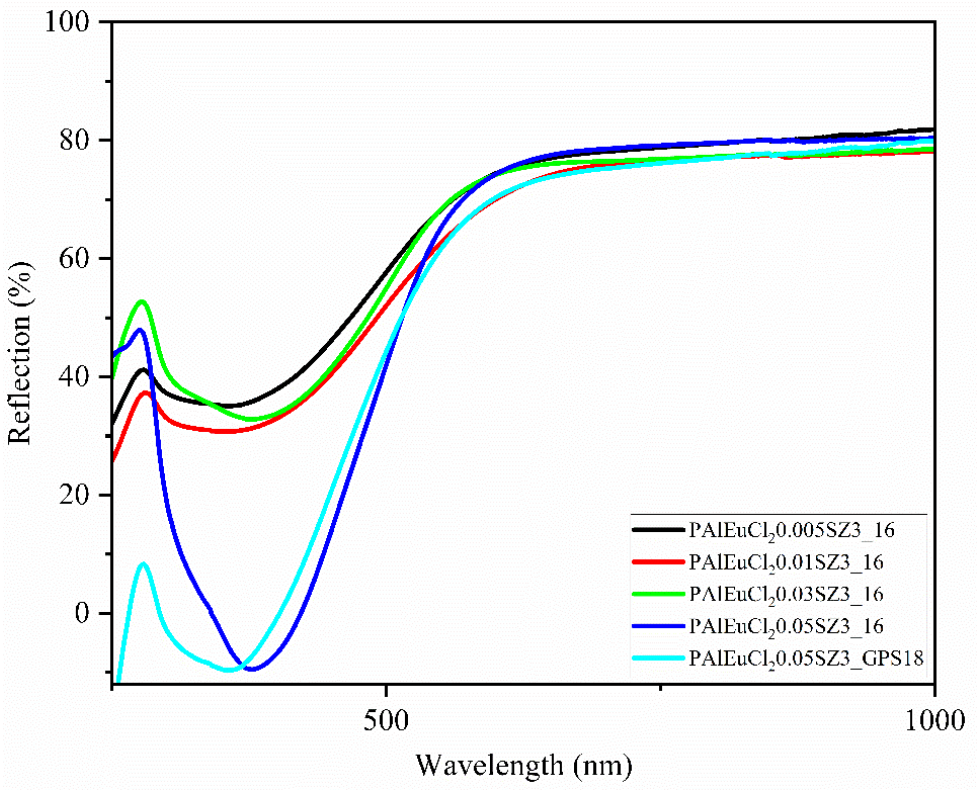

Figure IV.18. Optical absorption of the PAlEuCl$_2$YSZ3_16 (0.005 ≤ Eu:Si (Y) ≤ 0.05) and **PAlEuCl$_2$0.05SZ3_16** samples.

IV.3.4. Quantum efficiency

The term "quantum efficiency" refers to the effectiveness with which a material or device converts incident photons, which are particles of light, into usable electrical energy. In the context of optoelectronic devices, particularly photovoltaic systems like solar cells, the terms internal quantum efficiency (IQE) and external quantum efficiency (EQE) are frequently employed[43,53].

In contrast to previous investigations, changes occur between Eu^{2+}-doped β-SiAlON samples and Eu^{3+}-doped β-SiAlON samples. Their internal quantum efficiency ($\eta_{int.}$) and external quantum efficiency ($\eta_{ext.}$) are depicted in Figure IV.19((a), (b)) across different wavelengths ranging from 300 to 460 nm.

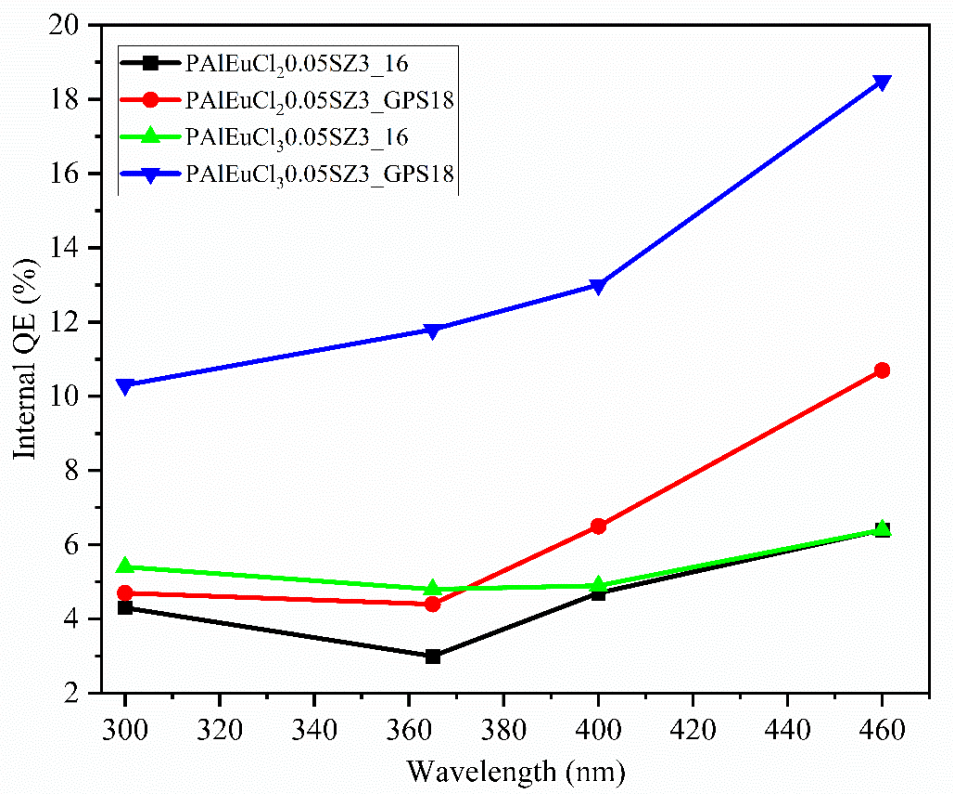

(a)

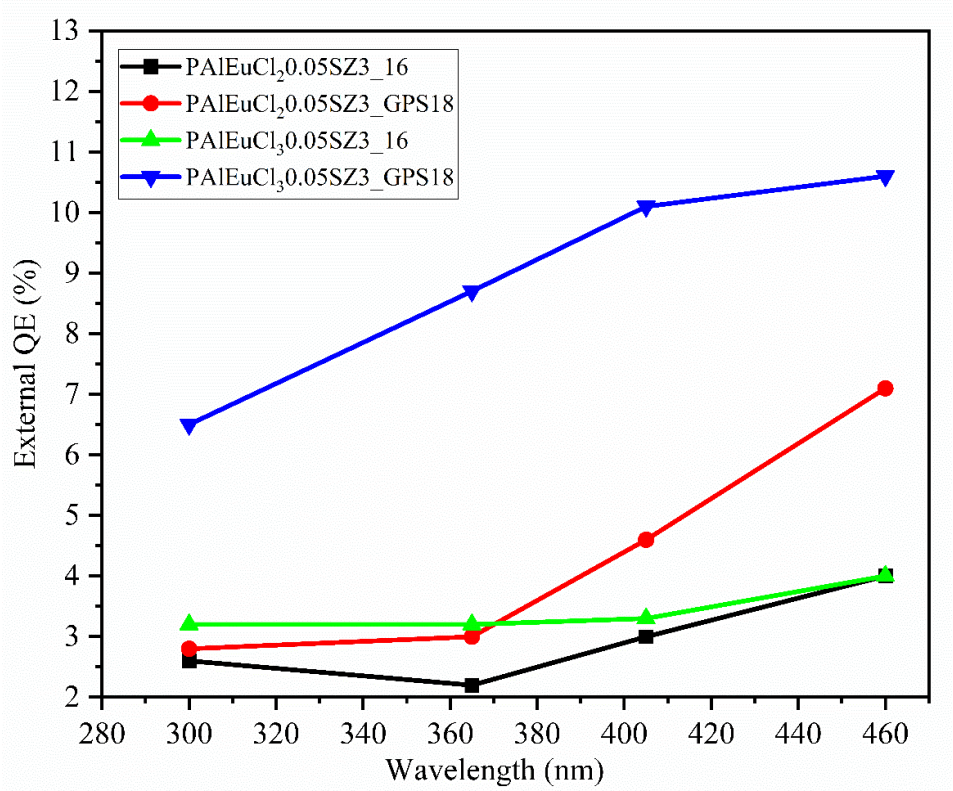

(b)

Figure IV.19. Quantum efficiency of the PAlEuCl$_x$0.05SZ3_16 (x = 2, 3) and PAlEuCl$_x$0.05SZ3_GPS (x = 2, 3) samples (a) Internal efficiency (b) External efficiency.

Both internal and external quantum efficiency exhibit an increasing trend at longer wavelengths, and the implementation of gas-pressure sintering (GPS) enhances the quantum efficiency.

The internal quantum efficiency of **PAlEuCl$_2$0.05SZ3_16** (Figure IV.19(a)) initially falls within the 4 to 6 % range and increases to 5 to 11 % after GPS. In contrast, the **PAlEuCl$_3$0.05SZ3_16** sample (Figure IV.19(a)) starts with an internal quantum efficiency of 5 to 6 %, rising to 10 to 18 % after GPS. These findings emphasize that samples doped with $EuCl_3$ exhibit higher internal quantum efficiency, indicating a higher presence of Eu^{2+} in $EuCl_3$ doped samples, fewer defects, or a predominant incorporation of Eu^{2+} into the host lattice of β-SiAlON. Regarding the external quantum efficiency (Figure IV.19(b)), **PAlEuCl$_2$0.05SZ3_16** shows a variation from 3% to 4%, increasing to 3 to 7 % after GPS. Similarly, **PAlEuCl$_3$0.05SZ3_16** has an initial external quantum efficiency of 3 to 4 %, which rises to 6 to 11 % after GPS. The observed quantum efficiency indicates that $EuCl_3$-doped ceramics exhibit higher quantum efficiency, and the impact of GPS is evident in the substantial increase.

IV.3.5. Extended X-ray Absorption Fine Structure (EXAFS)

Extended X-ray Absorption Fine Structure (EXAFS) is a spectroscopic method employed for the examination of the local atomic arrangement surrounding an absorbing atom within β-SiAlON:Eu^{2+} ceramics. This technique yields valuable insights into the distances separating the absorbing atom from its neighboring atoms, as well as the identity of these neighboring atoms[54,55].

The analysis of samples (**PAlEuCl$_2$0.05SZ3_16** and **PAlEuCl$_3$0.05SZ3_16**) demonstrates the presence of both Eu^{2+} and limited Eu^{3+} ions (Figure IV.20), resulting in the formation of β-SiAlON:Eu^{2+} ceramics. Remarkably, Figure IV.20 also illustrates that the high-temperature heating leads to the reduction of Eu^{3+} ions to Eu^{2+} (**PAlEuCl$_3$0.05SZ3_16**) to forms β-SiAlON:Eu^{2+}. The application of high-temperature heating and pressure induces the reduction and oxidation processes of rare-earth cations. In the **PAlEuCl20.05SZ3_16** sample, a minor fraction of Eu^{2+} ions undergo oxidation to Eu^{3+} owing to the stable oxidation state of Eu being +3. Similarly, $EuCl_3$-doped ceramics experience reduction, transforming Eu^{3+} into Eu^{2+}. This collective reduction and oxidation result in a higher concentration of Eu^{3+} cations in **PAlEuCl$_2$0.05SZ3_16**, while **PAlEuCl$_3$0.05SZ3_16** contains a lower amount of Eu^{3+} cations (Figure IV.20). This disparity could be a contributing factor to the observed lower luminescence in $EuCl_2$-doped samples, as the presence of Eu^{3+} is known to act as a luminescence killer[10,11].

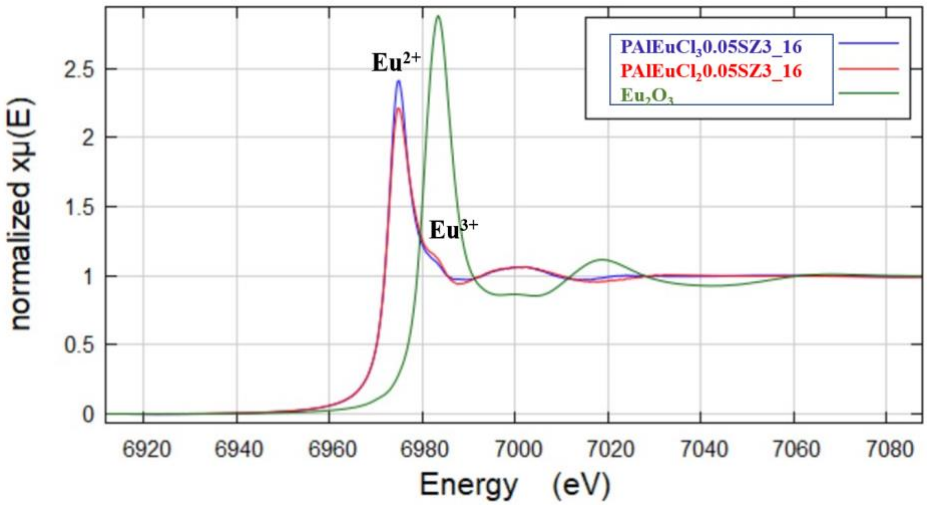

Figure IV.20. EXAFS information for β-SiAlON:Eu^{2+} and comparaison of Eu^{2+}, Eu^{3+} concentration in **PAlEuCl$_2$0.05SZ3_16** and **PAlEuCl$_3$0.05SZ3_16**.

IV.4. Conclusion

This chapter details the design process for low-oxygen β-SiAlON:Eu^{2+} ceramics using the **PAlSZ3_16** sample prepared in Chapter III where $EuCl_2$ and $EuCl_3$ serves as the dopant within the specified range ($0.005 \leq$ Eu:Si (Y) ≤ 0.05).

The chapter starts with the synthesis of the polymer without effect of the prior addition of $EuCl_2$ and $EuCl_3$ on the reaction between PSZ and the alane. Subsequent pyrolysis of as-prepared precursors at 1000 °C under ammonia, followed by a time-controlled exposure to air, results in amorphous samples in which the formation of Si-N, Al-O and Al-N bonds occurs. However, the presence of Eu in the amorphous network increases the oxygen content in the ammonia-treated samples most probably through the formation of Eu-O bonds. The further conventional heat treatment at 1600 °C resulted in the complete crystallization (at 1600 °C) into α-Si_3N_4, β-SiAlON, w-AlN and/or oxynitride-type, phases. The content of these phases depends on the Eu content ($0.005 \leq$ Eu:Si (Y) ≤ 0.05). The β-SiAlON phase content increased with increasing Eu content but it was limited to 75.6 % as determined for the **PAlEuCl$_2$0.05SZ3_16** sample. Only by investigating GPS on ammonia-treated samples at 1800 °C allowed to form almost pure β-SiAlON without the formation of both α-Si_3N_4 and AlN.

The microstructural analysis revealed the presence of the β-SiAlON phase in a cylindrical shape. SEM/CL emission confirmd the homogeneity of luminescence throughout the microstructure, and mapping illustrated a uniform distribution of Eu across the microstructure. The use of the GPS aided in elongating crystallite size, resulting in luminescence exclusively

from the β-SiAlON crystallite. This observation supports the confirmation of Eu solubility within the host lattice of the β-SiAlON crystallite.

Furthermore, the optical characteristics of the polymer-derived β-SiAlON:Eu^{2+} ceramics provided valuable insights into their luminescent properties. Under excitation at 410 or 460 nm, these ceramics emitted light in the green spectrum, specifically falling within the range of 542-554 nm. The occurrence of green emission suggests successful Eu incorporation within the host lattice (β-SiAlON), reinforcing the confirmation of Eu insertion within β-SiAlON.

Additionally, this study shows the reduction of Eu^{3+} to Eu^{2+} and elucidates its impact on the photoluminescent properties. Samples containing $EuCl_3$ exhibited higher emission intensity and higher quantum efficiency, highlighting the significant role of the reduction process in enhancing the luminescent characteristics of the Ceramics.

Bibliography

(1) Zhu, Y.; Liang, Y.; Liu, S.; Wu, X.; Xu, R.; Li, K. New Insight into the Structure Evolution and Site Preferential Occupancy of $Na_2Ba_6(Si_2O_7)(SiO_4)_2$: Eu^{2+} Phosphor by Cation Substitution Effect. *J. Alloys Compd.* **2017**, *698*, 49–59.

(2) Takeda, T.; Xie, R.-J.; Suehiro, T.; Hirosaki, N. Nitride and Oxynitride Phosphors for White LEDs: Synthesis, New Phosphor Discovery, Crystal Structure. *Prog. Solid State Chem.* **2018**, *51*, 41–51.

(3) Niu, J.; Saito, G.; Akiyama, T. A New Route to Synthesize β-SiAlON:Eu^{2+} Phosphors for White Light-Emitting Diodes. *Appl. Phys. Express* **2013**, *6* (4), 042105.

(4) Li, Y. Q.; Delsing, A. C. A.; De With, G.; Hintzen, H. T. Luminescence Properties of Eu^{2+} -Activated Alkaline-Earth Silicon-Oxynitride $MSi_2O_{2-\delta}N_{2+2/3\ \delta}$ (M = Ca, Sr, Ba): A Promising Class of Novel LED Conversion Phosphors. *Chem. Mater.* **2005**, *17* (12), 3242–3248.

(5) Xie, R.-J.; Hirosaki, N.; Li, H.-L.; Li, Y. Q.; Mitomo, M. Synthesis and Photoluminescence Properties of β-Sialon: Eu2+($Si_{6-z}Al_zO_zN_{8-z}$: Eu^{2+}): A Promising Green Oxynitride Phosphor for White Light-Emitting Diodes. *J. Electrochem. Soc.* **2007**, *154* (10), J314.

(6) Ryu, J. H.; Won, H. S.; Park, Y.-G.; Kim, S. H.; Song, W. Y.; Suzuki, H.; Yoon, C. Synthesis of Eu x Si 6- z Al z O z N 8- z Green Phosphor and Its Luminescent Properties. *Appl. Phys. A* **2009**, *95*, 747–752.

(7) Chen, W.-T.; Sheu, H.-S.; Liu, R.-S.; Attfield, J. P. Cation-Size-Mismatch Tuning of Photoluminescence in Oxynitride Phosphors. *J. Am. Chem. Soc.* **2012**, *134* (19), 8022–8025.

(8) Shannon, R. D. Revised Effective Ionic Radii and Systematic Studies of Interatomic Distances in Halides and Chalcogenides. *Acta Crystallogr. A* **1976**, *32* (5), 751–767.

(9) Mandal, H. New Developments in α-SiAlON Ceramics. *J. Eur. Ceram. Soc.* **1999**, *19* (13–14), 2349–2357.

(10) Gao, Y.; Murai, S.; Shinozaki, K.; Qiu, J.; Tanaka, K. Phase-Selective Distribution of Eu^{2+} and Eu^{3+} in Oxide and Fluoride Crystals in Glass-Ceramics for Warm White-Light-Emitting Diodes. *ACS Appl. Electron. Mater.* **2019**, *1* (6), 961–971.

(11) Li, S.; Wang, L.; Tang, D.; Cho, Y.; Liu, X.; Zhou, X.; Lu, L.; Zhang, L.; Takeda, T.; Hirosaki, N. Achieving High Quantum Efficiency Narrow-Band β-Sialon: Eu^{2+} Phosphors for High-Brightness LCD Backlights by Reducing the Eu^{3+} Luminescence Killer. *Chem. Mater.* **2018**, *30* (2), 494–505.

(12) Zavala-Sanchez, L. A.; Hirata, G. A.; Novitskaya, E.; Karandikar, K.; Herrera, M.; Graeve, O. A. Distribution of Eu^{2+} and Eu^{3+} Ions in Hydroxyapatite: A Cathodoluminescence and Raman Study. *ACS Biomater. Sci. Eng.* **2015**, *1* (12), 1306–1313.

(13) Guangsheng, F. U.; Zizhong, Z. H. U.; Yong, Y.; Zhiping, Y.; Panlai, L. I. Effect of Eu3+ Contents on Structure and Luminescence Properties of $Na_3Bi_{2-x}(PO_4)_3$:XEu^{3+} and $Na_3Bi_{1-x}(PO_4)_2$: XEu^{3+} Phosphors. *J. Rare Earths* **2016**, *34* (9), 857–862.

(14) Li, S.; Wang, L.; Tang, D.; Cho, Y.; Liu, X.; Zhou, X.; Lu, L.; Zhang, L.; Takeda, T.; Hirosaki, N. Achieving High Quantum Efficiency Narrow-Band β-Sialon: Eu^{2+} Phosphors for High-Brightness LCD Backlights by Reducing the Eu^{3+} Luminescence Killer. *Chem. Mater.* **2018**, *30* (2), 494–505.

(15) Jiang, J.-X.; Wang, P.-L.; He, W.-B.; Chen, W.-W.; Zhuang, H.-R.; Cheng, Y.-B.; Yan, D.-S. Eu Stabilized α-Sialon Ceramics Derived from SHS-Synthesized Powders. *Mater. Lett.* **2005**, *59* (2–3), 205–209.

(16) Chen, X.; Gan, L.; Zhang, Z.; Lu, P.; Zeng, X.; Zhang, L.; Yao, H.; Xu, F.; Zhao, J. Ca-α-SiAlON: Eu Phosphors: Oxidation States, Energy Transfer, and Emission Enhancement by Incorporation-Aimed Surface Engineering. *ACS Appl. Mater. Interfaces* **2017**, *9* (36), 30982–30991.

(17) Collins, J. Non-Radiative Processes in Crystals and in Nanocrystals. *ECS J. Solid State Sci. Technol.* **2015**, *5* (1), R3170.

(18) Hirosaki, N.; Xie, R.-J.; Kimoto, K.; Sekiguchi, T.; Yamamoto, Y.; Suehiro, T.; Mitomo, M. Characterization and Properties of Green-Emitting β-SiAlON: Eu2+ Powder Phosphors for White Light-Emitting Diodes. *Appl. Phys. Lett.* **2005**, *86* (21).

(19) Tada, S.; Mallmann, M. D.; Takagi, H.; Iihama, J.; Asakuma, N.; Asaka, T.; Daiko, Y.; Honda, S.; Nishihora, R. K.; Machado, R. A. F. Low Temperature in Situ Formation of Cobalt in Silicon Nitride toward Functional Nitride Nanocomposites. *Chem. Commun.* **2021**, *57* (16), 2057–2060.

(20) Asakuma, N.; Tada, S.; Kawaguchi, E.; Terashima, M.; Honda, S.; Nishihora, R. K.; Carles, P.; Bernard, S.; Iwamoto, Y. Mechanistic Investigation of the Formation of Nickel Nanocrystallites Embedded in Amorphous Silicon Nitride Nanocomposites. *Nanomaterials* **2022**, *12* (10), 1644.

(21) Garcia, J.; Allen, M. J. Developments in the Coordination Chemistry of Europium(II). *Eur. J. Inorg. Chem.* **2012**, *2012* (29), 4550–4563.

(22) Kocman, V.; Di Mauro, G. M.; Veglia, G.; Ramamoorthy, A. Use of Paramagnetic Systems to Speed-up NMR Data Acquisition and for Structural and Dynamic Studies. *Solid State Nucl. Magn. Reson.* **2019**, *102*, 36–46.

(23) Koppe, J.; Pell, A. J. Structure Determination and Refinement of Paramagnetic Materials by Solid-State NMR. *ACS Phys. Chem. Au* **2023**, *3* (5), 419–433.

(24) Lee, M.-H.; Jung, W.-S. Synthesis and Luminescence Spectra of Two Europium (II) Aluminates, $EuAl_2O_4$ and $EuAl_{12}O_{19}$. *Ceram. Int.* **2016**, *42* (2), 3113–3120.

(25) Bünzli, J.-C. Europium in the Limelight. *Nat. Chem.* **2010**, *2* (8), 696–696.

(26) Wang, C.-Y.; Takeda, T.; Melvin Ten Kate, O.; Funahashi, S.; Xie, R.-J.; Takahashi, K.; Hirosaki, N. New Deep-Blue-Emitting Ce-Doped $A_{4-m}B_nC_{19+2m}X_{29+m}$ (A = Sr, La; B =

Li; C = Si, Al; X = O, N; $0 \leq m \leq 1$; $0 \leq n \leq 1$) Phosphors for High-Color-Rendering Warm White Light-Emitting Diodes. *ACS Appl. Mater. Interfaces* **2019**, *11* (32), 29047–29055.

(27) Mitomo, M.; Uenosono, S. Gas Pressure Sintering of Silicon Nitride. *J. Mater. Sci.* **1991**, *26* (14), 3940–3944.

(28) Wang, Q.; Ge, Y.; Chen, Y.; Sun, S.; Tian, Z.; Zhang, J. SHS of Eu2+-Doped β-SiAlON Phosphors: Impacts of N_2 Pressure and Si Particle Size. *Ceram. Int.* **2017**, *43* (5), 4456–4461.

(29) Mitomo, M.; Uenosono, S. Microstructural Development During Gas-Pressure Sintering of A-Silicon Nitride. *J. Am. Ceram. Soc.* **1992**, *75* (1), 103–107.

(30) Ramesh, R.; Pomeroy, M. J.; Chu, H.; Datta, P. K. Effect of Gaseous Environment on the Corrosion of β-Sialon Materials. *J. Eur. Ceram. Soc.* **1995**, *15* (10), 1007–1014.

(31) LEE, D.-D.; KANG, S.-J. L.; YOON, D. N. Mechanism of Grain Growth and α-β'Transformation During Liquid-Phase Sintering of B′-Sialon. *J. Am. Ceram. Soc.* **1988**, *71* (9), 803–806.

(32) Shaler, A. J.; Wulff, J. Mechanism of Sintering. *Ind. Eng. Chem.* **1948**, *40* (5), 838–842.

(33) Acikbas, N. C.; Yurdakul, H.; Mandal, H.; Kara, F.; Turan, S.; Kara, A.; Bitterlich, B. Effect of Sintering Conditions and Heat Treatment on the Properties, Microstructure and Machining Performance of α-β-SiAlON Ceramics. *J. Eur. Ceram. Soc.* **2012**, *32* (7), 1321–1327.

(34) Camuşcu, N.; Thompson, D. P.; Mandal, H. Effect of Starting Composition, Type of Rare Earth Sintering Additive and Amount of Liquid Phase on Sialon Transformation. **1997**.

(35) Takahashi, K.; Yoshimura, K.; Harada, M.; Tomomura, Y.; Takeda, T.; Xie, R.-J.; Hirosaki, N. On the Origin of Fine Structure in the Photoluminescence Spectra of the β-Sialon: Eu^{2+} Green Phosphor. *Sci. Technol. Adv. Mater.* **2012**.

(36) Liu, L.; Xie, R.-J.; Hirosaki, N.; Takeda, T.; Zhang, C.; Li, J.; Sun, X. Photoluminescence Properties of β-SiAlON:Yb^{2+} , a Novel Green-Emitting Phosphor for White Light-Emitting Diodes. *Sci. Technol. Adv. Mater.* **2011**, *12* (3), 034404.

(37) Smet, P. F.; Moreels, I.; Hens, Z.; Poelman, D. Luminescence in Sulfides: A Rich History and a Bright Future. *Materials* **2010**, *3* (4), 2834–2883.

(38) Xie, R.-J.; Hirosaki, N. Silicon-Based Oxynitride and Nitride Phosphors for White LEDs—A Review. *Sci. Technol. Adv. Mater.* **2007**, *8* (7–8), 588.

(39) Chung, J. H.; Ryu, J. H. Photoluminescence and LED Application of β-SiAlON: Eu2+ Green Phosphor. *Ceram. Int.* **2012**, *38* (6), 4601–4606.

(40) Gao, Y.; Iihama, J.; Hamana, D.; Iwasaki, R.; Honda, S.; Asaka, T.; Kumari, M.; Hayakawa, T.; Bernard, S.; Thomas, P.; Iwamoto, Y. Polymer-derived B-SiAlON:Eu^{2+} Phosphors. *Int. J. Appl. Ceram. Technol.* **2023**, *20* (2), 768–779.

(41) GREEN, A.; XIE, R.-J.; HIROSAKI, N.; LI, H.-L.; LI, Y.; MITOMO, M. Synthesis and Photoluminescence Properties of β-Sialon: Eu^{2+} ($Si_{6-Z}Al_zO_zN_{8-z}$: Eu^{2+}). *J. Electrochem. Soc.* **2007**, *154* (10).

(42) Xie, R.-J.; Hirosaki, N.; Li, H.-L.; Li, Y. Q.; Mitomo, M. Synthesis and Photoluminescence Properties of β-Sialon: Eu^{2+}($Si_{6-z}Al_zO_zN_{8-z}$:Eu^{2+}): A Promising Green Oxynitride Phosphor for White Light-Emitting Diodes. *J. Electrochem. Soc.* **2007**, *154* (10), J314.

(43) Armin, A.; Zarrabi, N.; Sandberg, O. J.; Kaiser, C.; Zeiske, S.; Li, W.; Meredith, P. Limitations of Charge Transfer State Parameterization Using Photovoltaic External Quantum Efficiency. *Adv. Energy Mater.* **2020**, *10* (41), 2001828.

(44) Weber, M. J. Luminescence Decay by Energy Migration and Transfer: Observation of Diffusion-Limited Relaxation. *Phys. Rev. B* **1971**, *4* (9), 2932–2939.

(45) Wang, C.-Y.; Takeda, T.; ten Kate, O. M.; Xie, R.-J.; Takahashi, K.; Hirosaki, N. Synthesis and Photoluminescence Properties of a Phase Pure Green-Emitting Eu Doped JEM Sialon (LaSi6-zAl1+zN10-zOz, z 1) Phosphor with a Large Red-Shift of Emission and Unusual Thermal Quenching Behavior. *J. Mater. Chem. C* **2016**, *4* (43), 10358–10366.

(46) Suda, Y.; Kamigaki, Y.; Miyagawa, H.; Takeda, T.; Takahashi, K.; Hirosaki, N. Luminescence and Afterglow Due to Defects in β-SiAlON Crystal Powder. *J. Phys. Appl. Phys.* **2020**, *53* (16), 165108.

(47) Wang, F.; Guo, J.; Wang, S.; Qu, B.; Song, Z.; Zhang, S.; Geng, W.-T.; Liu, Q. Yellow Persistent Luminescence and Electronic Structure of Ca-α-Sialon: Eu^{2+}. *J. Alloys Compd.* **2020**, *821*, 153482.

(48) Wang, Z.; Ye, W.; Chu, I.-H.; Ong, S. P. Elucidating Structure–Composition–Property Relationships of the β-SiAlON:Eu $^{2+}$ Phosphor. *Chem. Mater.* **2016**, *28* (23), 8622–8630.

(49) Takeda, T.; Funahashi, S.; Takahashi, K.; Xie, R.-J.; Hirosaki, N. Structure Elucidation of Luminescent Centers in Green Emitting Eu^{2+} Doped $Si_{6-Z}Al_zO_zN_{8-z}$ Phosphors. *Scr. Mater.* **2022**, *207*, 114238.

(50) Zhu, X. W.; Masubuchi, Y.; Motohashi, T.; Kikkawa, S.; Takeda, T. Synthesis and Photoluminescence of Blue-Emitting 15R-Sialon: Eu^{2+} Phosphors. *J. Alloys Compd.* **2010**, *496* (1–2), 407–412.

(51) Suda, Y.; Kamigaki, Y.; Miyagawa, H.; Takeda, T.; Takahashi, K.; Hirosaki, N. Effects of Eu2+ on the Luminescence and Afterglow That Arise from Defects in β-SiAlON: Eu2+. *J. Phys. Appl. Phys.* **2020**, *54* (6), 065102.

(52) Michalik, D.; Pawlik, T.; Kukliński, B.; Lazarowska, A.; Leśniewski, T.; Barzowska, J.; Mahlik, S.; Grinberg, M.; Adamczyk, B.; P\lawecki, M. Dopant Concentration Induced Optical Changes in Ca, Eu-α-Sialon. *Crystals* **2017**, *7* (11), 342.

(53) Shim, J.-I. Internal Quantum Efficiency. In *III-Nitride Based Light Emitting Diodes and Applications*; Seong, T.-Y., Han, J., Amano, H., Morkoç, H., Eds.; Topics in Applied Physics; Springer Singapore: Singapore, 2017; Vol. 133, pp 163–207.

(54) Sjöberg, J.; Ericsson, T.; Lindqvist, O. Local Structure of B′-Sialons: An EXAFS Study Study. *J. Mater. Sci.* **1992**, *27* (21), 5911–5915.

(55) Cole, M.; O'Reilly, K. P. J.; Redington, M.; Hampshire, S. EXAFS Study of a Hot-Pressed ??-Sialon Ceramic Containing Erbium as the Modifying Cation. *J. Mater. Sci.* **1991**, *26* (19), 5143–5148.

Chapter V.

Low oxygen content β-SiAlON as host materials for blue-emitting Ce^{3+}-based phosphors

V.1. Introduction

Similar to Eu^{2+} investigated in Chapter IV, the emission of Ce^{3+} is characteristic of broad band and it is strongly related to the crystal structure of host lattices, which makes it possible to tailor and modify the luminescent properties by selecting different host materials. The Ce^{3+} ion has a very simple electron configuration in the ground and excited states, $4f^1$ and $5d^1$, respectively. The $4f^1$ ground state is split up in a doublet ($^2F_{7/2}$ and $^2F_{5/2}$) with an energy difference of about 2000 cm^{-1}[1]. The efficient absorption and luminescent properties of Ce^{3+} are due to their fully allowed 4f → 5d transitions. The emission of Ce^{3+} in most host lattices (e.g., oxides, fluorides, or borates) is usually in the ultraviolet (UV) region. However, it is significantly red-shifted in oxynitride/nitrides. For example, blue, yellow, and even red colors were seen in Ce^{3+}-doped Y–Si–O–N[2] and α-SiAlON[3,4], $MSi_2O_2N_2$ (M = Ca, Sr, Ba)[5], and $CaSiN_2$[6], respectively.

β-SiAlON:Ce^{3+}, known to emit in the blue spectrum, has emerged as a promising material for wavelength conversion in pc-WLEDs utilizing near-UV chips as the primary light source[7–9]. However, the reports investigating β-SiAlON as a host material of Ce^{3+} are quite limited especially compared to α-SiAlON[8–12]. Notably, α-SiAlON has large interstitial sites in the crystal structure to accommodate large rare-earth cations (Ce^{3+}) for charge compensation, while β-SiAlON has no apparent crystallographic sites for rare-earth cations (Ce^{3+})[4,13–16]. Thus, only a tiny quantity of dopants can be accommodated into the host lattice; thereby, the low dopant content leads to a smaller number of photons involved in the luminescence process[17].

The primary interest of the present chapter is to explore the polymer-derived ceramic (PDC) route to prepare β-SiAlON:Ce^{3+} phosphors. Herein, the low oxygen content β-SiAlON compounds prepared in Chapter III serve as host for Ce^{3+} cations through the controlled introduction of $CeCl_3$ in **PAlSZ3** as we did in Chapter IV for $EuCl_2$ and $EuCl_3$. We varied the Ce:Si ratio from 0.005 to 0.05 - thereby the Ce^{3+} content - in the early stage of the process (i.e., polymer synthesis) and the series of as-prepared precursors named **PAlCeYSZ3** with Y = Ce:Si has been pyrolyzed in flowing ammonia up to 1000 °C. Ammonia-treated samples have been then heat-treated in flowing nitrogen up to 1600 °C as done in Chapter III and Chapter IV. We have also explored the Gas Pressure Sintering (GPS) up to 1800 °C Chapter IV in order to adjust the phase composition; thereby the optical properties.

As reported in previous chapters, the elaboration of these compounds has been investigated using complementary characterization from the precursors to the final materials. As in Chapter IV, we also conduct a comprehensive evaluation of the optical properties. We particularly discuss the effects of Ce^{3+} concentration and heat-treatment process on the emission.

V.2. Results and Discussion

V.2.1. Synthesis and Characterization of SiAlON:Ce^{3+} precursors

The introduction of $CeCl_3$ in **PAlSZ3** (see Chapter III) has been achieved through different Ce:Si content ($0.005 \leq Ce:Si \leq 0.05$). Four representative polymers, denoted as **PAlCeYSZ3** (with Y representing the Ce:Si ratio), were synthesized to examine the effects of the Ce concentration on the structure of β-SiAlON and on the luminescence properties of the derived phosphors. Their synthesis is described in Chapter II. It occurs in toluene and it consists to first mix $CeCl_3$ and PSZ according to the targeted Ce:Si ratio before adding alane while maintaining a fixed Si:Al ratio of 3 which has been selected in Chapter III. After reaction and solvent extraction, as-synthesized samples are mainly white solid compounds at room temperature.

Elemental analysis confirms – with the representative **PAlCe0.05SZ3** sample – that the measured Si:Al ratio fits with that one fixed before the reaction (3), as specified in Table V.1.

Table V.1. Elemental analysis for Ce doped polymers (PAlCeYSZ3; $0.005 \leq Y \leq 0.05$).

Samples	Si	Al	O	N	C	H	Ce	Cl	Empirical Formula**
	in wt. %								
PAlSZ3	35.5	11.4	1.0	16.6	30.4	5.1			$Si_{1.0}Al_{0.3}N_{0.9}C_{2.0}H_{4.0}$
PAlCe0.05SZ3	28.1	8.9	0.9	16.5	26.5	8.0	7.0	4.1	$Si_{1.0}Al_{0.3}N_{1.2}C_{2.2}H_{7.9}Ce_{0.05}Cl_{0.01}$
PAlCe0.03SZ3	*	*	1.0	16.6	*	8.0	*	*	-
PAlCe0.01SZ3	*	*	1.0	17.9	*	8.2	*	*	-
PAlCe0.005SZ3	*	*	1.6	18.9	*	6.2	*	*	-

** not measured; ** reference to $Si_{1.0}$ and oxygen content omitted because of a content < 2wt. %*

Thus, as a first approximation, we can confirm that the reaction of alane with PSZ is not affected by the prior addition of $CeCl_3$ in PSZ. In addition, the results presented in Table V.1 indicate that the oxygen content in all samples is minimal and comparable to the pristine polymer (**PAlSZ3**, $Si_{1.0}Al_{0.3}N_{0.9}C_{2.0}H_{4.0}$). The N content is similar in **PAlCe0.05SZ3** compared to that one measured in **PAlSZ3** upon introduction of the highest Ce^{3+} content (**PAlCe0.05SZ3**). However, the N:Si ratio is much more important in **PAlCe0.05SZ3** (N:Si = 1.2) than in **PAlSZ3** (N:Si = 0.9). The N content then significantly increases (**PAlCe0.005SZ3**) with the decrease of the Ce content. Thus, the addition of $CeCl_3$ seems to affect the nitrogen-containing ligands bearing by **PAlSZ3** while the oxygen content stays very low.

Nitrogen-containing ligands are of two types in **PAlCe0.05SZ3**: silylamino groups (Si-N(H)-Si) bearing by PSZ and $N(CH_3)_2C_2H_5$ units present in alane which are introduced in the structure of PSZ (see Chapter III) after the mixing with $CeCl_3$. Harada et al. reported that the absorption spectra of pyridine-based ligands drastically changed in the presence of Ce^{3+} which was ascribed to metal-ligand interactions[18]. Bartoli et al. described that the $CeCl_3$ shows a strong affinity toward "hard bases" such as oxygen and nitrogen donor ligands[19]. Thus, we tentatively suggested that Ce^{3+} interacts with nitrogen-containing ligands in our system to favor the enrichment of precursor with nitrogen. Besides, the atomic Cl:Ce ratio calculated in **PAlCe0.05SZ3** matches that of $CeCl_3$ and the measured Si:Ce ratio is 0.05. Therefore, we can speculate that chloride ions are involved in reactions with reactive groups bearing by PSZ; most probably those containing nitrogen elements.

We then investigated FTIR spectroscopy of these samples. Their corresponding spectra are presented in Figure V.1.

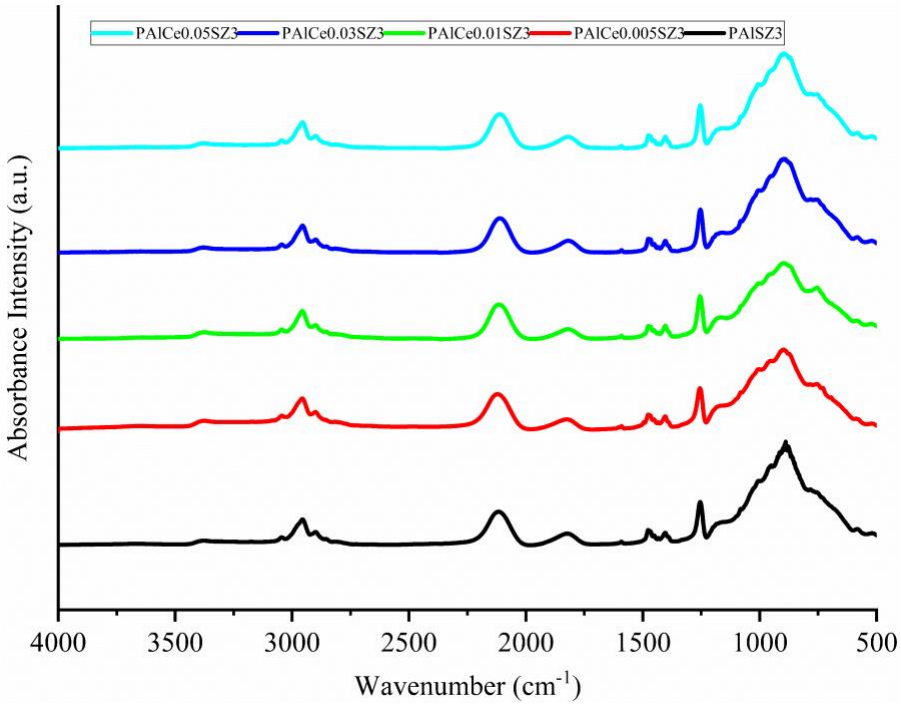

Figure V.1. FTIR spectra of PAlCeYSZ3 ($0.005 \leq Y \leq 0.05$) polymers.

The FTIR spectra have been normalized to the band of the methyl groups (1251 cm^{-1}), which are not expected to be inert during the synthesis of precursors. The FTIR spectra of PAlCeYSZ3 ($0.005 \leq Si:Ce \leq 0.05$) encompass the characteristic FTIR bands identified in **PAlSZ3** (Figure V.1 and discussed in Chapter III) without obvious changes in the band positions and intensities in the considered wavenumber range. A same observation can be made for solid-state NMR spectroscopy (Figure V.2) focused on the **PAlCe0.05SZ3** sample with the highest Ce content:

it does not allow to distinguish any obvious differences in terms of chemical environments around carbon, silicon, aluminum and nitrogen elements with the **PAlSZ3** sample.

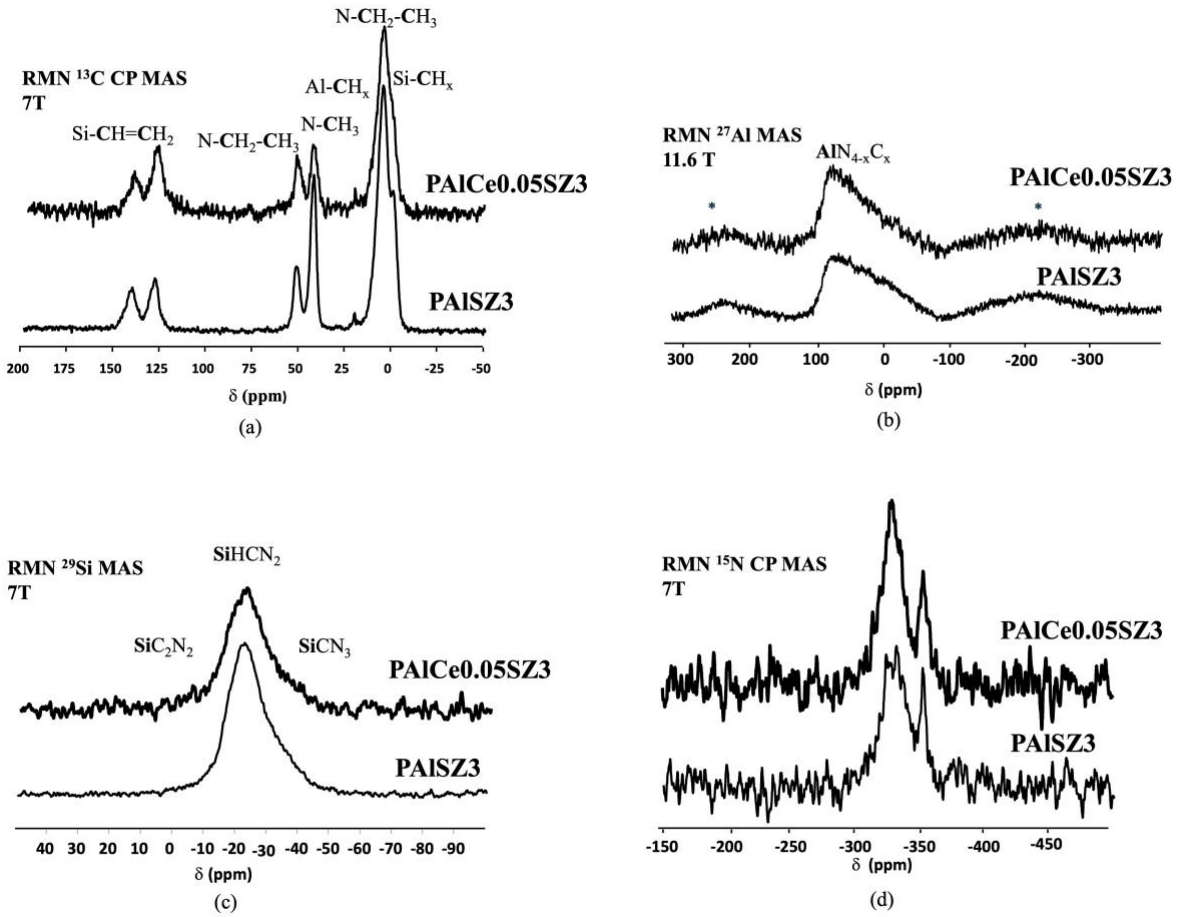

Figure V.2. Solid-state NMR spectra of **PAlCe0.05SZ3**: (a) ^{13}C CP MAS, (b) ^{27}Al MAS (* indicate spinning sidebands), (c) ^{29}Si MAS, (d) ^{15}N CP MAS. *Comparison is made with corresponding NMR spectra of **PAlSZ3** (Chapter III).*

Based on the elemental analysis, we speculated that $CeCl_3$ introduced in **PAlSZ3** preferentially interacts with nitrogen atoms because of their lone pair of electrons. However, FTIR and ^{15}N CP MAS NMR spectroscopies could not allow observing such an interaction (compared with data gained from **PAlSZ3**). Detecting how cerium (Ce) affects the chemical environment of polymers is indeed tricky because cerium behaves like a magnet. Polymers with heavy metals often show fuzzy signals in NMR observation because of this magnetic behavior. The magnetism makes the signals spread out, making it hard to see sharp peaks and learn detailed information about the chemical surroundings of the polymer[20,21].

V.2.2. Precursor-to-β-SiAlON:Ce^{3+} conversion

This section is divided into three segments. The thermo-chemical transformation of precursors as powders subjected to gradual heating from room temperature to 1000 °C in flowing ammonia

is firstly explored. Then, the microstructural evolution of ammonia-treated samples is investigated up to 1600 °C in flowing nitrogen via a conventional heat-treatment procedure as applied in Chapter III. The microstructural evolution of ammonia-treated samples has been also investigated by GPS as in Chapter IV.

V.2.2.1. Thermo-chemical transformation of precursors in flowing ammonia

Solid-state NMR has been achieved on the reference **PAlCe0.05SZ3_10** sample. A broad signal characterizes the ^{27}Al NMR spectrum of **PAlCe0.05SZ3_10** (Figure V.3) which indicates both the presence of $AlN_{4-x}O_x$ ($0 \leq x \leq 4$) and AlO_4 environments as in **PAlSZ3_10**; oxygen which is identified in the sample by elemental analysis (Table V.2).

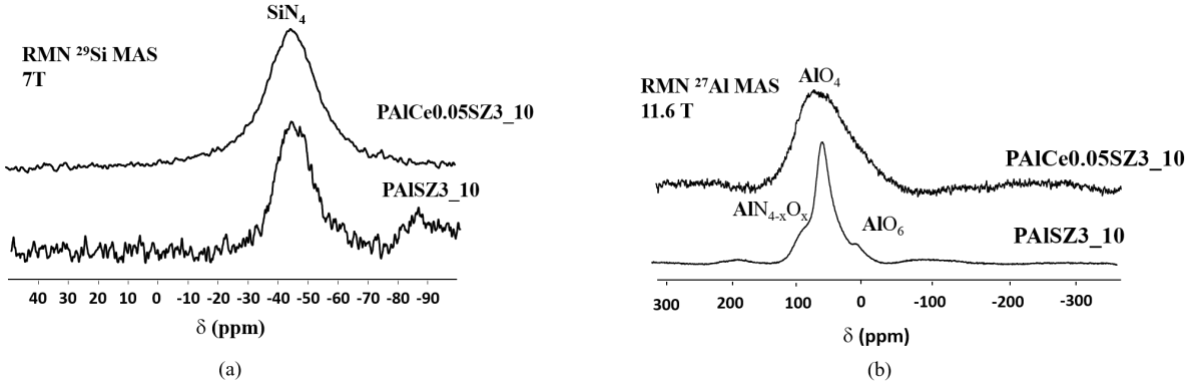

Figure V.3. Solid-state NMR spectra of **PAlCe0.05SZ3_10**: (a) ^{29}Si NMR and (b) ^{27}Al NMR. *Comparison is made with corresponding NMR spectra of **PAlSZ3_10** (Chapter III).*

However, the contribution of $AlN_{4-x}O_x$ ($0 \leq x \leq 4$) seems to be higher in **PAlCe0.05SZ3_10** than in **PAlSZ3_10** and AlO_6 environments characterizing the presence of alumina are absent. Thus, we suggest that the presence of Ce tends to enrich the nitrogen environment around Al. This is also the observation that can be made for Si. Indeed, the presence of Ce in the **PAlCe0.05SZ3_10** broadens and shifts the main signal in the corresponding ^{29}Si NMR spectrum which tends to integrate SiN_4 unit; a confirmation that Ce introduced in the early stage of the process tends to enrich the Si environment into nitrogen although the nitrogen content of the sample is comparable to than one measured in **PAlSZ3_10** (Table V.2). However, Table V.2 highlights that there is a tendency (although the differences are poor) that the nitrogen content increases with the increase of the Ce:Si ratio in the compound whereas it decreased in the corresponding precursors (see Table V.1). Besides, the Si:Al ratio measured in **PAlCe0.05SZ3_10** is retained if we compare to **PAlCe0.05SZ3** (= 0.3). Thus, we suggest that $CeCl_3$ acts as a catalyst for some reactions occurring during the precursor-to-ceramic conversion upon heat-treatment to 1000 °C in flowing ammonia. It is indeed reported that it

represents a selective Lewis acid for various activated bonds in organic synthesis; in particular in the cleavage of the Si-O bonds under neutral conditions[22]. Most probably, it could activate radical reactions to further lead to an enrichment of the Si environment to nitrogen. In addition, it is clear that the oxygen content in Ce-doped ceramics is higher than in **PAlSZ3_10**. Thus, the addition of Ce^{3+} in the early stage of the process has a clear effect on the ligands present in the material prepared at 1000 °C. X-ray diffraction confirms this suggestion.

Table V.2. Elemental analysis of the PAlCeYSZ3_10, ($0.005 \leq Y \leq 0.05$) samples.

Samples	Si	Al	O	N	C	H	Ce	Cl	Empirical Formula**
	in wt. %								
PAlSZ3_10	*	*	4.5	29.8	1.4	0.1	*		*
PAlCe0.05SZ3_10	35.3	12.3	6.2	29.6	1.6	0.8	9.2	5.0	$Si_{1.0}Al_{0.4}O_{0.4}N_{1.3}Ce_{0.05}Cl_{0.1}$
PAlCe0.03SZ3_10	*	*	6.1	29.2	*	0.8	*		*
PAlCe0.01SZ3_10	*	*	6.0	29.1	*	0.8	*		*
PAlCe0.005SZ3_10	*	*	6.0	28.7	*	1.3	*		*

** not measured; ** reference to* $Si_{1.0.}$

In Chapter III, we observed that the **PAlSZ3_10** sample exhibited amorphous nature ceramics. This amorphous structure was retained by doping the **PAlSZ3_10** sample with Eu^{2+} and Eu^{3+}. By doping with Ce^{3+} – whatever the Ce:Si ratio – the XRD patterns of PAlCeYSZ3_10 ($0.005 \leq Y \leq 0.05$) samples drastically changed (Figure V.4).

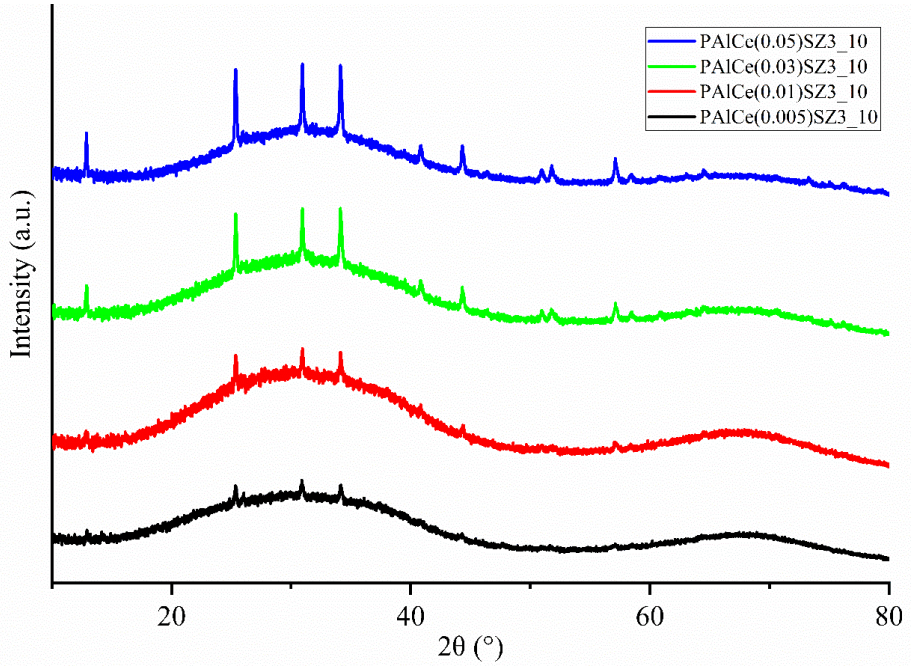

Figure V.4. XRD patterns of PAlCeYSZ3_10 ($0.005 \leq Y \leq 0.05$).

The PAlCeYSZ3_10 ($0.005 \leq Y \leq 0.05$) samples display the characteristics of the presence of an amorphous phase along with the identification of peaks characteristic to the CeClO phase (PDF 04-013-3145; Tetragonal space group P4/nmm)[23]. The peaks intensity increases with Ce:Si ratio. Therefore, contrarily to Eu^{2+}- and Eu^{3+}-doped samples, Ce^{3+}-doped samples tend to segregate by crystallizing at relatively low temperature.

This will have probably an effect on the high-temperature behaviour of these samples. This is investigated in the following section.

V.2.2.2. Conventional heat-treatment of ammonia-treated samples up to 1600 °C in flowing nitrogen

By increasing the temperature to 1600 °C in flowing nitrogen, the ^{29}Si MAS and ^{27}Al NMR spectra of **PAlCe0.05SZ3_16**, depicted in Figure V.5, exhibits distinct narrow signals, which can be attributed to **Si**N_4 (-48 ppm) and **Al**N_4 (115 ppm) environments similar to those in **PAlSZ3_16**.

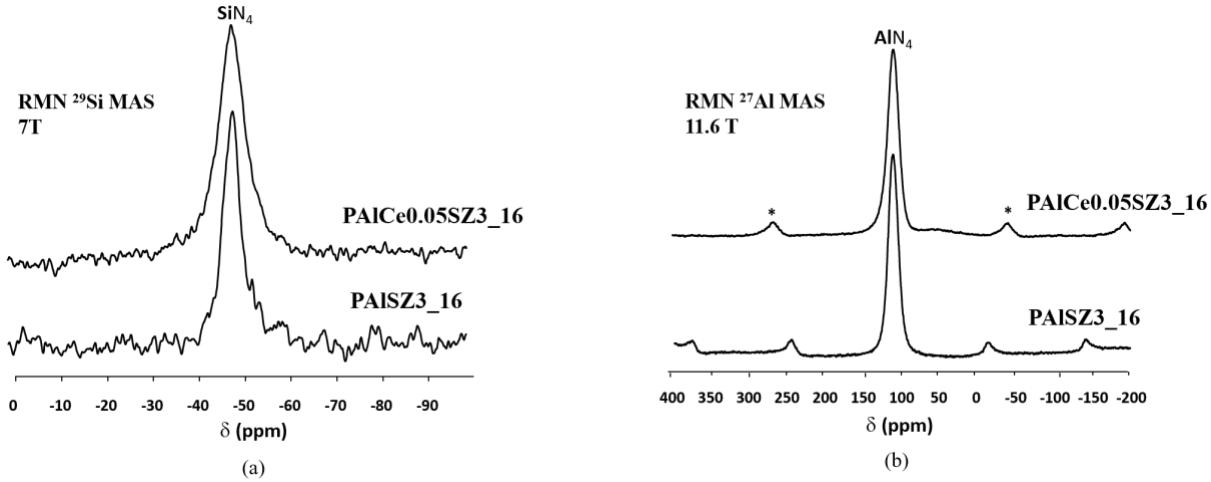

Figure V.5. Solid-state NMR spectra of **PAlCe0.05SZ3_16**: (b) ^{29}Si NMR (b) ^{27}Al (* indicate spinning sidebands). *Comparison is made with corresponding NMR spectra of **PAlSZ3_16** NMR spectra (Chapter III).*

Elemental analysis (Table V.3) confirms the presence of nitrogen and also shows that the sample is composed of oxygen. The calculated Si:Al ratio fits with the fixed one (= 3). X-ray diffraction analysis was done to monitor the structural changes occurring in PAlCeYSZ3_10 ($0.005 \leq Y \leq 0.05$) samples upon heat-treatment up to 1600 °C. The XRD patterns of PAlCeYSZ3_14 ($0.005 \leq Y \leq 0.05$) and PAlCeYSZ3_16 ($0.005 \leq Y \leq 0.05$) samples are depicted in Figure V.6 and Figure V.7 respectively.

Upon reaching a temperature of 1400 °C (Figure V.6), the XRD pattern reveals the appearance of crystalline phases. In case of the lowest Ce:Si ratio, we observed mainly the β-SiAlON[24]

(PDF 01-077-0755) phase whereas increasing the Ce:Si ratio ($0.01 \leq Y \leq 0.05$), the amount of secondary phases (α-Si_3N_4, w-AlN) increases. A new phase appears for highest Ce:Si ratio, which has been identified as JEM-SiAlON (PDF 01-086-0359; Orthorhombic, space group Pbcn)[25].

Table V.3. Elemental analysis of the PAlCeYSZ3_16 ($0.005 \leq Y \leq 0.05$) samples.

Samples	Si	Al	O	N	Ce	Empirical Formula*
	in wt. %					
PAlSZ3_16	47.9	16.7	3.8	31.4	-	$Si_{1.0}Al_{0.4}O_{0.1}N_{1.3}$
PAlCe0.05SZ3_16	39.5	13.1	2.3	32.7	10.7	$Si_{1.0}Al_{0.4}O_{0.1}N_{1.3}Ce_{0.07}$

** reference to $Si_{1.0}$*

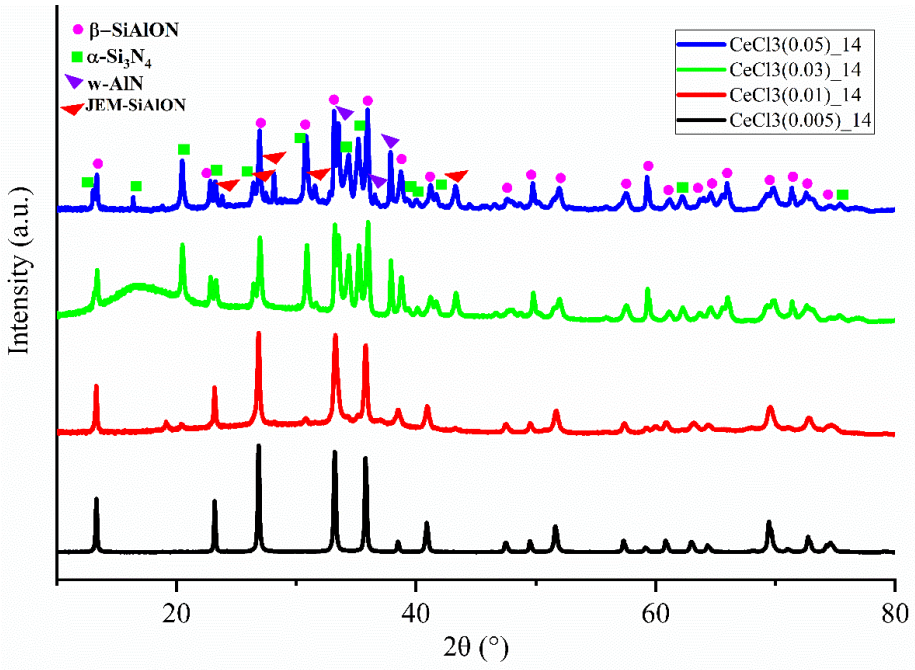

Figure V.6. XRD patterns of PAlCeYSZ3_14 ($0.005 \leq Y \leq 0.05$). *The halo shape around (10-20°) for* ***PAlCe0.03SZ3_14*** *sample comes from sample holder.*

Thus, X-ray diffraction of our samples demonstrate that PAlCeYSZ3_14 ($0.005 \leq$ Si:Ce (Y) ≤ 0.05) samples are mainly composed of β-SiAlON with nitrogen-containing secondary phases whose content increases with the Ce:Si ratio. In literature, it has been reported that large cations (Ce^{3+}, Sm^{3+}, Nd^{3+}, etc.) accelerate the phase transformation and promote the formation of nitrogen-containing intergranular phases[26,27]. Subjecting PAlCeYSZ3_16 (Figure V.7) samples to a heat treatment at 1600 °C results in clearly crystalline phases. The emerged peaks align with β-SiAlON, w-AlN, α-Si_3N_4, and JEM SiAlON. These patterns mirror the trend observed in PAlCeYSZ3_14 samples ($0.005 \leq$ Si:Ce (Y) ≤ 0.05), where an increase in the Ce:Si ratio

correlates with an increase in presence of secondary phases. Furthermore, there are no apparent characteristics of an amorphous phase, indicating that all the samples are (almost) completely crystallized.

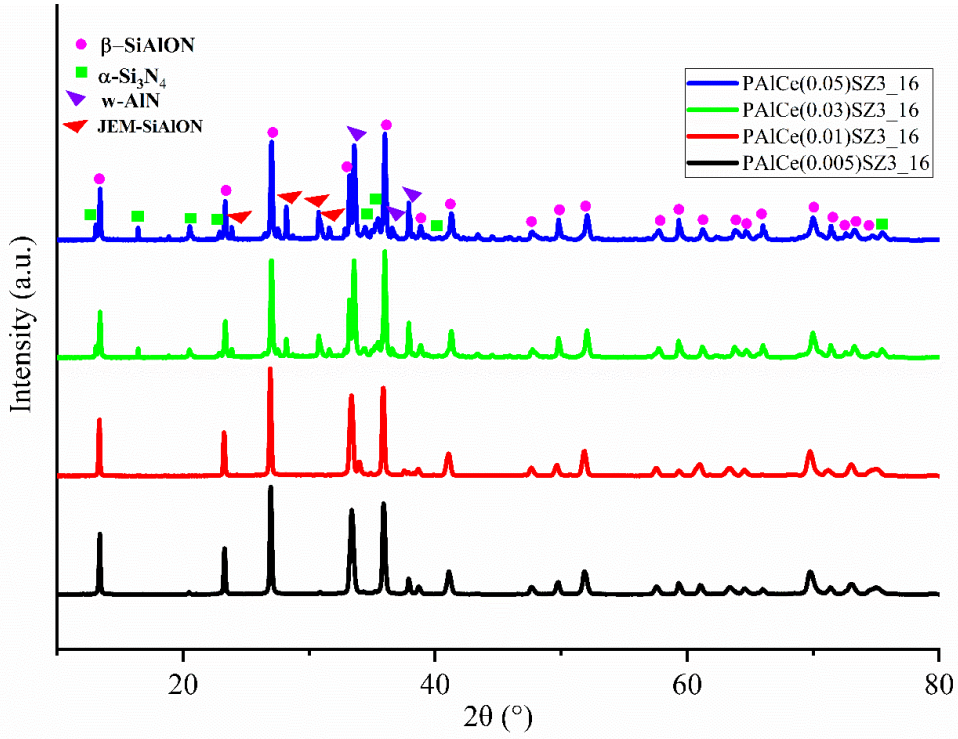

Figure V.7. XRD patterns of PAlCeYSZ3_16 ($0.005 \leq Y \leq 0.05$).

Rietveld refinement were performed using three phases (β-SiAlON, α-Si_3N_4 and w-AlN) for **PAlCe0.005SZ3_16** and four phases (β-SiAlON, α-Si_3N_4, w-AlN and JEM SiAlON) for **PAlCe0.05SZ3_16**. Let us note that in the Rietveld refinement the model used for JEM phase was based on Ce cation instead of La based JEM phase as proposed in literature.

Similar to Chapter III and Chapter IV, the refined parameters were scale factors, background, sample positioning error, and cell parameters. Figure V.8 illustrates the Rietveld fit for the two XRD patterns. The overall fit quality is good but again far from perfection with discrepancies in intensity. This results in relatively poor figures of merit (R_p = 11.4 %, R_{wp} = 12.4 %, R_{exp} = 1.46 % and GofF = 8.4) for **PAlCe0.005SZ3_16** and (R_p = 10.4 %, R_{wp} = 11.6 %, R_{exp} = 1.9 % and GofF = 5.9) for **PAlCe0.05SZ3_16**. We expect again that these discrepancies have no significant impact on the crucial refined parameters. The main results are outlined in Table V.4.

For β-SiAlON (**PAlCe0.005SZ3_16)**, the refined cell parameters a = b = 7.634 Å and c = 2.932 Å which are larger than those of β-Si_3N_4, confirming the presence of β-SiAlON. In addition, α-Si_3N_4 refined lattice parameters are a = b = 7.778 Å and c =5.663 Å which comes in the range of lattice parameter mentioned in Chapter I. Similarly, w-AlN lattice parameters aligned well

with reference values (a, b = 3.112 Å, c = 4.990 Å). The amount of β-SiAlON phase is 82 %, which is lower to the one obtained for **PAlSZ3_16** sample without Ce (92 %).

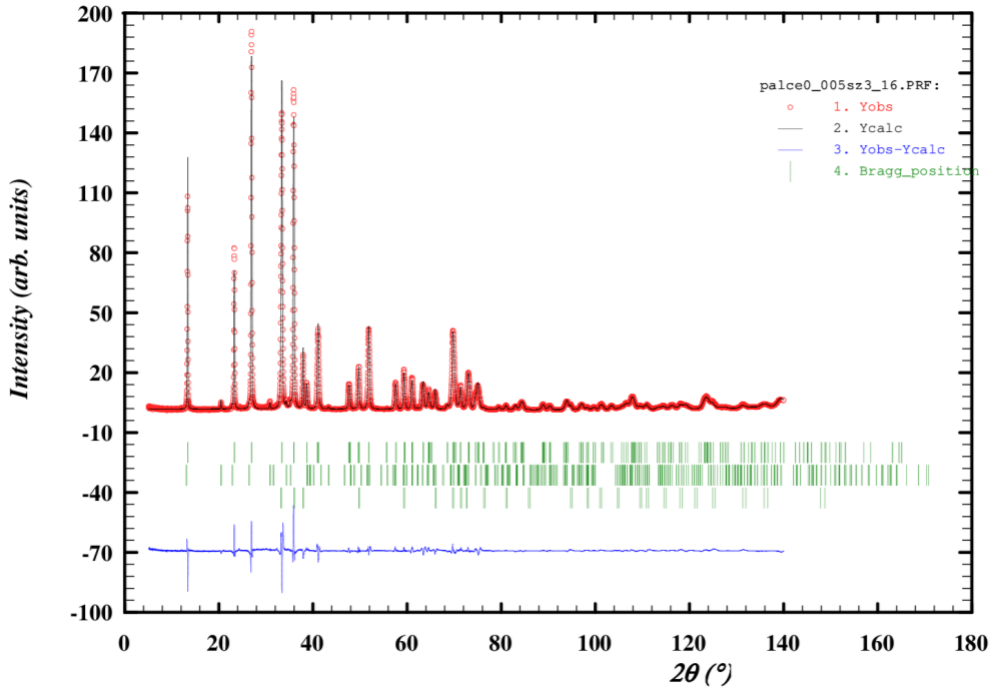

(a)

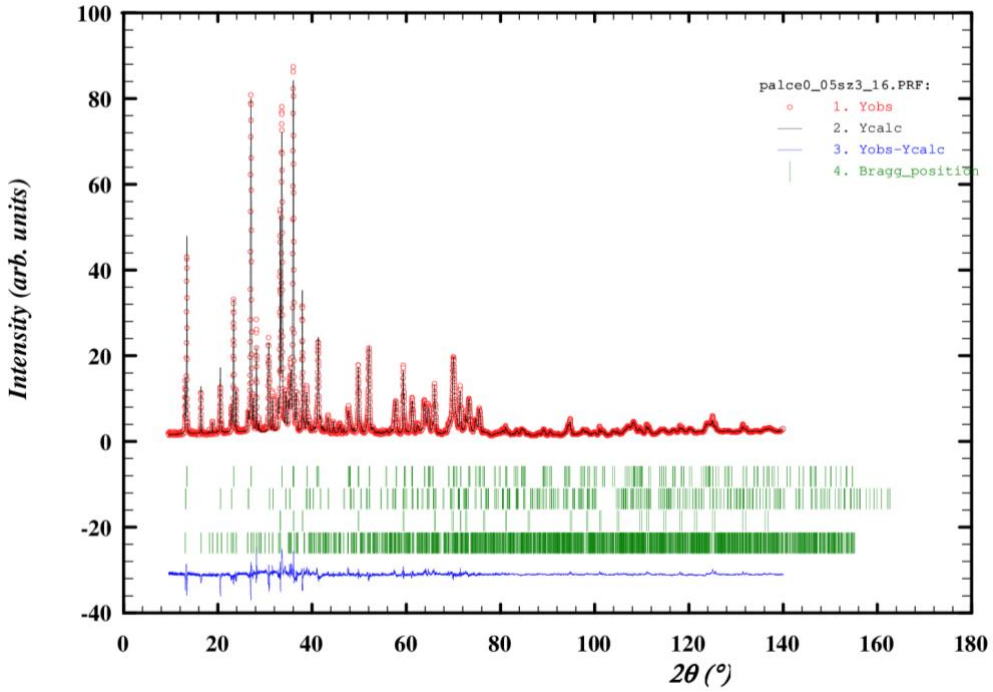

(b)

Figure V.8. Rietveld refinement of XRD patters of the Ce-doped samples; (a) **PAlCe0.005SZ3_16** (b) **PAlCe0.05SZ3_16**. *Observed (crosses) and calculated (red line) XRD patterns. Green vertical lines indicate positions of Bragg reflections. Blue line represents difference plot (observed/calculated) on the same scale.*

Table V.4. Main parameter obtained from Rietveld Refinement of the XRD patterns for the **PAlCe0.005SZ3_16** and **PAlCe0.05SZ3_16** and samples.

	PAlCe0.005SZ3_16			**PAlCe0.05SZ3_16**			
Phase parameters	**β-SiAlON**	**α-Si_3N_4**	**w-AlN**	**β-SiAlON**	**α-Si_3N_4**	**w-AlN**	**JEM SiAlON**
a, b (Å)	7.634(6)	7.778(1)	3.113(8)	7.617(2)	7.766(6)	3.112(2)	9.396(4), 9.745(4)
c (Å)	2.932(4)	5.663(2)	4.987(4)	2.915(4)	5.663(2)	4.982(2)	8.927(6)
Cell Volume ($Å^3$)	148.01(4)	296.75(1)	41.85(2)	146.53(4)	294.87(2)	41.79(2)	817.42(6)
Phase frac. (%)	82.5(6)	2.14(5)	15.3(2)	54.7(4)	13.1(1)	17.4(1)	15.1(1)

Moving to higher Ce content (**PAlCe0.05SZ3_16**) in β-SiAlON, the refined cell parameters show a decrease in values with a = b = 7.617 Å and c = 2.915 Å but still in the range of β-SiAlON value given in Chapter I. For the highest Ce:Si ratio, the refined cell parameters of JEM SiAlON are a = 9.396 Å, b = 9.745 Å, and c = 8.927 Å. They are reasonably close to the reference data based on La-JEM phase (a = 9.430, b = 9.768 and c = 8.938)[25]. The refined cell parameters for other secondary phases (α-Si_3N_4, w-AlN) remains same within the experimental error. Additionally, we observed a substantial decrease in the β-SiAlON phase content, from 83 % to 55 % while the secondary phases content increases (α-Si_3N_4 rises from 2% to 13%, JEM SiAlON phase 15%). This underscores the clear influence of Ce, indicating that β-SiAlON cell parameter changes to lower values.

As in Chapter IV, the Rietveld refinement did not allow us to conclude about the effective insertion of Ce within the β-SiAlON host structure because the change of phase content is too high from one sample to another. In literature, it has been mentioned that solubility of Ce in β-SiAlON is limited owing to its larger ionic size[15,16]. This question will be addressed by luminescence and elemental analysis mapping studies of sample in the following sections.

V.2.2.3. Gas Pressure Sintering of ammonia-treated samples

Following our work done in Chapter IV, we investigated the effect of gas-pressure sintering (GPS) at 1800 °C on the **PAlCe0.05SZ3_10** sample, leading to the **PAlCe0.05SZ3_GPS18** sample. As we can see in Figure V.9, GPS enables the attainment of nearly pure β-SiAlON with the presence of halo shape around (20-35°) possibly due to amorphous phase. As expected, GPS

acts effectively and serves the purpose to suppress the formation of secondary phases but it also probably retains small amounts of amorphous phase.

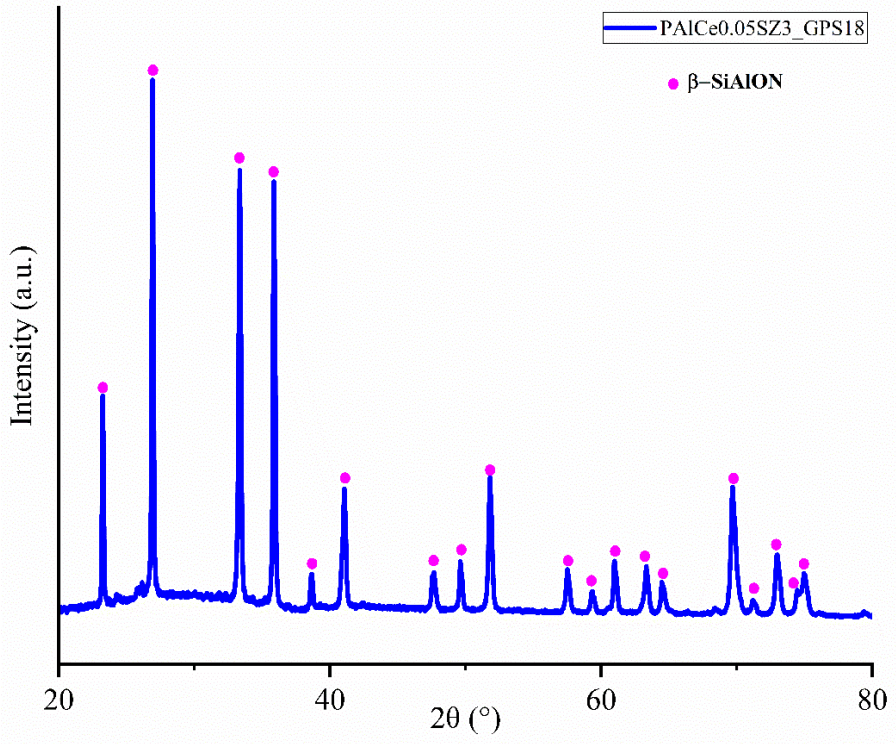

Figure V.9. X-ray diffraction of **PAlCe0.05SZ3_GPS18** sample.

The Rietveld refinement was performed for the **PAlCe0.05SZ3_GPS18** samples, using the single phase β-SiAlON. The Rietveld fit for **PAlCe0.05SZ3_GPS18** shown in Figure V.10 with figure of merit (R_p = 18.4 %, R_{wp} = 14.5 %, R_{exp} = 3.19 % and GofF = 4.5).

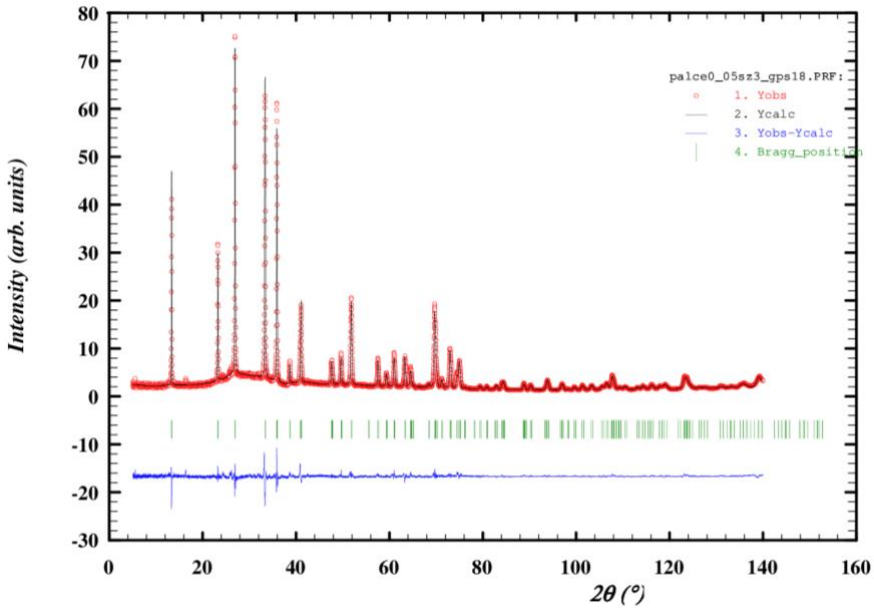

Figure V.10. Rietveld refinement of **PAlCe0.05SZ3_GPS18** sample. *Observed (crosses) and calculated (red line) XRD patterns. Green vertical lines indicate positions of Bragg reflections. Blue line represents difference plot (observed/calculated) on the same scale.*

The refined parameters, are detailed in Table V.5. The Rietveld refinement for the **PAlCe0.05SZ3_GPS18** sample reveals increase in cell parameters of a = b = 7.637 Å and c = 2.935 Å in comparison with **PAlCe0.05SZ3_16** (a = b = 7.617 Å and c = 2.915 Å) (at the same time with very small amount of secondary phase). The increase in cell parameter may be attributed to change in composition or the introduction of cerium into β-SiAlON, though certainty regarding this matter is currently lacking.

Table V.5. Cells parameter obtained from Rietveld refinement parameters of **PAlCe0.05SZ3_GPS18** sample.

Sample	**PAlCe0.05SZ3_GPS18**
	β-SiAlON
a, b (Å)	7.637 (8)
c (Å)	2.935 (4)
Cell Volume (Å^3)	148.264 (2)

We further go in more details regarding the microstructural investigation of these samples prepared at 1600 °C (PAlCeYSZ3_16; 0.005 ≤ Si:Ce (Y) ≤ 0.05).

V.2.3. Microstructural Analysis

Microstructural analysis includes examining materials at the microscopic and nanoscale levels, employing techniques such as scanning electron microscopy (SEM) combined with cathode-luminescence (CL) and transmission electron microscopy (TEM). SEM/CL and TEM analyses were conducted on **PAlCe0.01SZ3_16**, **PAlCe0.05SZ3_16** and **PAlCe0.05SZ3_GPS18**.

The SEM/CL analysis of **PAlCe0.01SZ3_16** ceramics is presented in Figure V.11.

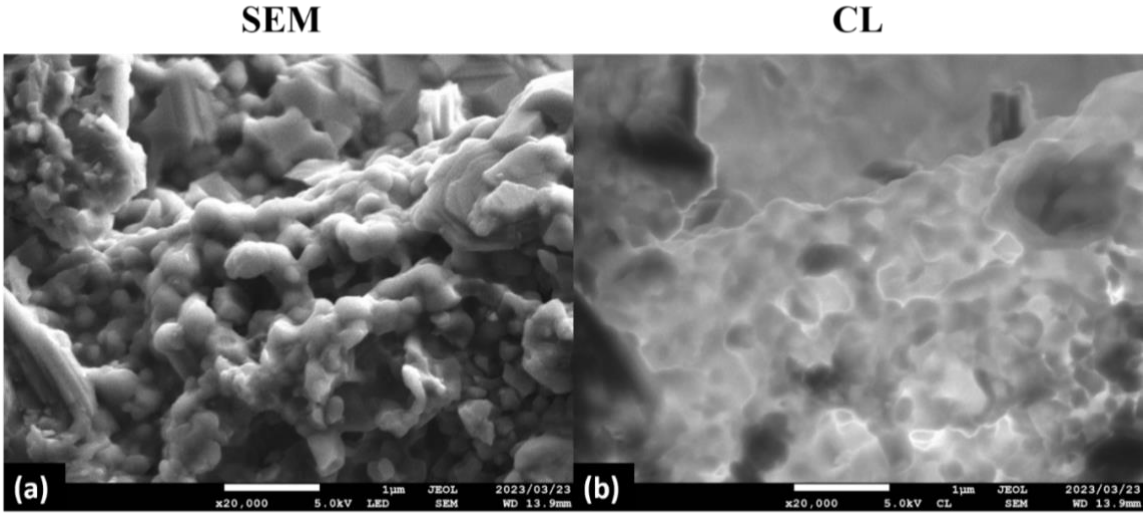

Figure V.11. SEM/CL microstructure of **PAlCe0.01SZ3_16**.

In SEM image (a), small crystal size and an inhomogeneous morphology are evident, as confirmed by XRD (refer to Figure V.7). Interestingly, in CL image (b), UV light is observed to transmit uniformly throughout the entire morphology, affirming a homogeneous distribution of Ce, with all parts transmitting light across the morphology.

The Figure V.12 illustrates the TEM analysis of **PAlCe0.01SZ3_16**, where two distinct crystals have been examined.

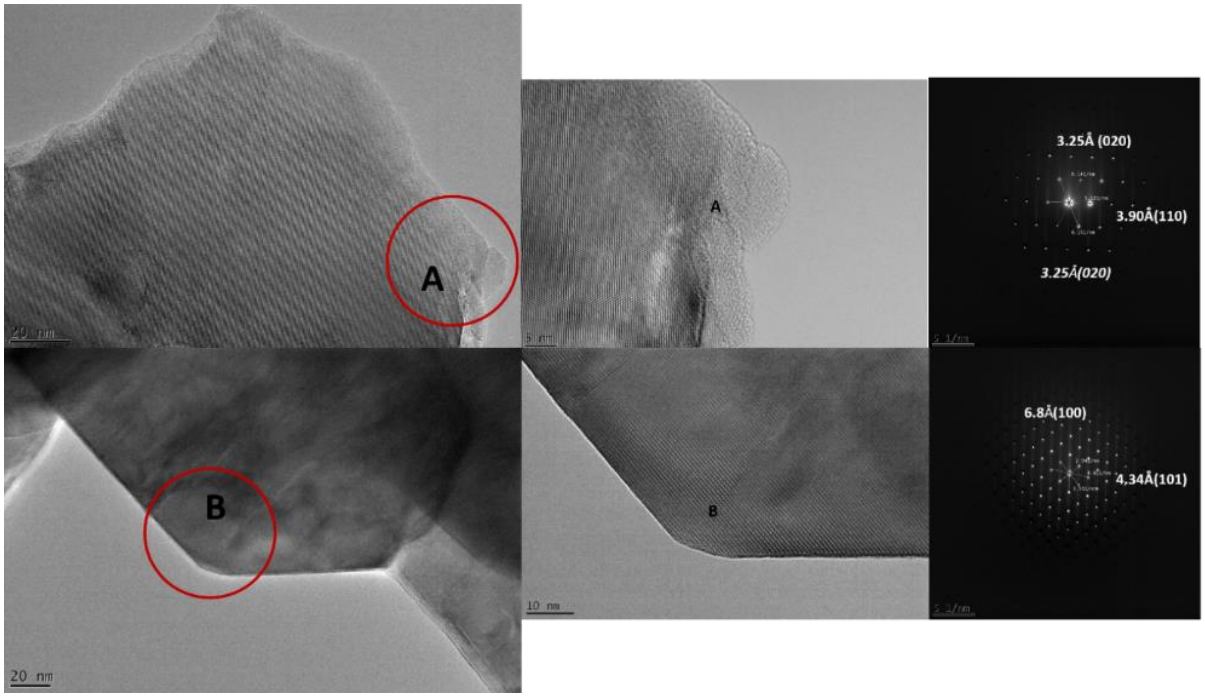

Figure V.12. TEM observations of **PAlCe0.01SZ3_16**.

In the first crystal (**A**), three diffraction patterns from β-SiAlON are observed at 23° (110), 26° (020), and 27° (0.20). The other crystal (**B**) also displays two diffraction patterns at 13° (100) and 20° (101) from α-Si_3N_4 phase.

Figure V.13 presents the SEM/CL analysis of **PAlCe0.05SZ3_16**, showcasing an evolved morphology compared to **PAlCe0.01SZ3_16**. The presence of multiple phases as shown with XRD (Figure V.7), results in a morphology that is challenging to recognize as the β-SiAlON crystal have cylindrical shape. Given the inhomogeneous morphology, CL emission is also non-uniform across the structure and is not observable in larger grains. The EDX analysis of these regions confirms that Al-rich SiAlON does not exhibit luminescence, while SiAlON with a fixed composition displays luminescence.

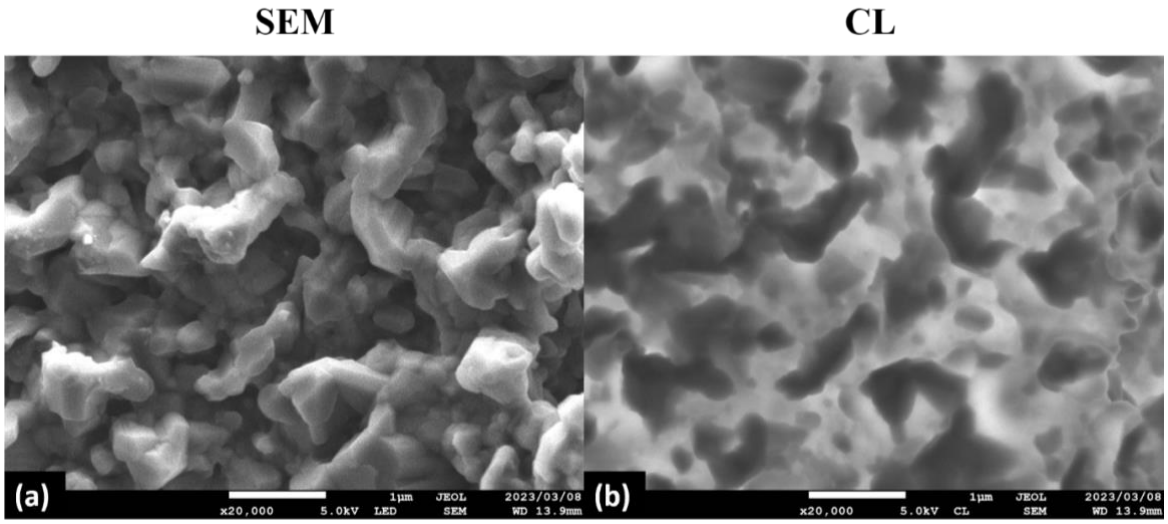

Figure V.13. SEM/ CL microstructural analysis of **PAlCe0.05SZ3_16**.

Figure V.14 depicts the TEM analysis of **PAlCe0.05SZ3_16**, revealing two distinct crystals, each demonstrating consistent crystalline behavior. In crystal (A), the identification of α-Si_3N_4 is evident with two diffraction patterns at 13° (100) and 20° (101). The second crystal (B) exhibits two diffraction patterns from β-SiAlON at 33.40° (011) and 33.40° (011).

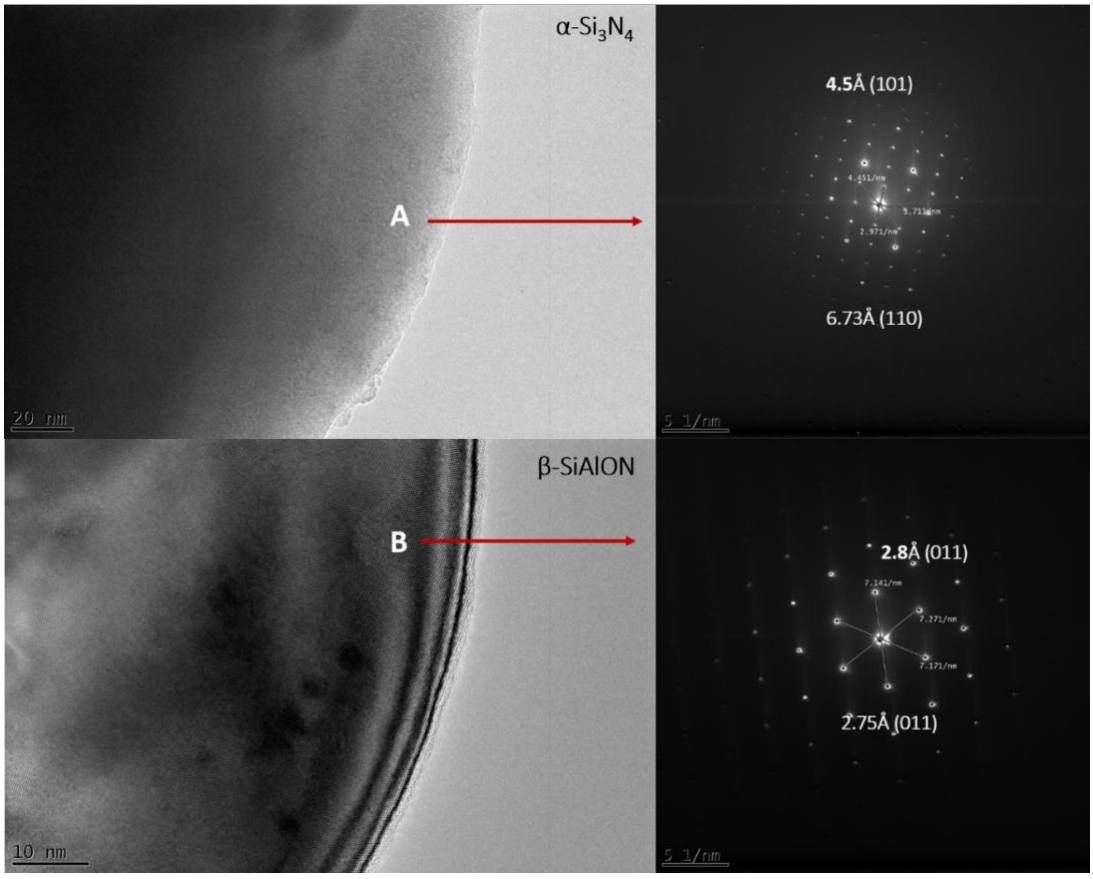

Figure V.14. TEM analysis of **PAlCe0.05SZ3_16**.

Figure V.15 illustrates the SEM/CL analysis of **PAlCe0.05SZ3_GPS18** ceramic produced through gas pressure sintering. Gas pressure sintering has influenced the morphology, resulting in a uniform cylindrical shape, characteristic of β-SiAlON (as confirmed by XRD). However, CL emission is not uniform; it appears to originate from the intergranular phase, as confirmed by the presence of an XRD-identified amorphous phase.

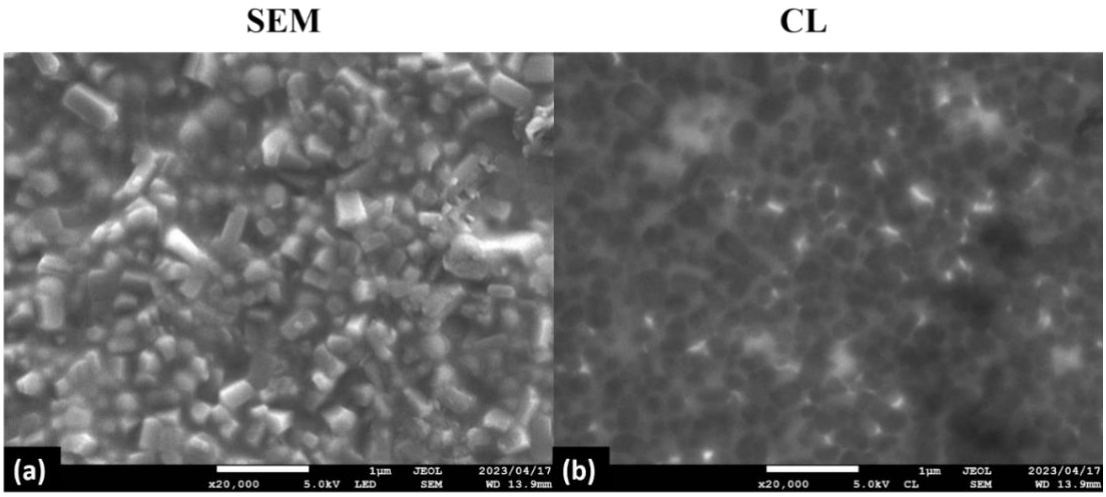

Figure V.15. SEM/ CL microstructural analysis of **PAlCe0.05SZ3_GPS18**.

Figure V.16 displays the TEM analysis of **PAlCe0.05SZ3_GPS18** ceramics.

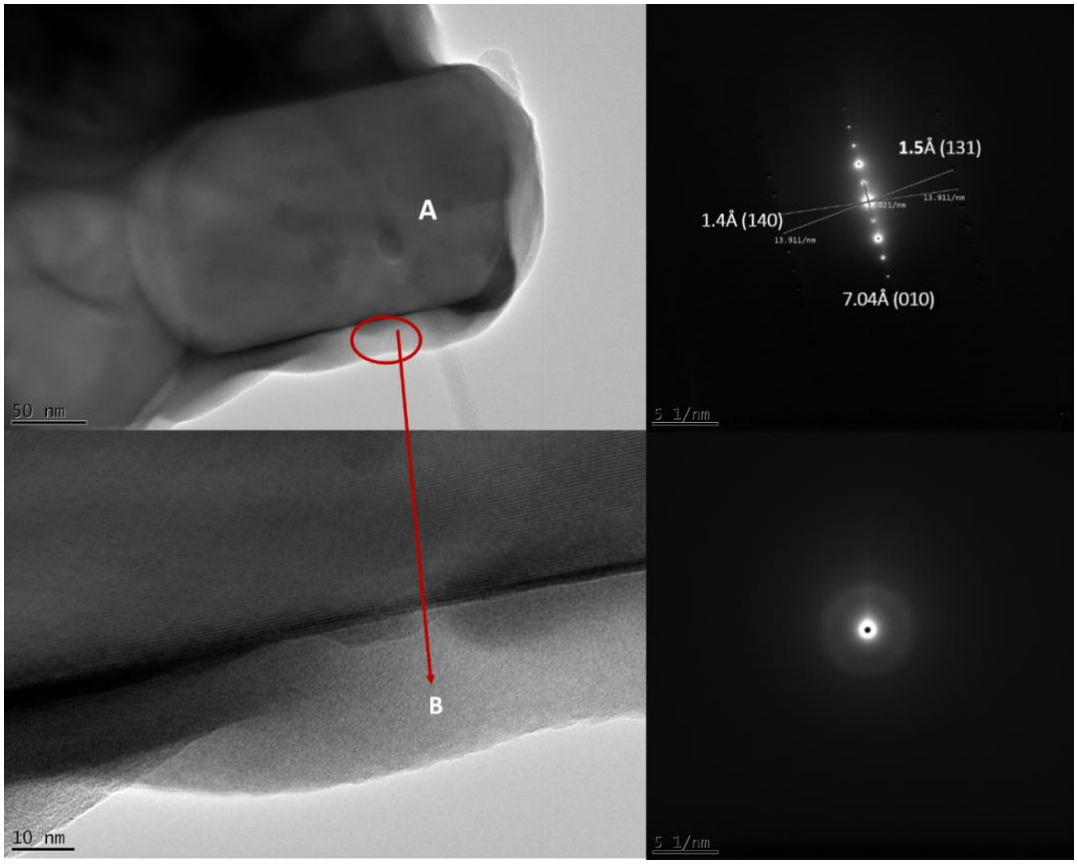

Figure V.16. TEM analysis of **PAlCe0.05SZ3_GPS18**.

The part (**A**) reveals three distinct diffraction peaks at 13° (010), 59° (131), and 64° (140). Conversely, the grain boundary (**B**) exhibits amorphous behavior in the ceramics, a characteristic confirmed by XRD (Figure V.9). It's noteworthy that detecting the presence of an amorphous grain boundary during TEM measurements was challenging due to the thin nature of the grain boundary.

Figure V.17 provides an example of Ce accumulation at the grain boundary. The crystal with a cylindrical shape is identified as β-SiAlON, and mapping of this region indicates lower Ce concentration within the β-SiAlON crystal. Thus, the majority of Ce is found to be accumulated at the grain boundary. This can be attributed to the higher dopant content and lower solubility of Ce^{3+} within the β-SiAlON lattice, causing most of the Ce to accumulate at grain boundaries or in the glassy phase.

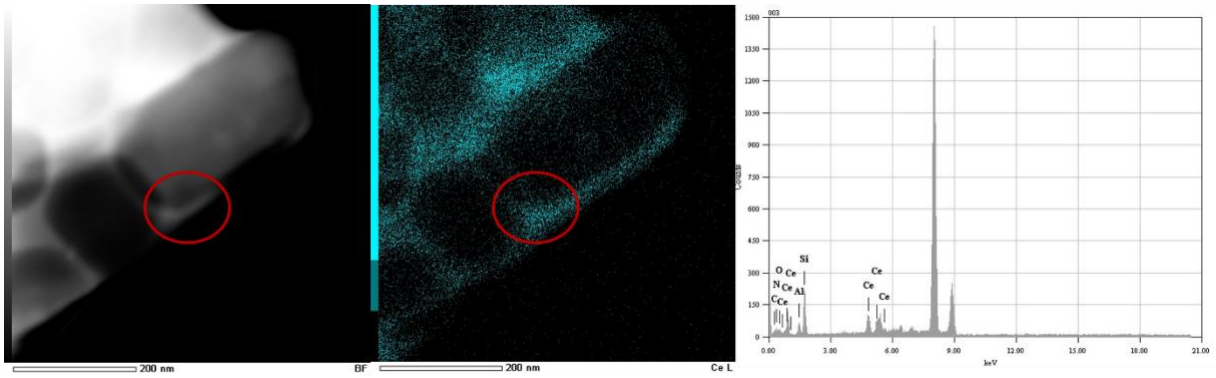

Figure V.17. Mapping and chemical composition of **PAlCe0.05SZ3_GPS18**.

V.2.4. Optical analysis

The optical analysis of β-SiAlON:Ce^{3+} samples previously analyzed is the topic of this section. Thus, this analysis aims to follow and interpret the emission and excitation behaviours exhibited by these samples. We particularly investigated photoluminescence characterization, cathodoluminescence behaviour, UV spectroscopy and lifetime analyses, to understand the detailed aspects of the material's optical behaviour. These analyses show how the introduction of cerium ions in the early stage of the process influences the absorption and emission of light within the low oxygen content β-SiAlON matrix.

V.2.4.1. Photoluminescence Analysis

The Figure V.18 illustrates the excitation and emission spectra at room temperature of the reference samples namely PAlCeYSZ3_16 ($0.005 \leq Y \leq 0.05$) samples and **PAlCe0.05SZ3_GPS18** sample.

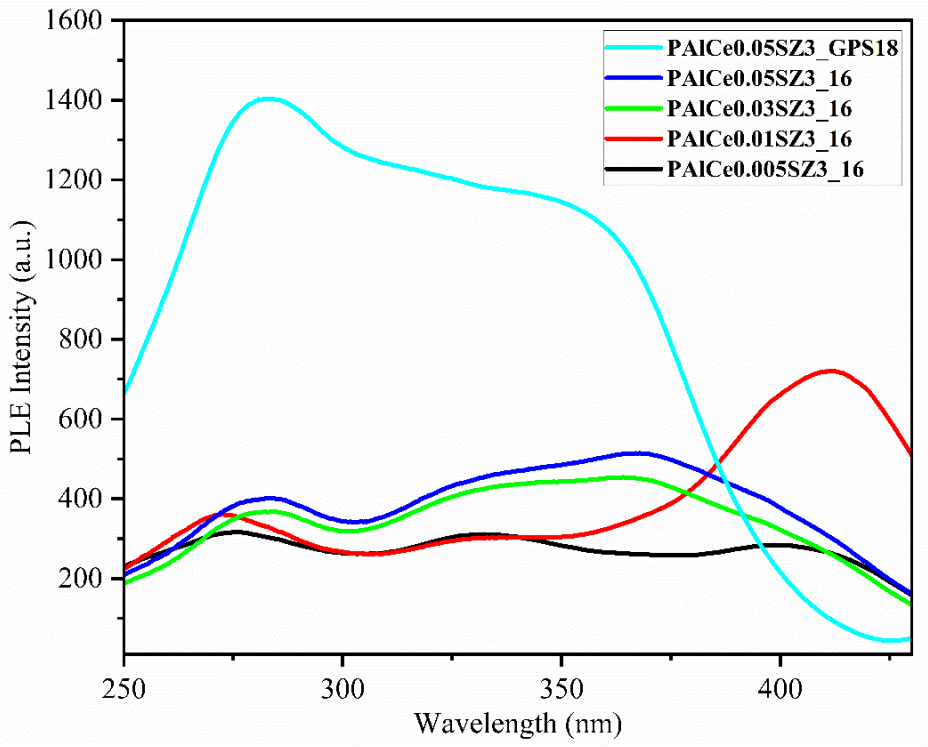

(a)

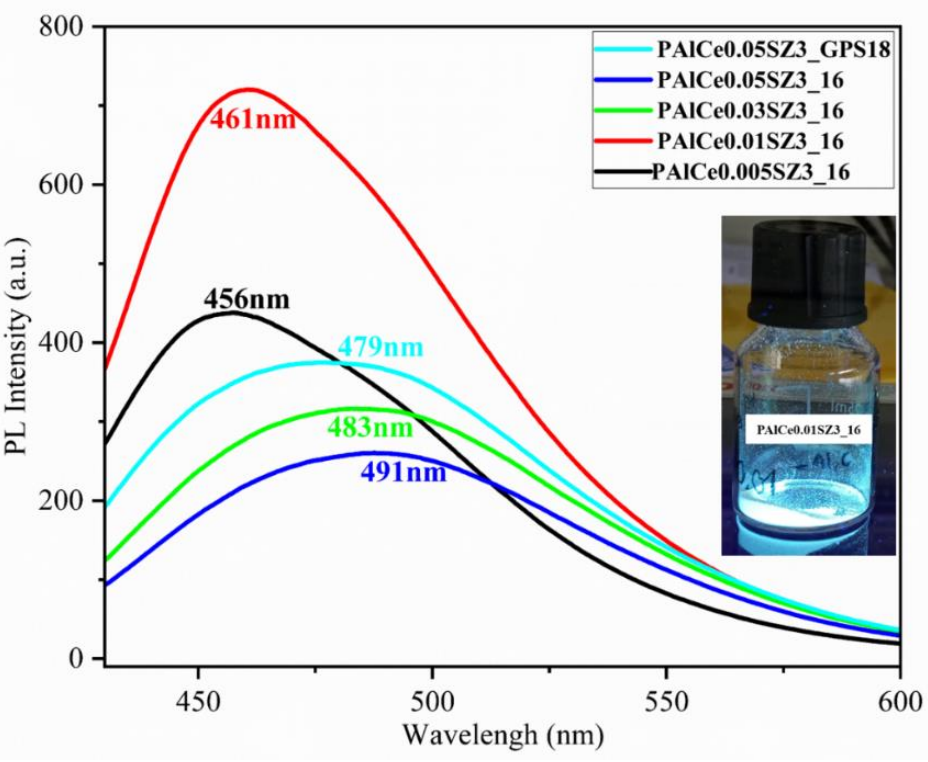

(b)

Figure V.18. Photoluminescence spectra of PAlCeYSZ3_16 ($0.005 \leq Y \leq 0.05$), and **PAlCe0.05SZ3_GPS18** samples where (a) $PLE_{em.}$ =460 nm (b) $Pl_{ex.}$ =405 nm.

The excitation spectrum (Figure V.18(a), $\lambda_{em.}$ = 460 nm) exhibits three distinct bands of Ce^{3+}: a dominant band in the visible range centered around 366 nm, 412 nm, and a weaker band

within the UV range peaking at approximately 272-282 nm which can to due to excitement of Ce^{3+} cations. Notably, the excitation sub-band at 272-282 nm can be attributed to both the host and Ce^{3+} excitation bands, as it falls below the absorption edge of the host lattice. This suggests a partial overlap between the highest energy Ce^{3+} excitation band and the bottom of the host's conduction band[13]. The existence of two luminescence centers can arise from the presence of two crystallographic sites in β-SiAlON:Ce^{3+}. Krevel et al.[2] reported that the one Ce center corresponds to the low-energy band of Ce^{3+} (412 nm) on the Si/Al site, while the other Ce center is associated with the high-energy bands (333 and 360 nm) on the Si/Al site. The latter exhibits the largest crystal-field splitting and the smallest Stokes shift, possibly attributed to its highest N/O ratio as mentioned in Table V.6. This arrangement gives rise to the expectation of two luminescent centers, potentially resulting in different shapes of emission and excitation spectra as shown in Figure V.18.

The luminescence of Ce^{3+} observed shifts of the 4f-5d transitions to lower energy (Figure V.18(a)) when the nitrogen content increases (Table V.6). This was explained by two factors like increase in covalency (nephelauxetic effect), and decrease of stokes shift[2,4]. The emission spectra (Figure V.18(b), excited under violet light $\lambda_{ex.}$ = 405 nm) exhibits a single broad emission band around (430-550) nm attributed to the $4f^05d^1 \rightarrow 4f^1$ electron transition of the Ce^{3+} ions[28–32].

The highest emission is achieved for **PAlCe0.01SZ3_16** ceramics, followed by a decline in photoluminescence emission when the dopant content increases PAlCeYSZ3_16 ($0.03 \leq Y \leq 0.05$). A noticeable red-shift of emission centers towards longer wavelengths (from 456 to 491 nm) is observed with increasing dopant concentration PAlCeYSZ3_16 ($0.005 \leq Y \leq 0.05$).

Table V.6. The oxygen and nitrogen (O/N) ratio with increase in dopant **PAlCeYSZ3_16** ($0.005 \leq Y \leq 0.05$).

Samples	N	O	O:N
	(wt. %)		
PAlCe0.005SZ3_16	30.27	2.71	0.089
PAlCe0.01SZ3_16	32.04	5.12	0.159
PAlCe0.03SZ3_16	32.26	2.22	0.068
PAlCe0.05SZ3_16	32.7	2.29	0.070

The observed shift can be attributed to crystal field splitting and energy transfer among Ce^{3+} ions. The increase in Ce^{3+} concentration brings about changes in the host lattice. Firstly, the crystal lattice undergoes mild expansion as Ce^{3+} occupies the interstitial site, leading to a mild crystal field splitting and a downward shift in the gravity center of 5d orbitals. Secondly, the proximity between activator ions decreases, enhancing the likelihood of reabsorption, consequently causing a red shift in the emission[31,33]. The decrease in photoluminescence emission at higher Ce concentrations (PAlCeYSZ3_16 ($0.005 \leq Y \leq 0.05$), Figure V.18(b)) is attributed to the presence of higher impurity phases and an abundance of defect formation traps, which suppresses the emission intensity[4,34–37].

The introduction of GPS (**PAlCe0.05SZ3_GPS18**, Figure V.18(b)) enhances the emission properties twofold, resulting in emission at 479 nm, emission shift to a shorter wavelength[34–36,38]. This increase in emission is associated with alterations in microstructure, as well as the removal of impurities and defects. Both excitation and emission processes can be optimized by adjusting the firing temperature and hold time, as well as employing post-heat treatment to achieve the desired particle size and morphology.

V.2.4.2. Optical absorption

For PAlCeYSZ3_16 ($0.005 \leq Y \leq 0.05$) samples, optical absorption specifically indicates the material's ability to absorb light. In this case, the photons are absorbed by cerium ions (Ce^{3+}) incorporated into the β-SiAlON lattice, resulting in an electronic transition. The absorption spectrum of β-SiAlON:Ce^{3+} reflects the wavelengths at which light is absorbed by the material, and reveals the energy levels associated with electronic transitions of Ce^{3+} ions[13,34,37].

The Figure V.19 depicts the diffuse reflection spectra of PAlCeYSZ3_16 ($0.005 \leq Y \leq 0.05$) and **PAlCe0.05SZ3_GPS18** ceramics. PAlCeYSZ3_16 ($0.005 \leq Y \leq 0.05$) samples show that reflection from the samples are about 70-80 % absorption within the spectral range of 200-1000 nm, in ultraviolet (UV) and visible spectra. Notably, the samples exhibit substantial light absorption in the UV and visible ranges, with a distinct dip in absorption occurring at 264 nm and 370 nm within the range of 230-500 nm. These samples exhibited a color spectrum ranging from white to grey, dependent on the Ce content ($0.005 \leq Y \leq 0.05$). In PAlCeYSZ3_16 ($0.005 \leq Y \leq 0.05$) samples, the absorption range spanned 264 - 465 nm, attributed to Ce^{3+} ions undergoing electronic transitions from the ground state (4f) to the excited state (5d) and shows blue color emission at 460 nm. With increasing Ce^{3+} ion concentration, there is a slight red-shift phenomenon in the absorption edge towards longer wavelengths[4,13,30,39]. This shift can be

attributed to the increased Ce^{3+} concentration leads to more compact energy in the crystal structure and a reduced band gap, resulting in a lower transition energy (E). In accordance with $E=hc/\lambda$, a higher Ce^{3+} concentration induces a red shift[37].

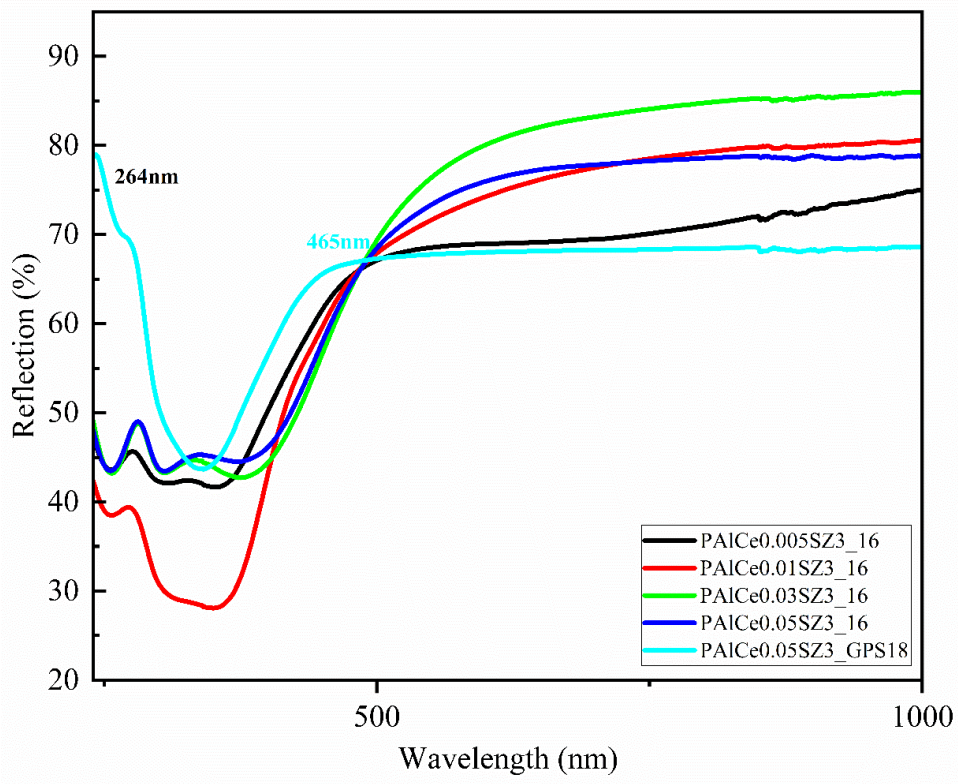

Figure V.19. Optical absorption of PAlCeYSZ3_16 ($0.005 \leq Y \leq 0.05$) and **PAlCe0.05SZ3_GPS18** samples.

The highest optical absorption is observed in **PAlCe0.01SZ3_16**, mirroring the phenomenon observed in photoluminescence emission spectra (Figure V.18). Remarkably, GPS had impact on the optical absorption: the **PAlCe0.05SZ3_GPS18** sample has a strong optical absorption at 264 and 330 nm most probably due to the highest β-SiAlON phase content. On the other hand, the highest reflection and lowest absorption in the visible spectral range due to the presence of the defects in the lattice[13].

V.2.4.3. Luminescence decay

In this study, the understanding of photoluminescent decay involves the interaction between Ce ions and the crystal lattice, followed by the relaxation of excited states. The decay occurs through electronic transition relaxation processes, either radiative or non-radiative. The duration for excited Ce ions to return to their ground state is defined as the lifetime of the excited states, indicating how long the material emits light post-excitation. This lifetime varies based on factors like Ce dopant concentration, crystal defects, temperature, and β-SiAlON ceramics

composition[31,32]. Figure V.20 depicts the decay curve of PAlCeYSZ3_16 ($0.005 \leq Y \leq 0.05$) and **PAlCe0.05SZ3_GPS18** ceramics phosphors under 350nm excitation at room temperature.

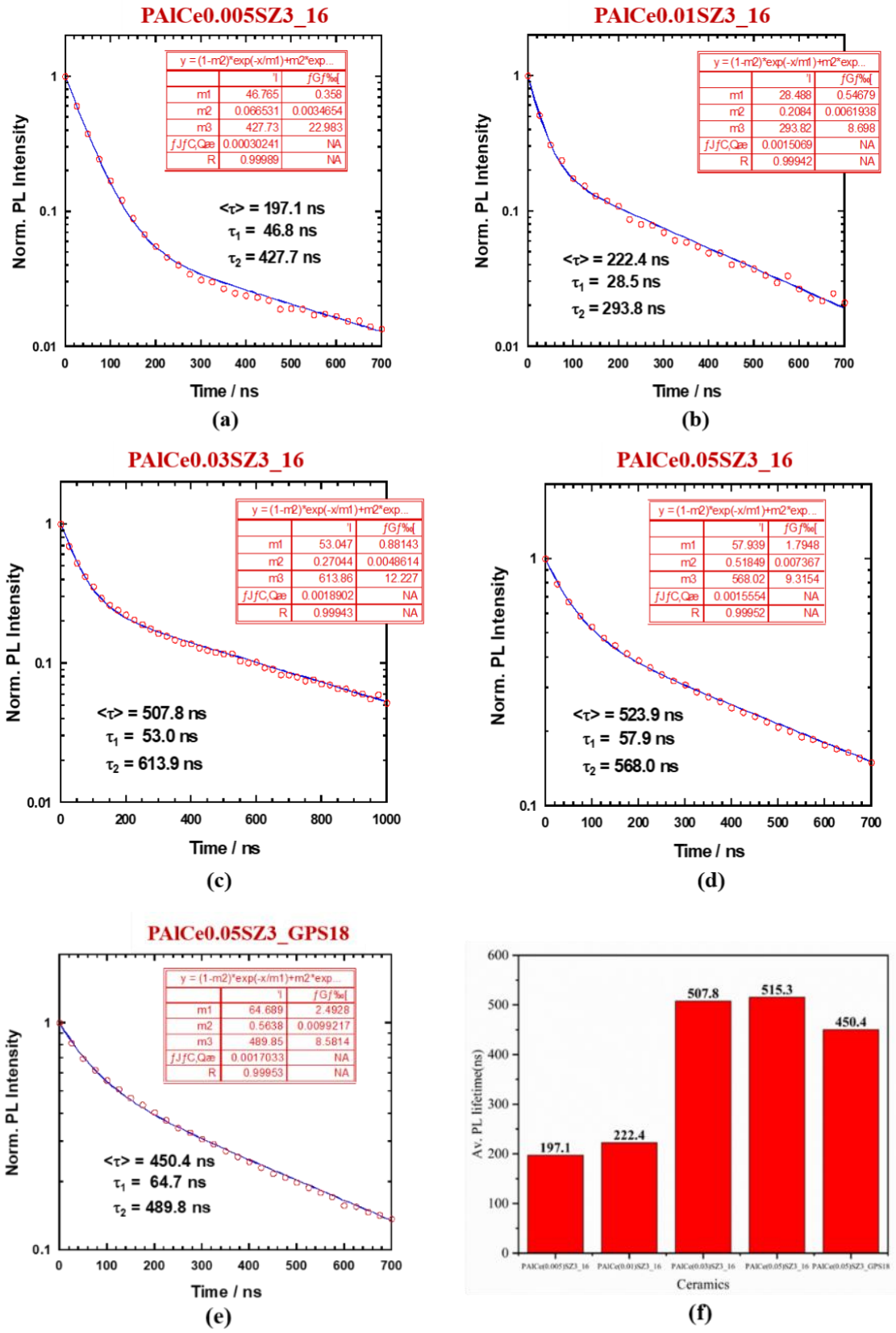

Figure V.20. Luminescent decay of (a) **PAlCe0.005SZ3_16**, (b) **PAlCe0.01SZ3_16**, (c) **PAlCe0.03SZ3_16**, (d) **PAlCe0.05SZ3_16**, (e) **PAlCe0.05SZ3_GPS18**, and (f) Average photoluminescent decay of all ceramics.

Lifetimes for all samples range from 197-515 ns, typical for Ce^{3+} ions, affirming that the blue photoluminescent emission results from 5d-4f transitions[31,37]. It is the observation that higher Ce content ($0.005 \leq Y \leq 0.05$) extends the photoluminescent decay duration. The **PAlCe0.05SZ3_GPS18** sample has, however, reduced the lifetime. This reduction is possibly linked to the presence of non-radiative transition, existence of defects or gain boundary (Figure V.16) induced by the sintering process.

V.2.4.4. Quantum efficiency

As we discussed about internal and external quantum efficiency in Chapter IV section, where Internal quantum efficiency focuses on the efficiency of the carriers inside the device, while external quantum efficiency considers the overall efficiency of the entire device, and accounts for losses (such as reflection or absorption) outside the device. A high internal quantum efficiency is desirable for efficient carrier recombination[40], and a high external quantum efficiency means that the incident photon is efficiently converted to useful form[41]. In Figure V.21, the internal and external quantum efficiencies of β-SiAlON:Ce^{3+} are presented for highest Ce concentrations (**PAlCe0.05SZ3_16**, **PAlCe0.05SZ3_GPS18**) both before and after gas pressure sintering (GPS) at wavelengths ranging from 300 to 365nm.

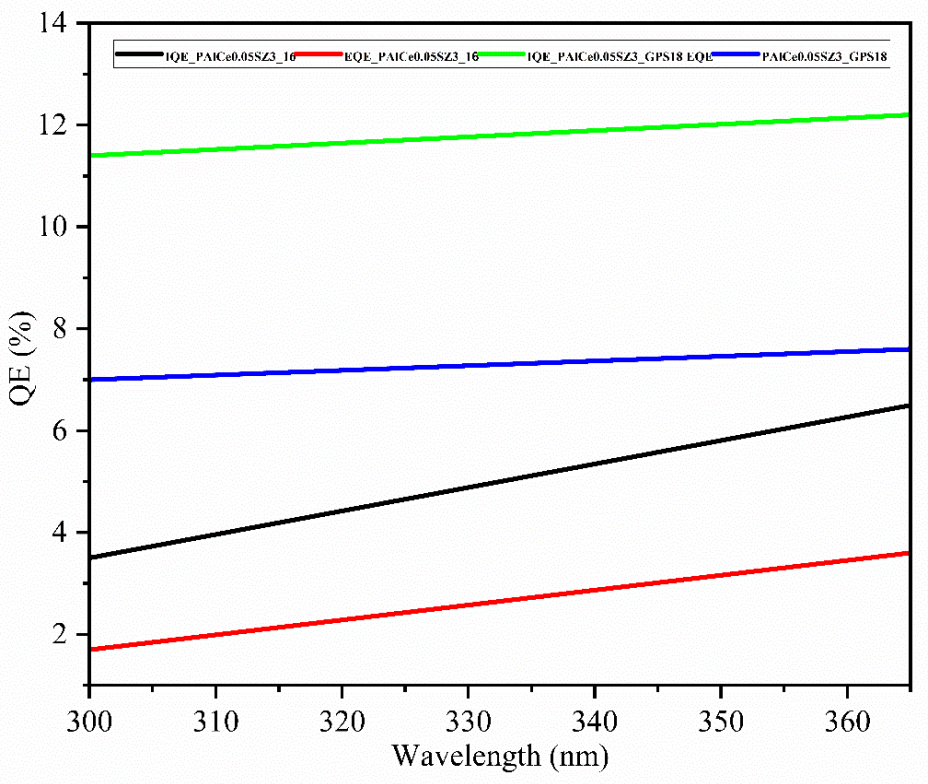

Figure V.21. Internal and External quantum efficiency of **PAlCe0.05SZ3_16** and **PAlCe0.05SZ3_GPS18**.

Notably, the internal quantum efficiency of the **PAlCe0.05SZ3_16** sample is 4-12 % which surpasses the external quantum efficiency 2-6 %. The **PAlCe0.05SZ3_GPS18** sample exhibits the highest quantum efficiency, reaching up to 12 %, particularly at longer wavelengths. This enhancement is attributed to alterations in microstructure and the elimination of impurities, as evidenced by XRD (Figure V.7) and PL measurements (Figure V.18(b)). In contrast, the **PAlCe0.05SZ3_16** sample demonstrates the lowest quantum efficiency, potentially linked to defects and impurities arising from the microstructure of ceramics, thereby impacting their overall quantum efficiency performance[29,31,35].

V.3. Conclusion

This chapter details the design process for low-oxygen β-SiAlON:Ce^{3+} ceramics, where $CeCl_3$ served as the dopant within the specified range $0.005 \leq Ce:Si \leq 0.05$. The precursor includes aluminum-modified polysilazanes (Si:Al=3, as discussed in Chapter III) modified by $CeCl_3$. Pyrolysis and annealing treatments are performed in flowing ammonia and nitrogen, respectively. As a proof of concept, gas pressure sintering (GPS) has been investigated on ammonia-treated samples.

The chapter starts with the synthesis of the polymers with increasing Ce:Si ratio from 0.005 to 0.05 to explore the effect of the Ce^{3+} content on the microstructure and optical properties of final materials. Ce^{3+} seems to interact with nitrogen at the polymer level based on elemental analyses although no proofs can be done through FTIR and solid-state NMR spectroscopies. Thus, we speculated that $CeCl_3$ introduced in **PAlSZ3** preferentially interacts with nitrogen. The subsequent pyrolysis at 1000 °C under ammonia results in the identification of peaks characteristic to the CeClO phase (PDF 04-013-3145; Tetragonal space group P4/nmm) emerging from an amorphous phase made of $AlN_{4-x}O_x$ and AlO_4 units alongside with SiN_4 environments. Therefore, contrarily to Eu^{2+}- and Eu^{3+}-doped samples, Ce^{3+}-doped samples tends to segregate by crystallizing at relatively low temperature. Further heat treatments up to 1600 °C result in complete crystallization into α-Si_3N_4, β-SiAlON, JEM-SiAlON (mullite), and/or w-AlN phases. The β-SiAlON phase content decreases with increasing Ce content, and the **PAlCe0.005SZ3_16** sample exhibits one of the highest β-SiAlON phase contents (over 82%). The use of GPS ensures the attainment of pure β-SiAlON, confirmed through Rietveld refinement and XRD in combination with intergranular phase analysis.

Under 405 nm excitation, β-SiAlON:Ce^{3+} displays blue emission, with the highest intensity observed for **PAlCe0.01SZ3_16**. The study demonstrates the significant influence of GPS on

microstructure, optical properties, and quantum efficiency. The microstructural analysis reveals less incorporation of Ce^{3+} into the β-SiAlON host lattice and more at the grain boundary (**PAlCe0.05SZ3_GPS18)**. The key conclusion is that **PAlCe0.01SZ3_16** represents the critical concentration for achieving the highest luminescent efficiency, emphasizing the considerable impact of gas pressure sintering on microstructure and optical properties, especially for Ce with lower dopant content, allowing complete Ce integration within the β-SiAlON host lattice.

Bibliography

(1) Blasse, G.; Grabmaier, B. C. A General Introduction to Luminescent Materials. In *Luminescent Materials*; Springer Berlin Heidelberg: Berlin, Heidelberg, 1994; pp 1–9.

(2) Van Krevel, J. W. H.; Hintzen, H. T.; Metselaar, R.; Meijerink, A. Long Wavelength Ce3+ Emission in Y–Si–O–N Materials. *J. Alloys Compd.* **1998**, *268* (1–2), 272–277.

(3) Van Krevel, J. W. H.; Van Rutten, J. W. T.; Mandal, H.; Hintzen, H. T.; Metselaar, R. Luminescence Properties of Terbium-, Cerium-, or Europium-Doped α-Sialon Materials. *J. Solid State Chem.* **2002**, *165* (1), 19–24.

(4) Xie, R.; Hirosaki, N.; Mitomo, M.; Yamamoto, Y.; Suehiro, T.; Ohashi, N. Photoluminescence of Cerium-Doped A-SiAlON Materials. *J. Am. Ceram. Soc.* **2004**, *87* (7), 1368–1370.

(5) Li, Y. Q.; Hintzen, H. T. Luminescence of a New Class of UV–Blue-Emitting Phosphors MSi 2O2-δN2+2/3δ: Ce^{3+}(M= Ca, Sr, Ba). *J. Mater. Chem.* **2005**, *15* (42), 4492–4496.

(6) Le Toquin, R.; Cheetham, A. K. Red-Emitting Cerium-Based Phosphor Materials for Solid-State Lighting Applications. *Chem. Phys. Lett.* **2006**, *423* (4–6), 352–356.

(7) Ryu, J. H.; Won, H. S.; Park, Y.-G.; Kim, S. H.; Song, W. Y.; Suzuki, H.; Yoon, C.-B.; Kim, D. H.; Park, W. J.; Yoon, C. Photoluminescence of Ce^{3+}-Activated β-SiAlON Blue Phosphor for UV-LED. *Electrochem. Solid-State Lett.* **2009**, *13* (2), H30.

(8) Akhmadullina, N. S.; Lysenkov, A. S.; Ashmarin, A. A.; Baranchikov, A. E.; Ishchenko, A. V.; Yagodin, V. V.; Shul'gin, B. V.; Kargin, Y. F. Synthesis and Luminescence Properties of Eu^{2+}-and Ce^{3+}-Doped AlONs. *Ceram. Int.* **2016**, *42* (1), 286–293.

(9) Hirosaki, N.; Suehiro, T.; Yamamoto, Y.; Mitomo, M. Sintering of Ca-Ce-Doped-α-Sialon. In *Preprints of Annual Meeting of The Ceramic Society of Japan Preprints of Fall Meeting of The Ceramic Society of Japan Preprints of Annual Meeting of The Ceramic Society of Japan, 2003*; The Ceramic Society of Japan, 2003; pp 486–486.

(10) Xia, Z.; Liu, R.-S. Tunable Blue-Green Color Emission and Energy Transfer of Ca2Al3O6F: Ce3+, Tb3+ Phosphors for near-UV White LEDs. *J. Phys. Chem. C* **2012**, *116* (29), 15604–15609.

(11) Shen, Z.; Ekstrom, T.; Nygren, M. Phases Formed in the Si 3 N 4-Rich Corner of the Ce-Al-Si-ON System. *J. Mater. Sci. Lett.* **1996**, *15*, 1638–1640.

(12) Xie, R. J.; Mitomo, M.; Hirosaki, N. Luminescence Properties of Rare-Earth Doped α-SiAlONs. In *Key Engineering Materials*; Trans Tech Publ, 2006; Vol. 317, pp 797–802.

(13) Li, Y.; Hirosaki, N.; Xie, R.; Li, J.; Takeda, T.; Yamamoto, Y.; Mitomo, M. Structural and Photoluminescence Properties of Ce^{3+} - and Tb^{3+} -Activated Lu-α-Sialon. *J. Am. Ceram. Soc.* **2009**, *92* (11), 2738–2744.

(14) Wang, C.-Y.; ten Kate, O. M.; Takeda, T.; Hirosaki, N. Efficient and Thermally Stable Blue-Emitting Ce^{3+} Doped $LaAl(Si_{6-Z}Al_z)(N_{10-Z}O_z)$(JEM: Ce) Phosphors for White LEDs. *J. Mater. Chem. C* **2017**, *5* (32), 8295–8300.

(15) Mishin, A. N.; Potapov, S. 5d-4f Radiative Transitions in Ce-Doped $Si_3AlO_yN_{4-y}$ Solid Solutions. In *Proceedings of SPIE*; 2002; Vol. 4766, p 143.

(16) Chernovetz, B. V.; Feopentov, A. V.; Grekov, F. F.; Mikhrim, S. B.; Mishin, A. N.; Potapov, A. S. 5d-4f Radiative Transitions in Ce-Doped $Si_{3x}Al_xO_yN_{4-y}$ Solid Solutions. In *XI Feofilov Symposium on Spectroscopy of Crystals Activated by Rare-Earth and Transition Metal Ions*; SPIE, 2002; Vol. 4766, pp 142–147.

(17) Wang, Z.; Ye, W.; Chu, I.-H.; Ong, S. P. Elucidating Structure–Composition–Property Relationships of the β-SiAlON:Eu^{2+} Phosphor. *Chem. Mater.* **2016**, *28* (23), 8622–8630.

(18) Harada, T.; Takamoku, K.; Nishiyama, K. Structural Analysis and Emission Properties of Ce3+ Complexes with N-Coordinating Tridentate Ligands in Solution. *J. Mol. Liq.* **2017**, *226*, 35–42.

(19) Bartoli, G.; Marcantoni, E.; Marcolini, M.; Sambri, L. Applications of $CeCl_3$ as an Environmental Friendly Promoter in Organic Chemistry. *Chem. Rev.* **2010**, *110* (10), 6104–6143.

(20) Koppe, J.; Pell, A. J. Structure Determination and Refinement of Paramagnetic Materials by Solid-State NMR. *ACS Phys. Chem. Au* **2023**, *3* (5), 419–433.

(21) Kocman, V.; Di Mauro, G. M.; Veglia, G.; Ramamoorthy, A. Use of Paramagnetic Systems to Speed-up NMR Data Acquisition and for Structural and Dynamic Studies. *Solid State Nucl. Magn. Reson.* **2019**, *102*, 36–46.

(22) Bartoli, G.; Bosco, M.; Marcantoni, E.; Sambri, L.; Torregiani, E. A Mild, Efficient, and Selective Method for the Desilylation of More Common Trialkylsilyl Ethers by Cerium(III) Chloride Heptahydrate and Sodium Iodide in Acetonitrile. *Synlett* **1998**, *1998* (2), 209–211.

(23) Wo\lcyrz, M.; Kepinski, L. Rietveld Refinement of the Structure of CeOCI Formed in Pd/CeO2 Catalyst: Notes on the Existence of a Stabilized Tetragonal Phase of La2O3 in LaPdO System. *J. Solid State Chem.* **1992**, *99* (2), 409–413.

(24) Vinograd, V. L.; Juarez-Arellano, E. A.; Lieb, A.; Knorr, K.; Schnick, W.; Gale, J. D.; Winkler, B. Coupled Al/Si and O/N Order/Disorder in BaYb[Si $_{4-x}$ Al $_{x}$ O $_{x}$ N $_{7-x}$]Sialon: Neutron Powder Diffraction and Monte Carlo Simulations. *Z. Für Krist.* **2007**, *222* (8), 402–415.

(25) Grins, J.; Shen, Z. J.; Nygren, M.; Ekström, T. Preparation and Crystal Structure of JEM-Phase Ln ($Si_{6-z}Al_{L+z}$)($N_{10-z}O_z$)(z-1.0, Ln= La, Ce, Nd, S). *J Mater Chem* **1995**, *5*, 2001–2006.

(26) Camuşcu, N.; Thompson, D. P.; Mandal, H. Effect of Starting Composition, Type of Rare Earth Sintering Additive and Amount of Liquid Phase on Sialon Transformation. **1997**.

(27) Joshi, B.; Lee, H. H.; Wang, H.; Fu, Z.; Niihara, K.; Lee, S. W. The Effect of Different Rare Earth Oxides on Mechanical and Optical Properties of Hot Pressed α/β-Sialon Ceramics. *J. Eur. Ceram. Soc.* **2012**, *32* (13), 3603–3610.

(28) Wang, S.; Song, Z.; Kong, Y.; Xia, Z.; Liu, Q. Crystal Field Splitting of 4fn−1 5d-Levels of Ce^{3+} and Eu^{2+} in Nitride Compounds. *J. Lumin.* **2018**, *194*, 461–466.

(29) Dierre, B.; Xie, R.-J.; Hirosaki, N.; Sekiguchi, T. Blue Emission of Ce^{3+} in Lanthanide Silicon Oxynitride Phosphors. *J. Mater. Res.* **2007**, *22* (7), 1933–1941.

(30) Yang, Z.; Zhao, Z.; Shi, Y.; Wang, C.; Wu, Q.; Wang, Y. Luminescence Properties and Energy Transfer of Ce^{3+}, Tb^{3+}-Coactivatedβ-SiAlON Phosphors. *J. Am. Ceram. Soc.* **2013**, *96* (6), 1815–1820.

(31) Chen, P.; Zhu, Q.; Takeda, T.; Hirosaki, N.; Xie, R.-J. A Promising Thermally Robust Blue-Green Li-α-Sialon: Ce^{3+} for Ultraviolet LED-Driven White LEDs. *J. Alloys Compd.* **2019**, *805*, 1004–1012.

(32) Wang, C.-Y.; ten Kate, O. M.; Takeda, T.; Hirosaki, N. Efficient and Thermally Stable Blue-Emitting Ce^{3+} Doped LaAl($Si_{6-z}Al_z$)($N_{10-z}O_z$)(JEM: Ce) Phosphors for White LEDs. *J. Mater. Chem. C* **2017**, *5* (32), 8295–8300.

(33) Xianqing, P.; Machida, K.; Horikawa, T.; Hanzawa, H. Synthesis and Luminescent Properties of Low Oxygen Contained Eu^{2+}-Doped Ca-α-SiAlON Phosphor from Calcium Cyanamide Reduction. *J. Rare Earths* **2008**, *26* (2), 198–202.

(34) Ryu, J. H.; Won, H. S.; Park, Y.-G.; Kim, S. H.; Song, W. Y.; Suzuki, H.; Yoon, C.-B.; Kim, D. H.; Park, W. J.; Yoon, C. Photoluminescence of Ce^{3+}-Activated β-SiAlON Blue Phosphor for UV-LED. *Electrochem. Solid-State Lett.* **2009**, *13* (2), H30.

(35) Gan, L.; Mao, Z.-Y.; Wang, Y.-F.; Xu, F.-F.; Zhu, Y.-C.; Huang, Q.; Liu, X.-J. Photoluminescence Properties of Ca–α-SiAlON:Ce^{3+} Phosphors as Function of Composition and Microstructure. *Ceram. Int.* **2013**, *39* (7), 8319–8326.

(36) Li, Y. Q.; Hirosaki, N.; Xie, R.-J.; Takeda, T.; Mitomo, M. Photoluminescence Properties of Rare Earth Doped α-Si3N4. *J. Lumin.* **2010**, *130* (7), 1147–1153.

(37) Hua, Y.; Li, X.; Zhang, D.; Ma, H.; Deng, D.; Xu, S. The Crystal Structure and Luminescence Properties of Novel Ce^{3+} and Ce^{3+}, Sm^{3+}-Activated Y_4SiAlO_8N Phosphors for near-UV White LEDs. *New J. Chem.* **2016**, *40* (6), 5458–5466.

(38) Gan, L.; Mao, Z.-Y.; Zhang, Y.-Q.; Xu, F.-F.; Zhu, Y.-C.; Liu, X.-J. Effect of Composition Variation on Phases and Photoluminescence Properties of β-SiAlON:Ce^{3+} Phosphor. *Ceram. Int.* **2013**, *39* (4), 4633–4637.

(39) Xie, R.-J.; Hirosaki, N.; Sakuma, K.; Yamamoto, Y.; Mitomo, M. Eu2+-Doped Ca-α-SiAlON: A Yellow Phosphor for White Light-Emitting Diodes. *Appl. Phys. Lett.* **2004**, *84* (26), 5404–5406.

(40) Shim, J.-I. Internal Quantum Efficiency. In *III-Nitride Based Light Emitting Diodes and Applications*; Seong, T.-Y., Han, J., Amano, H., Morkoç, H., Eds.; Topics in Applied Physics; Springer Singapore: Singapore, 2017; Vol. 133, pp 163–207.

(41) Armin, A.; Zarrabi, N.; Sandberg, O. J.; Kaiser, C.; Zeiske, S.; Li, W.; Meredith, P. Limitations of Charge Transfer State Parameterization Using Photovoltaic External Quantum Efficiency. *Adv. Energy Mater.* **2020**, *10* (41), 2001828.

General conclusion & Perspectives

The present work has focused on advancing the development of polymer-derived β-SiAlON with potential applications in phosphor-converted white light-emitting diodes (pc-WLEDs). The primary focus has been on synthesizing silicon alumina oxy-nitride (SiAlON) as the reference material using the Polymer-Derived Ceramics (PDC) route. The overarching objective was to introduce rare earth dopants ($EuCl_2$, $EuCl_3$, and $CeCl_3$) at molecular scale to form after heat-treatment in flowing ammonia up to 1000°C and then in nitrogen atmosphere up to 1600 °C Eu^{2+}/Eu^{3+}/Ce^{3+}-doped SiAlON ceramics with luminescence properties. Alternatively, Gas Pressure Sintering has been explored at high temperature. The anticipated outcome was to develop materials with superior compositional and structural uniformity, achievable at relatively low preparation temperatures.

Chapter I presented an up-to-date overview of the SiAlON-based phosphors, offering a comprehensive literature survey that encompasses synthesis techniques, microstructure examination, and photoluminescence properties. Additionally, the chapter delves into the realm of polymer-derived ceramics (PDC) methodology. The focus of this thesis centers on the PDC approach, as its primary advantage lies in the precise control it affords over material composition at the atomic level. The ability to design matter at molecular scale distinguishes the PDC route, providing a unique solution to challenges encountered in ceramic manufacturing with conventional powder-based technologies. This method allows for fine control over the chemical compositions and microstructure of advanced ceramics. Consequently, the research detailed in this manuscript revolves around the synthesis of β-SiAlON ceramic and rare-earth doped β-SiAlON ceramics.

Chapter II provided a description of the materials and methods employed in this thesis work. It presents an overview of the commercial preceramic polymers used, namely polysilazanes, as well as synthesis protocols aimed at modifying them, including the incorporation of divalent and trivalent europium chloride and cerium chloride at the molecular scale. The thermal processing equipment, and characterization methods employed are also described.

Chapter III provided a detailed outcome achieved in the development of low oxygen β-SiAlON ceramics by exploring the Polymer-Derived Ceramics (PDC) approach. The process involved the synthesis of aluminum-modified polysilazanes as precursors and ammonia and nitrogen atmospheres during pyrolysis and annealing treatments. The polysilazane used is Durazane®1800, a commercially available preceramic polymer. The chapter started by

elucidating the mechanisms governing the modification of this polymer with alane based on a complementary set of characterization tools such as elemental analysis and FTIR and solid-state NMR spectroscopy. They revealed that the synthesis involved major dehydrocoupling reactions, leading to the gradual formation of Al-N bonds with the decrease of the Si:Al ratio. Thus, polymer branching occurred upon decrease of the Si:Al ratio transforming the liquid Durazane®1800 into solid-state aluminum-modified polysilazanes. The latter were composed of Al-H bonds and tertiary amine groups as side groups because of the steric hindrance imposed by the gradual branching. Then, the low-temperature regime of the conversion into β-SiAlON has been shown to be primarily associated with transamination reactions, while the temperature range of 300 – 700 °C involved rearrangements, nucleophilic and coupling reactions, leading to the formation of $N(Si)_{3-x}(Al)_x$ units in the glassy ceramics formed at 1000 °C. Thus, the majority of the carbon-based groups bearing by the polymer are released in this temperature range while the material is enriched with nitrogen. The subsequent time-controlled room temperature oxidation of ammonia-treated samples involved the selective oxidation of Al, forming $AlN_{4-x}O_x$, AlO_4, and a small portion of AlO_6 units alongside SiN_4 environments. It was fixed at 1 minute before storing the samples in an inert atmosphere. The high temperature regime of the conversion into β-SiAlON occurred through the heat treatment of ammonia-treated samples up to 1600 °C in flowing nitrogen. It resulted in the complete crystallization (at 1600 °C) of the materials into a main phase - β-SiAlON – in presence of secondary phases - α-Si_3N_4, and/or w-AlN phases – whose contents depended on the Si:Al ratio. Notably, the β-SiAlON phase content decreased with an increase in the Si:Al ratio. Thus, it has been demonstrated that the **PAlSZ3_16** sample displayed the highest β-SiAlON phase content (more than 92 %) among all the samples. This sample (therefore its precursor **PAlSZ3**), characterized as a low-oxygen β-SiAlON material, has been selected for further consideration for doping in Chapter IV and V.

Chapter IV outlined the design process for low-oxygen β-SiAlON:Eu^{2+} . $EuCl_2$ and $EuCl_3$ have been introduced in the liquid Durazane®1800 within the specified range ($0.005 \leq Eu:Si \leq 0.05$) before the addition of alane on the mixture by fixing a Si:Al ratio of 3 according to the **PAlSZ3** synthesis discussed in Chapter III. The pyrolysis and annealing treatment procedures applied in Chapter III have been reproduced in this chapter. As an alternative high temperature process, we have explored the gas pressure sintering (GPS) of ammonia-treated samples. The polymer synthesis was not affected by the presence of europium as demonstrated by coupling elemental analysis and FTIR and solid-state NMR spectroscopies. Thus, solid-state precursors were

generated and their pyrolysis at 1000 °C under ammonia, followed by a time-controlled exposure to air, resulted in the formation of glassy ceramics. The latter subsequently underwent heat treatments at 1600 °C in flowing nitrogen and this delivered α-Si_3N_4, β-SiAlON, Phase_4, and/or w-AlN phases. The incorporation of europium luminescent centre in its chosen valence state Eu^{2+} or Eu^{3+} has been effectively discussed but no differences in the formation and microstructural characterization of β-SiAlON-based phosphors have been highlighted. However, the content of these phases was linked to the Eu content ($0.005 \leq Eu:Si \leq 0.05$) fixed in the early stage of the process. The β-SiAlON phase content increases with increasing Eu content but it could not reach the β-SiAlON phase content (75 % in **PAlEuCl$_2$0.05SZ3_16** with Eu:Si = 0.05) obtained for the **PAlSZ3_16** sample (92 %). The solubility of Eu in β-SiAlON owing to its larger cell parameters. Exploring GPS of ammonia-treated samples at 1800°C effectively reduced secondary phases and allowed to reach a β-SiAlON phase content as high as 99.4 % in the **PAlEuCl$_2$0.05SZ3_GPS18** sample. As a consequence, this significantly increased the intensity of photoluminescence emission. The optical characteristics of the polymer-derived β-SiAlON ceramics doped with Eu^{2+} and Eu^{3+} provided insights into their luminescent properties which comes out throughout all cylindrical particles that composed the materials. When excited at 410 or 460 nm, these ceramics emit light in the green spectral range (520-560 nm), exhibiting a red-shift towards longer wavelengths whatever the cation but the quantum efficiency differed when considering Eu^{2+} and Eu^{3+} dopants. Thus, it has been shown that the Eu^{3+} content was higher in materials derived from $EuCl_2$.

Chapter V investigated the development of low-oxygen β-SiAlON:Ce^{3+} ceramics through a methodology similar to that one developed in Chapter IV. $CeCl_3$ served as the dopant source to be mixed with the liquid Durazane®1800 within the specified range ($0.005 \leq Eu:Si \leq 0.05$) before the addition of alane on the mixture by fixing a Si:Al ratio of 3 according to the **PAlSZ3** synthesis discussed in Chapter III. The pyrolysis and annealing treatment procedures applied in Chapter III have been reproduced in this chapter. As an alternative high temperature process, we have also explored the gas pressure sintering (GPS) of ammonia-treated samples as in Chapter IV. The polymer synthesis was not affected by the presence of cerium as demonstrated by coupling elemental analysis and FTIR and solid-state NMR spectroscopies. Subsequent pyrolysis of precursors at 1000 °C in flowing ammonia and a time-controlled room temperature oxidation delivered an amorphous phase from which α-Si_3N_4 crystals emerged. Further heat treatments up to 1600 °C resulted in the complete crystallization into various phases, including α-Si_3N_4, β-SiAlON, JEM-SiAlON (mullite), and/or w-AlN. In contrast to the observations

made in Chapter IV, the β-SiAlON phase content decreased with increasing the dopant content, thereby the **PAlCe0.05SZ3_16** sample with the highest Ce:Si ratio (0.05) exhibited the lowest β-SiAlON phase content (54.7 %). This can be compared with the **PAlCe0.005SZ3_16** sample with the lowest Ce:Si ratio (0.005) which exhibited the highest β-SiAlON phase content (close to 82.6 %). Thus, the **PAlCe0.05SZ3_16** sample was selected to improve the β-SiAlON phase content. Exploring GPS of ammonia-treated samples at 1800°C effectively reduced secondary phases and allowed to reach a β-SiAlON phase content as high as 98.4 % in the **PAlCeCl$_3$0.05SZ3_GPS18** sample. Under 405 nm excitation, β-SiAlON:Ce^{3+} displayed blue emission, and microstructural analysis revealed a reduced incorporation of Ce^{3+} into the β-SiAlON host lattice. Incorporation occurred more at the grain boundary. The key conclusion is that **PAlCe0.01SZ3_16** represents the critical concentration for achieving the highest luminescent efficiency, allowing complete Ce integration within the β-SiAlON host lattice at lower dopant content.

The future developments and prospects of this thesis work encompass various levels, underscoring the breadth and openness of the research:

1. **At the 'SiAlON' level:**
    a. **Shaping of Aluminum-modified Polysilazanes:**

The polysilazanes modified by aluminum is a topic that requires further exploration in terms of shaping. It's noteworthy that the Si:Al ratio can be varied not only to tailor the β-SiAlON content but also the shaping potentiality of precereamic polymers. Thus, one objective is to prepare such materials as fibers in order to generate high temperature stable materials. This is currently done within the frame of the PhD thesis of Bastien Tolve-Granier.

2. **At the rare-earth-doped 'SiAlON' level:**
    a. **Doping with Rare Earth:**

Exploration of the preceramic polymeric precursor can be extended by incorporating multi rare earth cations in varying concentrations. This approach aims to provide a more detailed insight into the material. Additionally, focusing on applications of the obtained ceramics in biomedical fields, white light-emitting diodes (W-LED), or phosphor-converted LEDs (pc-LEDs) can enhance the practical implications of the research.

    b. **Design of Phosphor-in-Glass (PIG):**

The development of high-power white light-emitting diodes demands highly efficient and stable all-inorganic color converters. In this respect, phosphor-glass/ceramic composites show great

promise as they could combine the merits of high quantum efficiency of phosphors and high chemical and thermal stabilities of glass/ceramic matrices.

In summary, these proposed avenues for future work indicate the depth and scope of potential advancements. Exploring different precursors for polymer synthesis, understanding the impact of rare earth doping, leveraging the effects of gas evolution in the shaping process, and delving into the intricacies of thermal treatment techniques all contribute to expanding the knowledge base and practical applications of the research.

Synthèse à partir d'un polysilazane et caractérisation d'une céramique de type β-SiAlON à faible teneur en oxygène comme matériau hôte pour les luminophores émettant de la lumière bleue ou verte

Face au défi commun d'améliorer et de remplacer les techniques d'éclairage actuelles afin d'accroître l'efficacité et de réduire l'impact environnemental, l'utilisation de la technologie pc-WLED se présente comme une alternative prometteuse en s'affranchissant des inconvénients liés aux méthodes d'éclairage toxiques. Au cours de la dernière décennie, d'importantes recherches ont été consacrées à l'amélioration de l'efficacité luminescente et de la stabilité thermique des matériaux constituants cette technologie. Notre étude s'inscrit dans cette recherche.
Le β-SiAlON, réputé pour ses remarquables propriétés mécaniques, sa stabilité chimique et thermique, est un matériau hôte de référence pour les éléments terres rares et le développement d'une efficacité luminescente élevée. Il est synthétisé et dopé dans le cadre de cette thèse au moyen d'une voie 'précurseur' qui met en œuvre un polymère précéramique de type polysilazane, un complexe d'aluminium (Al) exempt d'oxygène et des chlorures d'europium (Eu) et de cerium (Ce).
Différents précurseurs ont été synthétisés en faisant notamment varier les rapports atomiques Si:Al et Eu/Ce:Si pour former par pyrolyse sous ammoniac jusqu'à 1000 °C puis traitement thermique à haute température sous azote des matériaux à base de β-SiAlON. Le matériau – dont la composition chimique et à la structure évoluent au cours de la montée en température - est analysée à chaque étape clé de la préparation du β-SiAlON - dopé ou non – et l'accent est plus particulièrement mis sur les effets du dopage par les éléments des terres rares sur la microstructure et les propriétés optiques des matériaux finaux.

Mots-clés : Diodes électroluminescentes à conversion par phosphore, céramiques dérivées de polymères, polysilazane, β-SiAlON, Europium, Cerium, synthèse, dopage, microstructure, environnement chimique, propriétés optiques.

Synthesis and characterization of polysilazane-derived low oxygen content β-SiAlON as host materials for blue- or green-emitting phosphors

Addressing the common challenge of enhancing and replacing current lighting techniques to improve efficiency and minimize environmental impact, the use of pc-WLED technology emerges as a promising alternative, eliminating the drawbacks associated with toxic lighting methods. Over the past decade, significant research and development efforts have been devoted to enhance luminescent efficiency and thermal stability. Our study is part of these efforts.

β-SiAlON, known for its outstanding mechanical properties, chemical stability, and thermal stability is an ideal host material for rare-earth elements in order to achieve high luminescence efficiency. It is prepared and doped within the framework of this PhD thesis using a 'precursor' route which uses a preceramic polymer such as a polysilazane, an oxygen-free aluminum (Al) complex and europium (Eu) and cerium (Ce) chlorides.

Different precursors have been synthesized by varying the Si:Al and Eu/Ce:Si atomic ratios to form materials based on β-SiAlON by pyrolysis under ammonia up to 1000 °C followed by heat treatment at high temperature under nitrogen. The material – whose chemical composition and structure evolve during the heat-treatments – is analyzed at each key stage of the preparation of β-SiAlON – doped or not – and the analysis is more particularly focused on the effects of doping with rare earth elements on the microstructure and optical properties of the final materials.

Keywords: Phosphor-converted white light diodes, polymer derived ceramics, β-SiAlON, Europium, Cerium, synthesis, doping, microstructure, chemical environment, optical properties.